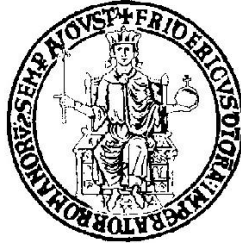


UNIVERSITÀ DEGLI STUDI DI NAPOLI “FEDERICO II”



Facoltà di Ingegneria

Dottorato di Ricerca in Ingegneria dei Sistemi Idraulici, di Trasporto e
Territoriali - XXV ciclo

TESI DI DOTTORATO

Depth-averaged models for dry granular flows

Coordinatore

Prof.ssa Arch. Elvira Petroncelli

Relatori

Prof. Ing. Armando Carravetta

Prof. Ing. Riccardo Martino

Prof.ssa Ing. Maria Nicolina Papa

Candidato

Luca Sarno

*To see a world in a grain of sand,
And a heaven in a wild flower,
Hold infinity in the palm of your hand,
And eternity in an hour.*
(William Blake)

Acknowledgements

Firstly, I would like to thank my supervisors, Prof. Ing. Armando Carravetta and Prof. Ing. Riccardo Martino, for giving me the great opportunity to experience this Ph.D. journey and for encouraging me during my research activity.

My warm thanks go also to my supervisor, Prof. Ing. Maria Nicolina Papa, who helped and supported me during my experimental research activities at the University of Salerno. Moreover, I wish to thank Ing. Nicola Immediata for his valuable help in experiments designing at the University of Salerno.

Special gratitude is due to Prof. Kolumban Hutter for giving me the opportunity to get in touch with Prof. Yih-Chin Tai, so as to have a fruitful international research period at the National Cheng-Kung University in Taiwan.

I would like to express my most sincere thanks to Prof. Yih-Chin Tai, who greatly helped me and taught me so much, during my research activities in Tainan. Moreover, I would like to thank Prof. Y. C. Tai again for making my stay in Taiwan very nice and profitable.

In Taiwan, I had also the pleasure of meeting many friends, Souta, Tsai and Lifan among the others (hoping they will forgive me for probably misspelling their names!), who helped me in many practical situations and contributed to make my experience in Taiwan wonderful.

I would like to sincerely thank Prof. Ing. Andrea Vacca for giving me many valuable suggestions to improve this dissertation.

I would like also to thank the Ph.D coordinators, Prof. Ing. Guelfo Pulci Doria and Prof.ssa Arch. Elvira Petroncelli, for their efforts to improve the quality of our Ph.D. School.

Finally, I wish to thank my parents and my girlfriend, Miriam, who have strongly encouraged me during these, sometimes tiring, years.

Napoli, April 2013

Abstract

Geophysical granular flows, such as snow avalanches and debris flows, represent a great hazard to man and infrastructures. These natural phenomena are characterized by the rapid flow of a granular solid phase, embedded in an ambient fluid. Since such events occur with little warning, in addition to investigating the triggering conditions, it is of crucial interest to predict their propagation and run-out distances.

The main purpose of the present research is to better understand the flow dynamics of dry granular flows, in the presence of no-slip bottom boundary conditions, and predict their propagation by using a depth-averaged approach. In this case, a stratification of different flow regimes, such as quasi-static and dense collisional, occurs and makes the utilization of the classical single layer depth-averaged models insufficient, because of important uncertainties about the velocity and shear stress distributions along the flow depth.

In the first part of the present work, an experimental-numerical study on dam-break flows of dry granular material is reported. It has been found that a modification to the formula, proposed in the Savage-Hutter model for calculating the earth-pressure coefficient, leads to an improved agreement with experimental data, in presence of no-slip bottom conditions.

In the second part, an experimental study on steady state velocity profiles of dry granular flows is reported. The granular material, used in this experimental research, was Ottawa sand (ASTM C-778 20/30). The velocity profiles at the side walls and free surfaces have been obtained, through granular PIV techniques. The measurements are in accordance with other experimental works on different granular materials and suggest the occurrence of a rheological stratification along the flow depth, in case of no-slip bottom condition.

In order to better describe such a complex flow dynamics, a two-layer depth-averaged model has been proposed. The dynamics of the two layers, ideally corresponding to dense-collisional and quasi-static regimes, have been considered independently. As well, mass exchanges between the layers have been calculated through a physically based closure equation. The well-known mathematical issue of the hyperbolicity loss in two-layer models has been carefully addressed. In order to overcome it, a local modification of source terms of the original mathematical model has been proposed. Such a treatment consists of introducing an extra resistance at the interface, if necessary, to avoid the hyperbolicity loss. This approach has been found to be robust and yields reasonable results, as long as the asymptotic steady state solution and boundary conditions fulfil the hyperbolicity requirements of the original model. Through comparisons with experimental data, the two-layer approach turns out to be very promising to describe the complex flow dynamics in case of no-slip bottom boundary conditions, although a more detailed description of the basal shear stress seems to be required.

In the third part of the present dissertation, the same two-layer approach has been used in order to rewrite the mathematical model in a curvilinear coordinates system, attached to the interface between the two layers. The model equations have been obtained, by using the same approach proposed in Tai and Kuo (2008). In the model derivation, the physically negligible quantities are identified in a more rational way than the previous model, by means of a scaling approximation.

Contents

1 Granular flows	1
1.1 Geophysical grain flows	2
1.2 Hydrodynamic approach	3
1.3 Flow regimes	7
1.4 Depth-Averaged models	11
1.5 Outline of the dissertation	13
2 Dam-break flows of dry granular material	19
2.1 The experimental apparatus	21
2.2 Experimental set-up for dam-break flows	21
2.2.1 The release gate	23
2.2.2 The granular material	23
2.2.3 Measuring instruments	26
2.2.4 The experiments	26
2.3 The Savage-Hutter model	26
2.3.1 The earth-pressure coefficient	27
2.3.2 Regularization formula for the early stages of dam break waves	28
2.4 Experimental validation	30
2.4.1 The numerical code	31
2.5 Parameter study	34
2.6 Conclusions	37
3 Steady state velocity profiles	40
3.1 Particle Image Velocimetry	41
3.1.1 Theoretical aspects	42
3.1.2 Granular PIV	44
3.2 Velocity profiles	45
3.2.1 Experimental apparatus	45
3.2.2 Granular PIV analysis	50
3.2.3 Experiments	51
3.2.4 Time averages	55
3.2.5 Side-wall velocity profiles	60
3.2.6 Free surface velocity	67

4	Two-layer depth-averaged models	75
4.1	Two-layer depth-averaged models	76
4.2	A two-layer approach to describe dry granular flows	82
4.2.1	Two-layer model derivation	83
4.2.2	Final model equations	89
4.2.3	The numerical scheme	92
4.2.4	Boundary conditions	97
4.3	Numerical Tests	99
5	Comparisons and discussion	113
5.1	Identification of the interface position in experimental velocity profiles	114
5.1.1	Inertial number distributions from experimental data	114
5.1.2	Critical inertial number	116
5.1.3	Interface positions in experimental velocity profiles	124
5.2	Friction angle at the interface	129
5.3	Comparisons	130
6	The two-layer model in curvilinear coordinates	137
6.1	The two-layer model in curvilinear coordinates	138
6.1.1	Mass and momentum equations in curvilinear coordinates	139
6.1.2	Upper layer boundary conditions	140
6.1.3	Depth-integration of the upper layer balance equations	143
6.1.4	Depth-integration of the lower layer balance equations	145
6.1.5	Depth integration of the momentum equation	147
6.2	Jump conditions at the interface	148
6.3	Mesh velocity	148
6.4	Scaling and approximations	149
6.4.1	The scaling of the upper layer equations	149
6.4.2	Dimensionless depth-averaged upper layer mass equation	152
6.4.3	Dimensionless depth-averaged upper layer momentum equations	153
6.4.4	Normal stresses in the upper layer	154
6.4.5	Expressions of the mixed tensor elements	155
6.5	The scaling of the lower layer equations	156
6.5.1	Dimensionless depth-averaged lower layer mass equation	157
6.5.2	Dimensionless depth-averaged lower layer momentum equation	157
6.6	Hypotheses about the velocity distribution	159
6.6.1	Lower layer	160
6.7	The final equations	160
6.8	Discussion and conclusions	162
7	Conclusions	165

<i>CONTENTS</i>	IV
A Mathematical notations and useful formulae	170
A.1 Main notations	170
A.2 Leibniz integral rule	171
A.3 Covariance and contravariance	171
A.3.1 Contravariant vectors	172
A.3.2 Covariant vectors	172
A.3.3 Tensor transformation	173
B Mathematical methods	174
B.1 The Unified Coordinate system	174
B.1.1 Useful relations	176
B.2 Coordinate transformation	178
B.2.1 The factorization of the Jacobian matrix	179
C <i>Big O</i> notation	182
Complete Bibliography	184

Chapter 1

Granular flows

Chapter Summary

In this chapter an introduction to geophysical granular flows is presented. The importance to better understand the propagation stages of such phenomena from the initiation to deposit is highlighted.

Particular attention is given to the mechanics that underlies such events, by focusing on the relatively simple case of *dry* granular flows. The main features observed in dry granular flows (e.g. the different flow regimes, force networks) are described.

Within the context of a *continuum mechanics* approach to granular flows, the most relevant findings in Literature are introduced and discussed. The still open problem of defining a *universal* constitutive law, capable to describe the rheology at the different flow regimes observed in dry granular flows and, especially, at the *dense collisional* transition regime, is highlighted.

Moreover, a review of depth-averaged models applied to dry granular flows, similar to the *Shallow Water* equations, is presented. Strengths and drawbacks of the existing background works are shown so that it is clear the direction taken by the present research.

The main goal of this chapter is to introduce the subject of the present dissertation. At the end of the chapter, a brief outline of the present dissertation is reported.

1.1 Geophysical grain flows

Geophysical grain flows, such as debris flows, snow avalanches, rock avalanches or pyroclastic flows, represent a great hazard to man and infrastructures. Although these events may seem very different from each other, they share many similarities. In fact, these natural phenomena are characterized by the rapid flow of a granular solid phase, embedded in an ambient fluid, which is usually water or air. Differently from the free surface flows typically observed in the context of river hydraulics, the flowing is *gravity-driven*, namely it is triggered and fed by the forces of gravity more than pressure gradients. By way of illustration, in Figs. 1.1 and 1.2 some pictures of avalanches and debris flows are shown.

Such events occur with little notice, typically exhibit high flow velocities, that can reach tens meters per second (e.g. Iverson, 1997; Ancey, 2001b), and are notorious for being able to travel unexpected long distances. The damage potential is usually high: by way of example, the volume involved in a large debris flow can reach 10^9 m³ and can release an enormous amount of potential energy, up to 10^6 J (Iverson, 1997). In Italy every year many snow avalanches and debris flows endanger human lives and damage structures located in mountain areas. It is worth to remind the catastrophic pyroclastic mudslides, occurred on 4th-6th May 1998 in the Apennine area near Vesuvius volcano (Naples, Southern Italy), that caused the death of more than 150 people, particularly in the town of Sarno. Furthermore, the risk of damage from such events is greatly increased over the last decades due to both an increased soil use and construction in high altitude and mountain areas.

On the one hand, it is very important to study the mechanisms leading to initiation or triggering. The study of the initiation stages of geophysical grain flows typically involves disciplines such as glaciology, hydrology and soil-mechanics. On the other hand, a proper description of the propagation stages, from initiation to deposit, is of great importance. In fact, a detailed knowledge of these phases would be very useful for a more reliable definition of risk areas, as well as for proper designing protection structures. The pressing need to better understand the dynamics of granular flows has recently caught the interest of many researchers from different fields (e.g. applied mathematics, fluid-dynamics, hydraulics and soil-mechanics).

The first step towards a better description of the propagation stage of geophysical granular flows would be to study the mechanics of the granular matter from a theoretical viewpoint. An in-depth study on the motion mechanisms of dry granular materials is also important in order to better design devices, used for transportation of granular material in industrial contexts.

Basically, two approaches could be chosen. The first one consists in describing the granular matter, as it is, namely, a set of discrete particles with some physical properties, that interact with each other and with physical boundaries according to the laws of classical dynamics. This approach has been followed e.g. by da Cruz et al. (2005) and, usually, makes use of discrete element numerical simulations, often referred to as *molecular dynamic simulations* (e.g Goldhirsch, 2003).

The second approach is the classical fluid-dynamic one. This approach requires to assume that the flowing granular matter can be treated as a *continuous medium*. This assumption, that could seem rather crude at first sight, is supported by the fact that grain flows, observed in nature, often exhibit a behaviour similar to viscous fluids (Ancey, 2001b). The hypothesis of continuous medium is acceptable as long as the flow domain is big enough with respect to the mean particle size. It is required for a proper application of the whole set of tools of *continuum* dynamics. Moreover, by

assuming that the processes under study are isothermal, the motion of grain flows can be described only by the mass and momentum balance equations, together with suitable boundary conditions and a proper constitutive law. This approach is often called *hydrodynamic* because it has been commonly adopted in an hydraulic engineering context in order to study the water dynamics.

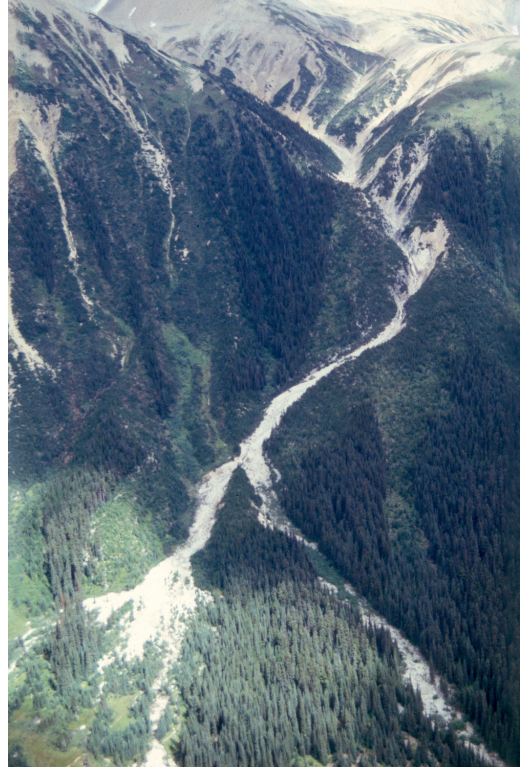


Figure 1.1: (left) Snow avalanche, source: R. Armstrong, NSIDC; (right) deposits of a channelized snow avalanche, source: Geological Survey of Canada.

For further information on snow avalanches the Reader is referred to monographic studies about this topic, e.g. Ancey (2001b), Salm (2004), or the comprehensive textbook Pudasaini and Hutter (2007).

For more information about debris flows, the Reader is referred e.g. to Iverson (1997) or Iverson and Vallance (2001) or to the monograph in Italian by Seminara and Tubino (1993).

Comprehensive reviews about the mechanics of granular flows are for example Savage (1984) and Ancey (2007). Further information about the gas-like regime could be found e.g. in reviews papers Campbell (1990) or Goldhirsch (2003).

1.2 Hydrodynamic approach

Firstly, by assuming that the grain matter can be described by an equivalent continuous fluid, every intensive physical property f , such as the flow velocity, is mathematically defined at every point \boldsymbol{x} of the spatial domain and represents the value of the following spatial mean over a reference



Figure 1.2: (left) Debris flow traces (Sarno, Southern Italy, May 1998); (right) rock avalanche, source: Geological Survey of Canada.

volume Ω that goes toward zero,

$$f(\mathbf{x}) = \lim_{\Omega \rightarrow 0} \frac{1}{\Omega} \int_{\Omega} f dV. \quad (1.1)$$

It should be pointed out that, from a physical viewpoint, the integral in Eq. (1.1) should be substituted by a summation over the discrete number of particles inside the reference volume, owing to the discrete character of granular matter.

Moreover, it should be kept in mind that the quantity expressed by Eq. (1.1) has a physical meaning only if the reference volume Ω is sufficiently bigger than the mean grain particle size. A “point-wise” measurement of an intensive physical quantity should be referred to the minimum volume on which the measurement is physically meaningful. This concept is reminiscent of the *Representative Elementary Volume (REV)*, widely used in groundwater hydraulics and environmental engineering.

Generally speaking, a constitutive law is a relation between the main physical quantities, involved in a given physical phenomenon. In the framework of hydrodynamics, it is also referred to as *rheological law* and consists of a relation between the shear rate tensor $\dot{\Gamma}$ and the stress tensor T .

By way of example, in plane shear of Newtonian fluids (e.g. water) the rheological law is represented by the well-known Newton’s law, that postulates the existence of a constant ratio, called *dynamic viscosity*, between the shear stress τ and the shear rate $\dot{\gamma}$.

Unfortunately, in grain flows things are much more complicated, because different momentum exchange mechanisms are involved and often coexist. The present dissertation is focused on dry granular flows, in which the ambient fluid is air. Therefore, this particular case will be discussed into detail hereafter. A detailed study of the complex interplay between the granular matrix and a dense ambient fluid (e.g. clear or muddy water), which is present in various granular flows such as debris flows or mud-flows, is beyond the scope of the present dissertation.

In the context of dry granular flows, the dynamic interactions between air and grain particles can be neglected, in the case of not too large grain velocities. Under these assumptions, the dynamics is uniquely governed by the momentum exchanges between the grains. The mechanisms of momentum exchange are mainly of two types: *frictional* and *collisional*. The first one occurs as a result of the relative sliding of grains, where the contacts between them are continuous over

time. The second one, conversely, occurs as a result of collisions between grains, which last for a short time compared to the time when the grains are free to move. These mechanisms are energy dissipative. During the grain sliding, part of the mechanic energy transforms into heat due to friction between grains. In collisions, the energy loss is mainly due to *non-elasticity* of grain collisions, owing to attrition, plastic deformation, micro-crack formations (Goldhirsch, 2003).

The relative importance of friction and collision mechanisms is related to another important quantity, the volume fraction ϕ . It is useful to give a definition of this physical quantity here because it will be widely used over the course of this dissertation. Given a reference volume inside the granular flow (big enough to be *representative*), the volume fraction ϕ is the ratio between the volume effectively occupied by the grain matter and the total reference volume. It is defined as follows,

$$\phi = \frac{V_g}{V_{tot}}. \quad (1.2)$$

By definition, ϕ is always between 0 and 1. For spherical particles with constant size, it can be shown that its maximum value is approximately 0.74. For natural grain matter at rest, typical values of ϕ are hardly found to be higher than 0.65 and mainly depend on the sedimentation history (e.g. Lambe and Whitman, 1991). Similarly to the stress tensor T , also the volume fraction, ϕ , depends on the shear rate $\dot{\gamma}$, in the case where ϕ is free to vary. In that case, such as in free-surface granular flows, an increase of $\dot{\gamma}$ typically produces a decrease of ϕ . This phenomenon is also known as *Reynolds' dilatancy* (Reynolds, 1885) and is mainly due to the fact that, owing to the shearing, the interlocking grains need to expand in volume in order to move around one another.

In the framework of *Rheometry*, laboratory shearing tests with granular material can be basically of two types: pressure-controlled or volume-controlled shearing tests (e.g. Forterre and Pouliquen, 2008). In the first kind of tests *dilatancy* is observed, because the volume fraction is free to adjust, analogously to what happen in free surface flows. Conversely, in the second kind of tests, the sample volume is kept constant during the shearing procedure and, thus, also the volume fraction is kept constant. In this case the normal pressures inside the shearing sample must increase in order to *counterbalance* the tendency of the grain material to expand.

The 1954 suspension experiment of Bagnold

A very first pioneering study on the rheology of granular mixtures was brought by Bagnold (1954). His experiments involved different neutrally buoyant granular mixtures, composed of spherical grains, made of paraffin wax and lead stearate, embedded in a Newtonian fluid of varying viscosity (water and a glycerine-water-alcohol mixture). Such mixtures were sheared in the annular space between two concentric drums. Although this work did not involve dry granular mixtures, we believe it is useful to report it here, because many of his findings are valid also in the context of dry granular flows and they represent a milestone for all researchers on the rheology of granular matter.

The experimental apparatus consisted of two concentric drums with diameter of 4.62 cm and 5.7 cm. The height of these cylinders was 5 cm. After placing the mixture in the space between the two cylinders, the outer cylinder was being rotated at a constant speed between 15 and 500 revolutions per minute, while the inside cylinder was kept at rest thanks to a spring, that allowed the measurement of torque M_t . By knowing the geometry of the inner cylinder and M_t , it was

possible to calculate the shear stress τ exerted by the mixture on the side surface of the inner cylinder. The side surface of the inner drum was made of a thin rubber sheet, that was able to deform owing to the normal pressure, exerted by the mixture. The volume inside the inner cylinder was permanently filled with water. Hence, by measuring the pressure of this fluid through a manometer, at the equilibrium it was possible also to estimate the normal pressure p exerted by the mixture on the side wall of the inner cylinder. The experiments were performed at different shear rates $\dot{\gamma}$, by keeping the volume fraction ϕ fixed.

Firstly, almost at every different shear rates, Bagnold observed a radial dispersive pressure. Moreover, interestingly such a dispersive pressure p was found to be roughly proportional to the shear stress τ .

Bagnold identified two different flow regimes. The first one, occurring at lower values of the shear rate, was called *macro-viscous* regime. In this regime the shear stress τ and the dispersive pressure p were found to depend linearly on $\dot{\gamma}$

$$\begin{aligned}\tau &\propto \lambda^{3/2} \mu \dot{\gamma} \\ p &\propto \lambda^{3/2} \mu \dot{\gamma}\end{aligned}$$

where λ is the *linear grain concentration*, namely the ratio between the grain diameter d and the mean distance between grains. The linear concentration is related to the solid volume fraction by

$$\lambda = \left[(\phi_0/\phi)^{1/3} - 1 \right]^{-1}$$

in which ϕ_0 is the maximum possible static volume fraction.

In this regime the main mechanism of momentum exchanges inside the mixture is due to the viscosity of the ambient fluid. This mechanism obviously does not take place in dry granular flows because of the negligible air viscosity. Moreover, it should be noted that these experiments have been performed under no-gravity like conditions, since the mixture was neutrally buoyant: therefore friction effects do not take place. Conversely, in free surface dry granular flows, because of gravity, the effect of friction is important and it strongly modifies the stress tensor T .

The second regime, called *grain-inertia* regime, occurs at high values of $\dot{\gamma}$ and exhibits a $\dot{\gamma}$ -quadratic dependence of the shear stress and dispersive pressure

$$\begin{aligned}\tau &\propto \rho d^2 \lambda^2 \dot{\gamma}^2 \\ p &\propto \rho d^2 \lambda^2 \dot{\gamma}^2\end{aligned}$$

where ρ is the grain density, which is equal to the ambient fluid density since the mixture is neutrally buoyant. In this case, the main mechanism of momentum exchange seems to be due to grain collisions. Although these results have been obtained for neutrally buoyant suspensions, this behaviour can be extended also to fast dry granular flows. In particular, these relations are valid in the collisional gas-like regime, that will be defined in detail further.

Bagnold also introduced a dimensionless number, named *Bagnold Number* after him, that is calculated as the ratio of collisional and viscous forces and can be written as follows,

$$N = \frac{\rho d^2 \lambda^2 \dot{\gamma}^2}{\mu \lambda^{3/2} \dot{\gamma}} = \frac{\rho d^2 \lambda^{1/2} \dot{\gamma}}{\mu}.$$

He found that the macro-viscous regime occurs approximately for $N < 40$, while the grain-inertia regime occurs for $N > 450$.

Although the Bagnold's findings have been partly criticized recently because of some possible issues of his experimental apparatus (Hunt et al., 2002), his significant contribution consists in having identified a link between shear stress and normal stresses in granular matter.

Nonetheless, it seems to be useful to remind that the experiments, performed by Bagnold, were at controlled volume fraction. What he called dispersive normal stresses only occurs when the volume fraction is kept constant. This phenomenon takes place since the granular material cannot decrease its volume fraction during the shearing (i.e. dilatancy). Conversely, in a free surface flow, in which there is no constraint, the volume fraction tends to decrease as the shear rate increases, owing to dilatancy.

1.3 Flow regimes

In dry granular flows, different motion regimes with different behaviours have been observed experimentally (e.g. Midi, 2004).

The shift from one to another regime is similar to a phase transition, because the granular material suddenly goes from a flowing state to another one with very different properties (e.g. Savage, 1984; Goldhirsch, 2003; Ancy, 2007). The main flow regimes are often referred to with terms that recall phase transitions: *solid-like*, *liquid-like* and *gas-like* regimes. Nonetheless, differently from actual phase transitions the molecular temperature does not play any role. In this regard, another kind of temperature, usually called *granular temperature* (Savage, 1984; Goldhirsch, 2003), can be defined as the average over a reference volume of the square of the fluctuating velocities of grain particles

$$T_g = \langle v'^2 \rangle. \quad (1.3)$$

The granular temperature T_g increases when the volume fraction decreases and is responsible for grain collisions.

In the case of small deformations and consequently high volume fraction, inter-granular contacts are long-lasting and momentum exchanges are mainly due to friction. Such a *solid-like* regime, often called *quasi-static* regime, can be roughly described by the classic models of the soil mechanics. Yet, the most of soil mechanic studies focus only on the failure mechanisms, i.e. the initiation of the motion, without being able to describe precisely what happens after the failure during long deformations.

At the opposite end, there is the *gas-like* regime, also called *dilute-collisional* regime, in which the particles interact with each other by means of short-lasting collisions, which often are binary and are due to the low volume fraction. In order to describe the gas-like regime, some kinetic theories, similar to the molecular gas theory, have been developed (for more details see e.g. Savage, 1984; Campbell, 1990; Goldhirsch, 2003). These theories, in addition to mass and momentum equations, need to consider also the kinetic energy balance equation. Moreover, the granular temperature, defined in Eq. (1.3), is used as *state variable* (e.g. Savage, 1984).

Between the aforementioned regimes, lies a transition regime, often called *dense-collisional* (to distinguish it from the dilute-collisional gas-like regime) or called *frictional-collisional* (Ancy, 2007), in which the behaviour of granular matter is *fluid-like* (Forterre and Pouliquen, 2008).

The volume fraction is smaller than the solid-like regime but it is large enough to allow that the momentum exchanges are due both to collisions and friction mechanisms.

Microscopic scale properties

A quantity often used to evaluate in a simple way the non-elasticity of grain collisions is the coefficient of restitution, e . It is a dimensionless quantity that can be defined as the ratio of the rebound velocity to initial velocity in a head-on binary collision and varies from 1 for perfectly elastic grains to 0 for perfectly inelastic grains. The coefficient of restitution e can be regarded as a microscopic scale property of the grain matter as it mainly depends on the material with which the grain particles are made. Molecular dynamic numerical simulations suggest that the restitution coefficient e does not influence very much the fluid dynamics in dense-collisional regime. Yet, e seems to be responsible for the transition from the *liquid-like* regime (i.e. *dense-collisional*) to the gas-like regime. For every given grain material, it could be found a critical value of volume fraction ϕ_c above which the gas-like regime is observed. The bigger is e , the smaller is ϕ_c and, thus, the wider is the domain where the gas-like regime is observed at the expense of the liquid-like regime (Forterre and Pouliquen, 2008).

Beside to e , another microscopic scale property can be defined: the inter-particle friction coefficient (e.g. Midi, 2004). It is a dimensionless quantity that accounts for the friction between the grain surfaces and, thus, only depend on the roughness of the grain surface.

Some experimental studies and molecular dynamic numerical simulations have shown that the influence of this property on the macro-scale flow dynamics is very limited (Midi, 2004). In particular, the inter-particle friction coefficient has almost no influence on the flow dynamics, as long as it is sufficiently far from zero, which is very common in real geophysical flows, that involve natural grain material. The reason of this apparently strange phenomenon is due to the fact that the *macroscopic* friction between grains is mainly due to the shape and size of grains, much more than inter-particle friction coefficient: the relative sliding of two layers of grain causes the grains of the upper layer to “climb” over the grains of the lower layer. Therefore, typically the bigger is the mean particle size, the bigger is the shearing resistance.

These findings are very interesting because suggest that the microscopic properties weakly influence the flow dynamics. As it will be clear further on, the properties that mostly influence the flow dynamics are at the scale of the grain size d (Midi, 2004).

Grain-scale properties

Differently from the microscopic properties, it has been found that the properties at the scale of grain size (d) are much more important in the flow dynamics (Midi, 2004).

The dimensional analysis permits to define some constraints to the formulation of constitutive law of dry granular flows. In the simple case of plane deformation of rigid grains of constant size and without ambient fluid, the rheological parameters must depend on two dimensionless numbers.

The first one is the macroscopic friction coefficient φ that accounts for the momentum exchanges, due to the Coulomb type momentum exchange between grain particles. As already stated in the previous section, this quantity mainly depends on the size and shape of grain particles. Under the plane shear condition, the Coulomb friction law relates the shear stress and the normal

stress by mean of the following relation

$$\tau = \sigma \tan \varphi. \quad (1.4)$$

The second dimensionless parameter is the so-called *Savage Number* (Savage, 1984), also known as *Coulomb Number* (Ancey et al., 1999). More recently, some scientific works often refer to the square root of the Savage number, renamed *inertial number* (e.g. da Cruz et al., 2005; Forterre and Pouliquen, 2008) and written as follows

$$I = \frac{\dot{\gamma}d}{\sqrt{P/\rho_s}} \quad (1.5)$$

in which $\dot{\gamma}$ is the shear rate, d the grain diameter, P the normal pressure exerted on the grain material and ρ_s the density of the grain. This dimensionless number can be regarded as the ratio between two time scales. The first one, $d/\sqrt{P/\rho_s}$, is a *microscopic* time scale and represents the time scale of grain rearrangements. It is the typical time it takes for a grain particle in order to fall into an hole of size d under the effect of the confining pressure P . Conversely, the second time scale, $1/\dot{\gamma}$, is of macroscopic type and represents the time scale of the mean deformation of the granular pile (e.g. Pouliquen, 2009).

In the quasi-static solid-like regime, I is very small because the macroscopic time scale of deformations is small compared with the microscopic type scale of grain rearrangements. On the contrary, in the dilute collisional gas-like regime, I exhibits large values because the macroscopic deformations occur faster than grain rearrangements, owing to grain collisions. Because of this connection with flow regimes, I can be also regarded as a measure of the ratio between the collision and friction effects on the momentum exchange.

The dense-collisional regime

As already stated in the previous sections, in the dense-collisional regime, friction mechanisms cannot be neglected as an effect of relatively high volume fraction. A rheological law is demanded also for this regime, but, to date, none of the proposed approaches is universally accepted. The main issue is the need to incorporate in a single law friction and inertial-collision effects.

One of the first rheological laws for describing the dense-collisional regime has been proposed by Savage (1979). The one-dimensional form of this approach, also reported by Ancey (2007), can be written as

$$\tau = \sigma \tan \varphi + \mu(T) \dot{\gamma} \quad (1.6)$$

where the first term represents the friction contribution, which is assumed of Coulomb type, while the second term stands for the collisional contribution and it is of viscous type with the viscosity μ depending on the granular temperature.

Recently, Midi (2004) and Jop et al. (2005) proposed a constitutive law for describing dense granular flows (i.e. liquid-like regime), that is based on a Coulomb friction law where the friction coefficient depends on the *inertial number*. The one-dimensional form of this rheological law can be written as follows

$$\tau = \sigma \mu(I). \quad (1.7)$$

In Jop et al. (2005) and Forterre and Pouliquen (2008) the following relations have been found from experimental data fitting.

$$\mu(I) = \mu_{min} + \frac{\mu_{max} - \mu_{min}}{I_0/I - 1}, \quad \phi(I) = \phi_{max} + (\phi_{min} - \phi_{max}) I$$

where μ_{min} is the friction coefficient at the beginning of the motion (i.e. at $I = 0+$), while μ_{max} is the maximum friction coefficient at high values of shear rates, namely when $I \rightarrow \infty$. The dependence of ϕ has been found to be almost linear with I and therefore increasing with distance from the free surface. A tensorial generalization of the constitutive equation (1.7) is given in Jop et al. (2006) and numerical simulations were compared successfully with experimental data, obtained in laboratory *heap-flow* geometrical configuration (e.g. Midi, 2004).

Although this model is very attractive because of its inner simplicity, it is not capable to describe some important features of the flow, such as the transition between the solid-like regime and dense-collisional regime or the hysteresis of the friction coefficient, observed experimentally between the initiation and stopping stages of flows.

Another approach is that one proposed by Josserand et al. (2004) that, differently from (Jop et al., 2005), introduce a rheological law where the shear stress depends on the volume fraction ϕ instead of the inertial number I ,

$$\tau = \sigma \mu(\phi) + \rho d^2 \mu_T(\phi) \dot{\gamma}^2. \quad (1.8)$$

where d is the grain size and ρ is the bulk density.

All of these aforementioned approaches typically yield results in agreement with experimental observations only for some particular flow conditions. Yet, they cannot capture all the features observed in different flow conditions and with different granular materials.

The formulation of a unified rheology to describe the *dense collisional* regime is still an open problem and it is a topic of great interest for physicists and engineers. Furthermore, a *universal* constitutive law, that would be capable to describe properly the grain motion at different flow regimes and also the transition from one regime to another, is still lacking.

The existence of a local rheology

Even before looking for an optimal rheology, another open problem that should be addressed concerns the existence of a local rheology, namely the existence of a relationship between the local stress tensor and local shear rate tensor. In fact, in dense-collisional regime and also in the solid-like regime the hypothesis of a local rheology is strongly undermined by the occurrence of *particle networks*. Such clusters or networks of particles with enduring contact are able to transmit and diffuse stresses and so they are often referred to as *force networks*.

It is understood that such networks influence the stress tensor by means of non-local effects (e.g. Pouliquen and Chevoir, 2002; Pouliquen, 2009). In this regard, in addition to the grain scale, another intermediate geometric scale, sometimes called *mesoscopic scale* (e.g. Goldhirsch, 2003), should be taken into account in order to describe the flow dynamics. Roughly speaking, such an intermediate scale should have the length of the mean force chain.

Nevertheless, it is not yet clear to what extent such non-local effects modify the local stresses and whether a local rheology can still be used as a working hypothesis or as a practical approximation for describing these phenomena in an engineering context.

Rheological stratification

Some experimental works have shown that a rheological stratification often occurs in free-surface dry granular flows (Drake, 1990), namely there is a coexistence of two (or even three) flow regimes in the same flow cross section. Such phenomenon takes place, mainly, in case of a *no-slip* boundary condition at the bottom surface. In fact, because of the no-slip bottom boundary condition, a lower domain in solid-like regime exists, where the granular material is subject to a slowly creeping flow, as observed experimentally by Komatsu et al. (2001).

Conversely, in the upper part of the flow, a liquid-like dense-collisional flow develops up to the free surface. This kind of flows is usually referred to as *surface flows*. This geometrical configuration in a laboratory context can be found in rough bed chutes and *heap-flows* as well as in rotating drums (Midi, 2004).

In case of high flow velocities, an additional gas-like layer develops up to the liquid-like layer. It is observed in Nature in the so-called *mixed-motion snow avalanches* that exhibit a lower dense flowing layer and an upper *air-borne* low density layer (e.g. Ancey, 2001b). The reason of such a rheological stratification is due to bottom boundary condition that imposes null shear rate. Such a kinematic boundary condition causes the increase of the volume fraction ϕ along the flow depth, from the free surface towards the bottom surface, owing to the increased confining normal pressure. In fact, the inertial number I that accounts for the relative effect of collisions and friction, decreases with the depth from the free surface because the confining pressure increases and the shear rate $\dot{\gamma}$ decreases owing to the basal boundary condition.

In Fig. 1.3 an explanatory picture, describing the stratification of flow regimes in *surface flows* is reported (Forterre and Pouliquen, 2008). A similar stratification has also been found in granular-liquid mixtures by Armanini et al. (2005, 2009), although the viscous effects due to the ambient fluid render much more complex the flow dynamics.

As well as the transition between the dense-collisional to dilute-collisional regime seems to be governed by a dimensionless parameter that is the restitution coefficient e , analogously also the transition between the quasi-static solid-like and dense-collisional regime is expected to be controlled by a dimensionless number that is likely to be the inertial number. Nevertheless, at present, the mechanisms that cause the transition from the solid-like to the dense-collisional regime are not completely understood.

1.4 Depth-Averaged models

Despite the big lack of knowledge about the dynamics of granular flows and still open problems about the constitutive law, in recent years many efforts have been made to solve practical technical problems related to geophysical granular flows. The main goals of such engineering approaches are to better define the risk areas due to avalanches and debris flows and to properly design protection infrastructures.

Most of these approaches are based on depth-averaged models. These models are obtained by integrating along the flow depth the mass and momentum balance equations together with proper boundary conditions and simplifying assumptions like the well-known *Long Wave Approximation*. As regards the one-dimensional case, the *Long Wave Approximation* consists in assuming that the characteristic length, related to the avalanche spreading in the flow direction x is much bigger

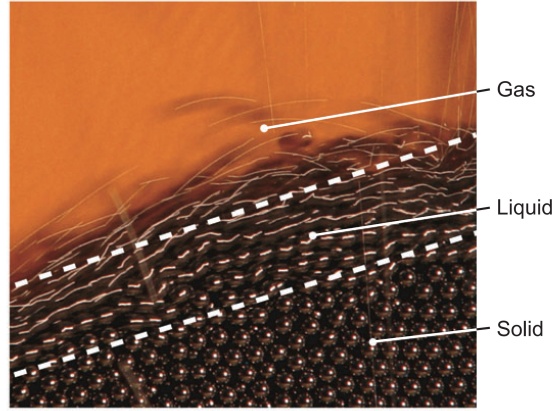


Figure 1.3: Rheological stratification (Forterre and Pouliquen, 2008).

than the characteristic length H along the normal to bed direction z . Such an assumption leads to shallow water type models that in their one-dimensional form are similar to the well-known *De Saint Venant* equations. The final equations typically consist of a partial differential equations (PDE) system of hyperbolic type. With this approach, the very complex rheology that influences the flow dynamics of granular flows, is enormously simplified by being incorporated into the basal shear stress and into the *Boussinesq coefficient*.

One of the earliest and most famous models with a depth-averaged approach in the context of the avalanches of dry material is the Savage Hutter model, proposed by Savage and Hutter (1989). Its original formulation consists of a hyperbolic system of two partial differential equations that describes the motion of a granular pile along an inclined plane

$$\begin{cases} \partial_t h + \partial_x(hu) = 0, \\ \partial_t(hu) + \partial_x(K(\varphi, \delta) g_z/2 h^2 + \beta hu^2) = g_x h - g_z h \tan \delta \operatorname{sgn}(u) \end{cases} \quad (1.9)$$

where u is the depth-averaged velocity, h is the flow depth, $g_x = g \sin \alpha$ and $g_z = g \cos \alpha$ represent the x - and z -component of the gravity acceleration, respectively, where α is the basal inclination angle, K is an earth-pressure coefficient, relating the normal pressure exerted on a surface normal to the flow direction with that exerted on a surface parallel to the basal surface, δ and φ are the basal and internal friction angles, respectively. The parameter β is the *Boussinesq coefficient*, whose value is determined by the velocity distribution along the flow thickness. In SH theory a uniform velocity distribution is assumed, i.e. $\beta = 1$. This model was afterwards generalized to more complex geometries (Hutter and Koch, 1991; Greve and Hutter, 1993; Greve et al., 1994; Gray et al., 1999). It is based on the assumption that the constitutive law at the basal surface of the flowing material is of Coulomb-type, i.e.

$$\tau|_b = \sigma_z \tan \delta \quad (1.10)$$

where σ represents the normal pressure at the basal surface and δ is the angle of friction between the granular material and the basal surface. The strong hypothesis of constant friction angles, φ and δ , is based on some experimental observations (e.g. Hungr and Morgenstern, 1984).

The model incorporates the anisotropy of the granular material, by using the earth pressure coefficient K that allows to write the normal stress exerted along the cross section surface σ_x as function of the normal stress exerted along the basal surface σ_z . In its original formulation, K is a two-value step function depending on the internal friction angle φ , the basal friction angle δ and the spatial derivative of the flow velocity u . A more detailed description of this formula can be found in Chapter 2 of the present dissertation.

The numerical integration of equations of SH model presents some difficulties because of the discontinuous behaviour of the earth pressure coefficient K . In order to overcome these numerical issues, a regularized version of the earth pressure coefficient has been proposed by Tai and Gray (1998). The numerical techniques adopted most successfully for solving numerically the SH model are the NOC schemes (e.g. Tai et al., 2002) or the finite volume schemes with approximate Riemann solvers HLL or HLLC (Vollmöller, 2004).

The main strength of the SH model relies on its very simple formulation: the model only has two parameters, that are the friction angles φ and δ . Those parameters can ideally be measured independently because they have a precise physical meaning. However, in real case situations, e.g. in order to predict snow avalanches run outs, the friction angles often need to be calibrated by means of a back analysis on previous data (Ancy, 2001b). Moreover, the model is scale independent. It permits to extend the validity of the model to real scale events, just by comparing its results with laboratory experiments. Numerous laboratory experiments showed that the SH model is capable to predict the propagation of granular avalanche in presence of steep slopes and smooth basal surfaces (Hutter et al., 2005). The same model has also been used with some success to describe the motion of solid phase in two-phase type models designed for studying debris flows (Iverson, 1997; Denlinger and Iverson, 2001).

Nonetheless, the SH model exhibits some limitations. Firstly, according to the rheological assumption of Coulomb type basal friction, the steady state flow is expected to occur only whenever the slope of the basal surface is equal to the basal friction angle δ . This is in contrast with some experimental observations (Ancy, 2001a; Pouliquen, 1999) that showed the existence of steady state motion for a rather large range of bottom inclination angles (of order of 5° - 10°).

In addition, some experimental studies showed (e.g. Pouliquen and Forterre, 2002) that in cases of rough bed surfaces, the SH model seems to be less suitable to properly describe the avalanche motion. Probably, neither the assumption of a pure Coulomb-type basal shear stress nor the assumption of a constant velocity distribution inside the flowing pile (i.e. *Boussinesq* coefficient set equal to 1) are acceptable in this situation.

1.5 Outline of the dissertation

In the previous section we have provided a brief overview on the existing depth-averaged models, with particular attention to the Savage-Hutter model (Savage and Hutter, 1989).

The Savage-Hutter model, that exhibits a basal shear stress independent from the shear rate, could be considered a zero-order model, because the rheology of flowing material is actually not specified. In fact, the assumed Coulomb law does not impose any condition to the shear rate $\dot{\gamma}$. Its main strength is the possibility to measure the two parameters by independent physical measurements. Nevertheless, in the case of *no-slip* basal boundary conditions, it has been observed

that such a simple Coulombian resistance is insufficient to predict with good accuracy the flow motion.

In that case, the observed stratification of quasi-static and dense-collisional regimes makes difficult a depth-averaged approach. A reliable model should be capable to predict the extent of the dense-collisional and quasi-static domains. Moreover, a more strong shear rate dependence of the shear stress is expected in the dense collisional regime, differently from the quasi-static regime. For this reason also the velocity profile in these different regimes is expected to be very different.

At this moment many questions arise: what is the extension of the dense-collisional flowing layer? Is the hypothesis of hydrostatic distribution of normal pressure acceptable in the whole physical domain? What is the influence of network forces in quasi-static and dense-collisional regions?

Moreover, particular attention should be paid to the choice of the earth-pressure coefficient that appears in the momentum equation of the SH model and serves to relate parallel and normal to bed stresses.

From this rather complex picture about the dynamics of dry granular flows, it emerges that a further improvement of depth-averaged models is hoped for better describing the propagation stages of dry granular flows in case of *no-slip* basal boundary condition. In this case, the hypothesis of a unique rheology for the flowing layer seems to be in contrast with the stratification of flow regimes observed experimentally in heap flows and rotating drum geometries.

A partial answer to these open questions could be given by a new model, capable to describe such a rheological stratification and the effective velocity distribution along the flow depth. After some experimental investigations on dry granular flows in transient and steady state, in the present dissertation we propose a two-layer depth-averaged approach with the aim of overcoming these issues.

In particular, the present dissertation focuses on dry granular flows with no-slip bottom boundary condition and it is aimed to partly answer some of these questions.

In Chapter 2, the reliability of Savage-Hutter type depth-averaged models in dam-break problems is addressed. Smooth and rough bed boundary conditions have been separately investigated. Particular attention is given to the optimal choice of the earth-pressure coefficient to be used at the early stages of dam-break flows.

In Chapter 3, an experimental research that makes use of Particle Image Velocimetry (PIV) applied to granular flows is presented. The main goal is to obtain information about the velocity profiles at the side walls of the channel, in order to identify the extension of the solid-like and dense-collisional domain in case of no-slip boundary condition.

In Chapter 4, a depth-averaged two-layer approach is proposed in order to better describe the transition from the solid-like regime to the dense-collisional regime. The main mathematical and numerical problems related to this approach are addressed and discussed.

In Chapter 5, comparisons between the proposed numerical model and experimental data are reported and discussed.

In Chapter 6, a two-layer depth-averaged model, written in curvilinear coordinates, is proposed. In this Chapter, the derivation of this mathematical model and its main features are presented and discussed.

In Chapter 7, the main findings of this dissertation are summarized and discussed. As well,

perspectives and further developments of the present research are highlighted.

References Used in This Chapter

- Ancey, C. (2001a). Dry granular flows down an inclined channel: Experimental investigations on the frictional-collisional regime. *Physical Review E* **65**, 1–19.
- Ancey, C. (2001b). Snow Avalanches. In Balmforth, N. J. and Provenzale, A., editors, *Geomorphological fluid mechanics - Lecture notes in Physics Volume 582*, pages 319–338. Springer.
- Ancey, C. (2007). Plasticity and geophysical flows: A review. *Journal of Non-Newtonian Fluid Mechanics* **142**, 4–35.
- Ancey, C., Coussot, P., and Evesque, P. (1999). A theoretical framework for granular suspensions in a steady simple shear flow. *Journal of Rheology* **43**, 1673–1699.
- Armanini, A., Capart, H., Fraccarollo, L., and Larcher, M. (2005). Rheological stratification in experimental free-surface flows of granular-liquid mixtures. *Journal of Fluid Mechanics* **532**, 269–319.
- Armanini, A., Larcher, M., and Fraccarollo, L. (2009). Intermittency of rheological regimes in uniform liquid-granular flows. *Physical Review E* **79**, 051306.
- Bagnold, R. A. (1954). Experiments on a Gravity-Free Dispersion of Large Solid Spheres in a Newtonian Fluid under Shear. *Proceedings of the Royal Society A: Mathematical, Physical and Engineering Sciences* **225**, 49–63.
- Campbell, C. S. (1990). Rapid granular flows. *Annual Review of Fluid Mechanics* **22**, 57–90.
- da Cruz, F., Emam, S., Prochnow, M., Roux, J.-N., and Chevoir, F. (2005). Rheophysics of dense granular materials : Discrete simulation of plane shear flows. *Physical Review E* **72**, 24.
- Denlinger, R. P. and Iverson, R. M. (2001). Flow of variably fluidized granular masses across three-dimensional terrain: 2. Numerical predictions and experimental tests. *Journal of Geophysical Research* **106**, 553.
- Drake, T. G. (1990). Structural features in granular flows. *Journal of Geophysical Research* **95**, 8681–8696.
- Forterre, Y. and Pouliquen, O. (2008). Flows of Dense Granular Media. *Annual Review of Fluid Mechanics* **40**, 1–24.
- Goldhirsch, I. (2003). Rapid Granular Flows. *Annual Review of Fluid Mechanics* **35**, 267–293.
- Gray, J. M. N. T., Irmer, A., Tai, Y. C., and Hutter, K. (1999). Plane and oblique Shocks in shallow granular flows. In *22nd International Symposium on Shock Waves*, pages 1447–1452, London, U.K. Imperial College.
- Greve, R. and Hutter, K. (1993). Motion of a Granular Avalanche in a Convex and Concave Curved Chute: Experiments and Theoretical Predictions. *Philosophical Transactions of the Royal Society A: Mathematical, Physical and Engineering Sciences* **342**, 573–600.

- Greve, R., Koch, T., and Hutter, K. (1994). Unconfined Flow of Granular Avalanches along a Partly Curved Surface. I. Theory. *Proceedings of the Royal Society A: Mathematical, Physical and Engineering Sciences* **445**, 399–413.
- Hungr, O. and Morgenstern, N. (1984). Experiments on the flow behaviour of granular materials at high velocity in an open channel. *Geotechnique* **34**,
- Hunt, M. L., Zenit, R., Campbell, C. S., and Brennen, C. E. (2002). Revisiting the 1954 suspension experiments of R. A. Bagnold. *Journal of Fluid Mechanics* **452**, 1–24.
- Hutter, K. and Koch, T. (1991). Motion of a Granular Avalanche in an Exponentially Curved Chute: Experiments and Theoretical Predictions. *Philosophical Transactions of the Royal Society A: Mathematical, Physical and Engineering Sciences* **334**, 93–138.
- Hutter, K., Wang, Y., and Pudasaini, S. P. (2005). The Savage-Hutter avalanche model: how far can it be pushed? *Philosophical transactions. Series A, Mathematical, physical, and engineering sciences* **363**, 1507–28.
- Iverson, R. M. (1997). The physics of debris flows. *Reviews of Geophysics* **35**, 245.
- Iverson, R. M. and Vallance, J. W. (2001). New views of granular mass flows. *Geology* **29**, 115.
- Jop, P., Forterre, Y., and Pouliquen, O. (2005). Crucial role of sidewalls in granular surface flows: consequences for the rheology. *Journal of Fluid Mechanics* **541**, 167–192.
- Jop, P., Forterre, Y., and Pouliquen, O. (2006). A constitutive law for dense granular flows. *Nature* **441**, 727–30.
- Josserand, C., Lagrée, P.-Y., and Lhuillier, D. (2004). Stationary shear flows of dense granular materials: a tentative continuum modelling. *The European physical journal. E, Soft matter* **14**, 127–35.
- Komatsu, T., Inagaki, S., Nakagawa, N., and Nasuno, S. (2001). Creep Motion in a Granular Pile Exhibiting Steady Surface Flow. *Physical Review Letters* **86**, 1757–1760.
- Lambe, T. and Whitman, R. (1991). *Soil Mechanics*. Series in Soil Engineering. Wiley.
- Midi, G. (2004). On dense granular flows. *The European physical journal. E, Soft matter* **14**, 341–65.
- Pouliquen, O. (1999). Scaling laws in granular flows down rough inclined planes. *Physics of fluids* **11**, 542–548.
- Pouliquen, O. (2009). Granular Flows. In *Séminaire Poincaré XIII*, pages 69–100.
- Pouliquen, O. and Chevoir, F. (2002). Dense flows of dry granular material. *Comptes Rendus Physique* **3**, 163–175.
- Pouliquen, O. and Forterre, Y. (2002). Friction law for dense granular flows: application to the motion of a mass down a rough inclined plane. *Journal of Fluid Mechanics* **453**, 133–151.

- Pudasaini, S. P. and Hutter, K. (2007). *Avalanche dynamics: dynamics of rapid flows of dense granular avalanches*. Springer.
- Reynolds, O. (1885). On the dilatancy of media composed of rigid particles in contact. *Philos. Mag. Ser. 5* **50**,.
- Salm, B. (2004). A short and personal history of snow avalanche dynamics. *Cold Regions Science and Technology* **39**, 83–92.
- Savage, S. (1984). The mechanics of rapid granular flows. *Advances in applied mechanics* **24**, 289–366.
- Savage, S. B. (1979). Gravity flow of cohesionless granular materials in chutes and channels. *Journal of Fluid Mechanics* **92**, 53–96.
- Savage, S. B. and Hutter, K. (1989). The motion of a finite mass of granular material down a rough incline. *Journal of Fluid Mechanics* **199**, 177–215.
- Seminara, G. and Tubino, M. (1993). Debris flows: Meccanica, controllo e previsione. *Gruppo Nazionale per la Difesa dalle Catastrofi Idrogeologiche. Roma, CNR, Presidenza del Consiglio del Ministri, Dipartimento della Protezione Civile* pages 3–8.
- Tai, Y. C. and Gray, J. M. N. T. (1998). Limiting stress states in granular avalanches. *Annals of Glaciology* **26**, 272–276.
- Tai, Y. C., Noelle, S., Gray, J. M. N. T., and Hutter, K. (2002). Shock-Capturing and Front-Tracking Methods for Granular Avalanches. *Journal of Computational Physics* **175**, 269–301.
- Vollmüller, P. (2004). A shock-capturing wave-propagation method for dry and saturated granular flows. *Journal of Computational Physics* **199**, 150–174.

Chapter 2

Dam-break flows of dry granular material

Chapter Summary

In this Chapter, an experimental-numerical study on dam-break flows of dry granular materials is reported and discussed.

The experimental activity has been performed at the LIDAM (Laboratory of Environmental and Maritime Hydraulics of the University of Salerno, Italy), under the supervision of Prof. Ing. Maria Nicolina Papa.

The main purpose of the present research is to better understand to what extent depth-averaged models, like the Savage-Hutter model, are capable to describe dry granular avalanches in presence of different bottom boundary conditions. Smooth and rough bed boundary conditions are separately analysed.

Moreover, an important issue is the determination of the earth-pressure coefficient K in Savage-Hutter type models, at the early stages of dam-break waves. In this time window, the main physical quantities, such as flow velocity and stresses, dramatically vary along the flow direction and also the normal to bed component of flow velocity is not negligible. Hence, the hydrostatic pressure assumption is not fulfilled at the flow initiation. However, models with hydrostatic pressure assumption are often employed beyond their formal limits in an engineering context.

In this regard, we tried to shed light on the following question: what is the optimal choice for the pressure coefficient in depth-averaged Savage-Hutter type models, to be used at the early stages of a dam-break problem?

This problem has already been addressed by Hungr (2008) in a Lagrangian numerical context (DAN model), and a correction of the formula proposed by Savage and Hutter, depending on the local free surface slope has been proposed. In this work we propose a new regularization formula that makes the earth-pressure coefficient K , at the early stages of dam-break flow, vary between a minimum value, which is calculated by means of the Rankine formula, and a maximum value, calculated by means of the original Savage-Hutter formula. This new formulation seems to be more stable in our finite-volume framework than the one proposed by Hungr (2008). The

comparison between numerical simulations and laboratory experimental data shows an apparent improvement in describing the early stages of dam-break waves over rough beds. The comparison with experiments over smooth bed surface exhibits minor evidence of improvement. Nonetheless, in this case the proposed formula yields results very similar to those obtained by the original Savage-Hutter formula.

The main results reported in this Chapter have been presented in Sarno et al. (2011) and Sarno et al. (2012).

2.1 The experimental apparatus

An 8-m-long chute (Fig. 2.1) designed for studying dry granular flows and granular-liquid mixtures, was set up at the LIDAM (Laboratory of Environmental and Maritime Hydraulics of the University of Salerno, Italy).



Figure 2.1: A picture of the channel at LIDAM (University of Salerno, Italy).

The channel inclination, which is constant for its whole length, can be varied from 0° to about 23° , by rotating the structure around its lower end, thanks to an hydraulic ram controlled by a pumping system. The channel width can be adjusted between 0 and 80 cm, as the right side wall position can be moved and adjusted thanks to a screw system. The 90-cm-high side walls and the bottom are both made of Plexiglas and are suitably supported by structural steels. At the upper end of the chute, there is a wide tank, integral with the chute structure, with a capacity of about 2.8 m^3 . In addition, at the lower end of the channel a collector tank, with about the same capacity as the upper one, is located. A detailed scheme of the chute is reported in Fig. 2.2 that pictures the channel in horizontal and inclined positions.

The experimental apparatus was originally designed with the main purpose of studying steady state flows: hence, it is also equipped with a screw pumping system (LK-130, manufacturer Sydex, Vicenza, Italy), that is capable to lift up granular mixtures from the lower collector tank to the upper tank. The maximum flow rate, allowed by the pump, is approximately 50 l/s and the maximum pressure at the delivery pipe is approximately equal to 5 bar.

The pump is capable to work with granular-liquid mixtures with a maximum volume fraction equal to 0.5. Moreover, the maximum allowed size of grain particles is around 12 mm.

2.2 Experimental set-up for dam-break flows

The here illustrated experimental activity concerns dam-break flows of dry granular material. In order to perform this kind of experiments, some modifications to the original design of the experimental apparatus have been carried out.

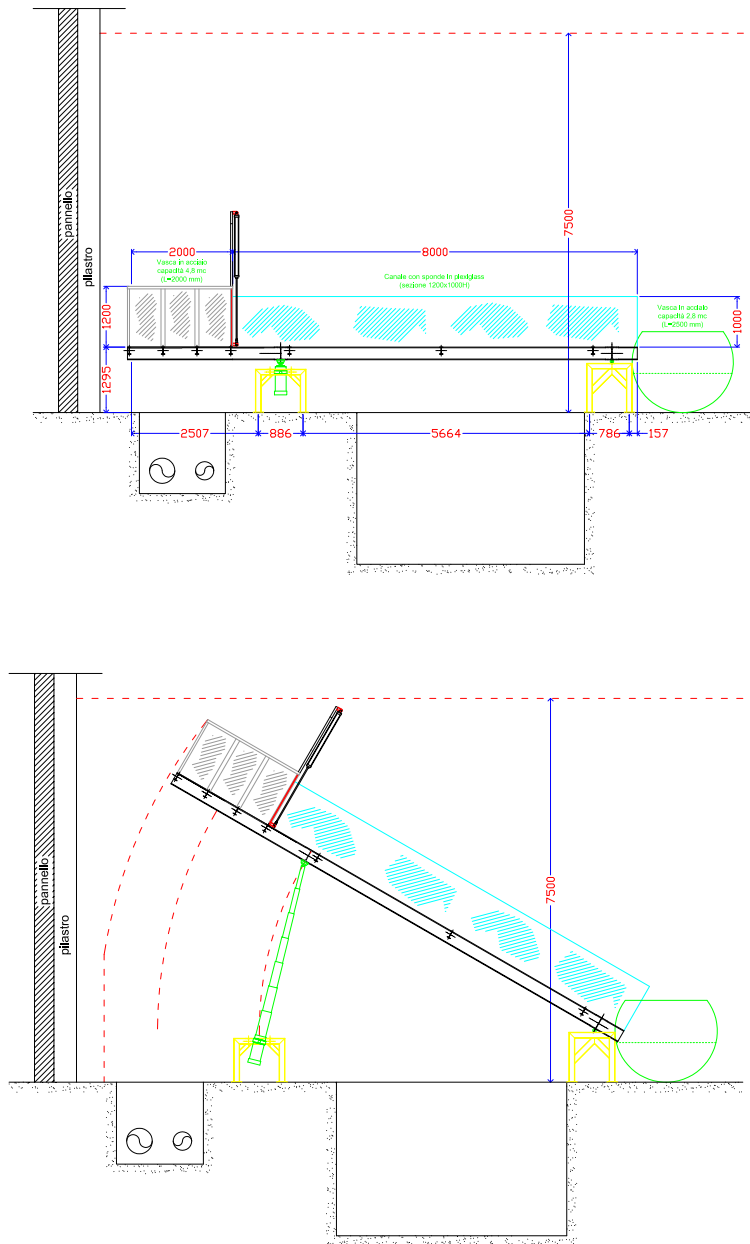


Figure 2.2: (Top) the experimental channel at LIDAM in horizontal position; (bottom) the same channel in inclined position.

Firstly, the upper tank was not utilized to store the granular material because too big for our purposes. On the contrary, the first upper part of the channel, 2 m-long, was used as reservoir. Such an arrangement is beneficial for two reasons:

- There is no variation in width between the reservoir and the rest of chute: hence, during the dam-break flow, at the reservoir outlet there is no flow contraction along the cross-flow direction. Such a flow geometry allows a direct comparison between experimental data and numerical simulations obtained through one-dimensional mathematical models.
- The small size of the reservoir allows to make use of a relatively small amount of granular material in order to observe sufficiently high flow depths for a reliable measurement through video-recording.

The channel width was set to 24 cm. Although the influence of the side walls on the flow mechanics is somehow reduced by a such large channel width, it is still evident and, thus, has to be accounted for in the mathematical model.

2.2.1 The release gate

At the beginning of each run, a granular pile was restrained in the upper part of the chute by a wooden plate, that was placed at exactly 2 m from the beginning of the chute. When closed, the plate is perpendicular to the channel bed. On the other hand, it is capable to release the material when rapidly rotated counter-clockwise, thanks to a spring mechanism. The wooden plate is composed of three pieces: a central one fixed together with a metal mechanism; two lateral flaps that are able to rotate when the gate opens. The lateral flaps, which are connected to the central part by means of metal hinges, are in contact with the chute side walls when the release gate is closed and ensure the seal. As soon as the plate opens, the two flaps rotate around the hinges and do not touch the side walls any more. This mechanism is useful to avoid incidental scratches of the Plexiglas walls and also reduces the *wake effect* on the granular material, due to the moving plate.

The opening apparatus has been designed to open quickly in order to avoid any significant influence on the forming dam-break wave. The total opening time results less than 2/12 s. Besides, only after 1/12 s, the frames, captured by a camera placed at the side of the channel, show that there is no contact between the gate and the upstream material. Therefore, the influence of the opening procedure on the flow is negligible and can be regarded as practically instantaneous.

2.2.2 The granular material

The granular material, used in the present experimental investigation, consists of spheroidal acetalic resin beads (HERAFORM R900). The major and minor diameter of grains are respectively equal to 3.9 mm and 2.8 mm. In Fig. 2.3 is reported a picture of the granular material. The most relevant features of the material are reported in Table 2.1.

The present experiments involved a mass of granular material of about 100 kg. At each run, the total mass (100 kg) of granular material was suddenly released by opening the wooden gate. Particular attention was given to set the initial position of the pile upstream the gate in order to impose the same initial condition in each test. A trapezoidal-shaped initial deposit was used for



Figure 2.3: The granular material (acetalic resin beads, HERAFORM R900).

Commercial name		HERAFORM R900
Material		POM Acetal copolymer
Grain density	ρ_g	1410 kg/m ³
Shape		spheroidal
Colour		Light grey
Minor diameter		2.8 mm
Major diameter		3.9 mm
Mean diameter		3.35 mm
Internal friction angle	φ_{int}	$\approx 27^\circ$
Basal friction angle with Plexiglas surface	δ_s	$\approx 17^\circ$
Basal friction angle with sandpaper surface	δ_r	$> 27^\circ$
Volume fraction at rest	ϕ_0	0.62

Table 2.1: The granular material, HERAFORM R900

all the runs and is reported in Fig. 2.4. The volume fraction at rest, ϕ_0 , typically depends on the loading procedure. In our experiments, thanks to a standardised loading procedure, it was found that ϕ_0 was almost constant and approximately equal to 0.62. During each experiment, the granular material was collected in a plastic bag, placed at the outlet of the channel, so that, after each experiment, it was possible to lift the bag containing the material and move it up to reservoir by using a bridge crane.

Friction angles

One of the main advantages of the Savage-Hutter type models is that its two parameters (i.e. the friction angles) have a clear physical meaning and can be measured independently.

The first parameter represents the internal friction angle φ and depends on the sole granular material. Although it was experimentally observed that the internal friction angle vary with the

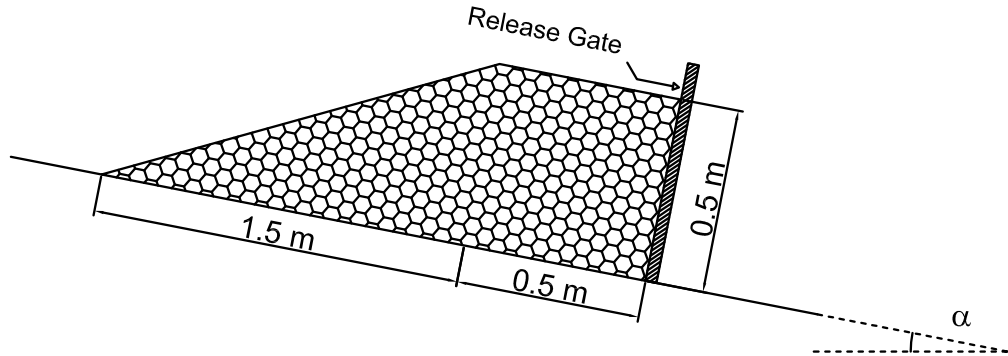


Figure 2.4: Initial position of the granular material before the release, where α is the inclination angle.

shear rate (Pouliquen, 1999), in its original form, the Savage-Hutter assumes a constant value of ϕ , which consists of the so-called *dynamic friction angle*. The dynamic friction coefficient is the angle of friction, observed after the beginning of shearing, and is typically smaller than the static friction angle by $2^\circ - 3^\circ$ (e.g. Hungr and Morgenstern, 1984a,b). In soil-mechanics, this value is also referred to as *constant-volume* friction angle. It represents the value measured at the end of laboratory shear tests, when dilatancy effects cease and the volume fraction of the sample does not vary any more.

The second parameter is the basal friction angle, δ , and depends on the granular material and on the basal surface. Also in this case, the dynamic friction angle has to be considered. Both of these angles can be measured by means of independent tests.

The following procedure was carried out to measure the angle of internal friction φ_{int} . A single layer of plastic beads was glued on two thin plywood sheets. Then, one of these sheets was placed in a inclined position with the granular layer upward. The second sheet was gently placed with the granular layer downward onto the inclined bumpy surface. The slope of the lower surface was being increased quasi-statically. The measured internal friction angle is $\varphi_{int} \approx 27^\circ$. This measurement can be considered a good estimate of the constant-volume friction angle. In fact, before the failure, the two overlapping layers of material are already weakly packed, because the particle have been glued on the plywood sheet and have a fixed position, and, thus, the interlocking is expected to be negligible.

An analogous procedure was performed in order to obtain estimate of basal friction angles δ_s and δ_r between the two basal surfaces and the granular material. A single layer of plastic beads was glued on a thin plywood sheet. Moreover, two wooden plates were lined with Plexiglas and sandpaper. Then, the plywood sheet was gently placed with the granular layer downward onto the inclined surface. The slope of the lower surface was being increased quasi-statically. A reliable measure of the static friction angle is obtained by choosing the minimum angle at which the static equilibrium of the plywood sheet on the inclined surface is no longer possible. For the smooth basal surface made of Plexiglas, $\delta_s \approx 19^\circ$ was measured. The measured angle is a good estimate of the static friction angle.

Because the dynamic friction angle is typically smaller (around $2\text{-}3^\circ$) than the static friction value (e.g. Hungr and Morgenstern, 1984a), we lowered the estimates of these angles by 2° , so that the best agreement between the Savage-Hutter model and experimental data was obtained. Hence, the basal friction angle in the Savage-Hutter model was set equal to $\delta_s = 17^\circ$.

An angle much greater than the internal friction angle, φ , was observed for the sandpaper bed $\delta_r > 27^\circ$. Therefore, in this latter case, failure is expected to occur only inside the pile (i.e. no-slip boundary condition). Hence, the friction angle of material φ_{int} , instead of the bed friction angle δ_r will be considered in order to calculate the basal shear stress in the Savage-Hutter model.

2.2.3 Measuring instruments

The motion was recorded by a CCD digital video camera (Sony Super HAD), capable to capture 12 frames per second, connected to a digital video recorder. The camera was installed at the side of the channel and, thanks to the side wall transparency, allowed for the view of about 80 cm downstream the gate. The effective resolution of the camera was about 450 lines, with a total accuracy of ± 5 mm, being assured in the chosen field of view.

In order to rectify the images, captured by the camera, a 2 cm grid was put on the opposite side wall. The recorded images were digitally post-processed. At first, the lens deformations were minimized by using a photo editing software. Then, the frames were subjected to a perspective rectification. Image rectification was accomplished by exploiting the fixed spots of the grid behind it. In order to minimize errors, a set of 8 fixed points of the back grid were taken for the rectification procedure. After this procedure, an evaluation of residual errors was carried out. Errors due to rectification were always less than 3 mm, so well below the total accuracy.

2.2.4 The experiments

After carefully checking the experimental repeatability with the aforementioned experimental apparatus, two kinds of tests were carried out. The first type of experiments were dam-break flows of dry granular material on a smooth Plexiglas bed. In the second type, dam-break experiments were performed on a bed, roughened by a lining of coarse sandpaper (grit P40 FEPA/ISO 6344). The chosen sand paper is coarse enough to ensure a *no-slip* condition at the bed surface.

Each series of tests involved the investigation of different channel slopes. The channel slope was varied between 19° and 22.7° for both of experimental configurations. Before each run, the channel slope was measured through geometric measurements and elementary trigonometric calculations. The overall accuracy of this measurement is very good and is less than 0.1° .

In Table 2.2 the complete list of experiments is reported.

2.3 The Savage-Hutter model

The Savage-Hutter model, hereafter briefly referred to as *SH* model, (Savage and Hutter, 1989, 1991) is a depth-averaged hyperbolic PDE model. For constant inclination angle α , its one-

Identification code	Incl.	Bed surface
S19	19.0°	smooth (Plexiglass)
S20	20.0°	smooth (Plexiglass)
S227	22.7°	smooth (Plexiglass)
R19	19.0°	rough (Sandpaper)
R20	20.0°	rough (Sandpaper)
R227	22.7°	rough (Sandpaper)

Table 2.2: List of dam-break experiments at LIDAM (University of Salerno, Italy)

dimensional expression can be written in the following conservative form

$$\begin{cases} \partial_t h + \partial_x (hu) = 0, \\ \partial_t (hu) + \partial_x (K g_z / 2 h^2 + \beta hu^2) = g_x h - g_z h \tan \delta \operatorname{sgn}(u) \end{cases} \quad (2.1)$$

where t means time, x -axis indicates the down-slope direction, h is the flow depth measured normally to the bed and u represents the x -component of the depth-averaged velocity. In Eqs. (2.1), $g_x = g \sin \alpha$ and $g_z = g \cos \alpha$ represent the x - and z -component of the gravity acceleration, respectively, so that $g_x h$ is the momentum gain due to the gravity, while the term $g_z h \tan \delta \operatorname{sgn}(u)$ is the momentum loss due to the basal Coulomb friction with δ the angle of friction at bottom. The parameter β is the *Boussinesq* coefficient, whose value is determined by the velocity distribution along the flow thickness. In SH theory a uniform velocity distribution is assumed, i.e. $\beta = 1$. It can be found that the SH equations mainly differ from the Shallow Water equation for its basal friction, which is of Coulomb type, and the anisotropy of the normal stresses, where the longitudinal stress σ_{xx} is related to the basal normal stress σ_{zz} by the earth-pressure coefficient K . Under the assumption of constant value of K over the depth, the depth-averaged values of the normal stress are related by

$$\overline{\sigma_{xx}} = \frac{1}{h} \int_h^b \sigma_{xx} dz = \frac{K}{h} \int_h^b \sigma_{zz} dz = K \overline{\sigma_{zz}} \quad (2.2)$$

where $\overline{\sigma_{xx}}$ and $\overline{\sigma_{zz}}$ stand for the averaged normal stresses over the flow thickness h .

2.3.1 The earth-pressure coefficient

Here, we only focus on 1D flows, so that a plane state of stress is assumed and the stress states at any given point can be geometrically represented by the Mohr's circle (e.g. Lambe and Whitman, 1991). In Savage and Hutter (1989, 1991) the granular matter is assumed to behave as a cohesion-less material of Mohr-Coulomb type, so that the value of K is given by

$$K = K_{SH}^{\mp} = \frac{2}{\cos^2 \varphi} \left[1 \mp \sqrt{1 - (1 + \tan^2 \delta) \cos^2 \varphi} \right] - 1 \quad (2.3)$$

in which φ is the angle of internal friction of the granular material and δ is the angle of friction at the bottom surface. In Eq. (2.3), the choice of the sign “ \mp ” depends on whether the spatial derivative of velocity, $\partial_x u$, is positive (active state) or negative (passive state), respectively; thus the value of K exhibits a discontinuity at $\partial_x u = 0$. This discontinuity causes some numerical

issues and some regularization for the transition between K_{SH}^- and K_{SH}^+ has been proposed, see e.g. Tai and Gray (1998). The K value in (2.3) is obtained under the hypotheses that the failure occurs simultaneously at the bed and inside the pile. Because of the non-null basal shear stress, formula (2.3) implies that the principal directions of stress are not parallel to the basal surface but counter-clockwise rotated. The detailed derivation of (2.3) makes use of Mohr's circles of stress and can be found in (Savage and Hutter, 1991).

Another way to take into account the anisotropy of normal stresses is represented by the Rankine formula (e.g. Hungr, 1995; Bartelt et al., 1999)

$$K = K_R^\mp = \frac{1 \mp \sin \varphi}{1 \pm \sin \varphi} \quad (2.4)$$

where K is assumed to depend only on the internal angle of friction, φ . Hungr (1995) proposed a linear dependence on the longitudinal strain to relate the two values of K in Eq. (2.4), by introducing two stiffness coefficients for compression and unloading. It is interesting to note that the SH formula (2.3) reduces to the Rankine expression (2.4) when $\delta \rightarrow 0$. In that case, the basal shear stress vanishes and, thus, the principal directions of stress become normal and parallel to the basal surface.

Recently, the fluid-like isotropic assumption (Pouliquen and Forterre, 2002; Gray et al., 2003; Mangeney-Castelnau et al., 2005), i.e.

$$K = 1 \quad (2.5)$$

has been applied to well developed granular flows. This hypothesis gives good results in predicting the flow behaviour in presence of a rough bed surface (Pouliquen and Forterre, 2002) and it is also supported by discrete particle numerical simulations (Ertas et al., 2001). In the simulation of (Gray et al., 1999) it is found that the assumption (2.5) gives quite acceptable results in the early stages but a huge under-estimation of the deposit has been observed in both longitudinal and lateral directions.

Although all of the above mentioned formulae have their strengths and drawbacks, the SH-formula (2.3) is supported by different laboratory experimental data (e.g. Greve and Hutter, 1993; Hungr, 1995; Tai et al., 2001; Hutter et al., 2005). In these works we found that trustworthy results can be obtained when the shallowness assumption is fulfilled and the basal surface is sufficiently smooth (i.e. δ is small compared to φ). If $\delta \approx \varphi$, (2.3) yields $K_{SH}^- \approx K_{SH}^+ \geq 1$, and the stress state along the bed is coincident with the internal failure state (i.e. it lies on the Coulomb envelope). As observed by some experimental studies (e.g. Pouliquen, 1999), a wedge of deposited material forms near the bed. In this regard, (Iverson, 1997) simply suggested to use the Rankine formula (2.4).

2.3.2 Regularization formula for the early stages of dam break waves

An important additional issue is the determination of the earth-pressure coefficient K at the early stages of dam-break waves. In this time window, the main physical quantities (e.g. velocity, stresses) strongly vary along the x -direction and also the z -component of velocity is not negligible. Hence, the hydrostatic pressure assumption is not fulfilled at the initiation of dam-break flow. However, models with hydrostatic pressure assumption are often employed beyond their formal

limits in an engineering context (e.g. Hutter et al., 2005). In this regard, the optimal choice of the earth-pressure coefficient K becomes an open problem.

Comparisons between numerical simulations and experimental data in Sarno et al. (2011) showed that none of the formulae (2.3), (2.4) or (2.5) could yield good agreement in the whole time domain. The numerical simulations with Rankine formula (2.4) generally yield a better agreement at the very beginning of dam-break flows but they systematically underestimate the avalanche spreading at later time points.

Hungr (2008) observed that formula (2.3) overestimates the value of the pressure coefficient K because the averaged direction of flow lines is far to be tangential to the bed at the beginning of dam-break waves. Thus, he proposed to modify the quantity δ in Eq. (2.3) by means of

$$\tan \delta_{\text{mod}} = \max \left(0, \tan \delta - \lambda K \left| \frac{\partial h}{\partial x} \right| \right) \quad (2.6)$$

in which λ is an empirical coefficient. The optimal value of λ is found to be around 0.333 in Hungr (2008). By reducing the friction angle, δ , formula (2.6) aims to describe a clockwise rotation of the stress principal axes, due the clockwise rotation of the failure planes inside the pile (i.e. the flow lines). Although the approach of Eq. (2.6) works very well in the Lagrangian framework by the DAN model, some oscillations are observed at the beginning of dam break flows in the distribution of the earth pressure coefficient, see Fig. 14 in Hungr (2008). We found that similar oscillations of the earth pressure coefficient cause numerical instability in our finite-volume framework.

In the present study, an alternative regularization for K is proposed. A new parameter $r(t)$ is introduced with respect to the effective flow domain, where velocities of the flow body are non-vanished. Namely,

$$r(t) = \frac{h_{\max}(t) - h_{\min}(t)}{L_{\text{effective}}(t)} \quad (2.7)$$

in which $L_{\text{effective}}$ is the length of the effective flow domain and h_{\max} and h_{\min} are the maximum and the minimum depths in the effective flow domain. The parameter $r(t)$ represents the tangent of the averaged inclination angle of the free surface in the effective flow domain, thus it can be regarded as an estimate of the averaged slope of the flow lines inside the flow. At the early stage, the spatial extent of the dam-break wave is quite small. Hence, it is reasonable to use a non-local value of K , to be calculated through the proposed regularization formula

$$K(r(t)) = K_R^- + (K_{\max} - K_R^-) \left(1 - \frac{1}{1 + e^{a(-r(t)+b)}} \right) \quad (2.8)$$

in which a and b are dimensionless positive parameters. The formula (2.8) yields the value K_R^- as $r \rightarrow \infty$ and a value very close to K_{\max} when $r = 0$, provided that the quantities a and b are sufficiently large. The value of K_{\max} can be set equal to K_{SH}^- or $K = 1$, depending on whether it is chosen Eq. (2.3) or Eq. (2.5) as the limiting model for small values of r . Eq. (2.8) exhibits a sigmoid shape as shown in Fig. 2.5.

The parameters a and b in Eq.(2.8) can be determined by solving the equation system

$$\begin{aligned} K(r = \tan(\gamma_1), a, b) &= K_R^- + (1 - \varepsilon)(K_{\max} - K_R^-) \\ K(r = \tan(\gamma_2), a, b) &= K_R^- + \varepsilon(K_{\max} - K_R^-) \end{aligned} \quad (2.9)$$

in which $\varepsilon > 0$ serves as a smoothness parameter, γ_1 and γ_2 represent the threshold angles at which the values K_R^- and K_{\max} are reached. When the ratio $r \approx 0$, the value of K is expected

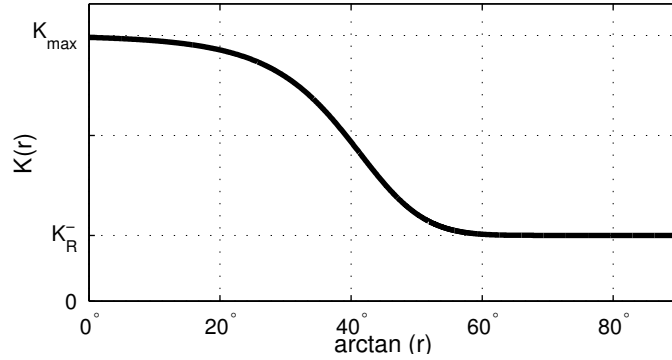


Figure 2.5: The regularization function $K(r)$ with $a = 5.632$ and $b = 0.816$ (obtained by imposing $\gamma_1 = 0^\circ$, $\gamma_2 = 58.5^\circ$, $\varepsilon = 0.01$).

to be close to K_{max} , (e.g. K_{SH}^-), because the flow lines are approximately parallel to the bed surface. Thus, it is logical to choose $\gamma_1 \approx 0^\circ$. On the other hand, a reasonable value for γ_2 is the inclination angle of the failure plane at Rankine's active state, $\phi_R = 45^\circ + \varphi/2$ (e.g. Lambe and Whitman, 1991). This value has a clear physical meaning since it is an estimate of the inclination angle of the lower wedge of deposit below the real surface flow (e.g. Crosta et al., 2009) and so it is a reasonable limiting value of the averaged slope of the flow lines.

2.4 Experimental validation

In this section we shall illustrate the comparison between the theoretical model and the laboratory experiments carried out at LIDAM and presented in Sarno et al. (2011).

The resistance due to side walls is taken into account in a way similar to Roberts (1969). Namely, an equivalent basal friction angle δ_{eff} is calculated, so that

$$\tan \delta_{eff} = \tan \delta \left(1 + k \frac{h}{W} \right) \quad (2.10)$$

where W indicates the cross-section width and k represents an empirical parameter. If a hydrostatic distribution of pressure is assumed along side walls, the parameter k can be recast as follows

$$k = K_y \frac{\tan \delta_{side}}{\tan \delta} \quad (2.11)$$

in which K_y is the lateral pressure coefficient and δ_{side} is the friction angle at the side walls. It was found that $K_y = 0.6$ yields the best agreement between the experimental data and the numerical simulation with the Savage-Hutter formula Eq. (2.3). As observed in (Sarno et al., 2011), it is worth noting that the chosen value of K_y is very similar to the value obtained by the Jaky formula, which is an estimate of the earth pressure coefficient at rest (Jaky, 1944). The friction angle at the side walls is $\delta_{side} = 17^\circ$, because the material is identical to the basal surface in tests with smooth bed (i.e. Plexiglas).

Numerical simulations with formulae (2.3), (2.4), (2.5) and the regularization formula (2.8) are performed and compared. The following values are used in the regularization formula: $\gamma_1 = 0^\circ$

, $\gamma_2 = \phi_R = 58.5^\circ$, $\varepsilon = 0.01$. The numerical solutions of the equation system (2.1) have been obtained through a finite volume scheme that uses the *f-wave* approach (Bale et al., 2002). A more detailed description of the numerical code is reported in the following section.

The performance of the agreement between numerical simulations and the experimental data is evaluated by an error index of the type of normalized *Holder* 1-norm,

$$I(t) = \frac{\sum_{i=1}^N |h_i^{SIM}(t) - h_i^{DATA}(t)|}{\sum_{i=1}^N h_i^{DATA}(t)}, \quad (2.12)$$

where N is the number of measurements at each time point, h_i^{SIM} represents the computed flow depth at the i -th spatial position, and h_i^{DATA} is the measured flow depth at the corresponding position.

2.4.1 The numerical code

A finite volume scheme using the *f-wave* approach, proposed by (Bale et al., 2002), has been implemented for solving the equation system (2.1). This scheme solves the Riemann problem at each cell interface by decomposing the jump of the flux function $\mathbf{f}(\mathbf{q})$

$$\mathbf{f}_i(\mathbf{q}_i) - \mathbf{f}_{i-1}(\mathbf{q}_{i-1}) = \sum_{p=1}^m \beta_{i-1/2}^p \mathbf{r}_{i-1/2}^p = \sum_{p=1}^m \mathbf{z}_{i-1/2}^p \quad (2.13)$$

where $\mathbf{q} = (h, hu)^T$ is the vector of unknowns, $\beta_{i-1/2} = R_{i-1/2}^{-1} (\mathbf{f}_i(\mathbf{q}_i) - \mathbf{f}_{i-1}(\mathbf{q}_{i-1}))$ in which $R_{i-1/2}$ is the matrix of the right eigenvectors at interface between cells $i-1$ and i , calculated using the Roe means (Roe, 1981). The updating formula of the second order reads

$$\mathbf{q}_i^{j+1} = \mathbf{q}_i^j - \frac{\Delta x}{\Delta t} (A^+ \Delta \mathbf{q}_{i-1/2} + A^- \Delta \mathbf{q}_{i+1/2}) - \frac{\Delta x}{\Delta t} (\hat{F}_{i+1/2} - \hat{F}_{i-1/2}), \quad (2.14)$$

where the *fluctuations* are written as functions of the *f-waves* in the following way,

$$A^+ \Delta \mathbf{q}_{i-1/2} = \sum_{p: s_{i-1/2}^p > 0} \mathbf{z}_{i-1/2}^p, \quad A^- \Delta \mathbf{q}_{i-1/2} = \sum_{p: s_{i-1/2}^p < 0} \mathbf{z}_{i-1/2}^p \quad (2.15)$$

and \hat{F} are the second order TVD flux corrections (LeVeque, 2002). To properly handle transonic rarefaction waves, the approach proposed by LeVeque and George (2008) is adopted so as to fulfil the entropy requirement by the *f-wave* scheme. As regards the first characteristic family at the interface $i - 1/2$ an entropy fix is needed if

$$\lambda_{i-1}^1 < 0 < 2\tilde{\lambda}_{i-1/2}^1 - \lambda_{i-1}^1. \quad (2.16)$$

In Eq. (2.16) λ_i^1 and λ_{i-1}^1 are the eigenvalues calculated at cells i and $i - 1$, while $2\tilde{\lambda}_{i-1/2}^1 - \lambda_{i-1}^1$ is an estimate for the characteristic speed at the center of rarefaction fan, with $\tilde{\lambda}_{i-1/2}^1$ the Roe speed at the interface. In such a case, Eqs. (2.15) need to be modified, as the *f-wave* $\mathbf{z}_{i-1/2}^1$ is split into two *f-waves* going into the cells i and $i - 1$,

$$(\mathbf{z}_{i-1/2}^1)^+ = \left[\frac{1 - (\tilde{\lambda}_{i-1/2}^1 - \lambda_i^1)}{\lambda_{i-1}^1 - \lambda_i^1} \frac{\lambda_{i-1}^1}{\tilde{\lambda}_{i-1/2}^1} \right] \mathbf{z}_{i-1/2}^1, \quad (2.17)$$

$$(\mathbf{z}_{i-1/2}^1)^- = \left[\frac{\tilde{\lambda}_{i-1/2}^1 - \lambda_i^1}{\lambda_{i-1}^1 - \lambda_i^1} \frac{\lambda_{i-1}^1}{\tilde{\lambda}_{i-1/2}^1} \right] \mathbf{z}_{i-1/2}^1 \quad (2.18)$$

where $(z_{i-1/2}^1)^-$ and $(z_{i-1/2}^1)^+$ are left-going and right-going f-waves, respectively. An analogous treatment has been implemented for the second characteristic family.

Due to the non-vanishing source terms in System (2.1), the operator splitting technique (LeVeque, 2002) is applied as follows. At first, the homogeneous system (i.e. without source term) is numerically solved by using the *f-wave* approach; in the second stage, the source term of the momentum equation is taken into account explicitly. In addition, a special treatment for the *dry/wet* interface on the wave front is needed and a thin layer ($h_0 = 10^{-5}$ m) is added over the whole domain in our scheme. This treatment is rather usual (e.g. Zhang and Cundy, 1989). In the present computations, a constant space mesh $\Delta x = 0.01$ m and Courant-Friedrichs-Lewy number ($CFL = 0.8$) for the time increment Δt are adopted.

ID	Incl. angle	Earth pressure parameters	$t=0.5$ s	$t=1.0$ s	$t=1.5$ s	$t=2.0$ s	$t=4.0$ s	Average
R19-1	$\alpha = 19.0^\circ$	$K = K_{SH}^- = 1.519$	0.3136	0.0912	0.0988	0.1030	0.1613	0.1536
R19-2	$\alpha = 19.0^\circ$	$K = K_R^- = 0.376$	0.1523	0.1345	0.1692	0.1928	0.2440	0.1786
R19-3	$\alpha = 19.0^\circ$	$K = 1$	0.2018	0.0413	0.0898	0.0986	0.1572	0.1177
R19-4	$\alpha = 19.0^\circ$	$\gamma_1 = 0^\circ, \gamma_2 = \phi_R, K_{max} = K_{SH}^-$	0.1651	0.1147	0.0345	0.0285	0.0902	0.0866
R19-5	$\alpha = 19.0^\circ$	$\gamma_1 = 0^\circ, \gamma_2 = \phi_R, K_{max} = 1$	0.1079	0.0364	0.0562	0.0884	0.1386	0.0855
R20-1	$\alpha = 20.0^\circ$	$K = K_{SH}^- = 1.519$	0.2377	0.0949	0.0573	0.0855	0.1654	0.1282
R20-2	$\alpha = 20.0^\circ$	$K = K_R^- = 0.376$	0.1337	0.0919	0.1554	0.1990	0.2441	0.1648
R20-3	$\alpha = 20.0^\circ$	$K = 1$	0.1342	0.0342	0.0459	0.0927	0.1633	0.0940
R20-4	$\alpha = 20.0^\circ$	$\gamma_1 = 0^\circ, \gamma_2 = \phi_R, K_{max} = K_{SH}^-$	0.1122	0.1594	0.0435	0.0304	0.0994	0.0890
R20-5	$\alpha = 20.0^\circ$	$\gamma_1 = 0^\circ, \gamma_2 = \phi_R, K_{max} = 1$	0.0754	0.1003	0.0738	0.1038	0.1460	0.0999
R227-1	$\alpha = 22.7^\circ$	$K = K_{SH}^- = 1.519$	0.2387	0.0792	0.0732	0.0897	0.1036	0.1169
R227-2	$\alpha = 22.7^\circ$	$K = K_R^- = 0.376$	0.1584	0.0361	0.1628	0.1858	0.2084	0.1503
R227-3	$\alpha = 22.7^\circ$	$K = 1$	0.1717	0.0323	0.0558	0.0947	0.1186	0.0946
R227-4	$\alpha = 22.7^\circ$	$\gamma_1 = 0^\circ, \gamma_2 = \phi_R, K_{max} = K_{SH}^-$	0.1092	0.1408	0.0328	0.0317	0.0624	0.0754
R227-5	$\alpha = 22.7^\circ$	$\gamma_1 = 0^\circ, \gamma_2 = \phi_R, K_{max} = 1$	0.1067	0.1072	0.0589	0.1026	0.1248	0.1000

Table 2.3: Error indexes I of numerical simulations (rough bed).

ID	Incl. angle	Earth pressure parameters	$t=0.5$ s	$t=1.0$ s	$t=1.5$ s	$t=2.0$ s	$t=4.0$ s	Average
S19-1	$\alpha = 19.0^\circ$	$K = K_{SH}^- = 0.604$	0.1477	0.0786	0.0366	0.0563	0.0775	0.0793
S19-2	$\alpha = 19.0^\circ$	$K = K_R^- = 0.376$	0.1213	0.0666	0.1088	0.1512	0.1512	0.1198
S19-3	$\alpha = 19.0^\circ$	$\gamma_1 = 0^\circ, \gamma_2 = \phi_R, K_{max} = K_{SH}^-$	0.0843	0.1057	0.0657	0.0465	0.0660	0.0737
S20-1	$\alpha = 20.0^\circ$	$K = K_{SH}^- = 0.604$	0.1278	0.0671	0.0440	0.0956	0.1608	0.0991
S20-2	$\alpha = 20.0^\circ$	$K = K_R^- = 0.376$	0.1299	0.0807	0.1119	0.1613	0.2201	0.1408
S20-3	$\alpha = 20.0^\circ$	$\gamma_1 = 0^\circ, \gamma_2 = \phi_R, K_{max} = K_{SH}^-$	0.1289	0.0943	0.0635	0.1007	0.1839	0.1143
S227-1	$\alpha = 22.7^\circ$	$K = K_{SH}^- = 0.604$	0.1731	0.0528	0.0837	0.1142	0.0549	0.0957
S227-2	$\alpha = 22.7^\circ$	$K = K_R^- = 0.376$	0.2523	0.0988	0.1356	0.1600	0.2396	0.1773
S227-3	$\alpha = 22.7^\circ$	$\gamma_1 = 0^\circ, \gamma_2 = \phi_R, K_{max} = K_{SH}^-$	0.2080	0.0735	0.0858	0.1264	0.0661	0.1119

Table 2.4: Error indexes I of numerical simulations (smooth bed).

Results on rough bed

Table 2.3 lists the error indexes I between numerical simulations (marked by identification codes) and experiments on rough bed. The ID Codes “Rxx-1”, “Rxx-2” and “Rxx-3” respectively

ID	Earth pressure parameters	$t=0.5$ s	$t=1.0$ s	$t=1.5$ s	$t=2.0$ s	$t=4.0$ s	Average
R20-4	$\gamma_1 = 0^\circ, \gamma_2 = \phi_R, K_{max} = K_{SH}^-$	0.1122	0.1594	0.0435	0.0304	0.0994	0.0890
R20-6	$\gamma_1 = 1^\circ, \gamma_2 = \phi_R, K_{max} = K_{SH}^-$	0.1165	0.1581	0.0430	0.0300	0.0999	0.0895
R20-7	$\gamma_1 = 5^\circ, \gamma_2 = \phi_R, K_{max} = K_{SH}^-$	0.1314	0.1526	0.0408	0.0275	0.1024	0.0910
R20-8	$\gamma_1 = 10^\circ, \gamma_2 = \phi_R, K_{max} = K_{SH}^-$	0.1460	0.1481	0.0380	0.0251	0.1055	0.0925

Table 2.5: Error indexes I of numerical simulations performed by using different values for the parameter γ_1 (20° , rough bed).

ID	Earth pressure parameters	$t=0.5$ s	$t=1.0$ s	$t=1.5$ s	$t=2.0$ s	$t=4.0$ s	Average
R20-4	$\gamma_1 = 0^\circ, \gamma_2 = \phi_R, K_{max} = K_{SH}^-$	0.1122	0.1594	0.0435	0.0304	0.0994	0.0890
R20-9	$\gamma_1 = 0^\circ, \gamma_2 = \phi_R - 10^\circ, K_{max} = K_{SH}^-$	0.0848	0.2131	0.0871	0.0505	0.0788	0.1029
R20-10	$\gamma_1 = 0^\circ, \gamma_2 = \phi_R + 10^\circ, K_{max} = K_{SH}^-$	0.1734	0.1275	0.0288	0.0356	0.1202	0.0971
R20-11	$\gamma_1 = 0^\circ, \gamma_2 = \phi_R - 20^\circ, K_{max} = K_{SH}^-$	0.2588	0.2655	0.1634	0.0870	0.0644	0.1678
R20-12	$\gamma_1 = 0^\circ, \gamma_2 = \phi_R + 20^\circ, K_{max} = K_{SH}^-$	0.2049	0.1093	0.0305	0.0604	0.1428	0.1096

Table 2.6: Error indexes I of numerical simulations performed by using different values for the parameter γ_2 (20° , rough bed).

indicate the simulation by using the formulae (2.3), (2.4) and (2.5), where “xx” denotes the corresponding basal friction angle. Besides, the ID Codes “Rxx-4” and “Rxx-5” are the results by using the regularization formula (2.8) with $K_{max} = K_{SH}^-$ and $K_{max} = 1$, respectively. For comparisons, the simulations “Rxx-1” are regarded as reference simulations.

Firstly, it is interesting to note that, for the three inclination angles, the simulations with $K = 1$ (R19-3, R20-3, R227-3) yield a better agreement than the reference simulations (R19-1, R20-1, R227-1). Yet, the early spreading is still considerably overestimated. Conversely, the simulations with K_R^- (R19-2, R20-2, R20-3) yield a good agreement with experimental data at $t = 0.5$ s but they underestimate the spreading of the avalanche very much at the later time points. The simulations that make use of the regularization formula (R19-4, R20-4, R227-4) exhibits a very good agreement at $t = 0.5$ s, with a reduction of I with respect to the reference simulations of 47%, 53% and 54% in 19.0° , 20.0° and 22.7° runs, respectively. Although the agreement of these simulations is worse than reference simulations at the time point $t = 1.0$ s, they fit the experimental data slightly better at the subsequent time points. Hence, the overall improvement is significant for all inclination angles (19.0° , 20.0° and 22.7°), with a decrease of I with respect to the reference simulations of 43%, 30% and 35%, respectively.

We also performed numerical simulations with $K_{max} = 1$ (R19-5, R20-5, R227-5). Such simulations exhibit an agreement at $t = 0.5$ s, even better than Rxx-4, with a reduction of I with respect to the reference simulations of 66%, 68% and 55% in 19.0° , 20.0° and 22.7° runs, respectively. Nevertheless, the averaged error indexes of R20-5 and R227-5 are slightly higher than R20-4 and R227-4. However, it is hard to conclude that $K_{max} = K_{SH}^-$ is the optimal choice, because the results might depend on the particular choice of regularization parameters. The depth profiles, related to runs with inclination angles of 19° and 22.7° , are reported in Figs. 2.6 and 2.8.

Results on smooth bed

As regards the smooth bed runs, Table 2.4 lists the error indexes I related to the numerical simulations. The ID Codes “Sxx-1”, “Sxx-2” and “Sxx-3” indicate the usage of formulae (2.3), (2.4), (2.5) and (2.8) with $K_{max} = K_{SH}^-$, respectively. The plots of flow depths, referring to runs with inclination angles of 19.0° and 22.7° , are reported in Figs. 5 and 6. We choose only to show the comparisons related to the time interval up to $t = 4$ s, although the flows on smooth bed do not stop at $t = 4$ s. However, we carefully checked that the model with the regularization formula (2.8) gives results almost identical to those obtained by using the formula (2.3) for all the subsequent time-points (i.e. $t > 4$ s).

Firstly, it should be noted that numerical simulations with the Rankine formula (i.e. S19-2, S20-2, S227-2) tend to underestimate the avalanche spreading. At the lowest inclination angle (i.e. 19.0°), the numerical simulation with the regularization formula, S19-3, yields a noticeable improvement at the time point $t = 0.5$ s (I decreases by 43% with respect to the reference simulation S19-1). Also the averaged error index of S19-3 is slightly smaller than that of reference simulation S19-1. Conversely, at $\alpha = 20.0^\circ$ and $\alpha = 22.7^\circ$, the regularization formula (2.8) cannot yield significant improvements. The reason of such a behaviour is suspected to be due to the fact that the whole granular pile moves altogether immediately after the release of the gate, due to the small value of the basal friction compared to the angle of the internal friction of the material. Thus, the average slope of the failure planes inside the pile (i.e. the flow lines) is somehow smaller than what expected by estimating r . This effect becomes dominant when the inclination angle increases, as one can easily see by comparing Figs. 2.7 and 2.9.

2.5 Parameter study

Sensitivity analyses on the parameters $(\gamma_1, \gamma_2, \varepsilon)$ of regularization formula are performed. In order to check the effects of γ_1 on numerical simulations, we let γ_1 vary between 0° and 10° . Table 2.5 lists the error indexes of numerical simulations, performed with different γ_1 and related to the rough bed run with $\alpha = 20^\circ$. The best agreement with experimental data is obtained by using $\gamma_1 = 0^\circ$. Nonetheless, we have found that the model exhibits very small sensitivity to γ_1 , provided that the chosen value is sufficiently close to 0° (i.e. $0^\circ < \gamma_1 < 5^\circ$). A similar behaviour has been observed also for different inclination angles. As regard smooth bed runs, an even smaller sensitivity on γ_1 has been noticed.

Additionally, we carried out different numerical simulations by varying γ_2 between $[\phi_R - 20^\circ, \phi_R + 20^\circ]$ (i.e. $38.5^\circ < \gamma_2 < 78.5^\circ$). Tables 2.6 lists the error indexes of the numerical tests, related to the 20° rough bed run. The best choice is found to be $\gamma_2 = \phi_R$; however, as long as $\gamma_2 > \phi_R - 10^\circ$, the average error is reasonably small. An analogous trend has been observed at different inclination angles both in rough and smooth bed runs. The parameter ε should be set as small as possible, in order to the asymptotic values K_R^- and K_{max} be effectively reached. Nevertheless, the smaller ε , the sharper the transition between K_R^- and K_{max} . We found that in presence of a too sharp regularization function (i.e. $\varepsilon < 0.01$) an unrealistic secondary wave is observed in numerical results. Therefore, ε is set carefully equal to 0.01 for all the simulations considered in the present study.

Finally, in Fig. 2.10 the evolution of the earth pressure coefficient, K , in simulations S20-3 and

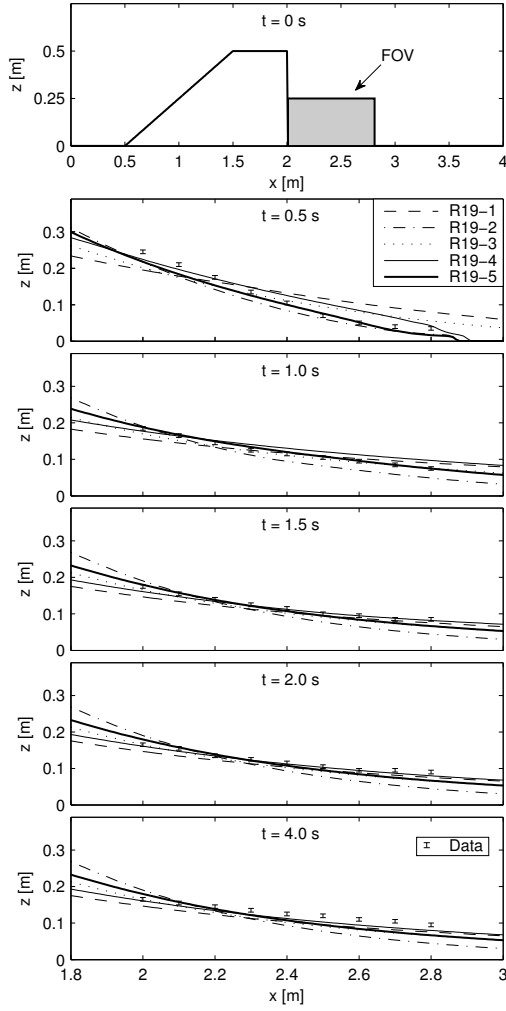


Figure 2.6: Comparisons between flow depths predicted by numerical simulations and experimental data (19° slope, rough bed). The whole channel with the initial condition and the field of view (FOV) of the side camera are shown in the first panel. The FOV is [2.0 m, 2.8 m]. From Sarno et al. (2012).

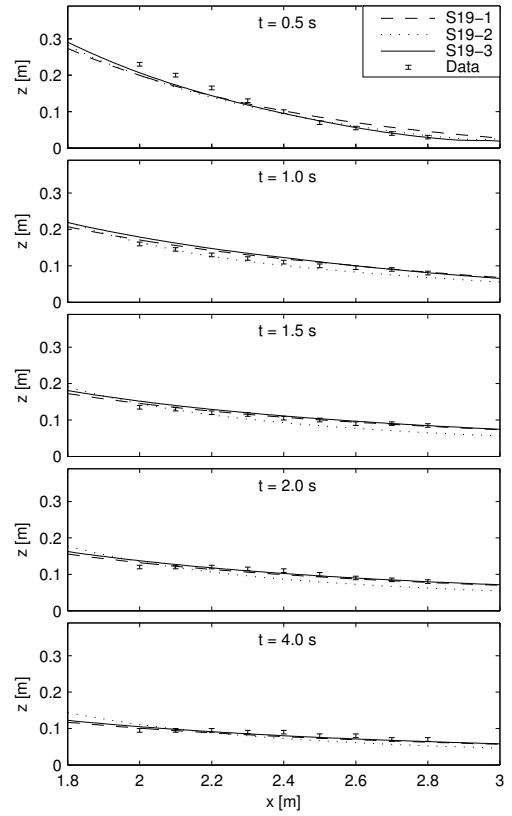


Figure 2.7: Comparisons between flow depths predicted by numerical simulations and experimental data (19° slope, smooth bed). From Sarno et al. (2012).

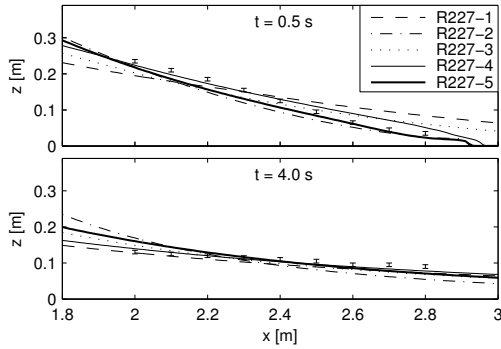


Figure 2.8: Comparisons between flow depths predicted by numerical simulations and experimental data (22.7° slope, rough bed). From Sarno et al. (2012).

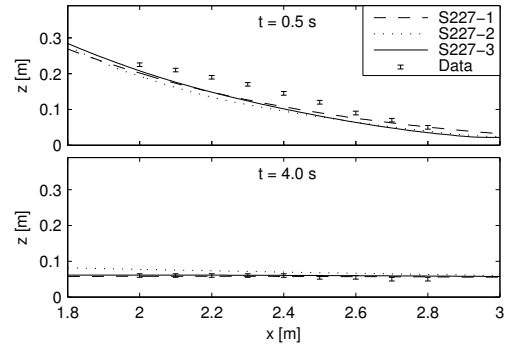


Figure 2.9: Comparisons between flow depths predicted by numerical simulations and experimental data (22.7° slope, smooth bed). From Sarno et al. (2012).

R20-4 is reported. K rapidly increases and reaches approximately 98% of K_{SH}^- at $t = 0.5$ s in S20-3 and at $t = 0.7$ s in R20-4. After those time points, K can be considered practically constant. The reason of such a slight difference between the K evolution in smooth and rough bed runs is due to the fact that the spreading of the avalanche also depends on the chute basal roughness. The evolution of K in the other numerical simulations over smooth bed (i.e. S19-3 and S227-3) is almost identical to what observed in S20-3. As well, a very similar behaviour to what observed in R20-4 has been found in numerical simulations R19-4 and R227-4.

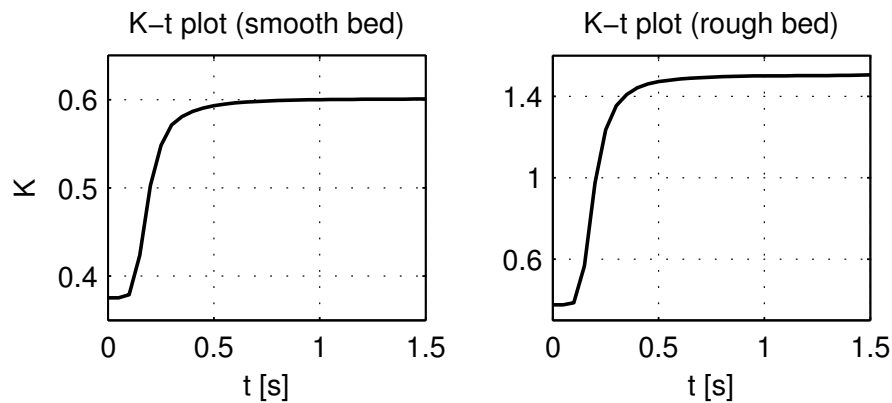


Figure 2.10: The evolution of the earth pressure coefficient K in numerical simulations with the regularization formula (2.8).

2.6 Conclusions

In this Chapter we showed the experimental apparatus, located at the LIDAM (University of Salerno), and provided a report about the experimental activity on dam-break flows of dry granular material. Dam-break experiments have been carried out over smooth and rough bed conditions. Acetatic resin beads, with mean diameter of 3.3 mm, have been used as granular material.

At first, the original Savage-Hutter model has been tested with different values for calculating the earth-pressure coefficient. The comparisons with experimental data showed that none of the earth-pressure coefficients, available in Literature, are able to provide successful results at the early stages of dam-flows as well as at the final time points. The results of this preliminary study have been published in Sarno et al. (2011).

Then, we proposed a formula for determining the value of the pressure coefficient K in the Savage-Hutter type models at the early stages of dam-break waves or collapses. This regularization formula is a function of the averaged free surface slope in the effective flow domain. The parameters of the regularization formula are determined by invoking physical arguments: i.e. the limiting averaged slope of flow lines is supposed to be close to the inclination angle of the failure plane in Rankine's active state. Numerical simulations are performed and compared with experimental measurements, where both smooth and rough bed surfaces are considered. The regularization formula exhibits a significant improvement in rough bed tests, both at the early stages of dam break and at the final time points. However, only minor improvement is obtained by smooth bed tests. In particular, the improvements become insignificant as the inclination angle increases. The reason of this discrepancy seems to be due to the fact that the failure at the bed occurs immediately after the release of the gate. As a general limitation of depth-averaged models, the assumption of hydrostatic vertical pressure distribution is not fulfilled in presence of large flow depth gradients and, thus, these models are not expected to produce very accurate results at flow initiation. The proposed correction could be regarded as an engineering tool more than a theoretical improvement. The parameter study shows that the model is weakly sensitive to γ_1 , γ_2 , provided that they are chosen close to physically reasonable values (i.e. $\gamma_1 \approx 0^\circ$, $\gamma_2 \approx \phi_R$). This proves the robustness of the proposed formula and reveals the potential for a general practical application. Especially, after further validation, this approach may become a practical engineering tool for better describing rock/snow avalanches as well as ridge collapses.

Finally, the different behaviours between smooth and rough bed runs highlight on the complexity of these kinds of flows. Moreover, it is worth reporting that, in the experimental runs over rough bed, we observed that the avalanche did not stop instantaneously in a given cross section. More precisely, it was noticed a progressive slowdown of the granular matter from the bottom up to free surface. This phenomenon suggests the occurrence of a flow regime stratification, similar to what has been observed in heap flows experiments in Midi (2004) or by Drake (1990). Obviously, since the motion of dam-break waves is in transient state, the ideal interface separating the lower quasi-static regime from the upper dense-collisional regime is in motion and moves progressively up to the free surface.

Further study is particularly needed on the influence of the basal surfaces and, hence, it would be particularly useful to obtain more information about the velocity profiles along the flow depth. In this regard, in Chapter 3 an experimental study about velocity profiles is reported.

References Used in This Chapter

- Bale, D. S., LeVeque, R. J., Mitran, S., and Rossmannith, J. A. (2002). A Wave Propagation Method for Conservation Laws and Balance Laws with Spatially Varying Flux Functions. *SIAM Journal on Scientific Computing* **24**, 955–978.
- Bartelt, P., Salm, B., and Gruber, U. (1999). Calculating dense-snow avalanche runout using a Voellmyfluid model with active/passive longitudinal straining. *Journal of Glaciology* **45**, 242–254.
- Crosta, G. B., Imposimato, S., and Roddeman, D. (2009). Numerical modeling of 2-D granular step collapse on erodible and nonerodible surface. *Journal of Geophysical Research* **114**,.
- Drake, T. G. (1990). Structural features in granular flows. *Journal of Geophysical Research* **95**, 8681–8696.
- Ertas, D., Grest, G. S., Halsey, T. C., Levine, D., and Silbert, L. E. (2001). Gravity-driven dense granular flows. *Europhysics Letters (EPL)* **56**, 214–220.
- Gray, J. M. N. T., Tai, Y. C., and Noelle, S. (2003). Shock waves, dead zones and particle-free regions in rapid granular free-surface flows. *Journal of Fluid Mechanics* **491**, 161–181.
- Gray, J. M. N. T., Wieland, M., and Hutter, K. (1999). Gravity-driven free surface flow of granular avalanches over complex basal topography. *Proceedings of the Royal Society A: Mathematical, Physical and Engineering Sciences* **455**, 1841–1874.
- Greve, R. and Hutter, K. (1993). Motion of a Granular Avalanche in a Convex and Concave Curved Chute: Experiments and Theoretical Predictions. *Philosophical Transactions of the Royal Society A: Mathematical, Physical and Engineering Sciences* **342**, 573–600.
- Hungr, O. (1995). A model for the runout analysis of rapid flow slides, debris flows, and avalanches. *Canadian Geotechnical Journal* **32**, 610–623.
- Hungr, O. (2008). Simplified models of spreading flow of dry granular material. *Canadian Geotechnical Journal* **45**, 1156–1168.
- Hungr, O. and Morgenstern, N. (1984a). Experiments on the flow behaviour of granular materials at high velocity in an open channel. *Geotechnique* **34**,.
- Hungr, O. and Morgenstern, N. (1984b). High velocity ring shear tests on sand. *Geotechnique* **34**,.
- Hutter, K., Wang, Y., and Pudasaini, S. P. (2005). The Savage-Hutter avalanche model: how far can it be pushed? *Philosophical transactions. Series A, Mathematical, physical, and engineering sciences* **363**, 1507–28.
- Iverson, R. M. (1997). The physics of debris flows. *Reviews of Geophysics* **35**, 245.
- Jaky, J. (1944). The coefficient of earth pressure at rest. *Journal of the Society of Hungarian Architects and Engineers* **78**, 355–358.
- Lambe, T. and Whitman, R. (1991). *Soil Mechanics*. Series in Soil Engineering. Wiley.

- LeVeque, R. (2002). *Finite volume methods for hyperbolic problems*, volume 31. Cambridge university press.
- LeVeque, R. and George, D. (2008). High-resolution finite volume methods for the shallow water equations with bathymetry and dry states. *Advanced numerical models for simulating tsunami waves and runoff* **10**, 43–73.
- Mangeney-Castelnaud, A., Bouchut, F., Vilotte, J., Lajeunesse, E., Aubertin, A., and Pirulli, M. (2005). On the use of saint venant equations to simulate the spreading of a granular mass. *Journal of Geophysical Research: Solid Earth (1978–2012)* **110**,.
- Midi, G. (2004). On dense granular flows. *The European physical journal. E, Soft matter* **14**, 341–65.
- Pouliquen, O. (1999). Scaling laws in granular flows down rough inclined planes. *Physics of fluids* **11**, 542–548.
- Pouliquen, O. and Forterre, Y. (2002). Friction law for dense granular flows: application to the motion of a mass down a rough inclined plane. *Journal of Fluid Mechanics* **453**, 133–151.
- Roberts, A. (1969). An investigation of the gravity flow of noncohesive granular materials through discharge chutes. *J. Eng. Ind.* **91**,.
- Roe, P. (1981). Approximate Riemann solvers, parameter vectors, and difference schemes. *Journal of Computational Physics* **43**, 357–372.
- Sarno, L., Carravetta, A., Martino, R., and Tai, Y.-C. (2012). The pressure coefficient in dam-breaks flows of dry granular matter. *Submitted to Journal of Hydraulic Engineering* .
- Sarno, L., Papa, M. N., and Martino, R. (2011). Dam-break flows of dry granular materials on gentle slopes. In Genevois, R., Hamilton, D. L., and Prestininzi, A., editors, *5th Int. Conf. on Debris-Flow Hazards Mitigation: Mechanics, Prediction and Assessment*. Italian Journal of Engineering Geology and Environment. Casa Editrice Università “La Sapienza”.
- Savage, S. B. and Hutter, K. (1989). The motion of a finite mass of granular material down a rough incline. *Journal of Fluid Mechanics* **199**, 177–215.
- Savage, S. B. and Hutter, K. (1991). The dynamics of avalanches of granular materials from initiation to runout. Part I: Analysis. *Acta Mechanica* **86**, 201–223.
- Tai, Y. C. and Gray, J. M. N. T. (1998). Limiting stress states in granular avalanches. *Annals of Glaciology* **26**, 272–276.
- Tai, Y. C., Hutter, K., and Gray, J. M. N. T. (2001). Dense granular avalanches: mathematical description and experimental validation. In Balmforth, N. and Provenzale, A., editors, *Lecture notes in Physics Volume 582*, volume 582, chapter Geomorphol, pages 339–366. Springer, Berlin.
- Zhang, W. and Cundy, T. W. (1989). Modeling of two-dimensional overland flow. *Water Resources Research* **25**, 2019–2035.

Chapter 3

Steady state velocity profiles

Chapter Summary

In this Chapter, an experimental study on the velocity distributions in dry granular free surface flows is reported.

The experimental activity has been performed at the Department of Hydraulic and Ocean Engineering of the National Cheng-Kung University (Tainan City, Taiwan), under the supervision of Prof. Y.-C. Tai. Such investigations on steady-state dry granular flows involved the use of the *Granular Particle Image Velocimetry* technique, also called *G-PIV*, which is a modified version of Particle Image Velocimetry applied to granular flows. Thanks to this technique, the velocity profiles at the side walls of the channel and at the free surface have been obtained.

The purposes of this experimental research are mainly two. The first one is achieving further information about velocity profiles of dry granular flows in case of different bottom boundary conditions (i.e. smooth and rough bed). Particular attention has been paid to the case with *no-slip* bottom boundary condition, that is expected to cause a rheological stratification inside the flowing pile. The second objective consists of comparing the experimental data with the mathematical two-layer model, that will be introduced in Chapter 4.

3.1 Particle Image Velocimetry

In this section a preliminary and concise description of the *Particle Image Velocimetry* technique is given, then its application to granular flows is discussed.

The Particle Image Velocimetry (*PIV*) is an optical non-invasive technique, developed in the mid 1980s in the field of experimental fluid mechanics, which allows to obtain instantaneous measurements of the velocity field. One of the original purposes of the *PIV* technique is towards better understanding the turbulence in Newtonian fluids. Such a technique typically makes use of seeding particles inside the fluid under investigation, in order to obtain optical reflections and be able to get information about the flow velocity field. Although the method of adding small objects to a fluid in order to get rough information about the motion has been sometimes used in the past centuries, the German scientist and engineer, L. Prandtl, was the first one to use this approach systematically at the beginning of 1900.

If we look into the recent past, the precursor technique of *PIV* might be identified into the *laser Doppler velocimetry* (often briefly called *LDV*), that uses the *Doppler effect* in a laser beam to measure the flow velocity at a given point. The great advantage of *PIV* and *LDV* over the former techniques, like e.g. the *hot-wire anemometry*, is the non-invasiveness, guaranteed by the fact that the measurements are optical and, thus, apart from the seeding particles, the experimental apparatus is completely outside the flow. Moreover, differently from the *laser Doppler velocimetry*, that is only capable to measure the flow velocity at a single point, the *PIV* technique produces a two-dimensional (or even three-dimensional) velocity vector field. For that reason, nowadays it represents the most popular tool of experimental fluid mechanics for studying turbulent structures and all other phenomena that require the knowledge of the entire velocity field to be correctly understood.

Roughly speaking, the *PIV* technique works by calculating the *cross-correlation function* of the *Image intensity field* (i.e. the matrix of pixel brightness) between a pair of two consecutive frames, taken by a camera and separated by a short time interval, Δt . The image is partitioned in rectangular shaped regions, called *interrogation areas*. The study of the cross-correlation function allows to determine the most likely displacements of each of these interrogation areas and, thus, an estimation of the flow velocity field. If the fluid under investigation is transparent (e.g. water or air), it needs to be seeded by some small reflective particles. By assuming that such seeding particles move together with the fluid, the knowledge of their velocity at any point is equivalent to knowing the flow velocity.

It is very important to underline that the displacement found by the *PIV* analysis, represents the most likely displacement of the gray scale brightness pattern inside each interrogation area. Thus, it is not related to the movement of a particular individual particle but to the entire set of moving particles inside the interrogation area. In this feature, *PIV* essentially differs from another important optical technique, the *Particle Tracking Velocimetry (PTV)*, that, instead, allows to obtain the velocities vectors of some individual seeding particles inside the flow under investigation. In this regard, by analogy to mathematical models, it could be said that, while the *PTV* technique adopts a *Lagrangian* type approach, the *PIV* uses an *Eulerian* type approach.

After dividing the displacements by the time interval between the two images, Δt , a velocity vector for each interrogation area is obtained. In order to ensure proper illumination of the area of interest inside the fluid under investigation, in the classical *PIV* technique a laser pulsating light

needs to be used. The laser is equipped with a series of lenses that spread the laser light into a thin sheet inside the fluid under investigation. The laser light has to be sufficiently powerful to allow capturing pictures with a very short exposure time (of order of nanoseconds). Moreover, it is required to produce the same illumination at different pulses, so that the image of a static object produces the same brightness pattern, under the same exposure time. This property is very important, because, otherwise, some brightness oscillation in the pictures, due to the illumination, would influence erroneously the cross-correlation analysis for determining the most likely displacements.

A typical *PIV* experimental apparatus is composed of the following components:

- a camera that records pairs of images of the illuminated plane inside the fluid under investigation,
- a laser equipment that produces a pulsating powerful light and allows the camera to capture images from a particular area under investigation inside the fluid,
- a synchronizer that synchronizes the camera exposure and the laser pulse,
- a computer that stores the recorded frames from camera and performs the data analysis (i.e. cross-correlation),
- the seeding particle that need to be inserted inside the fluid under investigation before the measurements,
- the fluid under investigation.

3.1.1 Theoretical aspects

In this section we briefly introduce some basic concepts of the PIV Theory.

The *Region of interest* represents the volume under investigation, that can be seen in the field of view of the camera. While, in general, the field of view is a larger area, the region of interest only consists of the volume of fluid, that is illuminated by the laser light. This region can be viewed as a three dimensional space with Cartesian coordinates $\mathbf{X} \equiv (X, Y, Z)$. It can be then partitioned in *Interrogation volumes*. The camera lens maps these volumes into *Interrogation areas*, that lie in a two-dimensional space (i.e. the recorded frame) with coordinates $\mathbf{x} \equiv (x, y)$. Namely, the camera lens operates a transformation between the region of interest in physical space and the recorded image in the imaging plane: everything in the physical space corresponds to something in the recorded image. In Fig. 3.1 the *geometric imaging arrangement* is reported.

In the physical space the seeding particles reflects a certain amount of the light energy. This phenomenon gives rise to a brightness distribution, often called *grey scale pattern*, in the recorded image. In fact, the pixel brightness in a digital image is a measure of the light reflected by the corresponding spot in physical space.

Mathematically, the brightness field is called *image intensity field*. It is a scalar field, I , defined as follows

$$I(\mathbf{x}, \Gamma) = \sum_{i=1}^N V_0(\mathbf{X}) \tau(\mathbf{x} - \mathbf{x}_i) \quad (3.1)$$

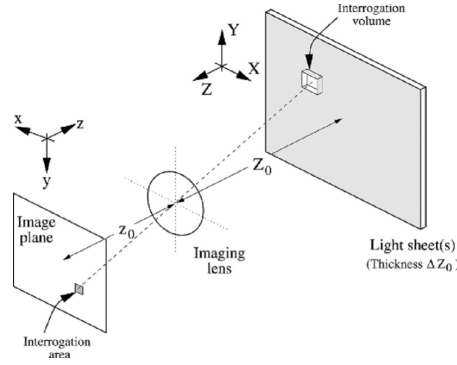


Figure 3.1: Geometric imaging arrangement showing the relation between interrogation volumes and interrogation areas (Raffel et al., 1998).

where $\Gamma = \{\mathbf{X}_1, \mathbf{X}_2, \dots, \mathbf{X}_N\}$ is the set of dots in the three dimensional space, V_0 is the transfer function and τ is the point spread function of the lens. The intensity function I is defined at any point \mathbf{x} and, formally, depends on all the particles in the region of interest.

After a time step Δt , the intensity field changes as follows

$$I'(\mathbf{x}, \Gamma + \mathbf{D}) = \sum_{i=1}^N V_0(\mathbf{X} + \mathbf{D}) \tau(\mathbf{x} - \mathbf{x}_i - \mathbf{d}) \quad (3.2)$$

where \mathbf{D} is the displacement in the three dimensional space and \mathbf{d} the corresponding displacement after the mapping into the imaging plane.

In PIV applications, it is widely assumed that interrogation areas only move rigidly without deformations. Even though, this assumption might seem gross, it turns to be acceptable as long as the time interval between the two picture is kept small.

The displacement in the imaging plane, \mathbf{d} , is unknown and can be determined by means of *pattern recognition* techniques based on statistical arguments. In this regard, the cross-correlation function for any given interrogation area α_I can be defined,

$$R_{I-I'}(\mathbf{s}, \Gamma, \mathbf{D}) = \frac{1}{\alpha_I} \int_{\alpha_I} I(\mathbf{x}, \Gamma) I'(\mathbf{x} + \mathbf{s}, \Gamma + \mathbf{D}) d\mathbf{x} = \frac{1}{\alpha_I} \sum_{i,j} V_0(\mathbf{X}_i) V_0'(\mathbf{X}_j + \mathbf{D}) \int_{\alpha_I} \tau(\mathbf{x} - \mathbf{x}_i) \tau(\mathbf{x} - \mathbf{x}_i + \mathbf{s} - \mathbf{d}) d\mathbf{x} \quad (3.3)$$

in which \mathbf{s} represent the generic displacement in the correlation plane.

The correlation plane contains every possible displacement, \mathbf{s} , to which corresponds a value of the cross-correlation function. The most likely displacement corresponds to the 1st maximum peak of the cross-correlation function. The reliability of this measure is usually accounted for by calculating the ratio between the 1st and the 2nd peak (also called *first noise peak*), that is a good estimate of the signal to noise ratio.

Once the displacement vector is calculated for each interrogation area, the velocity can be straightforwardly obtained by dividing the displacement by the time interval between the two frames (Katzenbach et al., 2011).

Finally, after obtaining the raw data of velocity field from the cross-correlation analysis, a validation procedure follows in order to eliminate faulty data. Such a procedure typically consists in the application of filters, such as the *Standard Deviation filter* and *Range filters* (e.g. Eckart and Gray, 2003).

For more details about the PIV techniques the Reader is referred to e.g. Raffel et al. (1998) or Adrian and Westerweel (2010).

3.1.2 Granular PIV

In the last decade, many attempts have been made in order to take advantage of the PIV technique also in the framework of granular flows. As a result, a slight different PIV technique, often called *granular PIV* (*G-PIV*), has been developed. Some of the first pioneering works, where *G-PIV* has been applied, are e.g. Eckart and Gray (2003) and Lueptow et al. (2000). Other remarkable experimental works that make use of this technique are e.g. Pudasaini and Hutter (2007); Pudasaini et al. (2007); Tai and Lin (2008); Katzenbach et al. (2011).

There are some small differences between the classical PIV technique and the granular PIV, that need to be reported here and briefly discussed.

Firstly, since the granular matter is a non-transparent *medium*, the PIV analysis can be performed only at the boundary surfaces of the motion domain. By way of example, in the case of channelized free surface flows, the PIV measurements can be performed at the free surface and at the bottom and side walls of the channel (if the channel is transparent). As a consequence of this fact, a laser equipment for illuminating the inner planes of the motion domain is not useful in G-PIV. Moreover, the use of laser beams for illuminating the boundary surfaces was found to be unreliable, because of unacceptable variations of illumination intensity (Lueptow et al., 2000). In fact, analogously to the classical PIV technique, the illumination intensity has to be as much as possible constant in time and space during the recording, in order to avoid errors in cross-correlation analysis. In this context, the illumination equipment is usually composed of stroboscopic flash lights, to be synchronised with the camera (Lueptow et al., 2000; Eckart and Gray, 2003), or high power LED light sources (Sheng et al., 2011). Since a non-standard light equipment is usually adopted in G-PIV, particular attention should be paid also to the light placement.

An important requirement for the light equipment is to have a sufficient brightness to avoid underexposed images in presence of short shutter times. In fact, the time delay between every couple of frames has to be small enough to allow a reliable pattern recognition (i.e. cross-correlation analysis). Also the shutter time has to be accordingly small. Moreover, a sufficiently short shutter time is important to avoid blurred pictures. The optimal values for the time delay between frames and shutter time have to be chosen on the basis of the maximum and minimum flow velocities. In typical laboratory applications for studying rapid granular flows with the G-PIV technique, the time delay is of order of hundreds microseconds (Katzenbach et al., 2011).

Another difference between G-PIV and the classical PIV technique consists of the fact that the seeding is usually unnecessary. Indeed, the granular material typically exhibits a reflective structure, that allows a reliable pattern recognition even without treatment (Katzenbach et al., 2011).

Further information about G-PIV can be found in Eckart and Gray (2003), (Pudasaini and Hutter, 2007) or Katzenbach et al. (2011).

3.2 Velocity profiles

The laboratory experimental activity carried out at the Department of Hydraulic and Ocean Engineering of the National Cheng-Kung University (NCKU, Taiwan) concerns the measurement of steady state velocity profiles in channelized dry granular flows. These measurements have been performed through using a high-speed camera and *granular PIV* techniques. The granular material used in the present research was Ottawa sand, a well-sorted sand compliant to the ASTM C-778 20/30 Standard.

3.2.1 Experimental apparatus

In this section a detailed description of the experimental apparatus is given.

Laboratory channels

The experimental apparatus is composed of two straight laboratory channels, 140 cm long and 4 cm wide, made of 10 mm thick polymethacrylate sheets (i.e. Plexiglas). Details are reported in Fig. 3.2, in which x and y represent the longitudinal and the transverse axes, respectively, while z is the axis normal to chute bottom. These chutes, specifically designed for the present research, have been built identical both in size and material. The first chute has been used for obtaining velocity profiles over a smooth bed surface, and thus, its original smooth bed surface made of Plexiglas has been kept unchanged. Instead, the second chute is equipped with a roughened bed. More precisely, a layer of grainy sandpaper has been glued on the original smooth bed surface in order to make it rough enough, so that a *no-slip* bed condition was guaranteed. A suitable sandpaper grit was chosen, so that the angle of friction between the sandpaper and the granular material was higher than the internal friction angle of the granular material.

The upper part of the channel, 28 cm long, has been designed to be used as reservoir for the granular material. The reservoir width is exactly the same of the rest of the chute, in order to reduce three-dimensional effects during the flow. Moreover, the height of side walls in the tank is much bigger (50 cm) than that of the lower part of the chute (12 cm), so that the amount of granular material stored in the tank was enough to ensure the occurrence of statistically steady state during the flow. The tank is separated from the lower part of the chute by a thin baffle, made of Plexiglas, with an opening, 5 cm high, close to the chute bottom. This aperture has the same width of the chute (i.e. 4 cm). It allows the granular material to flow from the upper tank to the chute without sensible deformations along the transverse y direction. During the tank loading, the aperture is kept closed, thanks to an additional plate made of Plexiglas, placed in front of the baffle, separating the upper tank from the rest of the chute, and fixed to it, thanks to some adhesive tape.

Such an additional plate was manually removed at the beginning of each experiment.

The channel was placed on two rigid frames so that the bottom slope in x direction could be chosen and adjusted before each experiment. The range of channel slopes, investigated in the present experiments, was chosen, so that it was possible to observe steady state flows, and is between 28° and 40° . Before each experiment the channel inclination was measured thanks to a digital level (model Bosch DNM 60L) with an accuracy of 0.05° .

Particular care was taken in checking that there was null inclination in y direction within an error of about 0.2° . In fact, an even small inclination in transverse direction could lead to a non-symmetrical velocity distribution along the transverse direction, which is highly undesired in the present study.

In order to collect the flowing granular material, a small container was placed at the lower outlet of the chute.

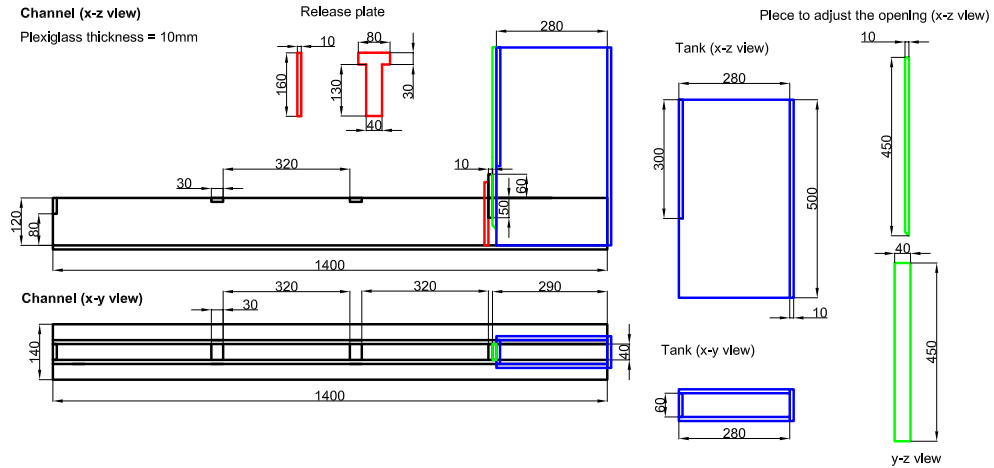


Figure 3.2: Details of the laboratory channels. Dimensions are expressed in millimetres.

Granular material

The granular material used in the whole set of experiments, performed at the NCKU, was Ottawa sand, compliant to ASTM C-778 20/30 Standard. It is a well-sorted round shaped silica sand, whose mean diameter is about 0.7 mm. More precisely, the Standard C-778 20/30 means that the most of the aggregate (99% of the total weight) passes through the sieve No. 20, with mesh size equal to 0.850 mm, while it is almost completely retained (97% of the total weight) by the sieve No. 30, with mesh size of 0.600 mm.

Table 3.1 shows the main properties of the granular material and in particular the friction angles that will be used in the mathematical model. The angle of repose of material φ_{rep} , which is by definition the maximum slope angle of a static pile of grains with respect to the horizontal plane, had been measured previously by Tai and Lin (2008), as well as the basal friction angle with Plexiglas surfaces. The dynamic angle of friction is typically smaller than the static friction angle, as widely reported in Literature (e.g. Hungr and Morgenstern, 1984a,b).

The angle of basal friction with the roughened surface of the Chute No.2, δ_r , was bigger than internal friction angle.

It has been observed that the seeding is usually unnecessary in G-PIV applications (Katzenbach et al., 2011), because granular materials are optically rough. Nonetheless, because the Ottawa sand has an almost uniform colour pattern, in order to further improve the quality of PIV analysis, a small amount of sand (about 10% of the total weight) has been coloured black through using

alcohol-based ink. We can reasonably exclude that this treatment could have changed the friction properties of the granular material because the friction angle mainly depends on the shape and size of particles more than the microscopic friction of the grain surfaces (e.g. Midi, 2004).

Standard Code		ASTM C-778 20/30
Mineral		Quartz (SiO_2), 99.8%
Grain Density	ρ_s	2650 kg/m ³
Hardness		7 (Mohs scale)
Diameter		0.725 ± 0.125 mm
Angle of repose	φ_{rep}	$34.1^\circ \pm 1.4^\circ$
Dynamic friction angle	φ	$\approx 30 - 31^\circ$
Basal friction angle with Plexiglas surface	δ_s	$23.0^\circ \pm 1.1^\circ$
Basal friction angle with sandpaper surface	δ_r	$> 34^\circ$
Volume fraction at rest	ϕ_0	0.64

Table 3.1: Granular material properties.

For each experiment, an amount approximatively equal to 6.66 kg of Ottawa sand, was loaded into the upper tank and let flow down, after releasing the gate. From the depth of the granular material deposit in the tank, it was possible to obtain a rough estimation of the volume fraction at rest, which has been found approximatively equal to 0.64 and it is in good agreement with many measurements on coarse sand widely reported in Literature (e.g. Lambe and Whitman, 1991). This value was found to be almost constant during the experiments, owing to a standardised loading procedure.

High-speed camera

The image acquisition of the granular flow has been performed through using a high-speed camera (model IDT XStream3-Plus), capable to capture pictures at an high frame rate. The camera has a CMOS panchromatic sensor with a resolution of 1280×1024 pixel, and is capable to record at the speed of 625 frames per second at its highest spatial resolution. Nonetheless, by reducing the spatial resolution, i.e. by selecting a smaller Region of Interest (*ROI*), it is possible to increase the maximum recording speed. The camera is equipped with a very bright lens, model Sugitoh TSL-50095 ($f/0.95$), with focal length equal to 50 mm, capable to obtain a good frame exposures, even with rather short shutter times. Moreover, the lens exhibits a negligible barrel distortion: no correction to captured frames was required before PIV analysis. The camera was carefully fixed on a tripod with a 360° adjustable tilt head (model Manfrotto 410 Junior Geared Head). The camera, together with its tripod, was placed at the side of the inclined channel, in order to capture images of the flow motion at the side wall.

After checking the repeatability of the experiments, different runs at the same slope and with the same bottom surface were performed, so that it was possible to take high-speed pictures at different cross sections. In particular, two cross sections have been investigated, the first one was 20 cm downstream the opening gate, while the second one is 35 cm downstream the opening gate. Moreover, each experiment was further repeated in order to take pictures at the free surface at the

two chosen cross sections. In this case the camera was placed above the channel in order the *ROI* to be centred on the cross section under investigation.

Because we are mainly interested in capturing velocity profiles at a particular cross section, the ideal *ROI* should be high enough to capture the entire flow depth from the chute bottom up to the free surface. Conversely, we are not very interested to have a wide field of view in x direction, i.e. in the direction of the flow. Therefore, the whole set of high-speed images has been recorded at a spatial resolution equal to 648×312 pixel, with a frame rate of 2000 fps. In order to capture velocity profiles at the side wall, the camera was placed at the side of the channel wall, about 25 cm far from it, with an inclination with respect to the horizontal plane equal to channel inclination, so that the *ROI* was a rectangle with a span of about 5 cm and 2 cm in the direction normal and parallel to the channel bottom, respectively. For side view recordings, the exposure time was set at $100 \mu\text{s}$ together with a lens aperture of $f/2$, so as to avoid blurred images and, at the same time, to get a sufficiently deep depth of field for obtaining easily a sharp focus.

The camera focus was obtained before each run by taking a series of pictures of a reference grid (mesh $1 \text{ cm} \times 1 \text{ cm}$), printed on a sheet of paper placed on the inner side of the side wall of the chute. Such a grid was also useful to measure the actual geometric scale in captured frames.

Regards the front view recordings, we had some problems to get the grains on the free surface in focus because the flow depth slightly oscillates, due to grain *saltation*. In order to overcome this problem, we used a reference grid, fixed on a rigid surface, about 2 cm far from the chute bottom, to set the focus before each run. Then, we had to reduce the lens aperture to $f/4$ in order to widen the depth of field. At the same time to preserve the exposure we increased the shutter time up to $200 \mu\text{s}$. Despite that, we did not observe blurry frames.

In Fig. 3.3 are reported typical images, recorded by the high-speed from the side of the channel (a) and from the front position (b). These images are presented as they are before any pre-processing treatment.

The high-speed camera is equipped with an internal memory of 2 GB, that allows to record up to 3352 frames at the selected spatial resolution and frame rate. In terms of time span, it equals to 1.675 s at 2000 fps.

Light equipment

In order to ensure a proper exposure of the images captured by the high-speed camera, it is crucial to use a convenient light equipment that provides constant and adequate brightness.

To do so, two lights, specifically designed for high-speed applications have been used. The first one was a high-power LED light source (9000 lumen). With the aim of properly illuminating the field of view of the camera, it was placed, from time to time, near the cross section under investigation at the same side of the high-speed camera. The distance of the LED light source from the channel was about 30 cm. In order to reduce a bit its brightness so as to avoid flares and undesired reflections on the grain surfaces, a thin film of paper was placed in front of the LED light source.

Particular care was taken to increase the image quality near the free surface. In particular, to reduce reflections from the farther side Plexiglas wall, a paper sheet completely printed with a white noise pattern was put at the outer side of the farer side wall. Thus, that white noise pattern is the background of all recorded frames and improves dramatically the PIV analysis at the free

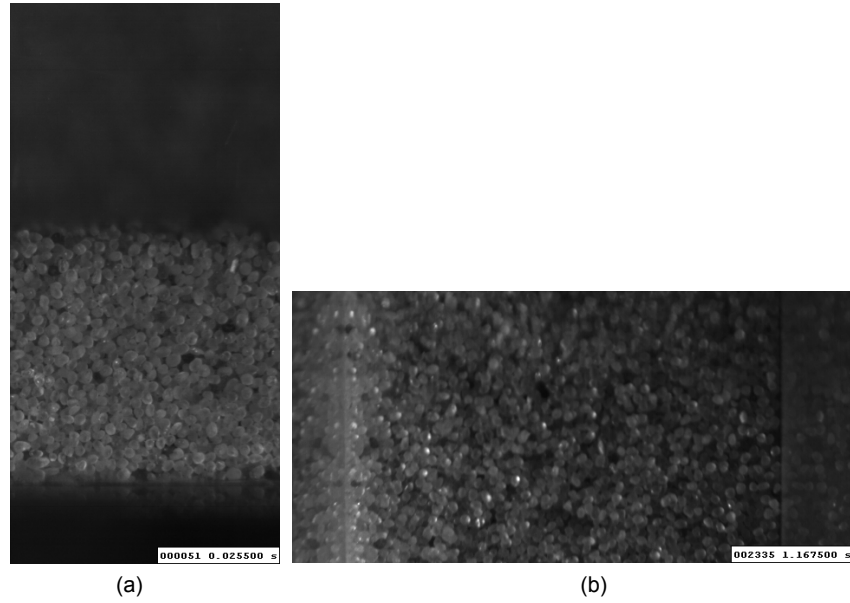


Figure 3.3: Typical frames, captured by high speed camera from the side position (a) and front position (b). In the white box frame number and time point are reported.

surface of the flowing material.

The second light, model MedalLight FL-220AN (6000 lumen), was of fluorescent type. Its main purpose is to increase the background illumination in order to reduce incidental shades. This second light was placed about 50 cm above the channel.

Differently from the most of previous works that make use of the G-PIV technique with flash lights (e.g. Pudasaini et al., 2007; Katzenbach et al., 2011), the lights, employed in the present research, are not of stroboscopic type, but constantly on. Yet, they do not suffer from brightness oscillations issues, thanks to a specifically designed power supply. This set-up turned out to be very convenient, at least for two reasons:

- no synchronization between the camera shutter and the light pulse is required, because the light is always on;
- the maximum acquisition rate is governed by the camera capabilities and does not depend on the charging time of the capacitors, commonly used in flash power supplies.

Figure 3.4 shows the experimental apparatus, during a front-view recording, where it is easy to identify the two lights and the high-speed camera.

Image acquisition software

After each run, the recorded pictures were downloaded from the camera to a notebook, via USB connection. The frames are saved in 8-bit gray-scale lossless format. The image acquisition procedures are controlled by the commercial software IDT X-Vision. The same software permits

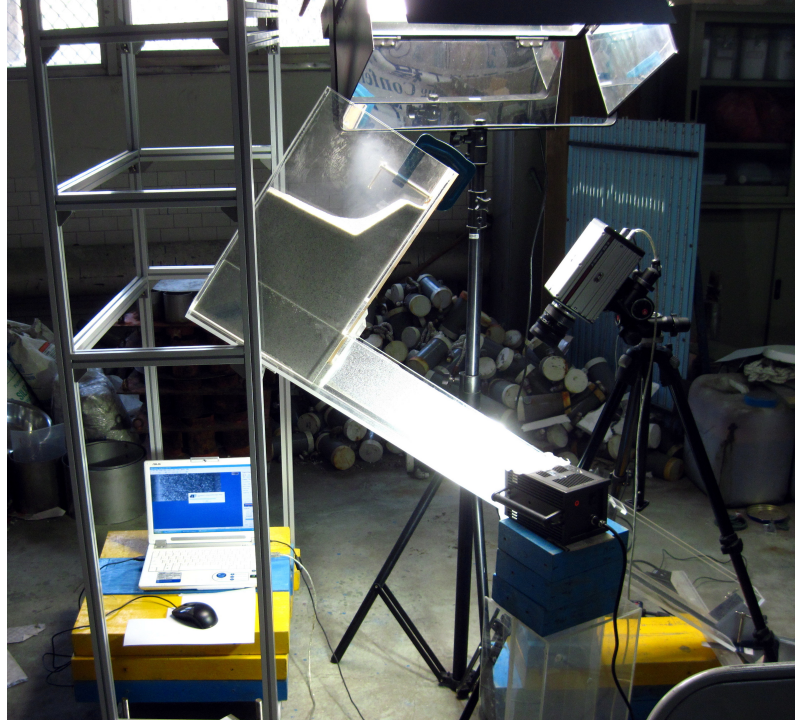


Figure 3.4: The experimental apparatus.

also to set all the recording parameters to the camera before each run and to trigger the recording. Conversely, the PIV analysis has been performed by using the commercial software IDT ProVision-XS. A detailed description of the PIV analysis is reported in the next section.

3.2.2 Granular PIV analysis

Each recording is composed of 3352 frames that have been analysed in separated pairs. The overall analysis procedure is composed of the following stages:

- Pre-processing of the images in order to improve the image quality,
- PIV analysis that yields an estimate of the velocity field in the Region of Interest,
- Post-processing of the raw data from PIV analysis, in order to remove faulty data.

Before the actual PIV analysis, all the frames have been subjected to a pre-processing digital treatment, aimed at improving the image quality. More precisely, to enhance the image contrast, a *contrast limited adaptive histogram equalization (CLAHE)* has been employed.

The software IDT ProVision-XS has been used for the PIV analysis of all recordings. The chosen coupling rule for PIV analysis was the following: we take the first two frames together, then the third one together with the fourth one and so on, i.e. 1-2, 3-4, 5-6 etc. In total, a set of 1676 couples of frames is obtained for each run. Each couple of frames yields a velocity field.

The main parameter of the PIV analysis is the size of the interrogation area. Obviously, the optimal choice of this value depends on the minimum and maximum displacements (in terms of pixel) in the recorded frame pairs. On the one hand, this value cannot be too small, otherwise the cross-correlation analysis will fail to properly recognize the motion of fastest particles. On the other hand, a too big interrogation area would reduce too much the sensitivity of the velocity field reconstruction, i.e. the minimum recognized velocity would be unacceptably high.

A thumb rule to obtain a reliable velocity field is that the maximum displacement should be less than 1/4 of the span of the interrogation area (Keane and Adrian, 1993). In our case, the aforementioned condition is globally fulfilled by choosing an interrogation area, 32×32 pixel wide, that corresponds approximately to a $2 \text{ mm} \times 2 \text{ mm}$ square in real scale. The mesh overlap is chosen equal to 50%, in order to fulfil the Nyquist sampling criterion.

After the PIV analysis, a vector validation of raw data has been carried out. During this stage, only a *Range Filter*, that removes the velocity vectors that lie beyond some given limits, has been used. In fact, especially in case of *no-slip* bottom boundary condition, the velocity field exhibits large velocity gradients: hence, the usage of a *Standard Deviation filter* would be detrimental. Faulty data, whose amount was typically around 5% in each frame pair, are substituted through interpolation of neighbour data. The obtained velocity field for each frame couple has a spatial extension of about 2 cm in x direction and is centred on the cross section under investigation, i.e. $x=20$ cm or $x=35$ cm. Because we are only interested in acquiring velocity profiles at these cross sections, only the velocity vectors related to these positions are kept from the PIV analysis and are reported in detail hereafter.

The software IDT ProVision-XS uses a proprietary cross-correlation algorithm, hence, it was not possible to know *a priori* the sensitivity of the PIV analysis, i.e. the minimum measurable displacement. However, from the calculated velocity field we estimate that, in our experimental set-up, the minimum measurable velocity is definitely below 0.01 m/s and corresponds to a sub-pixel accuracy of 1/10, at least.

3.2.3 Experiments

Two series of experiments have been performed. The first series was on smooth bed surface and was performed by using chute No. 1. The second one was on rough bed (chute No. 2). The purpose of this experimental research is to study the velocity profiles at different bed conditions in order to better understand the effects of bottom boundary conditions on the velocity profile.

The setting of each experiment requires the following procedures:

- the chute is carefully positioned on the aluminium frames with the chosen slope,
- the upper tank is loaded with Ottawa sand with a total amount of about 6.66 kg,
- the high-speed camera and lights are carefully positioned close to the cross section under investigation,
- the release plate is manually removed, so that the granular material could flow from the reservoir into the channel,
- after a few seconds after the opening, the high-speed camera is triggered so as to record images of the flowing pile.

Since we are interested in steady-state velocity profiles, the first concern was to check whether a *statistically* steady state was reached at the different channel slopes under investigation. With the term “*statistically* steady state”, or simply “steady state” hereafter, we mean that the time averages (of the Reynold’s type) of the main quantities, such as flow velocity and flow depth, are unchanging in time. The methods, used to check the occurrence of the steady state, are reported in the next subsection.

The opening between the tank and the chute is chosen to be 5 cm-high for all the experiments. This choice has been determined by two opposing needs. On the one hand, it is required that the opening be small enough to ensure a sufficiently long steady state before the complete emptying of the reservoir. On the other hand, in order to obtain an acceptable detail of the velocity profiles, the opening gate should be big enough to avoid that the flow depth be too small. After several tests, this choice turned out to be the best compromise between these two needs.

The complete list of experiments is reported in Table 3.2. In run R-28r steady state is not observed because of the premature stop of the granular avalanche. Therefore, the related data are not considered in the further analysis and discussion. Each run was repeated several times in order

ID code	Incl.	Chute	Bed surface
R-28s	28°	No. 1	smooth (Plexiglass)
R-31s	31°	No. 1	smooth (Plexiglass)
R-34s	34°	No. 1	smooth (Plexiglass)
R-40s	40°	No. 1	smooth (Plexiglass)
R-28r	28°	No. 2	rough (Sandpaper)
R-31r	31°	No. 2	rough (Sandpaper)
R-34r	34°	No. 2	rough (Sandpaper)
R-40r	40°	No. 2	rough (Sandpaper)

Table 3.2: Runs

to take recordings at the two different cross sections and different views (i.e. side and front views). Moreover, for each camera position, the experiment was repeated 4 times in order to verify the repeatability of the phenomenon and obtain further statistical information.

The first cross section under investigation, which is 20 cm downstream the release gate, will be hereafter referred to as *upper* cross-section, while the second one, which is 35 cm downstream the release gate, will be referred to as *lower* cross-section. The rationale for choosing the first cross section is the following: it has to be far enough from the opening gate to avoid strong curvatures of flow lines.

Moreover, since the flow depth typically is found to decrease with x , the second investigated cross section was chosen at the lowest point, where the flow depths were still big enough to allow to obtain a reasonable number of data points in the velocity profiles.

The complete set of recordings is reported in Table 3.3. The frame rate was set to 2000 fps for every recording. The Identification code of recording is reported in the first column. The position of the cross section is reported in the second column. The camera position is in Column 3. The number of experiment repetitions are reported in Column 4. Finally, information about the camera parameters, such as spatial resolution, lens aperture, shutter time, are reported in columns 5, 6

and 7, respectively.

Identification code	Cross section	View	Rep.	Spat. res.	Aperture	Shutter
R-28s-UP	x=20 cm	Side	4	312×648	f/2	100 μ s
R-28s-DOWN	x=35 cm	Side	4	312×648	f/2	100 μ s
R-28s-FRONTUP	x=20 cm	Front	4	312×648	f/4	200 μ s
R-28s-FRONTDOWN	x=35 cm	Front	4	312×648	f/4	200 μ s
R-31s-UP	x=20 cm	Side	5	312×648	f/2	100 μ s
R-31s-DOWN	x=35 cm	Side	4	312×648	f/2	100 μ s
R-31s-FRONTUP	x=20 cm	Front	4	312×648	f/4	200 μ s
R-31s-FRONTDOWN	x=35 cm	Front	4	312×648	f/4	200 μ s
R-34s-UP	x=20 cm	Side	4	312×648	f/2	100 μ s
R-34s-DOWN	x=35 cm	Side	4	312×648	f/2	100 μ s
R-34s-FRONTUP	x=20 cm	Front	4	312×648	f/4	200 μ s
R-34s-FRONTDOWN	x=35 cm	Front	4	312×648	f/4	200 μ s
R-40s-UP	x=20 cm	Side	5	312×648	f/2	100 μ s
R-40s-DOWN	x=35 cm	Side	4	312×648	f/2	100 μ s
R-40s-FRONTUP	x=20 cm	Front	4	312×648	f/4	200 μ s
R-40s-FRONTDOWN	x=35 cm	Front	4	312×648	f/4	200 μ s
R-31r-UP	x=20 cm	Side	4	312×748	f/2	100 μ s
R-31r-DOWN	x=35 cm	Side	4	312×748	f/2	100 μ s
R-31r-FRONTUP	x=20 cm	Front	4	312×648	f/4	200 μ s
R-31r-FRONTDOWN	x=35 cm	Front	4	312×648	f/4	200 μ s
R-34r-UP	x=20 cm	Side	3	312×648	f/2	100 μ s
R-34r-DOWN	x=35 cm	Side	4	312×648	f/2	100 μ s
R-34r-FRONTUP	x=20 cm	Front	4	312×648	f/4	200 μ s
R-34r-FRONTDOWN	x=35 cm	Front	4	312×648	f/4	200 μ s
R-40r-UP	x=20 cm	Side	4	312×648	f/2	100 μ s
R-40r-DOWN	x=35 cm	Side	4	312×648	f/2	100 μ s
R-40r-FRONTUP	x=20 cm	Front	4	312×648	f/4	200 μ s
R-40r-FRONTDOWN	x=35 cm	Front	4	312×648	f/4	200 μ s

Table 3.3: Complete list of high-speed recordings.

Steady state

The first problem was to verify the occurrence of a *statistically* steady state at the different channel slopes under investigation. It is important to point out that, strictly speaking, steady state does not occur in rapid granular flows, similarly to what happens in turbulent Newtonian flows. In fact, there are continuous fluctuations of the flow velocities, due to grain collisions (i.e. non-null *granular temperature*), and so the flow velocity field depends on time. Nonetheless, a statistically steady state can be defined. Namely, it is reached when the time averaged physical quantities are unchanging in time. The time average of a given physical quantity f can be calculated as follows

$$\bar{f} = \frac{1}{T} \int_0^T f(t) dt \quad (3.4)$$

where T is a sufficiently large time to avoid residual fluctuations of \bar{f} . The problem of practically choosing an optimal value for T , in the present experimental analysis, is addressed in the next subsection.

A preliminary side view recordings at the frame rate of 500 fps were carried out for each slope under investigation. Each of these recordings has a time extent of 6.7 s. These recordings are not for PIV analysis but for manually checking the evolution of flow depths in time. We verified that after a few seconds after the release, the flow depths became almost constant at the different cross sections, except for some oscillations, due to grain saltations at the free surface.

It is worth noting that, although the flow depth in the tank actually reduces as the time goes on, an almost steady state is observed after a few seconds after the beginning of the release. This behaviour is also confirmed by other experimental investigations on the same granular material, in which the mass flow rate was also measured (Tai and Lin, 2008). Such an apparently strange phenomenon is explained by the fact that, differently from what it is observed in clear water and Newtonian fluids, the outflow rate of dry granular material from a small orifice weakly depends on the *hydraulic head* (e.g. Savage, 1984).

In addition to this preliminary check, the occurrence of an almost steady state is further verified, through the PIV analysis of recordings at 2000 fps (i.e. those reported in Table 3.3), by comparing the velocity profiles at different time intervals. Each recording is composed of 1676 couples of frames which corresponds to a total recording time of 1.676 s. The PIV analysis provides as many velocity profiles at the two chosen cross sections. From PIV data, we calculated the time-averaged velocity profiles over three separate time intervals of 0.5 s (i.e. 500 frame pairs). In other words, from each recording, we used the first 500 frames pairs to obtain the first time-averaged velocity profile; then we used the frame pairs between 501th and 1000th to obtain the second velocity profile. Similarly, the third velocity profile has been obtained by calculating the time-average velocity profile from 1001th to 1500th frame pairs. These three profiles are carefully compared each other for each repetition of each recording.

Some examples of these preliminary comparisons are reported in Figs. 3.5 and 3.6 (recording R-40s-UP). Here and afterwards in this Chapter, the velocity profiles are plotted in dimensionless form, by following the same scaling proposed by Midi (2004); Forterre and Pouliquen (2008). In particular, the flow velocity is normalized by the quantity \sqrt{gd} , while the distance from the bed surface z is divided by d .

In Figs. 3.5 and 3.6, the left-hand diagrams represent the z -component of flow velocity along

the flow depth, while the right-hand one are the x -component of the flow velocity. As evident from the figures, the x and z components of flow velocities are weakly dependent on the chosen time interval. Similarly, also the relative standard deviations are almost independent on the time interval. The same behaviour is also observed, when comparing the time averaged velocity profiles, obtained from two different repetitions of the same experiment.

These comparisons have been performed for each experiment (at different repetitions) and yield analogous satisfactory results. Therefore, we can reasonably state that an almost steady-state is reached in every experiment, except for the run R-28r in which, as already said, a prematurely stop was observed.

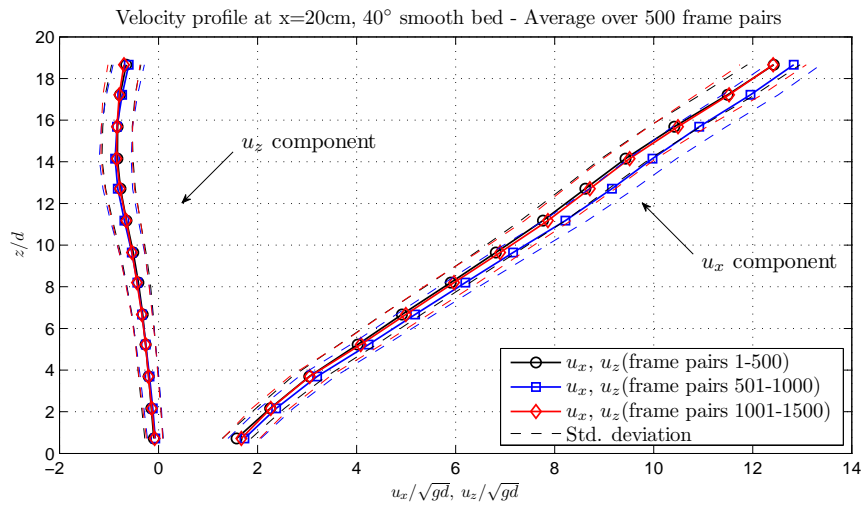


Figure 3.5: Time averaged velocity profiles over different time intervals (recording R-40s-UP, 1st repetition). Both x and z components of the velocity vector are reported.

3.2.4 Time averages

Another important concern is the identification of an acceptable value for the time window, T , to be used in time averages in Eq. (3.4). In order to get steady state velocity profiles, the time window, T , has to be big enough to filter out all velocity fluctuations. Hence, the minimum acceptable value of T is expected to depend on the flow dynamics and, in particular, on granular temperatures. Moreover, the PIV technique may introduce some errors, that add additional noise to the velocity profiles. A proper time averaging is also useful to eliminate this kind of additional *artificial* noise.

For every recording, different velocity profiles have been calculated over the following different time windows

$$T \in \{0.01 \text{ s}, 0.02 \text{ s}, 0.05 \text{ s}, 0.10 \text{ s}, 0.25 \text{ s}, 0.50 \text{ s}, 1.00 \text{ s}, 1.676 \text{ s}\}. \quad (3.5)$$

The maximum value, that has been investigated, $T_{max} = 1.676 \text{ s}$, corresponds to the total extent of every high-speed recording and, thus, cannot be exceeded. All different time averaged velocity profiles have been compared, in order to identify the minimum value of T , above which the velocity

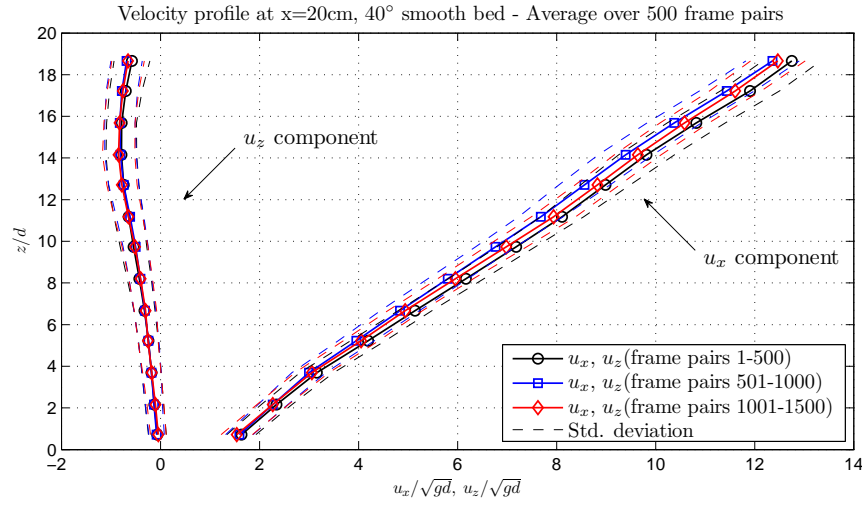


Figure 3.6: Time averaged velocity profiles over different time intervals (recording R-40s-UP, 2nd repetition). Both x and z components of the velocity vector are reported.

profile is found to be reasonably unchanging. In order to analytically estimate the deviations of different time averaged velocity profiles, an error index, of the type of the normalized 1-norm, is defined as follows

$$E(T) = \frac{\sum_{i=1}^N \|\overline{\mathbf{u}}_i(T)\| - \|\overline{\mathbf{u}}_i(T_{max})\|}{\sum_{i=1}^N \|\overline{\mathbf{u}}_i(T_{max})\|}, \quad (3.6)$$

where $\overline{\mathbf{u}}_i(T)$ represents the i -th velocity vector, time-averaged over T , and N is the total number of data points of the velocity profile. The error index, defined in Eq. (3.6), is an estimate of the deviation of a given time averaged velocity profile from that one, time averaged over the total recording time T_{max} . The critical value of T is defined as the minimum value over which $E(t) \leq 0.01$. In principle, such a value varies from one experiment to another.

By way of example, the comparisons among different time averaged velocity profiles from the recording R-40s-UP (smooth bed) and R-40r-UP (rough bed), are shown in Figs. 3.7 and 3.8, respectively. Also the velocity profiles, obtained without time averaging, have been added in these diagrams. Firstly, as one can easily see from Figs. 3.7 and 3.8, velocity fluctuations have stronger effects in z component velocity profiles. This is mainly due to the fact that u_z are about tenfold smaller than u_x . As well, in Tables 3.4 and 3.5, the error indexes E , corresponding to different time-averaged velocity profiles, are shown. From Table 3.4, one can notice that the critical time is approximately equal to $T = 1$ s. Similarly, as reported in Table 3.4, the critical time for experiment R-40r-UP is still around $T = 1$ s, though it is somehow smaller than the case R-40s-UP. Similar findings have been observed in the comparisons, related to different recordings. Generally speaking, it has been found that the critical value of T increases with the bottom slope and, in particular, with the maximum flow velocity. Moreover, experiments over smooth basal surface typically exhibit slightly bigger values of the critical T , if compared with experiments over rough basal surface at the same inclination. This finding suggests that there is a dependence of T on the granular temperature and, hence, on the flow regimes. Nonetheless, the differences among the critical values of T have

T	$E(T)$
0.01 s	0.0763
0.02 s	0.0577
0.05 s	0.0436
0.10 s	0.0426
0.25 s	0.0444
0.50 s	0.0171
1.00 s	0.0094

Table 3.4: Deviations of time averaged velocity profiles (exp. R-40s-UP), measured by means of error index, defined in Eq. (3.6).

T	$E(T)$
0.01 s	0.0287
0.02 s	0.0263
0.05 s	0.0107
0.10 s	0.0114
0.25 s	0.0181
0.50 s	0.0108
1.0 s	0.0069

Table 3.5: Deviations of time averaged velocity profiles (exp. R-40r-UP), measured by means of error index, defined in Eq. (3.6).

been found to be quite small in the present dataset.

Therefore, a time window equal to $T = 1.0$ s, corresponding to 1000 frame pairs, has been used for calculating all the velocity profiles presented in this Chapter and used in the rest of this dissertation.

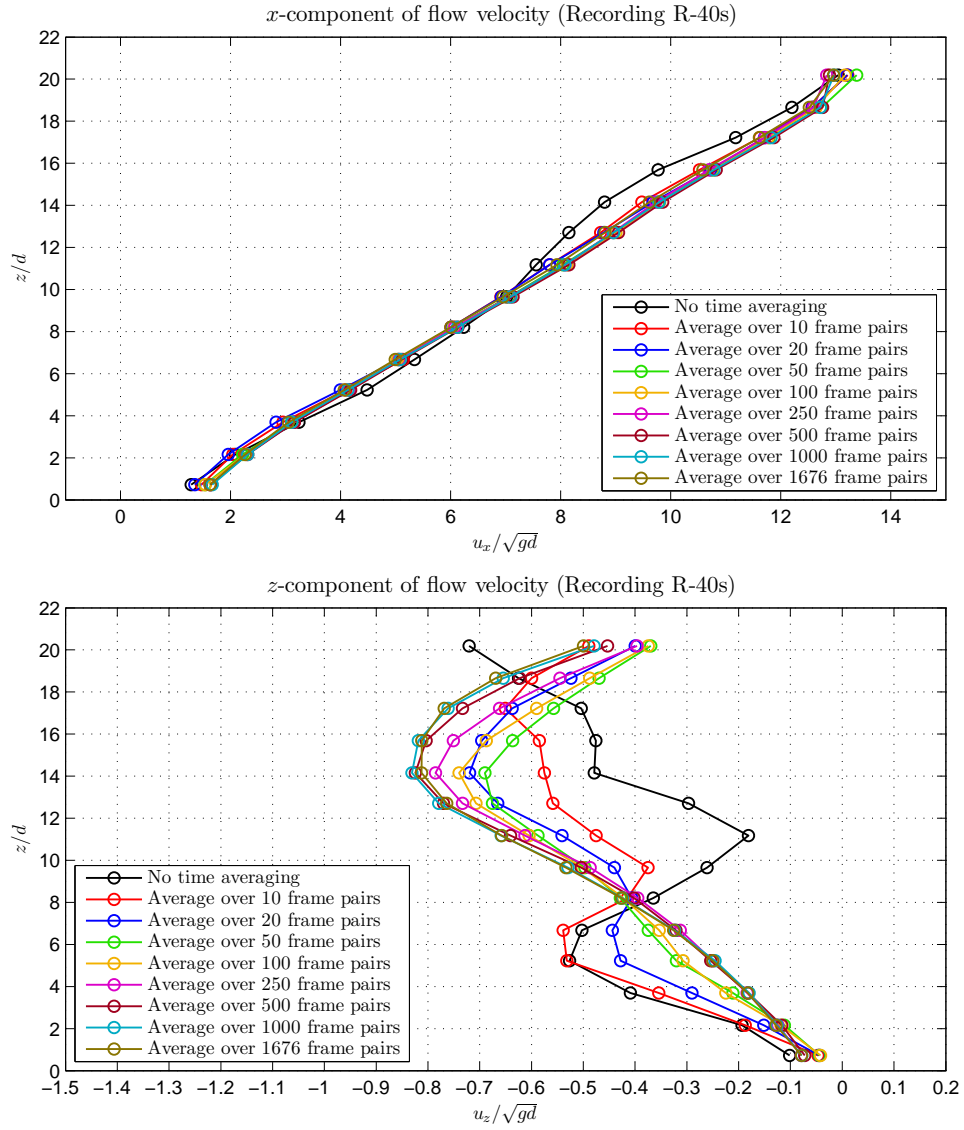


Figure 3.7: Comparisons among different time averaged velocity profiles from the recording R-40s-UP; x -components and z -components of the flow velocity vectors are reported in the top frame and in the bottom frame, respectively.

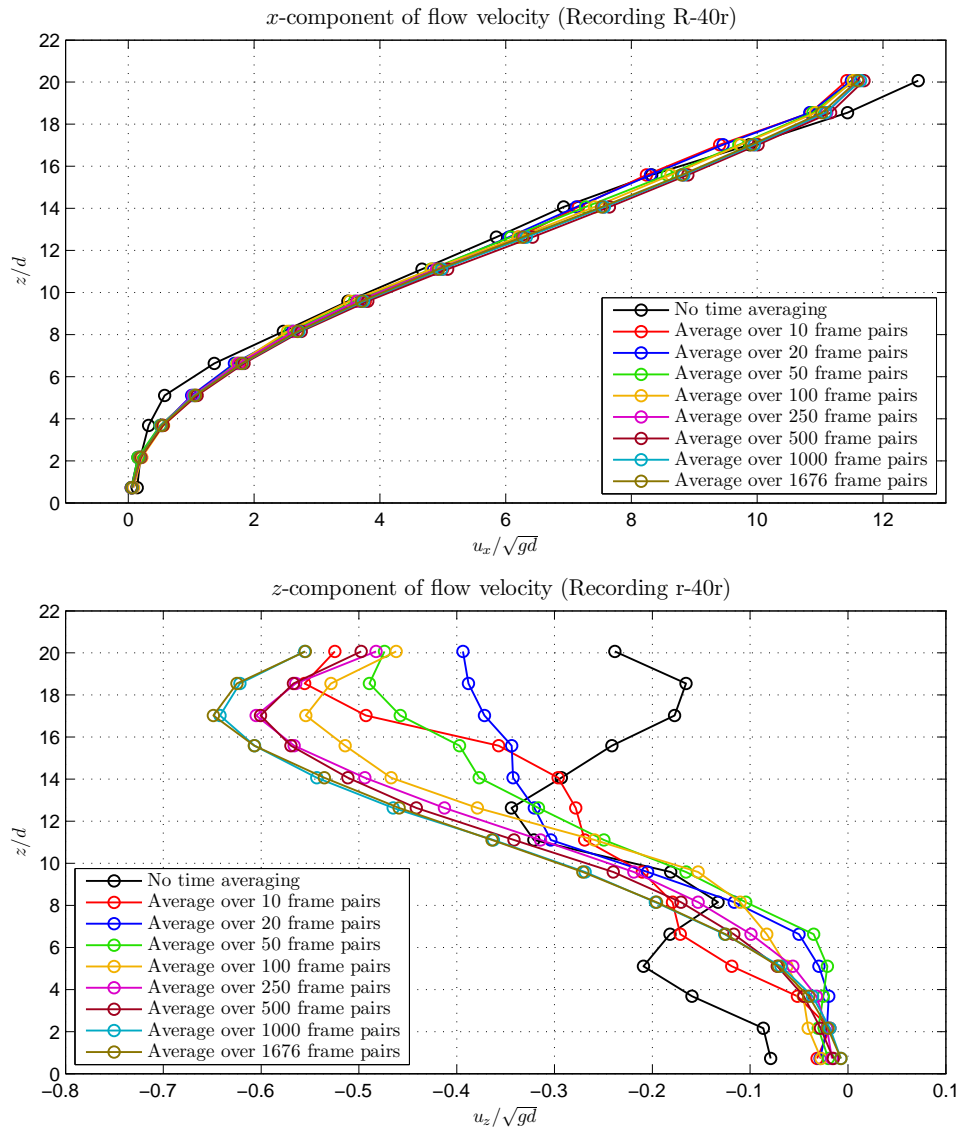


Figure 3.8: Comparisons among different time averaged velocity profiles from the recording R-40r-UP; x -components and z -components of the flow velocity vectors are reported in the top frame and in the bottom frame, respectively.

3.2.5 Side-wall velocity profiles

In this section the velocity profiles, measured at the side wall, are presented and carefully compared. All the diagrams here reported have been obtained by time-averaging the flow velocity measurements over a time window equal to 1 s (i.e. 1000 frame pairs).

Smooth bed runs

At first, we are going to show the data, related to the experiments, performed over smooth bed surface.

In Fig. 3.9 the x and z -components of the flow velocity vectors at the Upper cross section are reported. As well, in Fig. 3.10 the velocity profiles at the lower cross section are shown. Together with the time averaged values, the relative Standard Deviations are also reported.

As one can easily see from the x -component of velocity vectors in Figs. 3.9 and 3.10, at the small inclination angles (i.e. 28° and 31°) there is a lower zone almost at rest. This is very interesting because it means that a *no-slip* boundary condition could be found also in smooth bed runs. It could seem strange, if we consider that the basal friction angle, δ_s , in the case of smooth bed surface, is smaller than all the investigated inclination angles (cf. Table 3.1). Nonetheless, the reason of this apparently strange phenomenon can be found in the effect of side wall resistances. In fact, in channelized flows and, in particular if the channel width is narrow, compared to the flow depths, the side walls have an important influence on the flow dynamics. Conversely, at big inclination angles (i.e. 34° and 40°) there is a *slip* boundary condition, i.e. a non-null velocity at the basal surface. In such a case, the mass forces are stronger. Hence, the resistances at the basal and side wall surfaces are not sufficient to enforce a *no-slip* bottom boundary condition.

By focusing on the x -component of velocity vectors, we notice that the velocity profiles exhibit clearly different behaviours at different slopes. In the case of *no-slip* boundary condition, the x -component velocity profiles have a convex shape and seem to be composed of two zones with different behaviours. In the first one, which is near the free surface, the velocity exhibits an almost linear profile. In the second zone, that goes down to the basal surface, the velocity profile consists of an exponential tail, in which the x -component of velocity goes asymptotically to zero with a zero gradient. A similar behaviour has been observed in other experimental configurations and different granular materials, e.g. in *heap flows* and *rotating drum* experiments reported in Midi (2004). What there is in common among these different experimental set-ups is the occurrence of a *no-slip* bottom boundary condition. In the case of slip boundary condition, instead, the velocity profile is clearly linear, as observed in R-40s-UP and R-40s-DOWN. Somehow, Exp. R-34s represents an intermediate case. In fact, while in the Upper cross-section (cf. R-34s-UP) a slip boundary condition is observed but the velocity profile still has a slightly convex shape, in the Lower cross-section (cf. R-34s-DOWN) the slip velocity is bigger and the velocity profile is almost linear.

As regards the standard deviations in the x -component plots, it is interesting to note that they slightly increase with the flow velocity, although this behaviour is more evident in Experiments R-28s and R-31s. At the free surface, in some profiles the standard deviation increases rapidly. It could be mainly due to the fact that the flow depth is constant, only in a time-averaged sense, owing to grain saltation and rearrangements. Such saltating particles may induce additional velocity

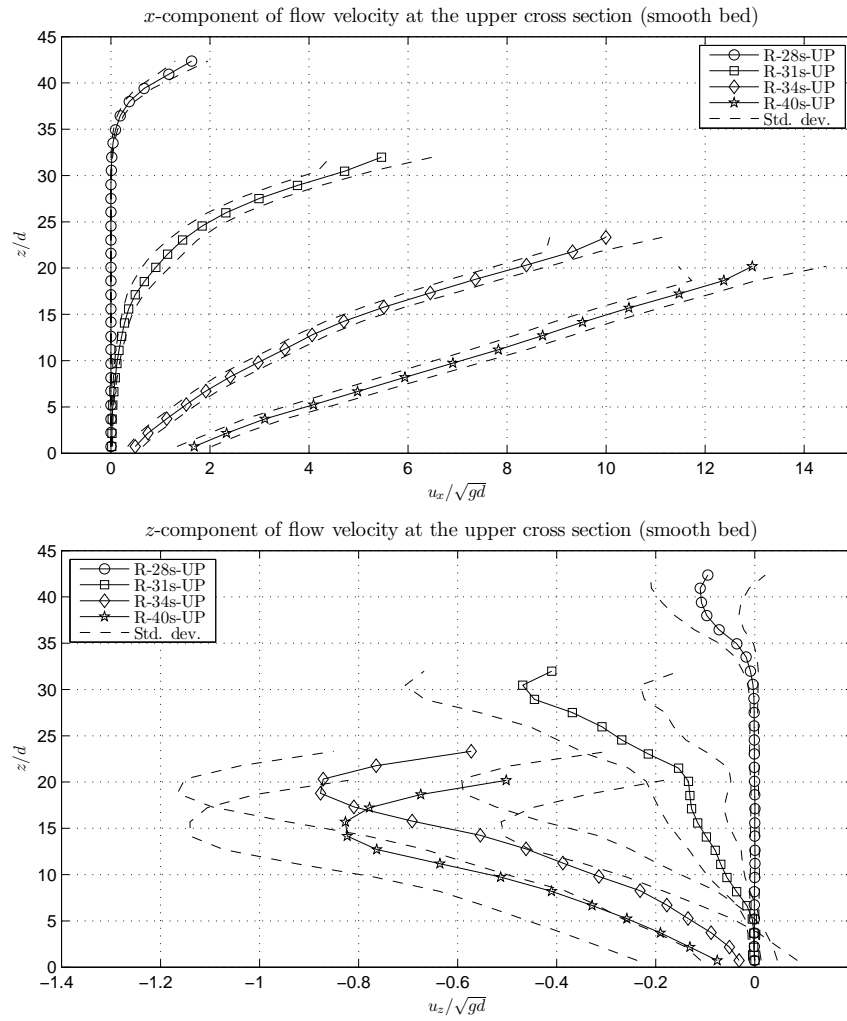


Figure 3.9: x and z components of the flow velocity at $x = 20 \text{ cm}$ from the release gate with related standard deviation (smooth bed condition). Velocity vectors have been averaged over 1000 frame pairs, from repetition No.1.

fluctuations at the free surface. Moreover, whenever the interrogation areas across the free surface were not completely “full” of grain particles, the PIV analysis might produce some calculation errors.

As regards the z -component velocity profiles in Figs. 3.9 and 3.10, firstly, it is important to point out that the z -component of velocity vector is much smaller (about 1/10) than the x -component. This behaviour is widely expected in shallow flows and partially supports the well-known assumption of *Long Wave Approximation*, usually employed for the derivation of depth-average mathematical models. Moreover, it is noteworthy that z -component of flow velocities are practically always negative, namely the grain particles are subjected to a slow, yet continuous, falling down. By observing several high-speed recordings in slow-motion with naked eyes, we found that this phenomenon seems to be due to the effect of grain rearrangements. Typically, during the motion, the granular pile is subjected to a continuous shearing that, from time to time, causes the development of “holes”. Such holes are rapidly filled up by other grain particles, that fall into them owing to gravity.

The z -components of flow velocity increase with the distance from the bottom surface but exhibit their maximum value noticeably below the free surface (within a distance of about 3-10 grain diameters). At the bottom surface, because of the kinematic boundary condition (i.e. $\mathbf{v} \cdot \mathbf{n} = 0$), the z -component velocity should be rigorously null. It seems to be in contrast with some of the PIV measurements, that yield non-null values, in particular for Experiments R-34s and R-40s. This disagreement is partially due to the fact that the first point of the velocity profile is not exactly on the bottom surface but a little bit above it, because it is referred to the centre of the interrogation area and not to its boundary. The standard deviations tend to increase with the time-averaged values, quite similarly to what observed about the x components, but are quite constant near at the free surface, although the time-averaged values here decrease.

Rough bed runs

In Figs. 3.11 and 3.12 are shown the dimensionless velocity profiles, obtained in rough bed runs, at the cross sections $x = 20$ cm and $x = 35$ cm, respectively.

As regards the x -component of velocity vectors, the shape of the velocity profiles is similar to what observed in Experiments R-28s and R-31s over smooth bed surface: there is a linear behaviour at the top and an exponential tail in the lower part with an almost zero velocity gradient at the bottom. In this case, a no-slip bottom boundary condition and convex shaped velocity profiles are observed for every inclination angle. Namely, in the case of rough bed condition, it was not possible to observe a slip bottom boundary condition, even at the highest inclination angle investigated (i.e. 40°). By observing the velocity profiles in Figs. 3.11 and 3.12, it could be inferred that the quasi-static zone can be further divided into two zones: a lower one where the granular material is at rest and an upper one where exhibits an exponential velocity profile. These two zones can be clearly identified in Exp. R-31. However, through taking long exposure photographs, Komatsu et al. (2001) observed that the effective flow depth is far bigger than what appears in high speed recordings, owing to a slow creep motion of grain particles. Therefore, a threshold velocity should be used to arbitrarily separate the “deposit” from the flowing zone.

Again, it is worth noticing that the kinematic boundary condition at the bottom is the main factor that governs the flow behaviour. However, owing to the bigger resistance at the bottom

surface, the flow velocities are always smaller, with respect to the smooth bed runs with the same inclination angle.

In velocity plots referred to runs R-34r-DOWN and R-40r-DOWN, a slight decrease of the partial derivative of time-averaged velocity, $\partial_z \overline{u_x}$, is observed near the free surface. It could be due to the already mentioned uncertainty of the PIV analysis at the free surface.

Regards the standard deviations, they have a trend, similar to what observed in smooth bed runs, although they are generally smaller.

Now, let us examine the diagrams of the z component of flow velocity. Analogously to what observed in smooth bed runs, the z -components are always negative. Moreover, they have their maximum value below the free surface. Since the z -components of flow velocities are likely to be induced by grain rearrangements, their maximum values are located where such arrangements are expected to be more frequent. Standard deviation follow a trend, similar to what observed in smooth bed experiments.

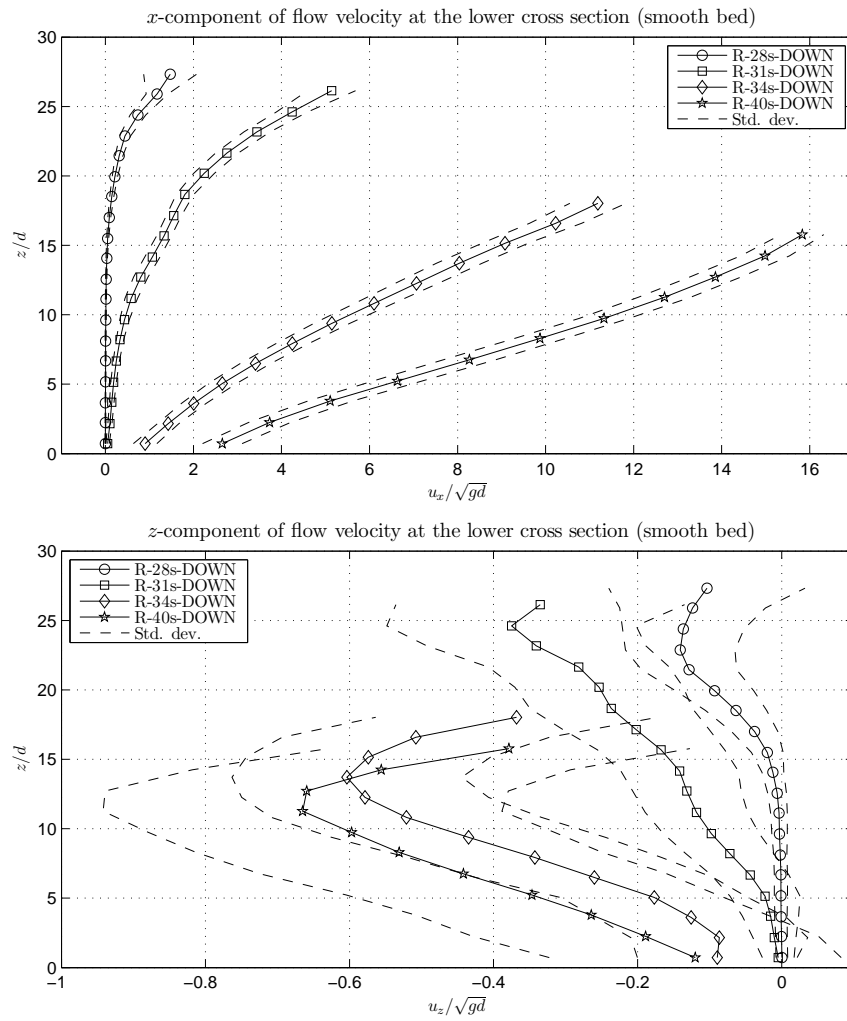


Figure 3.10: x and z components of the flow velocity at $x = 35$ cm from the release gate with related standard deviation (smooth bed). Average over 1000 frame pairs, from repetition No.1.

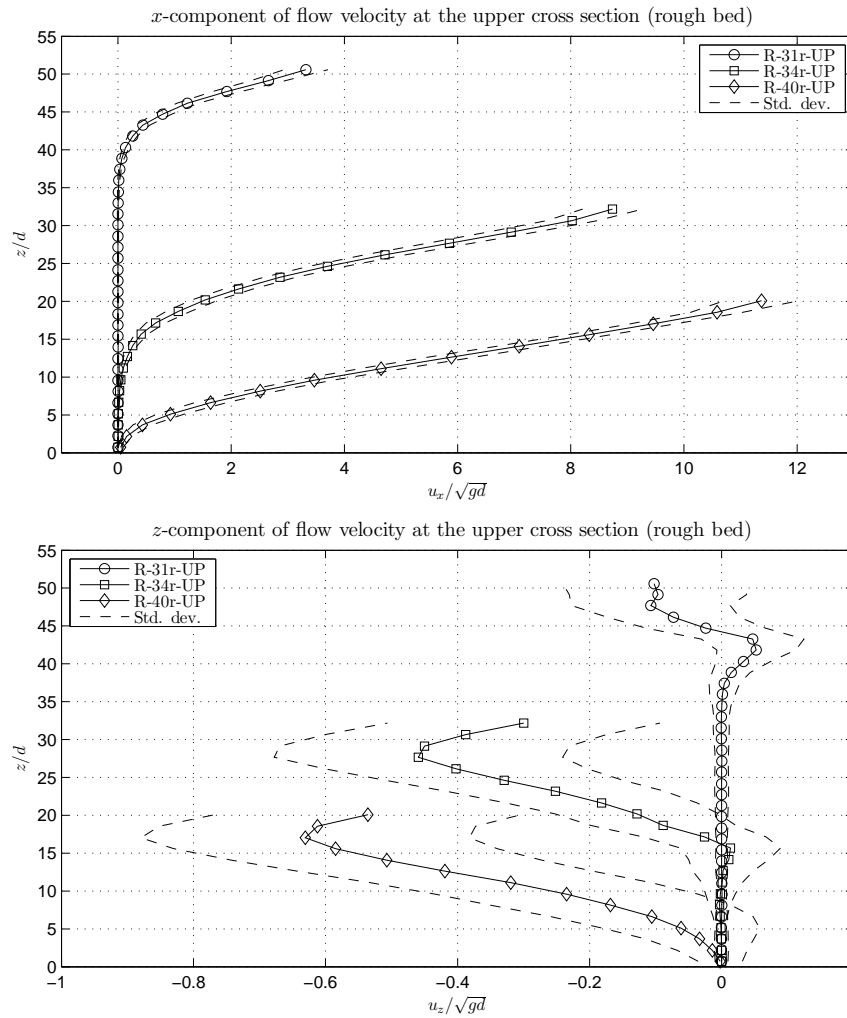


Figure 3.11: x and z components of the flow velocity at $x = 20\text{ cm}$ from the release gate with related standard deviation (rough bed condition). Average over 1000 frame pairs, from repetition No.1.

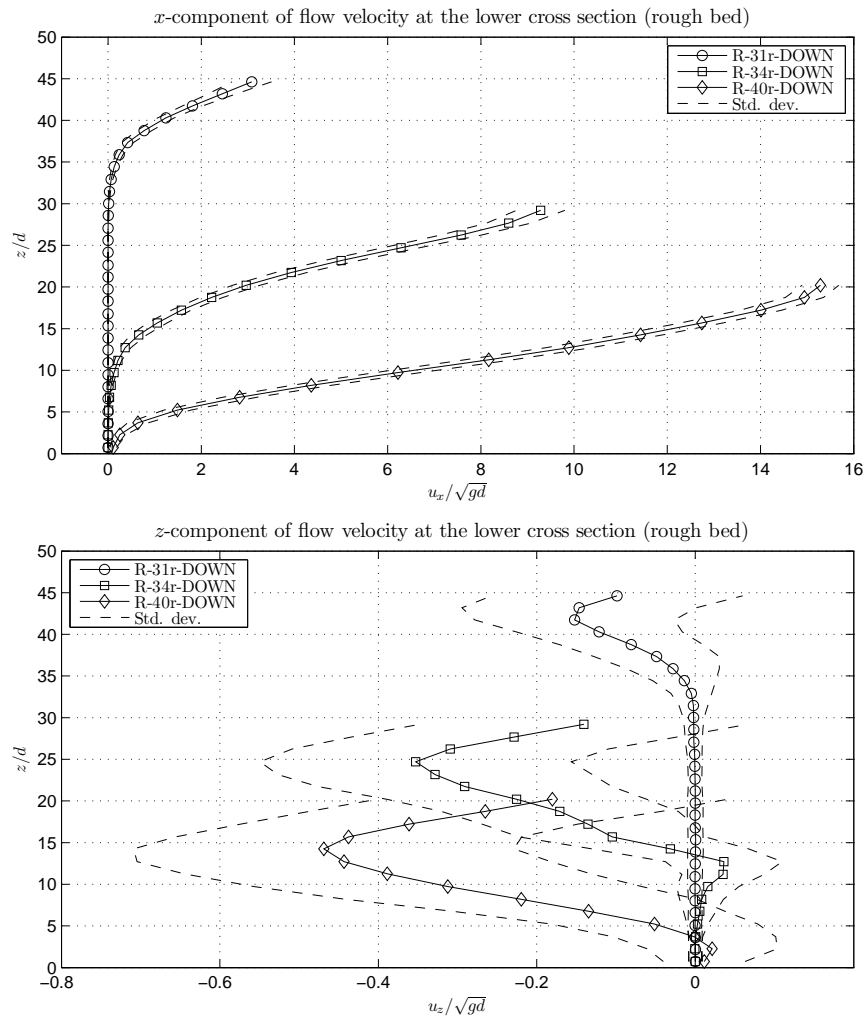


Figure 3.12: x and z components of the flow velocity at $x = 35$ cm from the release gate with related standard deviation (rough bed). Average over 1000 frame pairs, from repetition No.1.

Id.	$u_{x, \text{mean}} / \min u_x$	$\max u_x / \min u_x$
R-28s-FRONT-UP	1.64	1.91
R-28s-FRONT-DOWN	1.47	1.66
R-31s-FRONT-UP	1.23	1.29
R-31s-FRONT-DOWN	1.24	1.31
R-34s-FRONT-UP	1.13	1.15
R-34s-FRONT-DOWN	1.12	1.14
R-40s-FRONT-UP	1.07	1.09
R-40s-FRONT-DOWN	1.07	1.09

Table 3.6: Ratios between the mean value of u_x along the cross section and its minimum value (at the side wall). Smooth bed runs.

3.2.6 Free surface velocity

Beside the velocity profiles at the side wall, we obtained also the velocity distribution at the free surface at the Upper and Lower cross sections. In Figs. 3.13 and 3.14 the free surface velocities at $x = 20$ cm and $x = 35$ cm, related to smooth bed runs, are reported. As well, the free surface velocities related to rough bed runs are shown in Figs. 3.15 and 3.16.

As one can easily see, both x and z components of the flow velocity exhibit an almost symmetrical shape. While, the x component of the flow velocity have its maximum value at the centreline, the z component of flow velocity exhibits its maximum value not far from the side walls and has null values at the side walls and at the centreline.

In Table 3.6 are reported the ratios between the mean and the minimum values of u_x at the free surface, at different slopes and cross sections, related to smooth bed runs. In Table 3.7 are reported the ratios between the mean and the minimum values of u_x at the free surface, at different slopes and cross sections, related to rough bed runs. It is interesting to notice that the ratio between the mean velocity across the cross section and the value at the side walls, which also corresponds to the minimum value, slightly decreases as the inclination angle increases presumably together with the flow rate. This behaviour is rather different to what found e.g. in Jop et al. (2005). For instance, with reference to smooth bed experiments, there is an important difference between the smaller slopes (i.e. 28° and 31°), where the ratio is about 1.5-1.6, and the run at higher slope that exhibits values between 1.07-1.24. An analogous behaviour has been found in rough bed experiments (cf. Table 3.7).

The ratios between the mean and the minimum values of u_x at the free surface, will be used in Chapter 5 in order to estimate the velocity profile, depth-averaged across the transverse y direction. Such a treatment will be required for comparisons with numerical simulations, since the proposed model is one-dimensional.

Moreover, although the x component velocity is by far higher than the transverse y component, there is always a non-null y component due to the fact that the grains spread also laterally during the *fall* at the free surface. This phenomenon can be reasonably explained considering the random momentum exchanges after each collision between a given flowing grain with the underlying layer of grains. It is very interesting to note that while the mean value of the y component of free surface

Id.	$u_{x, \text{mean}} / \min u_x$	$\max u_x / \min u_x$
R-31r-FRONT-UP	1.70	1.93
R-31r-FRONT-DOWN	1.70	1.94
R-34r-FRONT-UP	1.14	1.18
R-34r-FRONT-DOWN	1.13	1.17
R-40r-FRONT-UP	1.10	1.13
R-40r-FRONT-DOWN	1.07	1.09

Table 3.7: Ratios between the mean value of u_x along the cross section and its minimum value (at the side wall). Rough bed runs.

velocity increases with the inclination angle (cf. runs R-28s-FRONT-UP and R-31s-FRONT-UP), its maximum value is reached in the run R-34s-FRONT-UP and R-34s-FRONT-DOWN and not at the highest inclination angle. In particular, the distribution of u_y in R-40s-FRONT-DOWN is much more blunt at the middle of the chute. This behaviour might be caused by the higher values of u_x at the highest chute inclination angle, that seems to reduce somehow such a secondary transverse spreading.

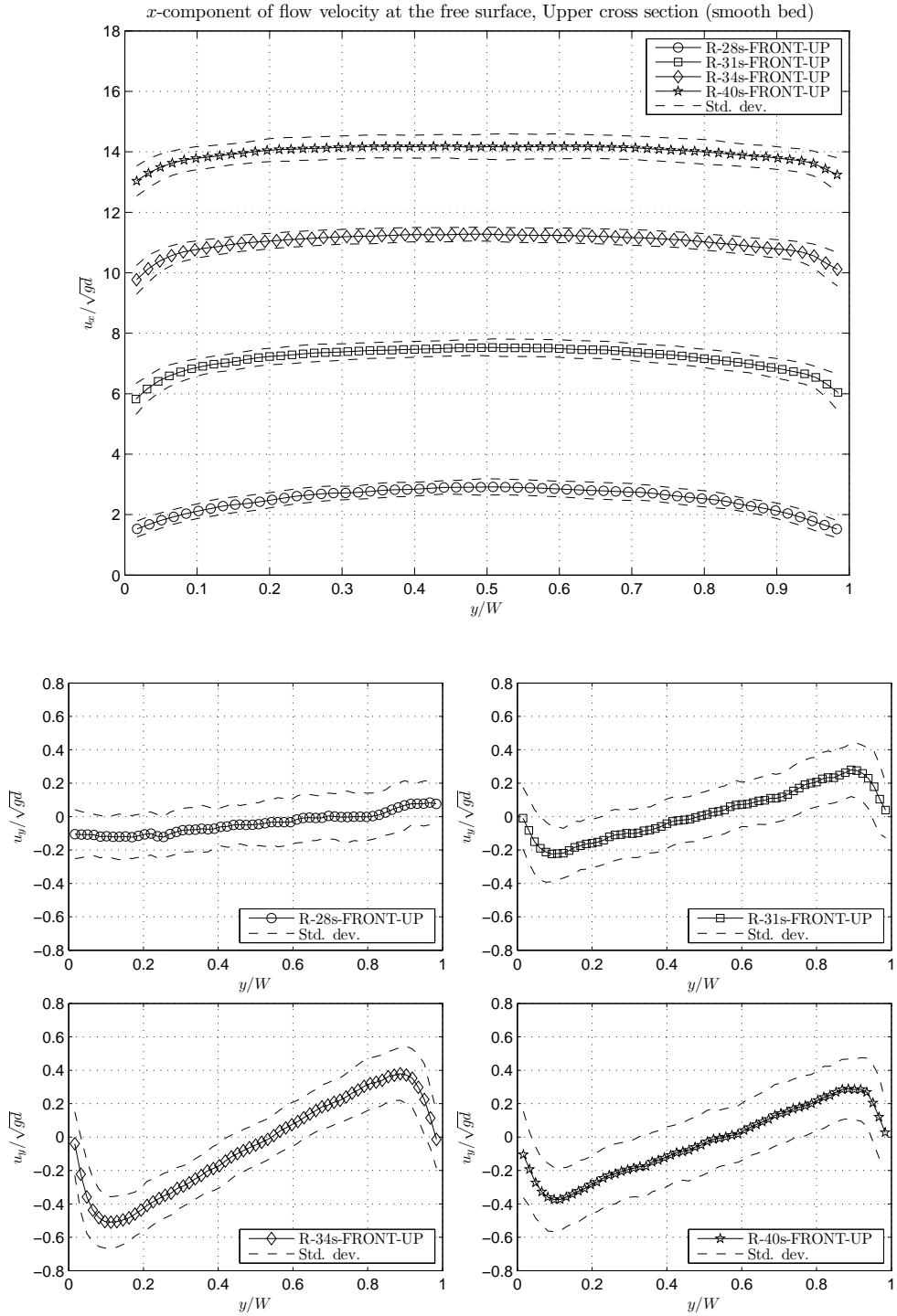


Figure 3.13: *x* and *z* components of flow velocity at free surface ($x = 20$ cm), smooth bed condition. Average over 1000 frame pairs, from repetition No.1.

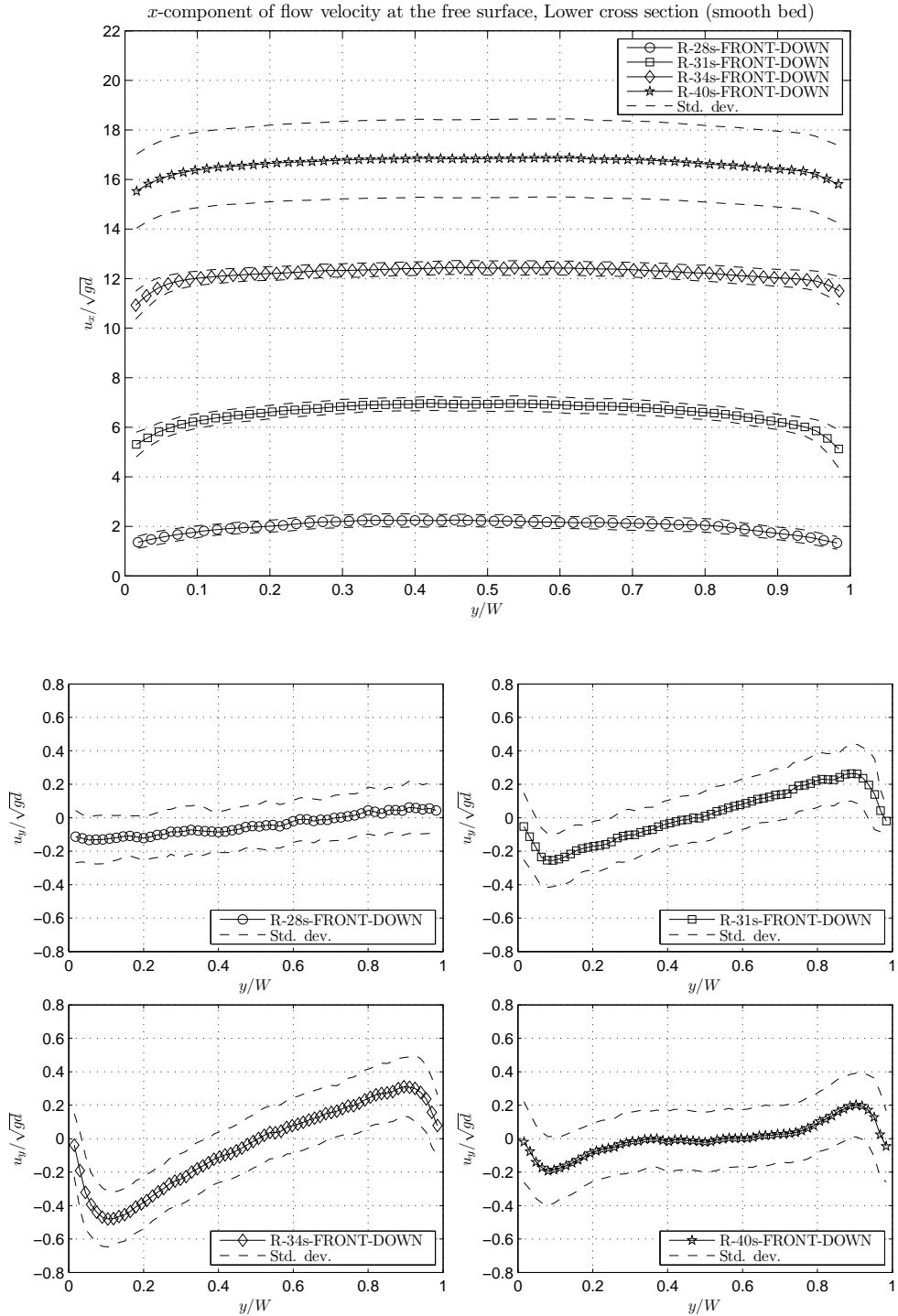


Figure 3.14: *x* and *z* components of flow velocity at free surface ($x = 35$ cm), smooth bed condition. Average over 1000 frame pairs, from repetition No.1.

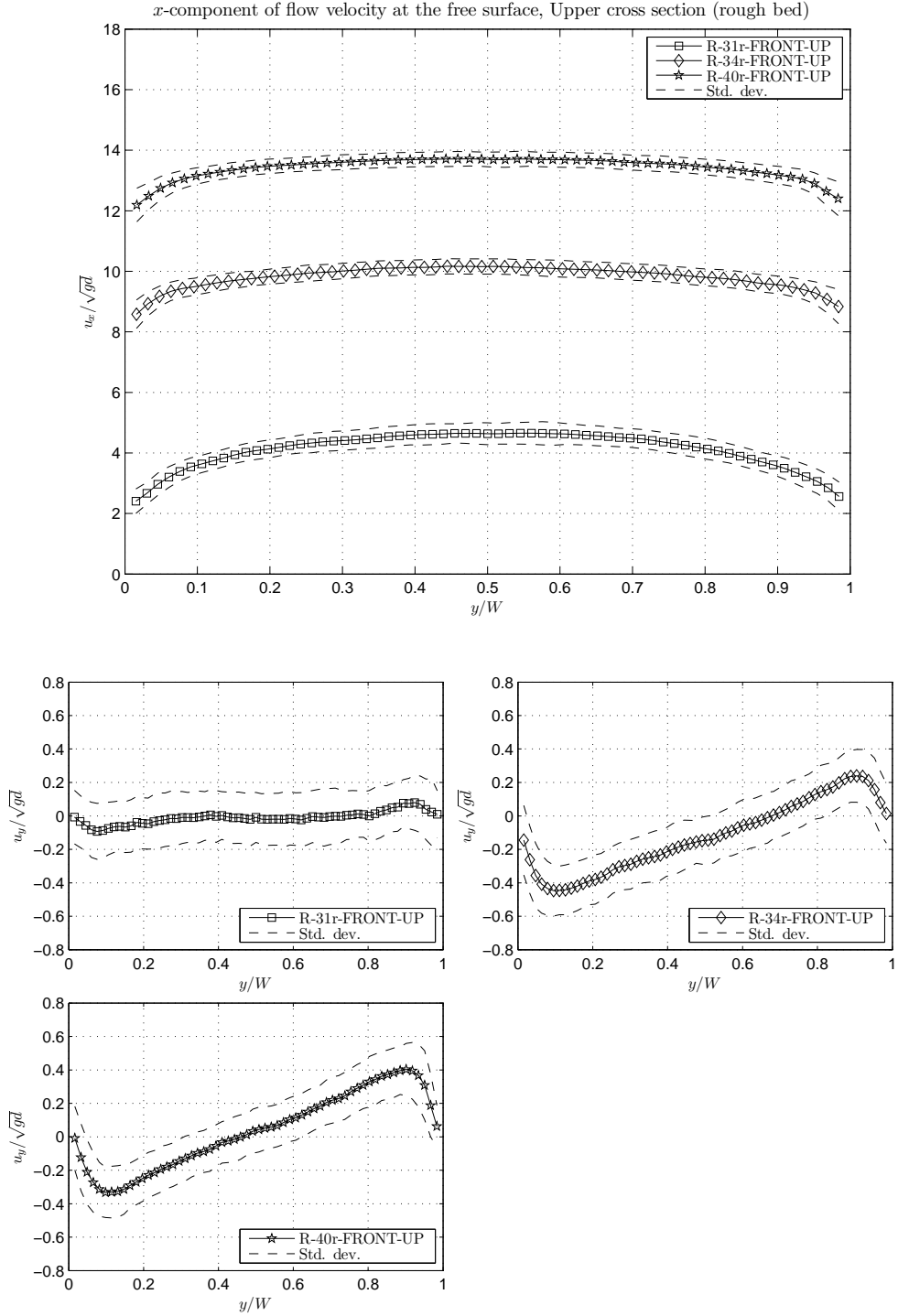


Figure 3.15: *x* and *z* components of flow velocity at free surface ($x = 20\text{ cm}$), rough bed condition. Average over 1000 frame pairs, from repetition No.1.

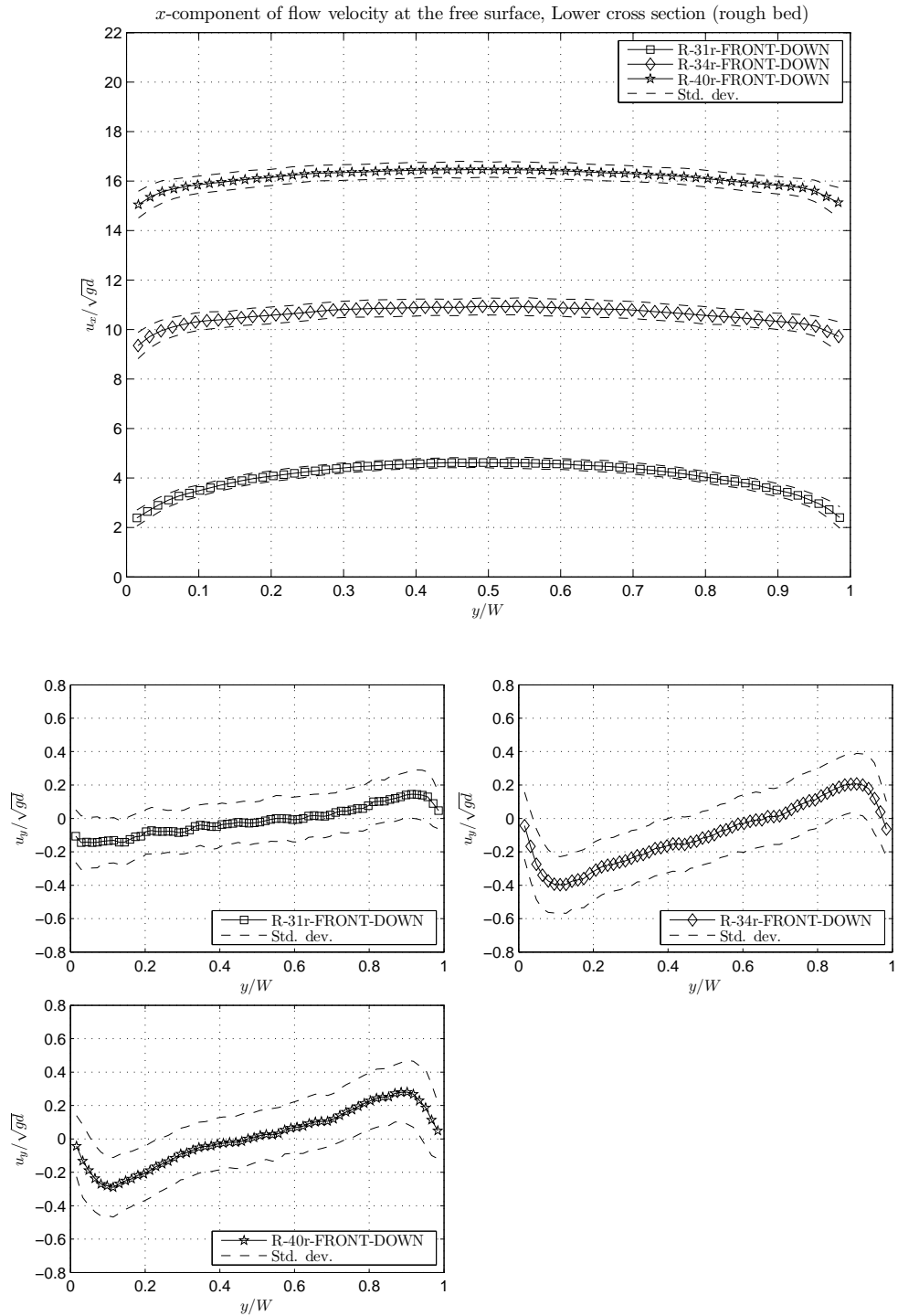


Figure 3.16: *x* and *z* components of flow velocity at free surface ($x = 35$ cm), rough bed condition. Average over 1000 frame pairs, from repetition No.1.

References Used in This Chapter

- Adrian, R. and Westerweel, J. (2010). *Particle image velocimetry*, volume 30. Cambridge University Press.
- Eckart, W. and Gray, J. M. N. T. (2003). Particle Image Velocimetry (PIV) for granular avalanches on inclined planes. In Hutter, K. and Kirchner, N., editors, *Lecture Notes in Applied & Computational Mechanics (Vol. 11)*, chapter Dynamic Response of Granular and Porous Materials under Large Catastrophic Deformations, pages 195–218. Springer.
- Forterre, Y. and Pouliquen, O. (2008). Flows of Dense Granular Media. *Annual Review of Fluid Mechanics* **40**, 1–24.
- Hungr, O. and Morgenstern, N. (1984a). Experiments on the flow behaviour of granular materials at high velocity in an open channel. *Geotechnique* **34**,
- Hungr, O. and Morgenstern, N. (1984b). High velocity ring shear tests on sand. *Geotechnique* **34**,
- Jop, P., Forterre, Y., and Pouliquen, O. (2005). Crucial role of sidewalls in granular surface flows: consequences for the rheology. *Journal of Fluid Mechanics* **541**, 167–192.
- Katzenbach, R., Bergmann, C., Bachmann, G., Gutberlet, C., and Hutter, K. (2011). *Particle Image Velocimetry Measuring Methods for Soil Movements in Geotechnics*. Number 20. Darmstadt, darmstadt edition.
- Keane, R. D. and Adrian, R. J. (1993). Theory of cross-correlation analysis of piv images. In *Flow visualization and image analysis*, pages 1–25. Springer.
- Komatsu, T., Inagaki, S., Nakagawa, N., and Nasuno, S. (2001). Creep Motion in a Granular Pile Exhibiting Steady Surface Flow. *Physical Review Letters* **86**, 1757–1760.
- Lambe, T. and Whitman, R. (1991). *Soil Mechanics*. Series in Soil Engineering. Wiley.
- Lueptow, R. M., Akonur, A., and Shinbrot, T. (2000). PIV for granular flows. *Experiments in Fluids* **28**, 183–186.
- Midi, G. (2004). On dense granular flows. *The European physical journal. E, Soft matter* **14**, 341–65.
- Pudasaini, S. P. and Hutter, K. (2007). *Avalanche dynamics: dynamics of rapid flows of dense granular avalanches*. Springer.
- Pudasaini, S. P., Hutter, K., Hsiau, S.-S., Tai, S.-C., Wang, Y., and Katzenbach, R. (2007). Rapid flow of dry granular materials down inclined chutes impinging on rigid walls. *Physics of fluids* **19**, 053302.
- Raffel, M., Willert, C., and Kompenhans, J. (1998). *Particle Image Velocimetry: A Practical Guide*. Experimental Fluid Mechanics. Springer.
- Savage, S. (1984). The mechanics of rapid granular flows. *Advances in applied mechanics* **24**, 289–366.

- Sheng, L.-T., Kuo, C.-Y., Tai, Y. C., and Hsiau, S.-S. (2011). Indirect measurements of stream-wise solid fraction variations of granular flows accelerating down a smooth rectangular chute. *Experiments in Fluids* **51**, 1329–1342.
- Tai, Y. C. and Lin, Y.-C. (2008). A focused view of the behavior of granular flows down a confined inclined chute into the horizontal run-out zone. *Physics of Fluids* **20**, 123302.

Chapter 4

Two-layer depth-averaged models

Chapter Summary

In Chapter 3 we have reported an experimental study on the velocity profiles in steady-state dry granular flows. By experimental results, it is clear that in case of *no-slip* bottom boundary condition there exists a stratification of flow regimes. This situation can be induced by a sufficiently rough basal surface, as observed in rough bed experiments, but also by the side wall friction, as observed in smooth bed experiments at low inclination angles. Moreover, in Chapter 2 we have shown some issues about using a Savage-Hutter type model for describing the avalanche spreading in case of rough bed conditions. The main uncertainties are found, particularly, in the choice of the earth pressure coefficient and the basal resistance.

We believe that the source of these problems relies on the rheological stratification occurring inside the flowing pile. For a proper description of such a stratification, we propose a two-layer depth-averaged approach that would be able to capture the main features of quasi-static and dense-collisional regimes. In this way, while preserving the simplicity and the small computational load of depth-averaged models, the capability of the mathematical model to describe the actual flow dynamics is increased.

Firstly, a short review of two-layer depth-averaged models is given. Particular attention has been paid to describe the main mathematical issues of a two-layer approach, like the loss of hyperbolicity.

Then, a two-layer depth-averaged model for describing dry granular flows is proposed. The important choice of the resistance formulae both at the basal surface and at the interface between the two layers is dealt with carefully. In order to prevent the loss of hyperbolicity, a local modification of the source terms is proposed. The numerical scheme, for the numerical integration of the proposed model, is, then, presented. Some tests are shown at the end of this Chapter with the aim to highlight the main features of the proposed approach. Conversely, a careful comparison between the two-layer mathematical model and experimental data will be reported in Chapter 5.

4.1 Two-layer depth-averaged models

The two-layer depth-averaged mathematical models have been formulated in a hydrodynamic context, in order to describe superimposed flows of two immiscible fluids with different densities (see e.g. Long, 1956; Lawrence, 1990). In stable conditions (hereafter it will clear in which sense), such kind of flows exhibits a sharp stratification of the two fluids, in which the denser fluid is below the lighter one, for the equilibrium stability.

The one-dimensional two-layer model, written in Cartesian coordinates (x, z) and without friction at the bottom and at the interface between layers, can be regarded as the simplest form of two-layer depth-averaged models. It consists of the following partial differential equations (PDE) system (e.g. Castro et al., 2002; Kim and LeVeque, 2008)

$$\begin{cases} \frac{\partial h_1}{\partial t} + \frac{\partial h_1 u_1}{\partial x} = 0 \\ \frac{\partial h_1 u_1}{\partial t} + \frac{\partial}{\partial x} \left(\frac{1}{2} g h_1^2 + \beta_1 h_1 u_1^2 \right) = -g h_1 \frac{\partial h_2}{\partial x} - g h_1 \frac{\partial b}{\partial x} \\ \frac{\partial h_2}{\partial t} + \frac{\partial h_2 u_2}{\partial x} = 0 \\ \frac{\partial h_2 u_2}{\partial t} + \frac{\partial}{\partial x} \left(\frac{\rho_1}{\rho_2} g h_1 h_2 + \frac{1}{2} g h_2^2 + \beta_2 h_2 u_2^2 \right) = \frac{\rho_1}{\rho_2} g h_1 \frac{\partial h_2}{\partial x} - g h_2 \frac{\partial b}{\partial x} \end{cases} \quad (4.1)$$

where, while the subscript 1 refers to the upper layer, the subscript 2 refers to the lower layer; t is time and x is the reference axis parallel to principal direction of motion, while the coordinate axis z is chosen parallel to the gravity field; h_1 , u_1 and h_2 , u_2 are the flow depths and the flow velocities of the upper layer and lower layer, respectively; g is the gravity acceleration; $b(x)$ is the bottom topography. Moreover, ρ_1 and ρ_2 represent the densities of each layer. Owing to the equilibrium stability, it is required that $\rho_1 \leq \rho_2$. The derivation of the PDE system (4.1) can be obtained similarly to the Shallow Water equations, after depth-integrating mass and momentum equations in both layers together with some simplifying assumptions (i.e. *Long wave approximation*). The symbols β_1 and β_2 stand for the *Boussinesq* coefficients. While the first and second equations in System (4.1) represent the mass and momentum balance equations of the upper layer, the third and fourth ones are the mass and momentum equation of the lower layer. For the sake of simplicity, in the following, $\beta_1 = \beta_2 = 1$ and a flat bottom topography (i.e. $b(x) = 0$) are assumed. A simple scheme of the flow geometry is reported in Fig. 4.1.

Although it is out of the scope of this dissertation, it seems useful to observe that a generalization of System (4.1) to more than two layers is not difficult to be derived and can be found for example in Audusse (2005).

Eigenvalue structure of the two-layer model

Firstly, differently from the single layer Shallow Water equations, in the right-hand side of system (4.1) there are two non-conservative terms, depending on the spatial derivatives of the lower layer flow depth, h_2 , by which the two momentum balance equations are coupled. These terms are intrinsically non-conservative, as they cannot be put inside the flux term in the left-hand side. From a physical viewpoint, these terms account for the momentum exchanges at the interface between the two layers, due to the interface slope. A first mathematical issue, arising from the

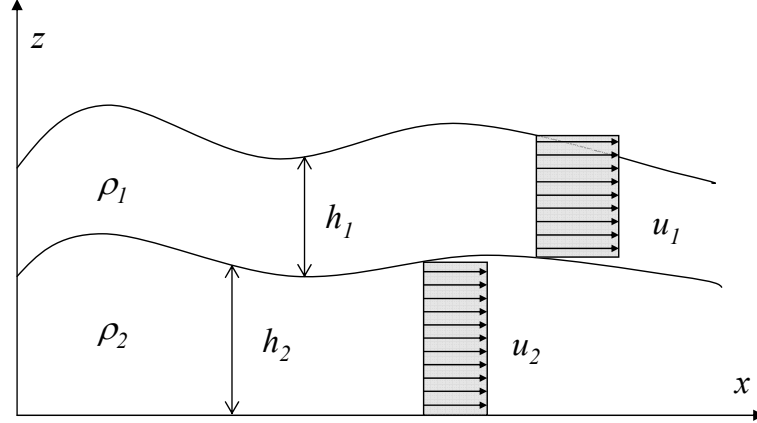


Figure 4.1: Geometry of one-dimensional two-layer flow (hypothesis of constant velocity profiles, i.e. $\beta_1 = \beta_2 = 1$).

presence of such non-conservative terms, is that the two-layer depth-averaged model (4.3) cannot be written in conservative form. This creates some difficulties in finding proper weak solutions, in presence of shock waves (e.g. Abgrall and Karni, 2009).

It is worth highlighting that the conservative pressure term in the lower layer momentum equation is actually composed of two terms. The reason of this expression is obvious. Provided that a pressure hydrostatic distribution is assumed in both layers (which directly comes from the *Long Wave approximation*, the pressure distribution in the lower layer is the sum of the pressure at the interface $\rho_1 g h_1$, plus a linear term, accounting for the distribution along the lower layer depth, $\rho_2 g (h_2 - z)$.

By using the product rule of partial differentiation, it is possible to recast the former term, as follows

$$\partial_x \left(\frac{\rho_1}{\rho_2} g h_1 h_2 \right) = \frac{\rho_1}{\rho_2} g h_1 \partial_x h_2 + \frac{\rho_1}{\rho_2} g h_2 \partial_x h_1. \quad (4.2)$$

Then, after cancelling out the term $\rho_1/\rho_2 g h_1 \partial_x h_2$, that appears both in the left hand side and right hand side of the lower layer momentum equation, the PDE system (4.1) is recast as follows

$$\begin{cases} \frac{\partial h_1}{\partial t} + \frac{\partial h_1 u_1}{\partial x} = 0 \\ \frac{\partial h_1 u_1}{\partial t} + \frac{\partial}{\partial x} \left(\frac{1}{2} g h_1^2 + \beta_1 h_1 u_1^2 \right) = -g h_1 \frac{\partial h_2}{\partial x} \\ \frac{\partial h_2}{\partial t} + \frac{\partial h_2 u_2}{\partial x} = 0 \\ \frac{\partial h_2 u_2}{\partial t} + \frac{\partial}{\partial x} \left(\frac{1}{2} g h_2^2 + \beta_2 h_2 u_2^2 \right) = -\frac{\rho_1}{\rho_2} g h_2 \frac{\partial h_1}{\partial x}. \end{cases} \quad (4.3)$$

Note that source terms, due to topography, vanish owing to the assumption that $b(x) = 0$.

In order to analyse the eigenvalue structure of a conservative PDE system, it is common to

rewrite the PDE system in quasi-linear form

$$\partial_t \mathbf{q} + \partial_{\mathbf{q}} \mathbf{f} \partial_x \mathbf{q} = \mathbf{s}(\mathbf{q}) \quad (4.4)$$

where $\partial_{\mathbf{q}} \mathbf{f}$ is the Jacobian matrix of the flux vector \mathbf{f} .

Although the two-layer system (4.3) is not in conservative form, it is equally possible to rewrite it in the following quasi-linear form

$$\partial_t \mathbf{q} + A \partial_x \mathbf{q} = \mathbf{s}(\mathbf{q})$$

with the slight difference that, in this case, the matrix A does not correspond to the Jacobian matrix of the flux vector because it comprises also non conservative terms on the right hand side of momentum equations. More properly, it will be called *pseudo-Jacobian matrix* hereafter.

Because the vector of unknowns is

$$\mathbf{q} = (h_1, h_1 u_1, h_2, h_2 u_2)^T = (q_1, q_2, q_3, q_4)^T, \quad (4.5)$$

the flux can be written as function of \mathbf{q} , as follows

$$\mathbf{f}(\mathbf{q}) = \left(q_2, \frac{1}{2} g q_1^2 + q_2^2 / q_1, q_4, \frac{1}{2} g q_3^2 + q_4^2 / q_3 \right)^T. \quad (4.6)$$

Therefore the pseudo-Jacobian matrix A can be written as sum of the Jacobian matrix $\partial_{\mathbf{q}} \mathbf{f}$ of the flux vector and the matrix $A_{non-cons}$ that collects non-conservative terms

$$\begin{aligned} A &= \partial_{\mathbf{q}} \mathbf{f} + A_{non-cons} = \\ &= \begin{pmatrix} 0 & 1 & 0 & 0 \\ g q_1 - q_2^2 / q_1^2 & 2 q_2 / q_1 & 0 & 0 \\ 0 & 0 & 0 & 1 \\ 0 & 0 & g q_1 - q_4^2 / q_3^2 & 2 q_4 / q_3 \end{pmatrix} + \begin{pmatrix} 0 & 0 & 0 & 0 \\ 0 & 0 & g q_1 & 0 \\ 0 & 0 & 0 & 0 \\ \rho_1 / \rho_2 g q_3 & 0 & 0 & 0 \end{pmatrix}. \end{aligned} \quad (4.7)$$

The calculation of the eigenvalues of the pseudo-Jacobian matrix A , consists in finding the algebraic roots of the characteristic polynomial

$$\det(A - \lambda I) = 0,$$

i.e. solving the following 4th order algebraic equation

$$\left((\lambda - u_1)^2 - g h_1 \right) \left((\lambda - u_2)^2 - g u_2 \right) = \frac{\rho_1}{\rho_2} g^2 h_1 h_2. \quad (4.8)$$

Generally speaking, a first order PDE system is *hyperbolic* when its pseudo-Jacobian matrix A is diagonalizable with real eigenvalues for every solution \mathbf{q} (e.g. LeVeque, 2002). Usually, mathematical models that describe the propagation of some physical quantities, i.e. *wave-like* phenomena, are hyperbolic. From a more physical viewpoint, the hyperbolicity of a mathematical model implies, as a direct consequence, that information propagates with a finite speed. Therefore, it takes a finite amount of time for a given perturbation of the solution to propagate from a position, \mathbf{x}_1 , to another position, \mathbf{x}_2 , of the spatial domain. Checking the hyperbolic character of a mathematical model is also very important in order to give well-posed boundary conditions, as it will be clearer further.

By way of example, the De Saint Venant equations, which are the one-dimensional form of the one-layer shallow water equations, have the well-know expressions for the eigenvalues: $\lambda_{1,2} = u \pm \sqrt{gh}$. Such eigenvalues represent the celerities of small free surface perturbations.

Conversely, in the case of two-layer shallow water model (4.3), it is not possible to have a straightforward access to the system eigenstructure (e.g. Abgrall and Karni, 2009). Most commonly, some approximate formulae are used to numerically calculate eigenvalues. Under the assumption of $\rho_1 \approx \rho_2$ and to $O(u_1 - u_2)$, Castro et al. (2002) reports the following formulae

$$\lambda_{out} = \frac{h_1 u_1 + h_2 u_2}{h_1 + h_2} \pm \sqrt{g(h_1 + h_2)}, \quad (4.9)$$

$$\lambda_{in} = \frac{h_1 u_2 + h_2 u_1}{h_1 + h_2} \pm \sqrt{g' \frac{h_1 h_2}{h_1 + h_2} \left[1 - \frac{(u_2 - u_1)^2}{g'(h_1 + h_2)} \right]}. \quad (4.10)$$

where $g' = g(1 - \rho_1/\rho_2)$ is a reduced gravity. The minimum and maximum eigenvalues, which are obtained through Eqs. (4.9), are sometimes called *barotropic* celerities (Audusse and Bristeau, 2007) or, simply *outer* eigenvalues, and refer to the celerities of small level perturbations at the free surface. It is interesting noting that with the current assumptions, these eigenvalues match with those of a single-layer current with a flow velocity equal to the depth-averaged velocity and a flow depth equal to the sum of the layer flow depths. On the other hand, eigenvalues calculated by means of Eqs. (4.10), usually called *baroclinic* celerities (Audusse and Bristeau, 2007) or simply *inner* eigenvalues, are the celerities of small level perturbations at the interface between the two layers.

Hyperbolicity Loss

It can be easily noticed that the *inner* eigenvalues are real numbers, as long as

$$\frac{(u_2 - u_1)^2}{g'(h_1 + h_2)} \leq 1. \quad (4.11)$$

When Cond. (4.11) is not fulfilled the approximate eigenvalues become conjugate complex numbers. It should be kept in mind that Cond. (4.11) is only a crude approximate condition for system hyperbolicity, since it is obtained from an approximated form for calculating the eigenvalues. Nonetheless, Eq. (4.11) is useful to better understand which role the different physical quantities play with respect to this kind of instability. In fact, from Eq. (4.11) one can immediately notice that the difference of flow velocities between the two layers has a very strong destabilizing effect, while the total flow depth $h_1 + h_2$ as well as the density ratio ρ_2/ρ_1 have a stabilizing effect. In particular, it can be easily shown that in the case of no density difference between layers, i.e. $\rho_1 = \rho_2$, the system is non-hyperbolic as soon as a non-null shear velocity between layers occurs.

From what has been said, the system (4.3) is only *conditionally* hyperbolic. More precisely, it becomes not hyperbolic for all values of solution \mathbf{q} that cause the inner eigenvalues to be complex conjugate numbers.

The hyperbolicity loss of the mathematical model sometimes corresponds to a particular physical phenomenon that is a dynamical instability of the interface between the fluids, called *Kelvin-Helmoltz* instability after L. Kelvin and H. von Helmholtz (e.g. Kim and LeVeque, 2008). It consists

of the occurrence of large eddies at the interface and causes a strong mixing and momentum exchange between the two layers. This kind of instability is often visible in planet atmospheres and is due to the velocity shear between the superimposed fluids at different densities. In Fig. 4.2 it is reported an example of Kelvin-Helmoltz instability, observed by Brown and Roshko (1974), consisting of a plane turbulent mixing between two streams of different gases. In other situations, the hyperbolicity loss is due only to the mathematical assumptions used for the derivation of the two-layer model, e.g. constant velocity distribution and hydrostatic pressure distribution inside the layers. Therefore, in these cases a better description of the physics would avoid this kind of instability.

Nonetheless, once the inner eigenvalues become conjugate complex numbers, the mathematical model ceases to be hyperbolic and becomes *elliptic*. Hence, the model breaks down as it is not useful for describing *wave-like* phenomena any more. From a mathematical viewpoint, an elliptic PDE system requires that boundary conditions be assigned along the all spatial-domain boundaries. In particular, in order to “predict” the flow evolution in a time interval T , the final solution should be known and set as boundary condition (e.g. Gray, 1999). Hence, the model is useless because of the lack of causality.

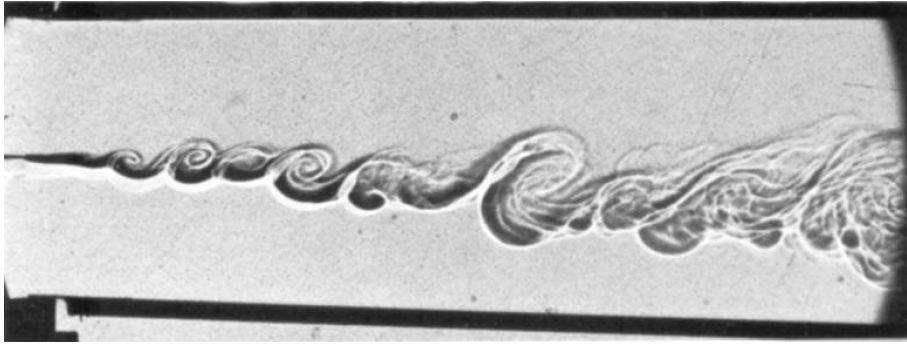


Figure 4.2: An example of Kelvin-Helmoltz instability (plane turbulent mixing between two streams of different gases). From Brown and Roshko (1974).

After choosing a particular value of the density ratio ρ_1/ρ_2 , it is possible to numerically calculate the hyperbolic and non-hyperbolic domains in the space of solutions. In Fig. 4.3 an example of such a computation, presented in Castro-Díaz et al. (2011), is shown. As one can easily see from Fig. 4.3, the higher is the density ratio, the wider is the non-hyperbolic domain. Moreover, it is worth noting that an hyperbolic region also exists where the flow shear velocity is very high (e.g. Greco et al., 2008; Castro-Díaz et al., 2011). Nevertheless, this situation is unlikely to be observed in real flows, because the system has to go across the non-hyperbolic domain and it causes a non-reversible mixing due the Kelvin-Helmoltz instability.

Stabilizing effect of resistances

The system (4.3) has been derived under the simplifying hypotheses of no resistances at the interface and at the bottom surface. Hence, it has to be regarded as an ideal case. In practical applications, we deal with real fluids and thus, non-null resistances at the bottom and at interface

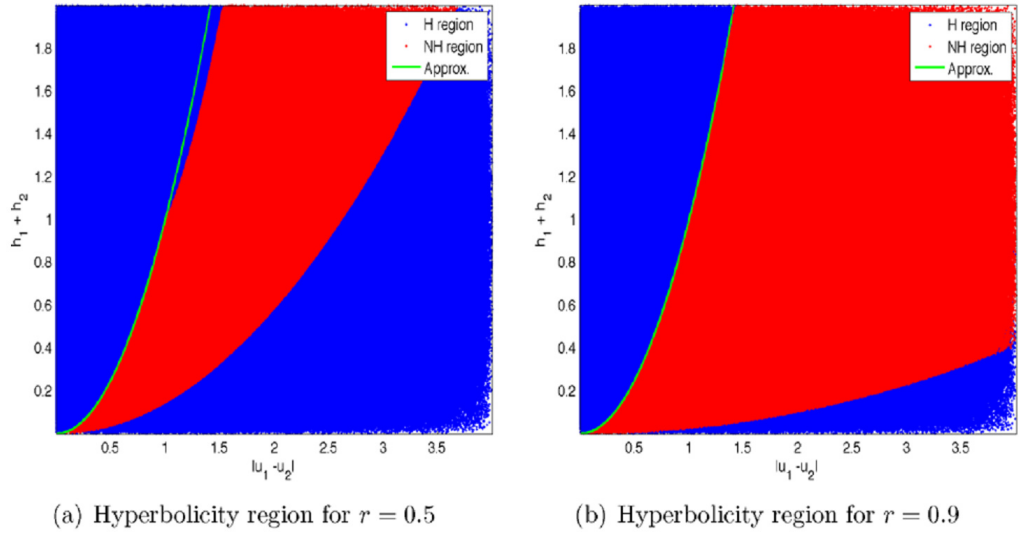


Figure 4.3: Hyperbolic (blue) and non-hyperbolic (red) domains at different density ratios ρ_1/ρ_2 . From Castro-Díaz et al. (2011).

are expected and depend on the particular fluid rheology. After choosing an appropriate rheology, at the interface typically there would be a non-null momentum flux, that goes from the faster layer towards the lower one and, hence, reduces somehow the shear velocity between the two layers, with respect to ideal case, i.e. System (4.3), (e.g. Kim and LeVeque, 2008).

Recent applications of two-layer and multi-layer depth-averaged models

Despite the important issue, related to the loss of hyperbolicity, the two-layer shallow water models and, in general, multi-layer models have attracted much interest in the field of fluid dynamics and hydraulic engineering. The possible applications go far beyond the simplest case of two immiscible fluids and turn out to be very attractive because of the relatively low computational load. Here, we like to cite only some of the most recent papers that made use of a multi-layer approach. By way of example, Capart and Young (2002) proposed a two-layer model for describing erosion and bed-load in the context of geomorphic flows; successively, Chen and Peng (2006) and Chen et al. (2007) used a similar two-layer model in order to study confluence problems and describe the intrusion of a mud flow into quiescent water. Fernández-Nieto et al. (2008) proposed a two-layer Savage-Hutter type model for studying submarine avalanches and the subsequent tsunamis; Luca et al. (2010) formulated a three-dimensional two-layer model in topography-adjusted coordinate system for geophysical mass flows, such as debris flows, hydraulic sediment transport and turbidity currents. Audusse (2005) and Audusse and Bristeau (2007) proposed a multi-layer approach in order to reproduce the dynamics of clear water free surface flows, as a cheaper computational alternative to the fully three-dimensional Navier-Stokes equations. Doyle et al. (2010) used a two-layer approach to modelling the transformation of dilute-collisional pyroclastic into dense pyroclastic flows. Castro et al. (2004) used a two-layer approach to model the stratified current, occurring at the Gibraltar Strait, owing to the superimposition of the less salty Mediterranean water on the

Atlantic Ocean water.

As a direct consequence of such a great interest on two-layer depth-averaged models, recently many studies have also dealt with the numerical problems, related to this kind of models. In particular, as regards the annoying issue of hyperbolicity loss, many attempts have been proposed. A relatively recent and brief summary of the possible stabilizations is reported by Noelle (2010). The proposed treatments to stabilize the hyperbolicity loss could be roughly divided into two types:

- treatments that operate at the mathematical “level”, by slightly changing the mathematical model, so as to it becomes strictly hyperbolic;
- treatments that operate at the numerical “level”, by preventing the occurrence of numerical instabilities, through specifically designed numerical treatments.

Yet, such a classification often turns out to be only apparent, since, sometimes, numerical schemes, specifically designed to stabilize the hyperbolicity issues, are convergent to the solution of another mathematical model which is strictly hyperbolic. This is the case of the modified multi-layer model, proposed by Audusse (2005), in which non-conservative terms are treated as source terms and integrated implicitly. An interesting approach to stabilize the hyperbolicity issue has been proposed recently by Castro et al. (2010) and consists of adding a third intermediate layer near the interface, that somehow describes the mixing layer that naturally occurs in presence of Kelvin-Helmoltz instability. In this approach, the two-layer model shifts into a three-layer model, that typically exhibits a wider extent of hyperbolic domain in the space of solutions. Differently, aimed at investigating in a simple way the eigenvalue structure of two-layer models, Abgrall and Karni (2009) proposed a relaxation approach that also avoids the hyperbolicity loss. Finally, another kind of treatments consists of adding friction at the interface of the two layers, as proposed e.g. in Castro-Díaz et al. (2011). This kind of approach will be discussed in detail hereafter, because it has some common points with that one, proposed in the present dissertation.

4.2 A two-layer approach to describe dry granular flows

In the previous section, we have seen that a two-layer approach can be employed in many contexts of applied fluid dynamics and hydraulic engineering. In the present dissertation, we propose a similar approach to better describe the rheological stratification, found in channelised dry granular flows in case of a no-slip bottom boundary condition.

In Chapter 2, the results of an experimental investigation, performed on Ottawa sand, showed that, in case of no-slip bottom boundary condition, the velocity profile is composed of two zones with quite different behaviours: an upper one, characterized by a linear velocity distribution, and a lower one, where the flow velocity follows a negative exponential behaviour and goes towards zero with zero gradient. Similar velocity profiles have also been found with different granular materials in different studies (e.g. Midi, 2004).

In our approach, differently from the most classical applications, there is no difference in material between the two layers: in fact, they are both composed of the same granular matter. The only difference is due to the volume fraction and, hence, the bulk density. However, such a density stratification is supposed to induce important differences in the flow dynamics, as the experimental velocity profiles suggest.

4.2.1 Two-layer model derivation

In this section, we derive the depth-averaged equations of a one-dimensional two-layer model for describing dry granular flows. At the first, we obtain the depth-averaged equations without simplifications, then, we simplify them by imposing the *long wave like approximation*. Note that the derivation of this model can be performed in different ways, nonetheless, the structure of the final system is similar to the two-layer shallow water model, presented in the previous Section.

In this case, a frame of reference be Cartesian is chosen such that the x -axis be parallel and oriented according to the mean bed slope. This is advantageous for the derivation of the model equations. Besides, let z -axis be upward oriented, so as to the coordinate system has a right-handed orientation.

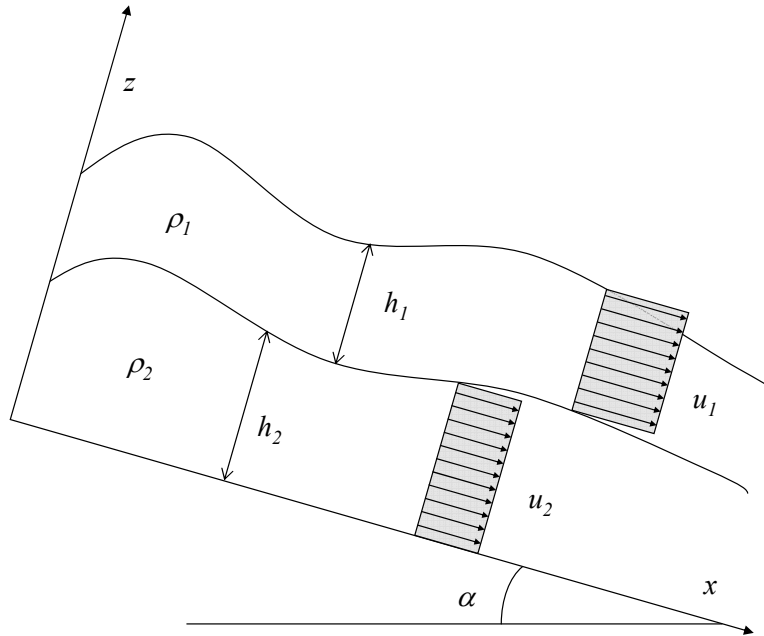


Figure 4.4: Flow geometry and frame of reference (x is parallel to the basal channel slope).

In a fluid dynamics context, mass and momentum balance equations can be written as follows in Cartesian coordinates

$$\begin{cases} \frac{\partial \rho}{\partial t} + \nabla_{\mathbf{x}} \cdot (\rho \mathbf{v}) = 0 & (4.12) \\ \frac{\partial \rho \mathbf{v}}{\partial t} + \nabla_{\mathbf{x}} \cdot (\rho \mathbf{v} \otimes \mathbf{v} - T) = \rho \mathbf{g} & (4.13) \end{cases}$$

where ρ is the fluid density, \mathbf{v} the flow velocity, T the stress tensor with tension positive convention and \mathbf{g} the gravity vector. For conciseness, we used the tensor relation $\nabla_{\mathbf{x}} \cdot (\mathbf{u} \otimes \mathbf{u}) = \mathbf{u} (\nabla_{\mathbf{x}} \cdot \mathbf{u}) + (\nabla_{\mathbf{x}} \mathbf{u}) \mathbf{u}$ (e.g. Gray et al., 1999).

In the present model, we assume that the whole granular flow is composed of two layers with different densities, one on top of the other, and they are separated by an interface Γ . Such an

interface, that represents a geometric separation between two flows with different constitutive laws, is supposed to be a non-material surface. Some similar assumptions can be found, for instance, in Fraccarollo and Capart (2002), Brivois et al. (2007) or Lê and Pitman (2010).

The model equations can be derived by depth-integrating the mass and momentum equations (4.12) and (4.13) along the flow depths of the two layers, together with suitable boundary conditions. After obtaining the exact depth-integrated equations, some further simplifications can be done, e.g. by using the well-known *Long Wave Approximation* or by means of an asymptotic analysis (e.g. Savage and Hutter, 1989).

In Fig. 4.4 a sketch of the frame of reference together with a scheme of the two layer flow is reported.

In the present two-layer model, we suppose that velocity and stress fields are continuous functions inside each layer but exhibit a jump across the interface. We refer to these functions using the subscripts 1 or 2 depending on whether they are calculated in the upper layer domain or in the lower one. Moreover, it is supposed that the bulk densities, ρ_1 and ρ_2 , are constant inside each layer.

Jump conditions at the interface

Let us assume that the interface, Γ between the two layers can be described by means of the following equation

$$F_i = z - i(x, t) = z - h_2(x, t) = 0. \quad (4.14)$$

where the distance i of the interface from the reference axis x . Because it is also assumed the basal topography is fixed and corresponds to the reference x axis, it turns out that i simply corresponds to the flow depth of the lower layer, h_1 . Please, note that the unit normal, $\mathbf{n}_i = \nabla F_i / \|\nabla F_i\|$ points upwards.

It is assumed that there is a jump at interface for any intensive quantity, defined in the flow domain. Namely, for any given function f , defined in the flow domain, it is assumed that

$$\lim_{z \rightarrow i^+} f_1(x, z, t) \neq \lim_{z \rightarrow i^-} f_2(x, z, t) \quad (4.15)$$

where i is the interface distance from the x axis.

We assume that a mass flux M_{flux} between the two layers may take place across the interface Γ . Such phenomenon gives rise to volume exchanges into the two layers, E_1 and E_2 . We prefer to name these quantities *volume exchanges* instead of *volume fluxes*, because actually $E_1 \neq E_2$, since $\rho_1 < \rho_2$. Nonetheless, the mass conservation between layers does hold

$$E_1 \rho_1 = E_2 \rho_2 = M_{flux}. \quad (4.16)$$

In order to obtain some useful conditions on the mass and momentum exchange across the interface Γ , the Rankine-Hugoniot jump conditions (Rankine, 1870), expressing local conservation of mass and momentum across a discontinuity, can be written with reference to the interface Γ as

$$[\rho(i) (\mathbf{v}(i) - \mathbf{v}_{int}) \cdot \mathbf{n}_i]_1^2 = 0 \quad (4.17)$$

$$[(\rho(i) \mathbf{v}(i) \otimes (\mathbf{v}(i) - \mathbf{v}_{int}) - T(i)) \mathbf{n}_i]_1^2 = \mathbf{0} \quad (4.18)$$

where $f_{1,2}(i) = \lim_{z \rightarrow i^+, i^-} f_{1,2}(x, z, t)$, \mathbf{v}_{int} is the interface velocity (i.e. the velocity of a pseudo-particle attached to the interface) and $\mathbf{n}_i = \nabla F_i / \|\nabla F_i\|$ is the unit normal to the interface Γ .

By using Eq. (4.17), the volume exchange of the upper layer, E_1 , can be written as follows,

$$E_1 = \frac{M_{flux}}{\rho_1} = [\mathbf{v}_1(i) - \mathbf{v}_{int}] \cdot \mathbf{n}_i, \quad (4.19)$$

where $\mathbf{v}_1(i)$ indicates the flow velocity at the interface, as limit from above. We followed the sign convention according to which, $E_1 > 0$, if the upper layer volume increase at the expense of the volume of the lower layer. As well, the volume exchange of the lower layer, E_2 can be written as follows,

$$E_2 = \frac{M_{flux}}{\rho_2} = [\mathbf{v}_2(i) - \mathbf{v}_{int}] \cdot \mathbf{n}_i, \quad (4.20)$$

where $\mathbf{v}_2(i)$ indicates the flow velocity at the interface, as limit from below. $E_2 > 0$ when the lower layer volume decreases, according to the aforementioned convention. Eqs. (4.19) and (4.20) can be recast in the following expression

$$\boxed{[\mathbf{v}(i) \cdot \mathbf{n}_i]_1^2 = [E]_1^2 = \frac{[\rho(i)]_1^2}{\rho_1(i) \rho_2(i)} M_{flux}.} \quad (4.21)$$

This equation relates velocity and density jumps at the interface.

Moreover, by slightly manipulating the momentum jump condition (4.18), we get

$$\boxed{[\rho \mathbf{v} \cdot (\mathbf{v} - \mathbf{v}_{int}) \mathbf{n}_i - T \mathbf{n}_i]_1^2 = \mathbf{0} \quad \Rightarrow \quad [\mathbf{v}]_1^2 M_{flux} = [T \mathbf{n}_i]_1^2} \quad (4.22)$$

which is a general relation between the jump of the stress tensor and the velocity jump across the interface. Such a condition turns out to be very useful in the derivation of the present two-layer model. In fact, the closure equation to calculate the mass flux across the interface, will be defined by means of the x component of Eq. (4.22), as it will be shown in detail in the following.

Depth-averaged mass equations

By integrating Eq. (4.12) along the upper layer flow depth, through using the Leibnitz rule (A.3), the mass balance equation in the upper layer can be written as follows

$$\frac{\partial}{\partial t} \int_i^{h_T} \rho_1 dz + \left[\rho_1 \frac{dz}{dt} \right]_{h_T}^i + \frac{\partial}{\partial x} \int_i^{h_T} \rho_1 v_{1,x} dz + \left[\rho_1 v_{1,x} \frac{dz}{dt} \right]_{h_T}^i + [\rho_1 v_{1,z}]_i^{h_T} = 0 \quad (4.23)$$

where $h_T = h_1 + h_2$, i is the distance of the interface form the reference x axis, h_1 and h_2 are the flow depths measured along the z direction of the upper and lower layer, respectively. In the present model we assume that the basal topography is constant, thus, $i = h_2$.

It is useful to write the *Kinematic boundary conditions* (also referred to as *KBC* hereafter) at free surface and at interface. Let us assume that the free surface can be described by means of the following equation

$$F_s = z - h_T(x, t) = 0. \quad (4.24)$$

The normal unit vector points towards increasing z . Since the free surface is a material surface, the KBC condition there can be written as follows

$$\frac{dF_s}{dt} = 0 \quad \Rightarrow \quad -\frac{\partial h_T}{\partial t} - \frac{\partial h_T}{\partial x} v_{1,x} + v_{1,z} = 0. \quad (4.25)$$

Differently from the free surface, the interface is a non-material surface, hence the KBC there has to be written as follows

$$\frac{dF_i}{dt} = 0 \quad \Rightarrow \quad \frac{\partial F_i}{\partial t} + \mathbf{v}_{int} \cdot \nabla F_i = 0 \quad \Rightarrow \quad -\frac{\partial h_2}{\partial t} - \frac{\partial h_2}{\partial x} v_{int,x} + v_{int,z} = 0 \quad (4.26)$$

with \mathbf{v}_{int} being the interface velocity, instead of flow velocity.

By adding the term $\mathbf{v}_1 \cdot \nabla F_i$ to both sides of Eq. (4.26) and using equation, expressing the volume exchange in the upper layer, (4.19), Eq. (4.26) is recast as follows

$$-\frac{\partial h_2}{\partial t} - \frac{\partial h_2}{\partial x} \cdot v_{1,x} + v_{1,z} = (\mathbf{v}_1 - \mathbf{v}_{int}) \cdot \nabla F_i = E_1 \|\nabla F_i\|. \quad (4.27)$$

By substituting Eqs. (4.25) and (4.27) into Eq. (4.23) and after some simplifications, we obtain the following depth-integrated mass balance equation

$$\frac{\partial h_1}{\partial t} + \frac{\partial (\overline{v_{1,x} h_1})}{\partial x} = \frac{M_{flux}}{\rho_1} \|\nabla F_i\|. \quad (4.28)$$

Here and hereafter, we use the over-bar to denote the averaged value over the flow thickness, i.e.

$$h_1 \overline{f} = \int_{h_2}^{h_T} f dz \quad \text{for the upper layer,} \quad h_2 \overline{f} = \int_0^{h_2} f dz \quad \text{for the lower layer.} \quad (4.29)$$

Analogously, we depth-integrate the mass equation along the flow depth of the lower layer. By using the Leibnitz rule (A.3), we obtain

$$\frac{\partial}{\partial t} \int_0^{h_2} \rho_2 dz + \left[\rho_2 \frac{dz}{dt} \right]_{h_2}^0 + \frac{\partial}{\partial x} \int_0^{h_2} \rho_2 v_{2,x} dz + \left[\rho_2 v_{2,x} \frac{dz}{dt} \right]_{h_2}^0 + [\rho_2 v_{2,z}]_0^{h_2} = 0 \quad (4.30)$$

Generally speaking, the bottom surface can be described by a function $F_b = z - b(x, t) = 0$. Nonetheless, because a fixed plane bottom is assumed, i.e. $b = 0$, the corresponding KBC at the bottom surface can be written in the following simplified way,

$$\frac{dF_b}{dt} = 0 \quad \Rightarrow \quad -\frac{\partial b}{\partial t} - \frac{\partial b}{\partial x} v_{2,x} + v_{2,z} = 0 \quad \Rightarrow \quad v_{2,z} = 0. \quad (4.31)$$

Thanks to KBCs at the interface and at the bottom surfaces (4.26) (4.31) and after dividing all terms by ρ_2 , Eq. (4.30) is recast as follows

$$\frac{\partial (h_2)}{\partial t} + \frac{\partial (\overline{v_{2,x} h_2})}{\partial x} = -\frac{M_{flux}}{\rho_2} \|\nabla F_i\|. \quad (4.32)$$

Depth-averaged momentum equations

Similarly, the depth-averaged momentum balance equations are derived. As regards the upper layer, it can be written as follows

$$\begin{aligned} & \frac{\partial}{\partial t} \int_i^{h_T} \rho_1 \mathbf{v}_1 dz + \left[\rho_1 \mathbf{v}_1 \frac{\partial z}{\partial t} \right]_{h_T}^i + \frac{\partial}{\partial x} \int_i^{h_T} (\rho_1 \mathbf{v}_1 \otimes \mathbf{v}_1) \hat{\mathbf{e}}_x dz + \\ & \left[(\rho_1 \mathbf{v}_1 \otimes \mathbf{v}_1) \hat{\mathbf{e}}_x \frac{\partial z}{\partial x} \right]_{h_T}^i + [(\rho_1 \mathbf{v}_1 \otimes \mathbf{v}_1) \hat{\mathbf{e}}_z]_i^{h_T} \\ & - \frac{\partial}{\partial x} \int_i^{h_T} T_1 \hat{\mathbf{e}}_x dz - \left[T_1 \hat{\mathbf{e}}_x \frac{\partial z}{\partial x} \right]_{h_T}^i - [T_1 \hat{\mathbf{e}}_z]_i^{h_T} = \int_i^{h_T} \rho_1 \mathbf{g} dz \end{aligned} \quad (4.33)$$

where $\hat{\mathbf{e}}_x = (1, 0)^T$ and $\hat{\mathbf{e}}_z = (0, 1)^T$ represent the coordinate unit vectors and T_1 represents the stress tensor, defined in the upper layer domain.

The x component of Eq. (4.33) can be written as

$$\begin{aligned} & \frac{\partial}{\partial t} (\overline{v_{1,x}} h_1) + \left[v_{1,x} \frac{\partial z}{\partial t} \right]_{h_T}^i + \frac{\partial}{\partial x} (\overline{v_{1,x}^2} h_1) + \left[v_{1,x}^2 \frac{\partial z}{\partial x} \right]_{h_T}^i + [v_{1,x} v_{1,z}]_i^{h_T} - \frac{\partial}{\partial x} (\overline{t_{1,xx}} h_1) \\ & - \left[t_{1,xx} \frac{\partial z}{\partial x} \right]_{h_T}^i - [t_{1,xz}]_i^{h_T} = g_x h_1 \end{aligned} \quad (4.34)$$

Since the free surface is assumed to be stress free, the Dynamic boundary condition (DBC) there can be written as follows

$$T_1 \mathbf{n} = \mathbf{0} \Rightarrow -t_{1,xx} \partial_x h_T + t_{1,xz} = 0 \quad (4.35)$$

By using the KBC at free surface (4.25) and at interface (4.27), together with the DBC at the free surface (4.35), Eq. (4.34) is recast

$$\frac{\partial}{\partial t} (\overline{v_{1,x}} h_1) + \frac{\partial}{\partial x} (\overline{v_{1,x}^2} h_1) - \frac{\partial}{\partial x} \left(\frac{\overline{t_{1,xx}}}{\rho_1} h_1 \right) - v_{1,x}|_i \frac{M_{flux}}{\rho_1} \|\nabla F_i\| - \frac{t_{1,xx}}{\rho_1} \Big|_i \frac{\partial h_2}{\partial x} + \frac{t_{1,xz}}{\rho_1} \Big|_i = g_x h_1 \quad (4.36)$$

where the symbol $|_i$ indicates that the argument is calculated at the interface i .

Similarly, the x -component of the lower layer depth-averaged momentum balance equation can be written as follows

$$\frac{\partial}{\partial t} (\overline{v_{2,x}} h_2) + \frac{\partial}{\partial x} (\overline{v_{2,x}^2} h_2) - \frac{\partial}{\partial x} \left(\frac{\overline{t_{2,xx}}}{\rho_2} h_2 \right) + v_{2,x}|_i \frac{M_{flux}}{\rho_2} \|\nabla F_i\| + \frac{t_{2,xx}}{\rho_2} \Big|_i \frac{\partial h_2}{\partial x} + \left[\frac{t_{2,xz}}{\rho_2} \right]_i^0 = g_x h_2 \quad (4.37)$$

Analogous derivations of the z components of depth-averaged momentum equations can be done. Nonetheless, we do not to report them because they will not be used in the final model.

Approximations

Equations (4.28), (4.32), (4.36) and (4.37) have been obtained with the only simplifying assumption of constant bulk densities inside each layer. In this section, we are going to discuss about some further simplifications that lead to the final PDE system.

Since granular geophysical flows are typically thin and long, we employ a *long-wave* like approximation along the x -direction. With this assumption, we basically assume that z -component of any vector field is much smaller than its x -component and that any quantity f varies smoothly along x -direction, i.e. $\partial_x f$ is small. Thanks to the first assumption, we are allowed to ignore the z -component of flow velocities and their derivatives in z -component depth-averaged momentum equations. It directly follows that an hydrostatic normal pressure distribution holds over the depth in both layers, namely

$$t_{1,zz}(z) = -\rho_1 g_z (h - z) \quad \Rightarrow \quad t_{1,zz}(i) = -\rho_1 g_z h_1 \quad (4.38)$$

$$t_{2,zz}(z) = t_{1,zz}(z_i) - \rho_2 g_z (h_2 - z). \quad (4.39)$$

Now, we need to relate the normal pressure exerted on a surface parallel to the bed, t_{zz} with that exerted on a surface perpendicular to it, t_{xx} . By following the same assumptions of Savage-Hutter model (Savage and Hutter, 1989), the following relations between the normal stresses are assumed

$$t_{1,xx}(z) = K_1 t_{1,zz}(z), \quad t_{2,xx}(z) = K_2 t_{2,zz}(z) \quad (4.40)$$

where K_1 and K_2 are earth-pressure coefficients, that can be defined as functions of internal and basal friction angles, analogously to what proposed in Savage and Hutter (1989). Thanks to Eqs. (4.39), together with Eq. (4.40), it is possible to calculate the depth-averaged normal stresses $\overline{t_{1,xx}}$ and $\overline{t_{2,xx}}$ in Eqs. (4.36) and (4.37).

From the second assumption of the *long-wave* approximation, it follows that the interface slope with respect to the x -axis, $\partial_x h_2$, is expected to be very small compared to 1 and, hence

$$\|\nabla F_i\| = \sqrt{\partial_x h_2^2 + 1} \approx 1. \quad (4.41)$$

Hence, it follows also that

$$\mathbf{n}_i \approx (0, 1)^T. \quad (4.42)$$

In addition, some assumptions have to be made about the flow velocity distributions inside each layer. In fact, in Eqs. (4.36) and (4.37), terms accounting for momentum exchange due to the mass flux across at the interface, $v_{1,x}|_i M_{flux}/\rho_1 \|\nabla F_i\|$ and $v_{2,x}|_i M_{flux}/\rho_2 \|\nabla F_i\|$, require that flow velocities be calculated at the interface. As well, the velocity distribution influences also the terms $\overline{v_{1,x}^2}$ and $\overline{v_{2,x}^2}$. Because at the moment we are interested to study the main properties of a two layer-approach, we use the simplest hypothesis that x -component of velocity are approximately constant within each layer. In this way, it holds

$$\overline{v_{1,x}^2} \approx (\overline{v_{1,x}})^2, \quad \overline{v_{2,x}^2} \approx (\overline{v_{2,x}})^2 \quad (4.43)$$

$$v_{1,x}(i) \approx (\overline{v_{1,x}}), \quad v_{2,x}(i) \approx (\overline{v_{2,x}}) \quad (4.44)$$

Finally, thanks to Eqs. (4.44) and (4.42), the x component of the momentum jump condition (4.22) can be recast as follows

$$M_{flux} = \frac{t_{1,xz} - t_{2,xz}}{\overline{v_{1,x}} - \overline{v_{2,x}}}. \quad (4.45)$$

This equation, which is similar to that reported after a slightly different derivation in Fraccarollo and Capart (2002), will be used as closure equation of the PDE system, in order to calculate the mass flux at the interface.

The aforementioned assumptions lead to the definition of the final PDE system. It should be said that a more rigorous derivation of the model equations can be done through an asymptotic analysis of depth-averaged equations (e.g. Savage and Hutter, 1989, 1991; Gray et al., 1999). In this regard, a small dimensionless parameter, ε , representing the ratio between the typical flow depths, H , and the typical spread of the avalanche, L , is defined. Then, such a parameter is used to isolate physically negligible terms in mass and momentum depth-averaged equations. The application of this technique will be reported in Chapter 6, when a slightly different two-layer model will be derived in curvilinear coordinates.

4.2.2 Final model equations

The proposed model is a PDE system composed of the following five equations,

$$\left\{ \begin{array}{l} \frac{\partial h_1}{\partial t} + \frac{\partial (\overline{v_{1,x}} h_1)}{\partial x} = \frac{M_{flux}}{\rho_1}, \\ \frac{\partial}{\partial t} (\overline{v_{1,x}} h_1) + \frac{\partial}{\partial x} \left(\overline{v_{1,x}}^2 h_1 + \frac{1}{2} K_1 g_z h_1^2 \right) = \\ \quad g_x h_1 - g_z h_1 \frac{\partial h_2}{\partial x} + \frac{M_{flux}}{\overline{v_{1,x}} \rho_1} - \frac{t_{1i,xz}}{\rho_1} - R_{1,side}, \\ \frac{\partial h_2}{\partial t} + \frac{\partial (\overline{v_{2,x}} h_2)}{\partial x} = -\frac{M_{flux}}{\rho_2}, \\ \frac{\partial}{\partial t} (\overline{v_{2,x}} h_2) + \frac{\partial}{\partial x} \left(\overline{v_{2,x}}^2 h_2 + \frac{1}{2} K_2 g_z h_2^2 \right) = \\ \quad g_x h_2 - g_z \frac{\rho_1}{\rho_2} h_2 \frac{\partial h_1}{\partial x} - \frac{M_{flux}}{\overline{v_{2,x}} \rho_2} + \frac{t_{2i,xz}}{\rho_2} - \frac{t_{2b,xz}}{\rho_2} - R_{2,side}, \\ M_{flux} = \frac{t_{1,xz} - t_{2,xz}}{\overline{v_{1,x}} - \overline{v_{2,x}}}. \end{array} \right. \quad (4.46)$$

The vector of unknowns is $\mathbf{q} = (h_1, h_1 \overline{v_{1,x}}, h_2, h_2 \overline{v_{2,x}})^T$, in which $\overline{v_{1,x}}$ and $\overline{v_{2,x}}$ are the depth-averaged x -components of the flow velocity in the upper and lower layers, respectively, and h_1 and h_2 are the flow depth of upper and lower layer, respectively. $g_x = g \sin \alpha$ and $g_z = g \cos \alpha$ where α is the inclination angle of the reference axis x with respect to the horizontal plane. The bulk densities of the upper and lower layer are represented by the symbols ρ_1 and ρ_2 , respectively. These values can be calculated as the product of the grain density ρ_g and the volume fractions, ϕ_1 and ϕ_2 , supposed to be constant in each layer. Differently from the classical two-layer shallow water System (4.3) and from the two-layer shallow water model proposed by Capart and Young (2002), two earth-pressure coefficients, K_1 and K_2 , are introduced in order to express the x -normal stresses, σ_x , as functions of normal to bed normal stresses, σ_z . This treatment is analogous to that proposed by (Savage and Hutter, 1989, 1991). In a first approximation, these earth-pressure coefficients can be calculated by means of the formula proposed by (Savage and Hutter, 1989), i.e. as a function of internal and basal friction angles. While the first two equations represent the balances of mass and x -component momentum in the upper layer, the third and fourth ones represent the mass and x -component momentum balances in the lower layer. Finally, the fifth equation of System (4.46) represents a closure equation, that is used to calculate the M_{flux} between the two layers. It has been obtained by employing the Rankine-Hugoniot jump condition at the interface, in a similar fashion to that used in Fraccarollo and Capart (2002).

Although the pseudo-Jacobian matrix associated with the mathematical System (4.46) is slightly different from that of classic two-layer shallow water model (cf. Eq. (4.7)) because of the earth pressure coefficients K_1 and K_2 , it can be easily shown that also this system is conditionally hyperbolic. Also in this case, according to what reported in Eq. (4.11) of Section (4.1), the shear velocity between the two layers has a destabilizing effect, while the inverse density ratio and total flow depth have stabilizing effects on the system hyperbolicity.

Now, let us describe more in detail the source terms of the System (4.46). In the mass balance equations the terms M_{flux}/ρ_1 and M_{flux}/ρ_2 represent the volume exchanges in the upper and lower layer, respectively. Please note that, while the mass flux is unique in both equations because the

physical system, composed of two layers, is mass-conservative, the volume exchanges are different because of different densities. As regards the momentum balance equations, there are three types of source terms. For sake of conciseness, let us examine only the momentum balance equation, referred to the upper layer. Analogous considerations can be done for the momentum balance equation, referred to the lower layer.

- the term $g_x h_1$ stands for the accelerating effect of the gravity force;
- the term $\overline{v_{1,x}} M_{flux} / \rho_1$ represents the momentum flux, due to the mass exchange between the two layers;
- the term $t_{1i,xz} / \rho_1$ represents the momentum flux, due the shear stress at the interface;
- the term $R_{1,side}$ accounts for the effects of side wall resistances.

Accordingly to what has been extensively explained in Section (4.1), the term $-g_z h_1 \partial_x h_2$ cannot be regarded as a source term, as it represents a non-conservative term, depending on the spatial derivative of the unknown h_2 .

By supposing a Coulomb-type friction at the side walls, analogously to what assumed in the single layer model of Chapter 1, the side walls resistances in the upper layer momentum equation can be specified as follows

$$R_{1,side} = -\frac{g_z h_1^2 K_y \tan \delta_{side} \operatorname{sgn}(\overline{v_{1,x}})}{W}, \quad (4.47)$$

where W is the width of the channel cross-section, δ_{side} the friction angle at the side walls and K_y is an earth-pressure coefficient, relating the normal pressure exerted on a surface parallel to the side wall, σ_y , to that one exerted on a surface parallel to the basal surface, σ_z . In (Sarno et al., 2011), it has been observed that a good estimation of K_y can be the earth pressure coefficient at rest calculated by means of the Jaky formula (Jaky, 1944).

Similarly, the side walls resistances in the lower layer momentum equation can be written as follows

$$R_{2,side} = -\frac{2g_z (\rho_1 / \rho_2 h_1 + h_2 / 2) h_2 K_y \tan \delta_{side} \operatorname{sgn}(\overline{v_{2,x}})}{W}. \quad (4.48)$$

Shear stresses

Now, it is needed to specify the formulae for calculating the effects of the shear stresses at the interface and at the bottom surface. By following (Savage and Hutter, 1989), a Coulomb-type friction law is supposed at the bed surface. Thus, the shear stress there can be simply written as follows

$$t_{2b,xz} = g_z (\rho_1 h_1 + \rho_2 h_2) \tan \delta \operatorname{sgn}(\overline{v_{2,x}}) \quad (4.49)$$

where δ represent the angle of basal friction.

Such an assumption is supported by the fact that the lower layer exhibits a quasi-static flowing regime, where the main momentum exchange mechanism is expected to be due to friction.

At the interface two values of the shear stresses have to be defined: $t_{2i,xz}$ as limit from below and $t_{1i,xz}$ as limit from above. Obviously, the chosen analytic expressions of these terms depend on

the constitutive laws assumed in the two layers. In the lower layer, in which a solid-like quasi-static regime is observed, a purely Coulomb-type constitutive law is supposed: therefore, it holds

$$t_{2i,xz} = g_z \rho_1 h_1 \tan \varphi_{int} \operatorname{sgn}(\overline{v_{1,x}} - \overline{v_{2,x}}) \quad (4.50)$$

where φ_{int} is the internal friction angle of the granular material at the interface.

Conversely, since the upper layer is in friction-collision (i.e. dense-collisional) regime, the shear stress as limit from above, $t_{2i,xz}$, is supposed to be composed of two terms. While the first one, which is rate independent, takes into account the momentum exchange due to friction, the second one depends on the shear velocity between layers and thus it takes into account the momentum exchange due to collisions (e.g. Bagnold, 1954). More precisely, we postulate the following expression

$$t_{1i,xz} = g_z \rho_1 h_1 k \tan \varphi_{int} \operatorname{sgn}(\overline{v_{1,x}} - \overline{v_{2,x}}) + r \rho_1 (|\overline{v_{1,x}} - \overline{v_{2,x}}|)^\beta \operatorname{sgn}(\overline{v_{1,x}} - \overline{v_{2,x}}) \quad (4.51)$$

where k and r are empirical parameters, β is an exponent depending on the chosen constitutive law. On the basis of existing works available in Literature, β is typically between 1 and 2 (e.g. Bagnold, 1954; Nishimura, 1991). The dimensionless parameter k , supposed to be always smaller than 1, is aimed to account for the relative diminution of the friction effects, due to the volume fraction jump, $\phi_1 - \phi_2$. In fact, it is expected that, once the volume fraction reduces, also the time for the friction effects to influence the flow dynamics does reduce (e.g. Ancey, 2007). Conversely, the parameter, r accounts for the relative influence of collision effects. Please note that r is dimensionless only if β is chosen equal to 2.

It should be noted that Eq. (4.51) is reminiscent of the constitutive law proposed by Josserand et al. (2004), although it is written in a non-local form.

Mass flux

By substituting Eqs. (4.50) and (4.51) into the fifth equation of System 4.46, it is recast as follows

$$M_{flux} = \frac{t_{1i,xz} - t_{2i,xz}}{v_{1,x} - v_{2,x}} = r \rho_1 (|\overline{v_{1,x}} - \overline{v_{2,x}}|)^{\beta-1} - \frac{(1-k) g_z \rho_1 h_1 \tan \varphi_{int}}{|\overline{v_{1,x}} - \overline{v_{2,x}}|} \quad (4.52)$$

In a slight different context, Fraccarollo and Capart (2002) considered the process of mass exchange across the interface between the flowing layer and the stationary bed as a relaxation law of the upper layer flow depth towards an equilibrium condition. In this fashion, by neglecting the advection term $\partial_x (\overline{v_{1,x}} h_1)$, the first Eq. of System (4.46) can be written as follows

$$\frac{dh_1}{dt} = \frac{M_{flux}}{\rho_1} \Rightarrow \frac{dh_1}{dt} = \frac{h_{1,eq} - h_1}{t_M} \quad (4.53)$$

where $h_{1,eq}$ represents the upper layer equilibrium depth, at which $M_{flux} = 0$, and t_M is a relaxation time reflecting the rapidity of the process towards the equilibrium state. Hence, the value of $h_{1,eq}$, can be determined by imposing $M_{flux} = 0$, i.e. $t_{1i,xz} = t_{2i,xz}$. With the help of Eqs. (4.50) and (4.51), it reads

$$h_{1,eq} = \frac{r (\overline{v_{1,x}} - \overline{v_{2,x}})^\beta}{g_z \tan \varphi_{int} (1-k)} \geq 0. \quad (4.54)$$

This alternative formulation of the process of mass exchange will be very useful in designing the numerical scheme.

Likewise, the relaxation time t_M can be written as follows

$$t_M = \frac{|\overline{v_{1,x}} - \overline{v_{2,x}}|}{g_z \tan \varphi_{int} (1 - k)}. \quad (4.55)$$

4.2.3 The numerical scheme

The PDE system (4.46) has been numerically integrated through a finite volume scheme. Such a numerical scheme is similar to that proposed by Fraccarollo et al. (2003), as regards the treatment of advection terms and non-conservative terms. In particular, it is based on the HLL approximate Riemann solver with a *lateralized* treatment of non-conservative terms. Since the equation system exhibits non-null source terms, the *Operator Splitting* technique (e.g. LeVeque, 2002) has been used for taking into account the effects of source terms, separately from the effects of advection. Moreover, after each time step, an additional stage is introduced in order to check whether it is needed to *regularize* the hyperbolicity loss. In case of loss of hyperbolicity of the original system, a final step, in which the source terms in the momentum equations of System (4.46) are slightly modified by adding an extra friction at the interface, is performed so that the hyperbolicity loss is avoided.

The numerical scheme, here presented, is composed of four steps that can be briefly summarized as follows:

1. the homogeneous conservation PDE system, associated with the complete PDE system (4.46), is used in order to calculate the advection effects to the solution at each time step,
2. the effect of source terms are accounted for by solving the ordinary differential system (ODE) associated with the source terms; two sub-steps have been used: the first one for accounting the effects of mass flux between the layers, the second one for accounting the effects of shear stresses and mass forces;
3. after updating the numerical solution, the eigenvalues of System (4.46) are numerically calculated in order to check if they are real,
4. in the case that the inner eigenvalues of System are complex numbers, in order to avoid the hyperbolicity loss, an extra momentum flux at the interface is added in the source terms of the original System, strictly sufficient to keep the numerical solution inside the hyperbolicity domain.

Let us discuss the aforementioned steps more in detail.

First step: calculation of advection effects

In the first step, only the advection effects are calculated. In order to do so, the homogeneous PDE system, associated with System (4.46),

$$\frac{\partial \mathbf{q}}{\partial t} + A \frac{\partial \mathbf{q}}{\partial x} = \mathbf{0} \quad (4.56)$$

is considered, in which A is pseudo-Jacobian matrix that also takes into account the non-conservative terms.

The lateralized HLL (often referred to as LHLL) scheme proposed by Fraccarollo et al. (2003) has been applied to numerically solve the homogeneous system (4.56). This numerical scheme can be regarded as an extension of the classical HLL approximate Riemann solver (Harten et al., 1983) to treat non-conservative systems. The scheme is explicit and is conditionally stable, provided that the Courant-Friedrichs-Levy (CFL) number be smaller than 1. In a finite-volume framework, the following explicit formula is used to update the vector of unknowns \mathbf{q} ,

$$\mathbf{q}_i^{PDE} = \mathbf{q}_i^j - \frac{\Delta t}{\Delta x} \left(\mathbf{F}_{i+1/2}^j - \mathbf{F}_{i-1/2}^j \right) \quad (4.57)$$

where \mathbf{q}_i^{PDE} represents the numerical solution at the i -th cell, $\mathbf{F}_{i+1/2}^j$ and $\mathbf{F}_{i-1/2}^j$ are the numerical fluxes, to be computed at the interfaces of i -th cell at the time level j .

At first, by following the original HLL approach (Harten et al., 1983), the numerical fluxes at cell interfaces can be written by disregarding the non-conservative terms, i.e.

$$\mathbf{F}_{i+1/2}^{*j} = \frac{S_R \mathbf{F}_i^{*j} - S_L \mathbf{F}_{i+1}^{*j} + S_R S_L \left(\mathbf{q}_i^j - \mathbf{q}_{i+1}^j \right)}{S_R - S_L}. \quad (4.58)$$

Here S_R and S_S are some lower and upper bounds of the eigenvalues set of the Jacobian matrix $\partial \mathbf{F} / \partial \mathbf{q}$. In the present numerical scheme, they are calculated by using the following formulae

$$\begin{aligned} S_R &= \min \left\{ 0, \min \left[\text{eig} \left(\partial \mathbf{F} / \partial \mathbf{q} \Big|_i^j \right), \text{eig} \left(\partial \mathbf{F} / \partial \mathbf{q} \Big|_{i+1}^j \right) \right] \right\}, \\ S_L &= \max \left\{ 0, \max \left[\text{eig} \left(\partial \mathbf{F} / \partial \mathbf{q} \Big|_i^j \right), \text{eig} \left(\partial \mathbf{F} / \partial \mathbf{q} \Big|_{i+1}^j \right) \right] \right\} \end{aligned} \quad (4.59)$$

where the symbol ‘‘eig’’ denotes the eigenvalue-set. The eigenvalues in (4.59) have been calculated numerically because there are no simple analytical formulae. In order to take into account the non-conservative terms, we follow the *lateralised* approach proposed by (Fraccarollo et al., 2003). Namely, it is assumed that the numerical fluxes are double valued functions at cell interfaces, owing to the effects of non-conservative terms. More precisely, the numerical flux jump at the interface is supposed to be the following

$$\mathbf{F}_{1+1/2}^L - \mathbf{F}_{1+1/2}^R = \begin{pmatrix} 0 \\ [(h_2)_{i+1} - (h_2)_i] (g_z h_1)_{i+1/2} \\ 0 \\ [(h_1)_{i+1} - (h_1)_i] (g_z \rho_1 / \rho_2) (h_2)_{i+1/2} \end{pmatrix} \quad (4.60)$$

where the superscripts L and R indicate the left-hand and right-hand values of the numerical fluxes at the cell interface. As a result, the original HLL numerical fluxes reported in Eq. (4.58) have to be modified according to Eq. (4.60). More precisely, Eq. (4.57) can be recast as follows

$$\mathbf{q}_i^{PDE} = \mathbf{q}_i^j - \frac{\Delta t}{\Delta x} \left(\mathbf{F}_{i+1/2}^{j, L} - \mathbf{F}_{i-1/2}^{j, R} \right) \quad (4.61)$$

with the flux correction

$$\mathbf{F}_{i+1/2}^{j, L} = \mathbf{F}_{i+1/2}^{*j} + \frac{S_L}{S_R - S_L} \begin{pmatrix} 0 \\ [(h_2)_{i+1} - (h_2)_i] g_z (h_1)_{i+1/2} \\ 0 \\ [(h_1)_{i+1} - (h_1)_i] g_z \rho_1 / \rho_2 (h_2)_{i+1/2} \end{pmatrix} \quad (4.62)$$

where $(h_1)_{i+1/2}$ and $(h_2)_{i+1/2}$ are taken equal to the arithmetic mean values of the i -th and $(i+1)$ -th cells.

By means of the first calculation step, the solution of System (4.56), referred to as \mathbf{q}^{PDE} hereafter, is advanced by the time step Δt . The new value, calculated at each finite volume cell, will be used as initial condition of the following calculation step.

Step 2: Source terms treatment

The second calculation step is in order to calculate the effects of source terms on the solution, advanced by a time step Δt . This step basically consists of solving the following ordinary differential system (ODE), by using as initial condition the solution coming from the first calculation step,

$$\frac{d\mathbf{q}}{dt} = \mathbf{s}_m + \mathbf{s}_r \quad \text{with} \quad \mathbf{q}(0) = \mathbf{q}^{PDE}. \quad (4.63)$$

There are two sub-step in order to solve the ODE system (4.63).

First sub-step

In the first sub-step, we calculate explicitly (i.e. by using the *backward Euler scheme*) the mass flux during the generic time step Δt . Only the flow depths of both layers are updated during this sub-step, i.e.,

$$\begin{aligned} (h_1)_i^I &= (h_1)_i^{PDE} + \Delta t M_{flux}^* / \rho_1 \\ (h_2)_i^I &= (h_2)_i^{PDE} + \Delta t M_{flux}^* / \rho_2 \\ (h_1 u_1)_i^I &= (h_1 u_1)_i^{PDE} \\ (h_2 u_2)_i^I &= (h_2 u_2)_i^{PDE}, \end{aligned} \quad (4.64)$$

where, while with the superscript PDE we denote the solution obtained from the first calculation step, with the superscript I we denote the updated solution after this first sub-stage. Moreover, M_{flux}^* represents a constrained value, as to avoid negative layer depths or overshooting the equilibrium depth, $h_{1,eq}$. More precisely, the value of M_{flux}^* is determined by

$$M_{flux}^* = \begin{cases} \min(M_{lim1}, M_{flux}), & \text{if } M_{flux} > 0, \\ \max(M_{lim2}, M_{flux}), & \text{if } M_{flux} \leq 0, \end{cases} \quad (4.65)$$

in which the value of M_{flux} is obtained by Eq. (4.52), M_{lim1} and M_{lim2} are the limiting values, i.e.

$$\begin{aligned} \Delta t M_{lim1} &= \min(\rho_1 (h_{1,eq} - h_1^{PDE}), \rho_2 (h_2^{PDE} - h_{th})), \\ \Delta t M_{lim2} &= \max(\rho_1 (h_{1,eq} - h_1^{PDE}), \rho_1 (h_{th} - h_1^{PDE})). \end{aligned} \quad (4.66)$$

In Eqs. (4.66), $h_{1,eq}$ is the equilibrium depth computed by (4.54) and h_{th} is a very small threshold value that avoids negative flow depths.

Second sub-step

In this stage, we deal with the momentum exchanges, due to the term \mathbf{s}_r that accounts the source terms in the momentum balance equations. Since the terms in \mathbf{s}_r that depend on the flow velocities may be very large during the computation, i.e. they exhibit a *stiff-like* behaviour (e.g. LeVeque, 2002), it is convenient to treat them in an implicit fashion. In this numerical scheme an

implicit *backward Euler* scheme has been used, similarly to the approach of Chen et al. (2007). The main advantage of a implicit treatment is that it is unconditionally stable. We use as initial condition the solution vector obtained from the previous sub-step, marked by the superscript I . The updating formula can be written as follows

$$\mathbf{q}_i^{II} = \mathbf{q}_i^I + \Delta t \mathbf{s}_{r,i}^{II} \quad (4.67)$$

where the source vector $\mathbf{S}_{r,i}^{II}$ is calculated at the end of the time step and, thus, is function of the unknown \mathbf{q}_i^{II} . Therefore, the vector Eq. (4.67) is a non-linear algebraic system, composed of 4 scalar equations, with the unknown \mathbf{q}_i^{II} . Nonetheless, since $s_r(1) = s_r(3) = 0$, then $q_i^{II}(1) = q_i^I(1)$ and $q_i^{II}(3) = q_i^I(3)$. Therefore, Eq. (4.67) can be simplified into a 2×2 non-linear algebraic system with unknowns $q_i^{II}(2)$ and $q_i^{II}(4)$. In computing \mathbf{s}_r , it is required to make use of formulae for shear stresses, i.e. Eqs. (4.49), (4.50), and (4.51).

We observed some oscillation issues due to the *sign* function around zero in the shear stress formulae (4.49), (4.50), and (4.51). In order to overcome this numerical issue, we replaced the *sign* function with the following regularized function in Eqs. (4.49), (4.50), and (4.51)

$$R(\Delta u) = \frac{2}{1 - e^{-\alpha \Delta u}} - 1 \quad (4.68)$$

in which α is a shape parameter. The regularization function (4.68) depends on the shear velocity Δu and exhibits a sigmoid shape, as shown in Fig. 4.5. This treatment, yet simple, turns out to be very useful to reduce flow depth oscillations around the state of rest. Through several comparisons, we found that numerical results are roughly identical by using any reasonable $\alpha > 300$. Therefore, in the here presented numerical simulations we set $\alpha = 300$.

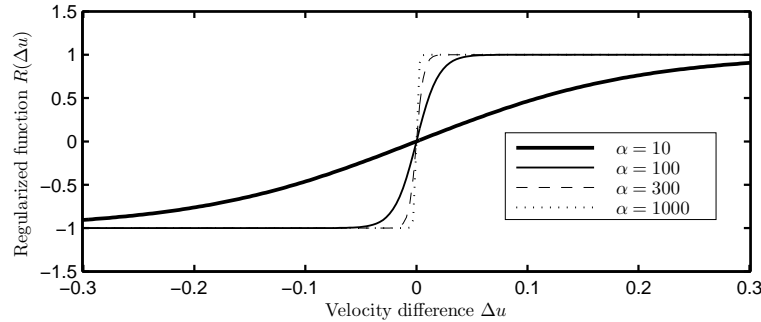


Figure 4.5: Regularization function R .

Hyperbolicity check and regularization

The original System (4.46) is only conditionally hyperbolic. The loss of hyperbolicity typically occurs in presence of a too large relative velocity between the two layers. In such a case, the inner eigenvalues of the pseudo-Jacobian matrix, A , associated with the System (4.46), become conjugate complex numbers. In this situation, the mathematical model breaks down and, consequently, also the numerical solution give unreliable results. As reported in Section 4.1, in the space of solutions

\mathbf{q} , there exists a multi-connected domain where the mathematical model is hyperbolic. By ignoring the particular case of hyperbolic solutions with very large shear velocity, which is unrealistic in free surface granular flows that start from a state of rest, the hyperbolic domain is characterized by a relatively small shear velocity between layers.

In order to avoid the loss of hyperbolicity, we propose a local modification of the source terms of the original two-layer model (4.46). Although the treatment consists of a local modification of the mathematical model; however, the criterion to apply such a modification is designed inside the numerical scheme. Therefore, this method could be regarded as of *hybrid* type with respect to the classification made in Section 4.1.

The proposed treatment consists of the following steps.

At first, after advancing in time the solution by means of the second sub-step of the source term treatment, the hyperbolicity of numerical solution is checked at each finite volume cell, by numerically calculating the eigenvalues of the pseudo-Jacobian matrix. Namely, at any given i -th finite volume cell, the eigenvalues set,

$$eig(A(\mathbf{q}_i^{II})) \quad (4.69)$$

is numerically calculated.

If all the eigenvalues are real, the solution \mathbf{q} is simply updated at the new time point $j+1$ with the vector obtained through the second sub-step of the source term treatment, i.e.

$$\mathbf{q}_i^{j+1} = \mathbf{q}_i^{II}. \quad (4.70)$$

Instead, if the inner eigenvalues are complex numbers, it means that the original model (4.46) enters the non-hyperbolic domain, during the latest time step. In order to avoid non-hyperbolic solutions, the source terms of the second sub-step are modified, by adding an extra resistance at the interface,

$$\mathbf{q}_i^{II} = \mathbf{q}_i^I + \Delta t \mathbf{s}_{R,i}^{II} + \Delta t \begin{pmatrix} 0 \\ -R(\Delta u) F_{extra}/\rho_1 \\ 0 \\ R(\Delta u) F_{extra}/\rho_2 \end{pmatrix} \quad (4.71)$$

where $\Delta u = u_1 - u_2$ is the shear velocity. The second sub-step is, thus, repeated in the modified form (4.71).

The extra resistance F_{extra} acts like an additional shear stress at the interface and, thus, causes a net momentum flux from the faster layer to the slower one. As a result, the shear velocity between the two layer reduces. We take advantage of this effect, in order to bring back the solution inside the hyperbolic domain. Obviously, the optimal amount of this extra resistance is the minimum value necessary for obtaining an hyperbolic solution. The calculation of such an optimal amount is obtained through an iterative algorithm:

1. a tentative value of F_{extra} is assigned;
2. the second sub-step of the source term treatment is repeated accordingly to the modification (4.71);
3. the eigenvalues of the new solution \mathbf{q}_i^{II} are numerically calculated;

4. if the inner eigenvalues, λ_2 and λ_3 , are still complex numbers, the next tentative value of F_{extra} is chosen larger than the previous one and the algorithm comes back to Point No. 1;
5. if the inner eigenvalues, λ_2 and λ_3 , are real numbers but $|\lambda_2 - \lambda_1| > \nu_{th}$, with ν_{th} being a small threshold celerity, the next tentative value of F_{extra} is chosen smaller than the previous one and the algorithm comes back to point No. 1;
6. the algorithm converges, as soon as the inner eigenvalues are real numbers and $|\lambda_2 - \lambda_1| < \nu_{th}$.

This approach is similar to that proposed in Castro-Díaz et al. (2011), although in the present case we do not use a simplified formula for checking the hyperbolicity but the actual eigenvalues of pseudo-Jacobian matrix. From a more theoretical viewpoint, this numerical treatment corresponds to solving a slightly different two-layer model. More precisely, in the new *regularized* model, the source terms of the balance momentum equations are locally modified as follows

$$\begin{aligned} \frac{\partial}{\partial t} (\overline{v_{1,x}} h_1) + \frac{\partial}{\partial x} \left(\overline{v_{1,x}^2} h_1 + \frac{1}{2} K_1 g_z h_1^2 \right) &= s(2) - \frac{F_{extra}}{\rho_1} R (\overline{v_{1,x}} - \overline{v_{2,x}}) \\ \frac{\partial}{\partial t} (\overline{v_{2,x}} h_2) + \frac{\partial}{\partial x} \left(\overline{v_{2,x}^2} h_2 + \frac{1}{2} K_2 g_z h_2^2 \right) &= s(4) + \frac{F_{extra}}{\rho_2} R (\overline{v_{1,x}} - \overline{v_{2,x}}), \end{aligned} \quad (4.72)$$

in which $s(2)$ and $s(4)$ represent the original source terms of System (4.46).

After this treatment the solution \mathbf{q} is updated at the new time point $j + 1$ with the vector obtained through the latest iteration of the aforementioned algorithm, which corresponds to an hyperbolic solution.

This approach seems to be very stable in cases when the loss of hyperbolicity are limited in time and space, since it permits to overcome some local hyperbolicity losses of the original model. From an engineering viewpoint, the modification of source terms can be justified as long as it is small, compared with the other source terms and, in particular, if it is comparable with the already existent uncertainties in accounting the shear stress terms at the interface.

Moreover, the proposed treatment has some interesting properties. Firstly, the linear momentum of the global system, composed of the two layers, is not modified by the extra resistance F_{extra} . In fact, such a treatment only transfers momentum from the faster layer to the slower one. Secondly, the inclusion of an extra resistance at the interface mimics somehow the effects due to a Kelvin-Helmoltz type instability. In fact, in this case a turbulent momentum flux goes from the slower layer to the faster one.

As an important limitation, it should be noted that this approach requires that the boundary conditions of the PDE System be hyperbolic. In fact, such a condition is necessary to fulfil the well-posedness of the mathematical model.

4.2.4 Boundary conditions

The boundary conditions have to be studied carefully and require to be implemented in the numerical code in a proper way, in order to obtain a well-posed mathematical problem. As a general rule, in a PDE hyperbolic problem, at each boundary there should be assigned as many simple boundary conditions (i.e. scalar equations of the unknowns \mathbf{q}) as they are the characteristic curves ingoing the spatial domain. The remaining unknowns at the boundaries can be calculated

as function of the solutions at the previous times in the physical domain, together with the imposed values at the boundary. In fact, information propagates from the physical domain to the boundary along the outgoing characteristic families. These relations are usually named *compatibility boundary equations* because they require to be fulfilled in order the mathematical problem to be well-posed. Which are outgoing and which are ingoing characteristic families is very straightforward to be checked by calculating the sign of the eigenvalues of the pseudo Jacobian matrix, A , associated with the PDE system. For instance, at the left-hand boundary an ingoing characteristic family occurs when its celerity, i.e. the related eigenvalue, is a positive number. On the other hand, when it is negative it means that information propagates outside the physical domain, hence it is a outgoing characteristic family.

In the case we are not interested in assigning specific values at the boundaries, it is useful to simply use *non-reflecting* boundary conditions (also called *absorbing boundary conditions*) at the both ends of the computational domain. This kind of conditions is straightforward to be implemented and guarantees that any perturbation at the boundaries does not propagate inside the computational domain (e.g. LeVeque, 2002). This treatment avoids the occurrence of spurious reflections of the outgoing waves inside the computational domain. Non-reflecting boundary conditions can be implemented in a numerical scheme by means of a zero-order extrapolation of the solution \mathbf{q} at the boundaries. In other words, we add *ghost* cells beyond the boundaries with symmetrical values with respect of the unknowns \mathbf{q} at the first and last physical numerical cells, respectively. These boundary conditions can be written as follows

$$\mathbf{q}_1^{j+1} = \mathbf{q}_2^{j+1}, \quad \mathbf{q}_{end}^{j+1} = \mathbf{q}_{end+1}^{j+1}. \quad (4.73)$$

It is worth noting that this treatment does not involve the computation of the eigenvalues signs.

Nevertheless, there are other situations in which it is needed to assign particular values of the physical quantities at the domain boundaries, e.g. flow depths or flow rates. For example, it is needed in case of comparisons between numerical simulation and experimental data, reported in Chapter 5. In this case we have to assign as many boundary conditions as they are required by the mathematical model. The other values of the solution at the boundaries, can be calculated by means of compatibility equations. The approach used in the present numerical code is similar to that one proposed by Savary and Zech (2007). It is composed of the following stages. Firstly, at each time step the eigenvalues associated with the hyperbolic System (4.46) are numerically calculated at the boundaries of the computational domain, in order to check how many boundary conditions have to be imposed. Secondly, these required conditions are imposed according with the experimental data. Usually, discharges are imposed at the left-hand boundary, while flow depth are assigned at the right-hand boundary. Then, the compatibility equations need to be considered for calculating the other values at the boundaries. By following the work by Savary and Zech (2007), for a given outgoing characteristic with eigenvalue λ_i , it holds

$$l_{i1} \left(\frac{dq_1}{dt} \right)_{\lambda_i} + l_{i2} \left(\frac{dq_2}{dt} \right)_{\lambda_i} + l_{i3} \left(\frac{dq_3}{dt} \right)_{\lambda_i} + l_{i4} \left(\frac{dq_4}{dt} \right)_{\lambda_i} = 0 \quad (4.74)$$

where q_1, q_2, \dots are the components of the unknown vector \mathbf{q} and the l_{ij} is the j th component of the left eigenvector \mathbf{L}_i , that is the i -th row of the matrix L , defined as follows,

$$A = L^{-1} \Gamma L \quad (4.75)$$

in which A is the pseudo-Jacobian matrix associated with the hyperbolic system (4.46) and Γ represents the diagonal matrix of eigenvalues.

Please note that the time derivative $(dq/dt)_{\lambda_i}$ is a total derivative along the i -th characteristic line. Formally, in non linear problems the eigenvalues vary with time, hence the characteristic line is actually a curve. Nevertheless, we refer to the linearized hyperbolic problem, i.e. we numerically calculate L at the time-step j and assume that for a small time step Δt the eigenvalues can be considered constant.

Therefore, the time derivatives in (4.74) can be calculated by means of the ratio $\Delta q_i/\Delta t$, where Δq_i has to be calculated as difference between the unknown value $q_{boundary}^{j+1}$ at the boundary at the new time point t_{j+1} and the known value q_i^* on the same characteristic line at the previous time point $t_j = t_{j+1} - \Delta t$. This value necessarily lies into the cell adjacent to the boundary because Δt is chosen, so that $CFL < 1$.

Assuming, for instance, that the second characteristic family is outgoing at the left-hand boundary, the discrete form of (4.74) can be written as follows

$$l_{21} \left(\frac{(h_1)_{boundary}^{j+1} - (h_1)_1^j}{\Delta t} \right) + l_{22} \left(\frac{(h_1 u_1)_{boundary}^{j+1} - (h_1 u_1)_1^j}{\Delta t} \right) + \\ l_{23} \left(\frac{(h_2)_{boundary}^{j+1} - (h_2)_1^j}{\Delta t} \right) + l_{24} \left(\frac{(h_2 u_2)_{boundary}^{j+1} - (h_2 u_2)_1^j}{\Delta t} \right) = 0 \quad (4.76)$$

in which subscripts refer to the cell position in the numerical code and superscripts specify the time point.

After writing Eq. (4.76) for each outgoing characteristic line, we get a linear system. The unknowns are the values of $\mathbf{q}_{boundary}$ at the boundary that cannot be assigned as boundary conditions because depend on the solution at the previous time point. After solving this system we have the complete solution $\mathbf{q}_{boundary}$.

4.3 Numerical Tests

Some numerical tests, performed by using the mathematical model (4.46) with the proposed modification of source terms to recover the hyperbolicity (4.72), are reported here. These tests are intended to show the main features of the proposed two-layer approach and the robustness of the numerical scheme. Some further comparisons between the numerical model and experimental data are reported in Chapter 5. The numerical results, presented here, have been also reported in Sarno et al. (2011).

Simulation parameters

In the present numerical tests, a spatial domain $L=10$ m long is considered, where the spatial mesh is uniform and equal to $\Delta x = 0.05$ m. The Courant-Friedrichs-Levy (CFL) number is set equal to 0.8, for determining the time interval Δt at each time step. Non-reflecting boundary conditions, calculated by means of a zero-order extrapolation, are assigned at the boundaries of numerical spatial domain. The mass balance is verified after each numerical simulation within an error typically smaller than 0.5% of the initial mass. The average CPU time per point, at each

time-advancing, is found to be around $3.8 \cdot 10^{-3}$ s (on a 2.2 GHz processor), in the case that the hyperbolicity correction is not present. Instead, in case of hyperbolicity correction, the average CPU time per point is approximately $1.1 \cdot 10^{-2}$ s. Such a noticeable increase of the computation time is due to the fact that the hyperbolicity correction consists of an iteration algorithm, in which the second sub-step, to account the source terms effects, has to be repeated several times. Nonetheless, it should be remarked that, since the hyperbolicity correction operates only when necessary (i.e. locally in time and space), the impact of this additional computation time on the global time, required to complete a numerical simulation, is typically limited.

The volume fractions of the two layers are set to be $\phi_1 = 0.4$ and $\phi_2 = 0.6$. This choice is congruent with many experimental studies, in which the volume fraction of dry granular flows are reported to typically range between $[0.3, 0.7]$ (e.g. Ancey, 2001; Midi, 2004). The shear resistance at the interface as limit from above, i.e. Eq. (4.51), is chosen to have a quadratic dependence on the shear velocity, namely $\beta = 2$ is chosen. In this fashion, Eq. (4.52) for calculating the mass flux M_{flux} becomes

$$M_{flux} = r \rho_1 \frac{|\overline{v_{1,x}} - \overline{v_{2,x}}|}{|\overline{v_{1,x}} - \overline{v_{2,x}}|} - \frac{(1-k) g_z \rho_1 h_1 \tan \varphi_{int}}{|\overline{v_{1,x}} - \overline{v_{2,x}}|}. \quad (4.77)$$

The effect of side walls is neglected, i.e. $R_{1,side} = R_{2,side} = 0$. From a physical viewpoint, this condition corresponds to an infinitely large cross-section, $W \rightarrow \infty$.

Both of the internal, φ_{int} , and basal friction angles, δ , are set to be equal to 30° . In the computation, non-reflective boundary condition at both ends of the computational domain are adopted and the depth threshold, h_{th} in Eq. (4.66) is chosen to be $h_{th} = 10^{-4}$.

Depositional scenario

In order to highlight the importance of a non-null mass flux between layers, we compare the results from the System (4.46) with and without the mass exchange M_{flux} . The initial velocities of the upper and the lower layer are chosen to be 2 m/s and 1 m/s, respectively. The initial depths of both of the layers are equal to 1 m. In the computation, the inclination angle of the chute is 20° , r is 0.2 and k is 0.9. The test parameters are concisely reported in Table 4.1. The total duration of simulation is 4 s.

α	δ	φ_{int}	r	k
20°	30°	30°	0.2	0.9

Table 4.1: Parameters used in Test No. 1.

Figure 4.6 illustrates the evolution of the depth distribution with and without the mass exchange. Because the bottom slope is less than the basal and internal friction angles, both of the two layers are in a decelerating motion. With the parameters in Table 4.1, Eq. (4.77) implies that $M_{flux} < 0$, i.e. there is a net mass flux from the upper layer into the lower one. In the simulation with $M_{flux} \neq 0$, the mass merges rapidly from the upper layer into the lower layer, so that the volume of the upper layer decreases with time.

At $t = 2$ s, only the front of the upper layer exists. This is probably due to the large acceleration by the high surface gradient at $t = 0$ s and to the thin flow thickness of the front part (cf. Eq.

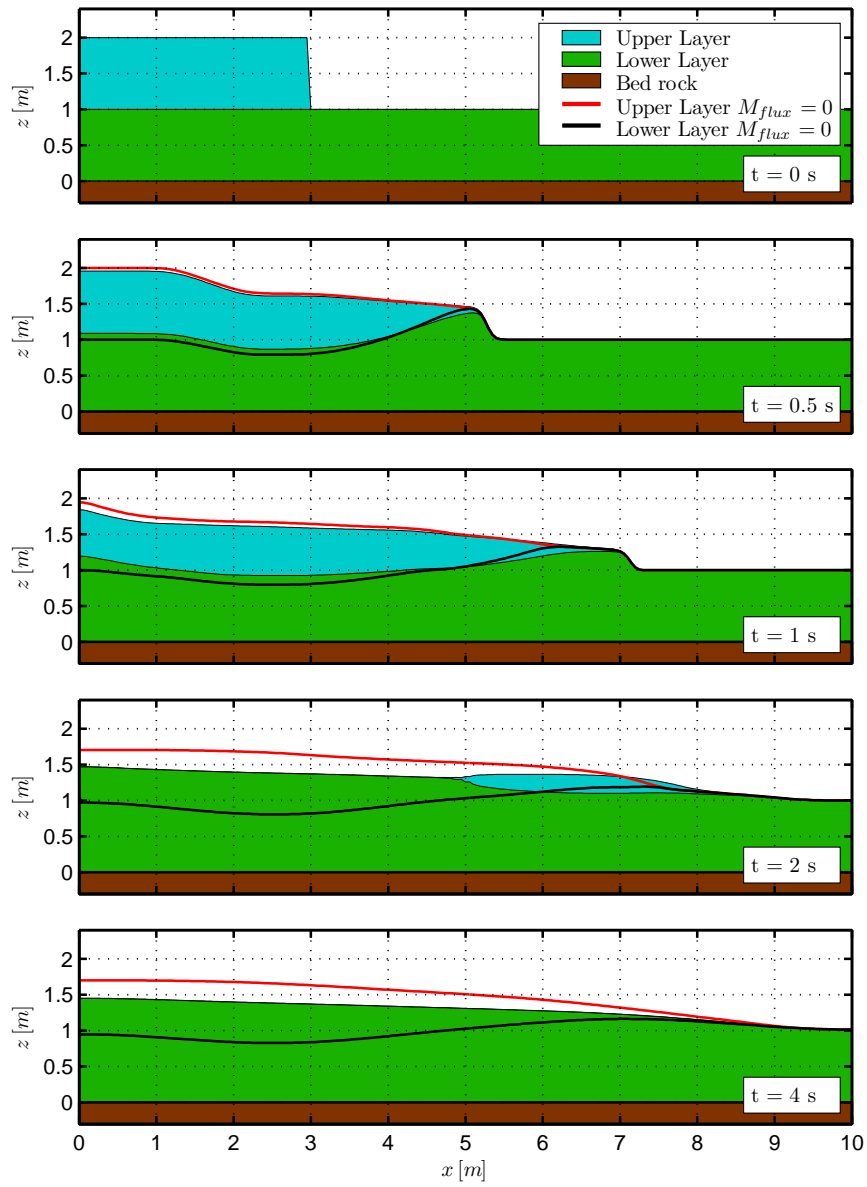


Figure 4.6: Evolution of flow depths (depositional scenario, Test No. 1).

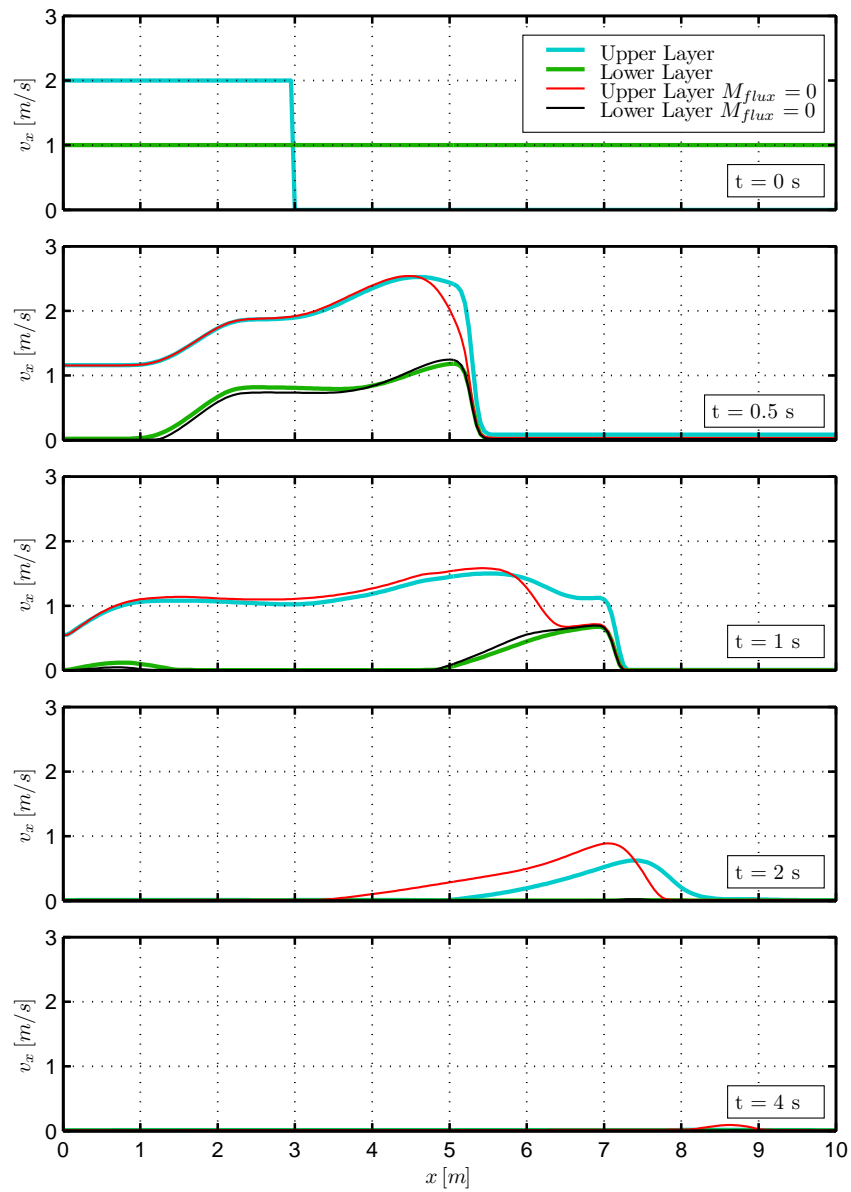


Figure 4.7: Evolution of flow velocities (depositional scenario, Test No. 1).

(4.77)). At $t = 4$ s, the whole flow body is at the state of rest, and it is entirely composed of the lower frictional layer. It should be noted that, the total volume reduces whenever there is a mass flux across the interface from the upper into the lower layer. This is due to the fact that the lower layer exhibits a higher density. In the simulation with null mass exchange $M_{flux} = 0$, both of the two layers decelerate without merging into each other. In Fig. 4.6, the red and black lines depict the evolution of the flow surface and the interface, respectively. Fig. 4.7 illustrates the velocity distributions of the upper and lower layers along the downstream x -direction. In both cases, the lower layer decelerates rapidly and reaches a state of rest between $t = 1$ s and $t = 2$ s, whilst the upper layer is still in motion. Before $t = 1$ s, there is no significant difference found either in the depth or in the velocity distribution of the upper layer in the rear part. Yet, with $M_{flux} \neq 0$, the velocity surge of the upper layer propagates ahead of the one with $M_{flux} = 0$. After $t = 1$ s, the results with $M_{flux} = 0$ exhibit slightly higher velocities, although the front surge is behind that obtained by the simulation with $M_{flux} \neq 0$. Apparently, this phenomenon seems to be due to the fact that the upper layer gets a lower loss of momentum across the interface when $M_{flux} = 0$, cf. Eq. (4.46). Yet, with $M_{flux} \neq 0$ the depth of the upper layer reduces as well, so that the velocity does not decrease noticeably. Therefore, the velocity differences are more likely due to different depth gradients that develop during the time and are only indirectly induced by the mass flux. Finally, approximately at $t = 4$ s, all the flow layers reach a state of rest.

Erosional scenario

In this section, the flow behaviours are examined when the lower layer is being eroded. Higher values for the inclination angle α , r and k in Eq. (4.51) are chosen and reported in Table 4.2.

The initial conditions are identical to the previous test, as well as the basal and internal friction angles φ and δ .

α	δ	φ_{int}	r	k
40°	30°	30°	0.4	0.99

Table 4.2: Parameters used in Test No. 2.

Figures 4.8 and 4.9 display the evolution of the flow layer depths and flow velocities in cases of null and non-null mass flux, M_{flux} . Since the beginning, the depth evolutions from simulations with $M_{flux} \neq 0$ exhibit a rapid increase of the upper layer flow depth, at the expense of the lower layer flow depth. Moreover, the front of the upper layer propagates slightly faster than that obtained, by assuming $M_{flux} = 0$. The flow depth of the lower layer keeps decreasing notably at subsequent time points and reaches a very small depth at the final time point $t = 6$ s. It is worth noting that, as time goes by, the total flow depth increases. This is due to the fact that the net mass flux goes from the lower layer, characterised by a higher volume fraction, to the upper layer with an lower volume fraction.

By comparing the flow velocity evolutions, reported in Fig. 4.9, firstly we can notice that both of the layers are in accelerating motion. The velocity diagrams at $t = 0.5$ s and $t = 1$ s are congruent with what already observed by studying the flow depth evolution: in the simulation with $M_{flux} \neq 0$, the front of the upper layer wave is ahead with respect to that predicted by the

simple model with $M_{flux} \neq 0$. Nevertheless, the velocity differences between the two simulations are slightly smaller than those observed in the depositional scenario.

At $t = 4$ s, both of the flows are still in accelerating motion because the inclination angle α is bigger than the friction angles δ and φ . Nonetheless, it should be noted that the velocity difference between the two layers reach a stationary value. This is due to the rate-dependent term in the shear stress at the interface, computed by Eq. (4.51).

Sensitivity of the parameters k and r

Two additional tests have been performed in order to investigate the model sensitivity on parameters k and r that appear in the formula for calculating the shear stress at interface, as limit from above (Eq. (4.51)).

Sensitivity tests on parameter k

Firstly, we aim to investigate the effects on the flow dynamics of variations of the parameter k .

From a physical viewpoint, the parameter k is related to the volume fraction jump across the interface, since a smaller value of volume fraction in the upper layer reduces the effective time, in which the friction contacts between grains take place. Therefore, k is expected to be smaller than 1. Nonetheless, it should be noted that the effective jump of volume fractions is likely to be smaller than that assumed in the present model, because the real volume fraction distribution is not piece-wise constant. At first glance, one could be tempted to roughly assume that k is equal to the ratio of volume fraction $\phi_1/\phi_2 = 2/3$ between the layers. However, a reliable estimation of k can only be obtained through careful comparisons with experimental data. At this moment, our purpose is to observe and study the variations of flow depth evolutions, owing to a variation of k .

In this test, the initial conditions, the inclination angle and the friction angles, used in this sensitivity test, are identical to those of Test No. 1 (depositional scenario), so that the analysis refers to a scenario of deposition. Conversely, different values of k have been investigated in a range between 0.1 and 0.99. The test parameters are listed in Table 4.3. Besides, Fig. 4.10 reports the flow depths evolutions observed in the numerical simulation with $k = 0.99, 0.66, 0.1$.

α	δ	φ_{int}	r	k
20°	30°	30°	0.2	[0.1, 0.99]

Table 4.3: Parameters used in Test No. 3.

As one can see in Fig. 4.10, the results computed with higher value of k generally exhibit a slower deposition. This is due to the fact that higher values of k imply higher values of equilibrium depth $h_{1.eq}$ (cf. (4.77)). As well, it is remarkable that the differences in depth profiles rely mostly in the first time steps (i.e. $t = 1$ s, $t = 2$ s). It is of important to note that at the end, all the numerical simulations tend to converge to the same profile of deposit. These numerical results are very interesting because they show that the parameter k only influence the flow motion in the transient state. Moreover, by comparing several numerical simulations it has been found that the sensitivity of the model on parameter k dramatically increases as k approaches to 1. This is due to the fact that, as k approaches 1, it causes bigger and bigger variations of the equilibrium depth $h_{1.eq}$. Furthermore, it should be noted that, in the ideal case that $k \rightarrow 1$, though $h_{1.eq}$ tends to

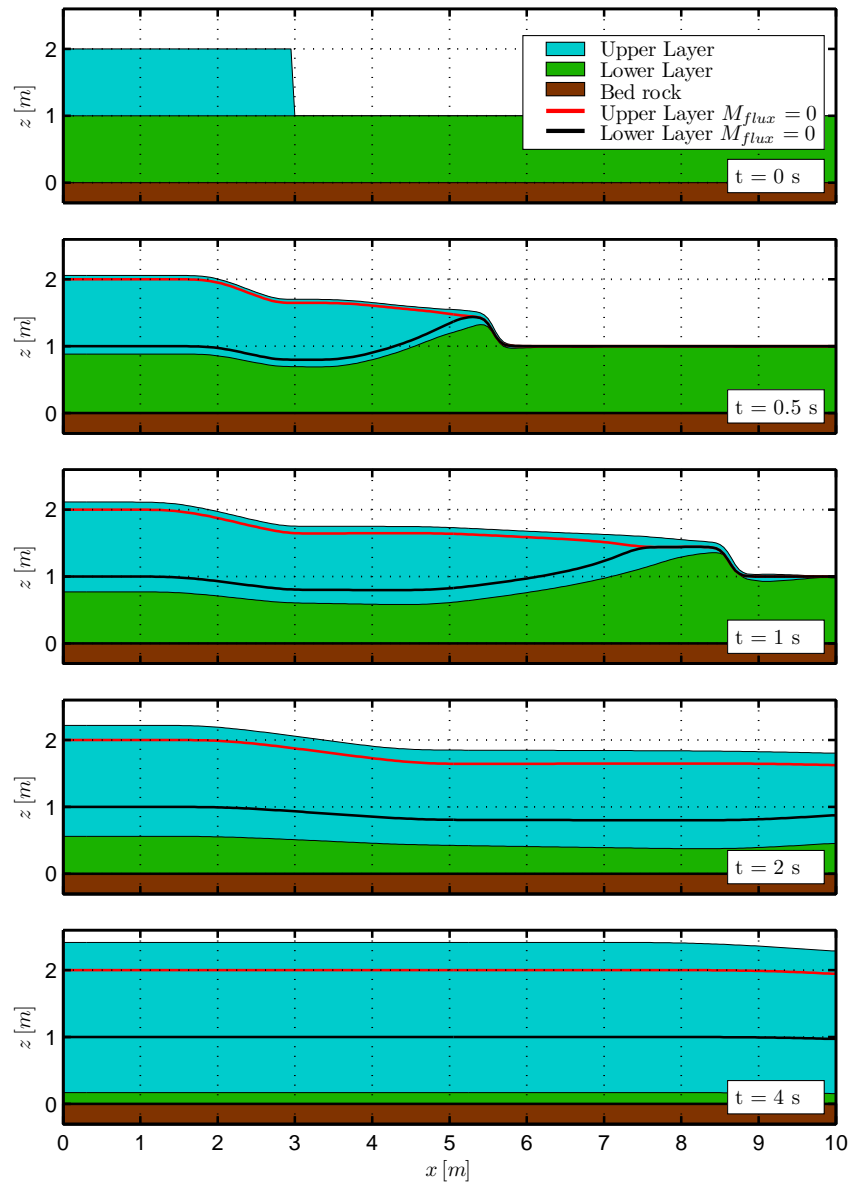


Figure 4.8: Evolution of flow depths (erosional scenario, Test No. 2).

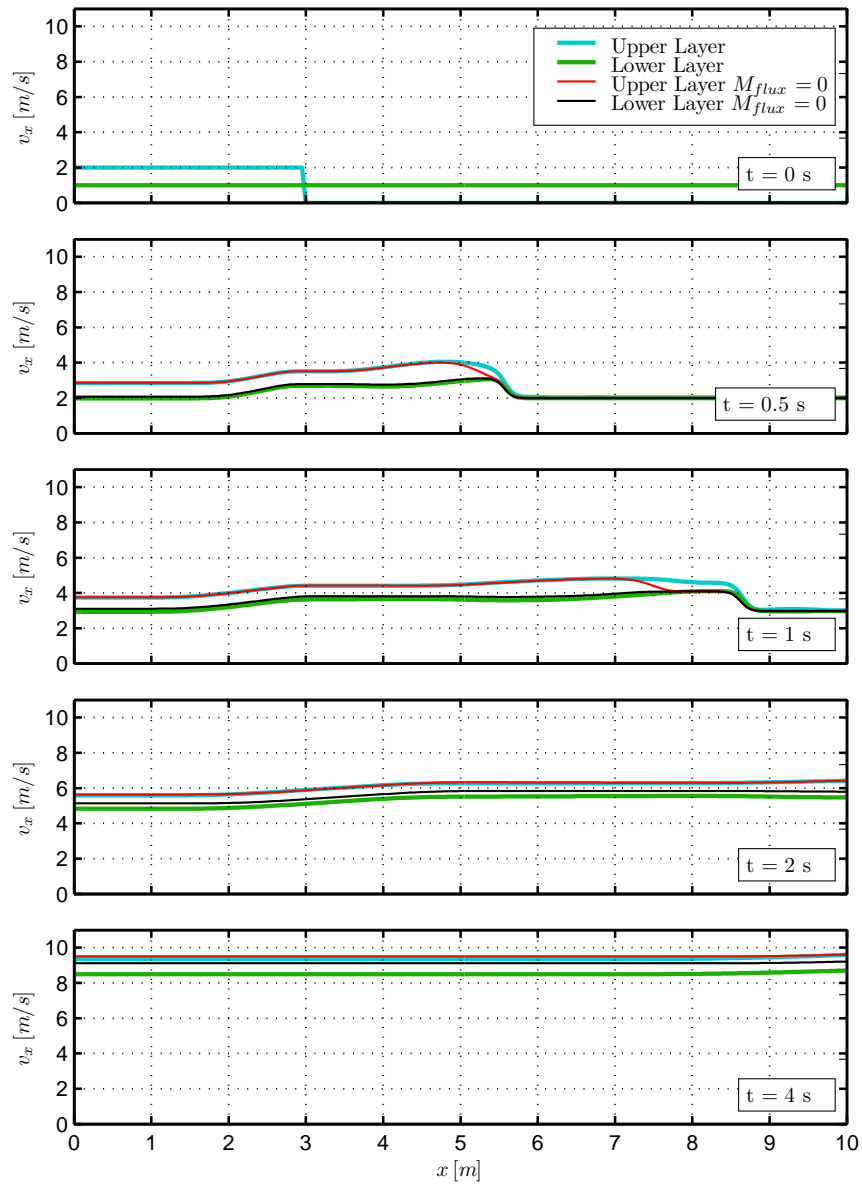


Figure 4.9: Evolution of flow velocities (erosional scenario, Test No. 2).

infinity, the mass flux tends to the finite value

$$M_{flux} \rightarrow r\rho_1 |\overline{v_{1,x}} - \overline{v_{2,x}}|, \quad (4.78)$$

as it can be easily found from Eq. (4.77).

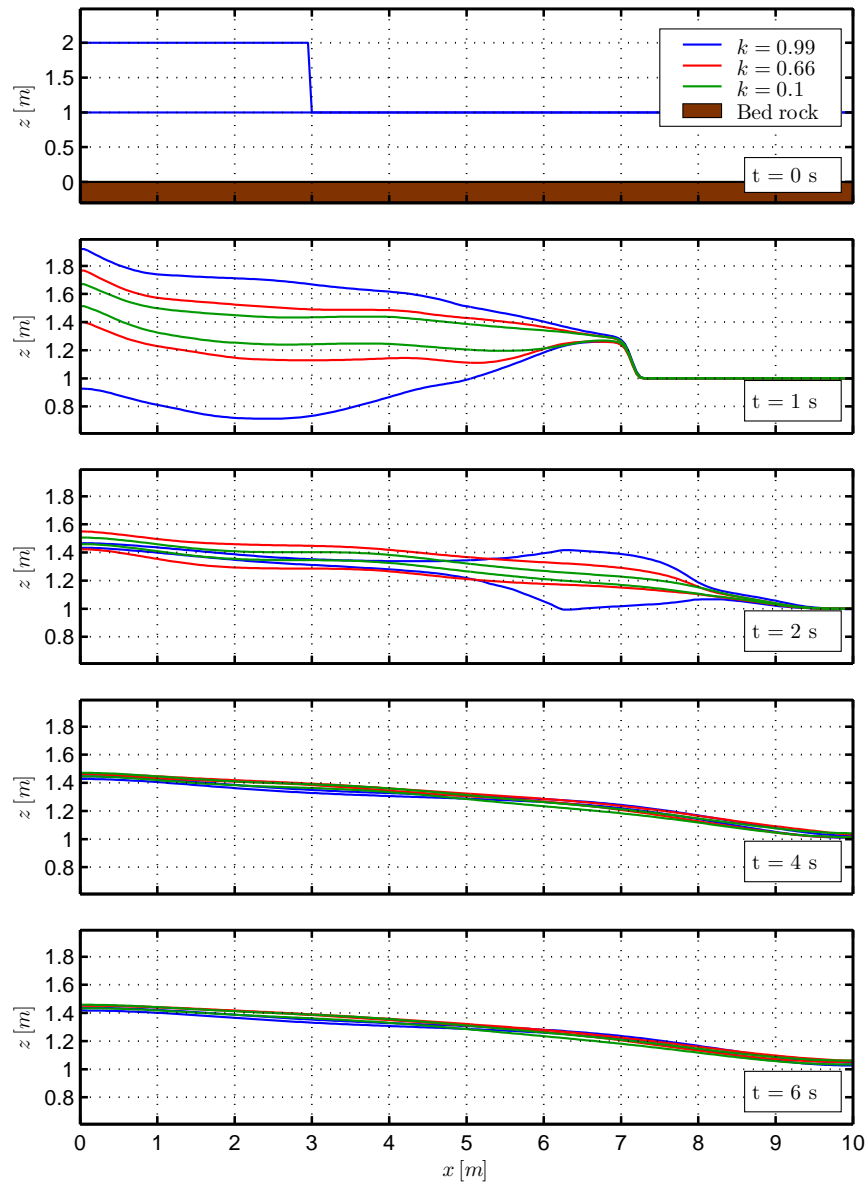
Sensitivity tests on parameter r

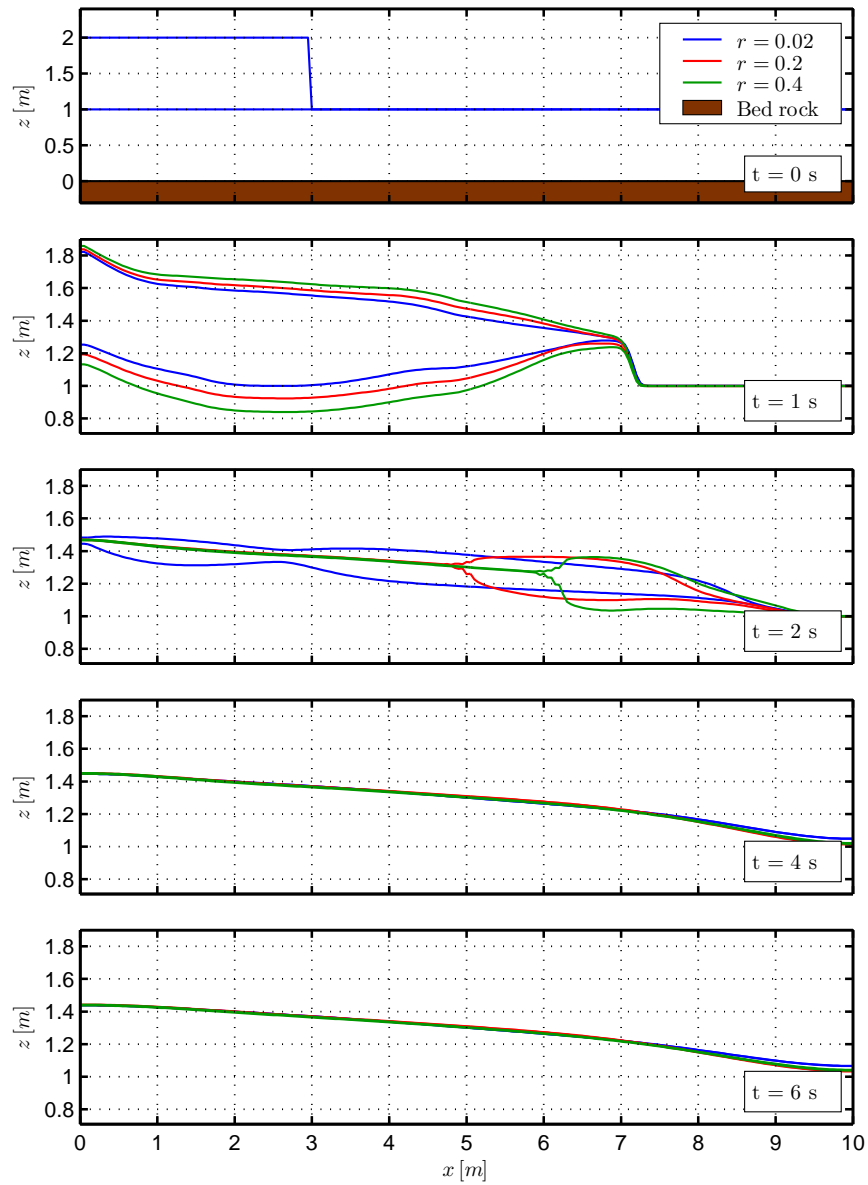
Similarly to what done in Test No. 3, a sensitivity test on the parameter r has been carried out. The initial conditions, inclination angle and friction angles are kept identical. The test parameters are listed in Table 4.4.

α	δ	φ_{int}	r	k
20°	30°	30°	[0.02, 0.4]	0.9

Table 4.4: Parameters used in Test No. 4.

Computations have been performed by varying the value of r in the range between 0.02 and 0.4. Figure 4.11 illustrates the evolution of the depth profiles at different r . The trends are generally similar to what observed in Fig. 4.10. Yet, it is very interesting to note that, while at $t = 1$ s the higher is r the bigger is the upper layer depth, at $t = 2$ s the behaviour reverses completely. This is due to the fact that, though $h_{1,eq}$ is proportional to r , a higher value of r also means that there is more shear resistance at interface and so velocity difference between the two layer decreases faster over time. Thus, $h_{1,eq}$ strongly reduces because of such a decrease. At the end, all the simulations converge quite exactly to a common profile. Even though it is not reported in Fig. 4.11, we also carried out numerical simulations with smaller values of r , down to $r = 0.005$, but the results are substantially identical to those obtained by using $r = 0.02$. Sensitivity on r is quite small compared to that on parameter k . However, in order to confirm this trend further numerical tests with different geometries and boundary conditions would be needed.

Figure 4.10: Sensitivity analysis on parameter k (Test No. 3), flow depth evolution.

Figure 4.11: Sensitivity analysis on parameter r (Test No. 4), flow depth evolution.

References Used in This Chapter

- Abgrall, R. and Karni, S. (2009). Two-Layer Shallow Water System: A Relaxation Approach. *SIAM Journal on Scientific Computing* **31**, 1603–1627.
- Ancey, C. (2001). Dry granular flows down an inclined channel: Experimental investigations on the frictional-collisional regime. *Physical Review E* **65**, 1–19.
- Ancey, C. (2007). Plasticity and geophysical flows: A review. *Journal of Non-Newtonian Fluid Mechanics* **142**, 4–35.
- Audusse, E. (2005). A multilayer Saint-Venant model: Derivation and numerical validation. *Discrete and Continuous Dynamical Systems - Series B* **5**, 189–214.
- Audusse, E. and Bristeau, M.-O. (2007). Finite-Volume Solvers for a Multilayer Saint-Venant System. *International Journal of Applied Mathematics and Computer Science* **17**, 311–320.
- Bagnold, R. A. (1954). Experiments on a Gravity-Free Dispersion of Large Solid Spheres in a Newtonian Fluid under Shear. *Proceedings of the Royal Society A: Mathematical, Physical and Engineering Sciences* **225**, 49–63.
- Brivois, O., Bonelli, S., and Borghi, R. (2007). Soil erosion in the boundary layer flow along a slope: a theoretical study. *European Journal of Mechanics - B/Fluids* **26**, 707–719.
- Brown, G. L. and Roshko, A. (1974). On density effects and large structure in turbulent mixing layers. *Journal of Fluid Mechanics* **64**, 775–816.
- Capart, H. and Young, D. (2002). Two-layer shallow water computations of torrential geomorphic flows. In *Proceedings of River Flow*, pages 1003–1012.
- Castro, M., Macías, J., and Parés, C. (2002). A Q -scheme for a class of systems of coupled conservation laws with source term. Application to a two-layer 1-D shallow water system. *ESAIM: Mathematical Modelling and Numerical Analysis* **35**, 107–127.
- Castro, M. J., Frings, J., Noelle, S., Parés, C., and Puppo, G. (2010). On the hyperbolicity of two-and three-layer shallow water equations. In *Series in Contemporary Applied Mathematics: Proceedings of the 13th International Conference on Hyperbolic Problems*.
- Castro, M. J., García-Rodríguez, J. A., González-Vida, J. M., Macías, J., Parés, C., and Vázquez-Cendón, M. (2004). Numerical simulation of two-layer shallow water flows through channels with irregular geometry. *Journal of Computational Physics* **195**, 202–235.
- Castro-Díaz, M. J., Fernández-Nieto, E. D., González-Vida, J. M., and Parés-Madroñal, C. (2011). Numerical Treatment of the Loss of Hyperbolicity of the Two-Layer Shallow-Water System. *Journal of Scientific Computing* **48**, 16–40.
- Chen, S.-C. and Peng, S.-H. (2006). Two-dimensional numerical model of two-layer shallow water equations for confluence simulation. *Advances in Water Resources* **29**, 1608–1617.
- Chen, S.-C., Peng, S.-H., and Capart, H. (2007). Two-layer shallow water computation of mud flow intrusions into quiescent water. *Journal of Hydraulic Research* **45**, 13–25.

- Doyle, E. E., Hogg, A. J., and Mader, H. M. (2010). A two-layer approach to modelling the transformation of dilute pyroclastic currents into dense pyroclastic flows. *Proceedings of the Royal Society A: Mathematical, Physical and Engineering Sciences* **467**, 1348–1371.
- Fernández-Nieto, E., Bouchut, F., Bresch, D., Castro Díaz, M., and Mangeney, A. (2008). A new Savage-Hutter type model for submarine avalanches and generated tsunamis. *Journal of Computational Physics* **227**, 7720–7754.
- Fraccarollo, L. and Capart, H. (2002). Riemann wave description of erosional dam-break flows. *Journal of Fluid Mechanics* **461**, 183–228.
- Fraccarollo, L., Capart, H., and Zech, Y. (2003). A Godunov method for the computation of erosional shallow water transients. *International Journal for Numerical Methods in Fluids* **41**, 951–976.
- Gray, J. (1999). Loss of hyperbolicity and ill-posedness of the viscous-plastic sea ice rheology in uniaxial divergent flow. *Journal of physical oceanography* **29**, 2920–2929.
- Gray, J. M. N. T., Wieland, M., and Hutter, K. (1999). Gravity-driven free surface flow of granular avalanches over complex basal topography. *Proceedings of the Royal Society A: Mathematical, Physical and Engineering Sciences* **455**, 1841–1874.
- Greco, M., Iervolino, M., and Vacca, A. (2008). Boundary conditions in a two-layer geomorphological model: Application to a hydraulic jump over a mobile bed. *Journal of Hydraulic Research* **46**, 856–860.
- Harten, A., Lax, P., and Leer, B. V. (1983). On upstream differencing and Godunov-type schemes for hyperbolic conservation laws. *SIAM review* **25**, 35–61.
- Jaky, J. (1944). The coefficient of earth pressure at rest. *Journal of the Society of Hungarian Architects and Engineers* **78**, 355–358.
- Josserand, C., Lagrée, P.-Y., and Lhuillier, D. (2004). Stationary shear flows of dense granular materials: a tentative continuum modelling. *The European physical journal. E, Soft matter* **14**, 127–35.
- Kim, J. and LeVeque, R. J. (2008). Two-layer shallow water system and its applications. In *12th International Conference on Hyperbolic Problems*, volume m, pages 1–8, College Park, Maryland.
- Lawrence, G. A. (1990). On the hydraulics of Boussinesq and non-Boussinesq two-layer flows. *Journal of Fluid Mechanics* **215**, 457.
- Lê, L. and Pitman, E. B. (2010). A Model for Granular Flows over an Erodible Surface. *SIAM Journal on Applied Mathematics* **70**, 1407–1427.
- LeVeque, R. (2002). *Finite volume methods for hyperbolic problems*, volume 31. Cambridge university press.
- Long, R. R. (1956). Long waves in a two-fluid system. *Journal of Meteorology* **13**, 70–74.

- Luca, I., Hutter, K., Kuo, C. Y., and Tai, Y. C. (2010). Two-layer models for shallow avalanche flows over arbitrary variable topography. *International Journal of Advances in Engineering Sciences and Applied Mathematics* **1**, 99–121.
- Midi, G. (2004). On dense granular flows. *The European physical journal. E, Soft matter* **14**, 341–65.
- Nishimura, K. (1991). Studies on the Fluidized Snow Dynamics. In *Contributions from the Institute of Low Temperature Science A37*, pages 1–55.
- Noelle, S. (2010). The dynamics of shallow fluid flows : Modeling and numerical analysis. In *i-MATH School on Numerical Solutions of Partial Differential Equations*, pages 1–9, Malaga.
- Rankine, W. M. (1870). On the thermodynamic theory of waves of finite longitudinal disturbance. *Philosophical Transactions of the Royal Society of London* pages 277–288.
- Sarno, L., Carravetta, A., Martino, R., and Tai, Y.-C. (2011). A two-layer approach to describe granular flows over rough surface. In *The 35th National Conference on Theoretical and Applied Mechanics*. Society of Theoretical and Applied Mechanics of the Republic of China.
- Sarno, L., Papa, M. N., and Martino, R. (2011). Dam-break flows of dry granular materials on gentle slopes. In Genevois, R., Hamilton, D. L., and Prestininzi, A., editors, *5th Int. Conf. on Debris-Flow Hazards Mitigation: Mechanics, Prediction and Assessment*. Italian Journal of Engineering Geology and Environment. Casa Editrice Università “La Sapienza”.
- Savage, S. B. and Hutter, K. (1989). The motion of a finite mass of granular material down a rough incline. *Journal of Fluid Mechanics* **199**, 177–215.
- Savage, S. B. and Hutter, K. (1991). The dynamics of avalanches of granular materials from initiation to runout. Part I: Analysis. *Acta Mechanica* **86**, 201–223.
- Savary, C. and Zech, Y. (2007). Boundary conditions in a two-layer geomorphological model. Application to a hydraulic jump over a mobile bed. *Journal of Hydraulic Research* **45**, 316–332.

Chapter 5

Comparisons and discussion

Chapter Summary

In Chapter 3 an experimental study on steady state free surface flows has been presented. The velocity profiles, in case of no-slip bottom boundary condition, exhibit a linear behaviour close to the free surface and an exponential tail in the lower zone. This suggests the occurrence of a rheological stratification along the flow depth. In Chapter 4 a two-layer depth-averaged model has been proposed in order to describe such a rheological stratification. The model aims to reproduce the dynamics of each layer separately, by assuming two different constitutive laws and a closure equation at the interface for calculating the mass-flux between the layers.

In experimental velocity profiles, such an interface could be, ideally, located where the velocity profile becomes almost linear, but this criterion would be uncertain and, somehow, arbitrary. In this Chapter, a more objective criterion for identifying the interface position in experimental velocity profiles is proposed. The rationale of its formulation consists of linking the interface position to a critical value of the inertial number, already defined in Chapter 1.

After identifying the interface position in experimental velocity profiles, depth-averaged flow velocities and flow depths of both of the layers have been calculated through numerical integration of experimental data. Finally, experimental data have been compared with numerical results, obtained by using the two-layer model introduced in Chapter 4.

5.1 Identification of the interface position in experimental velocity profiles

In this section we are going to present a criterion for identifying the position of the interface, separating the dense-collisional and the quasi-static domain in experimental velocity profiles.

In the two-layer model, the interface is assumed to be a non-material surface, where main physical quantities (e.g. flow velocities and flow densities) exhibit a jump. Nevertheless, it should be reminded that, in reality, such an interface does not separate two immiscible fluids but it only consists of an ideal surface, separating two regions in which the flow dynamics experiences different rheological regimes (i.e. quasi-static in the lower zone and dense-collisional in the upper zone). Time-averaged experimental velocity profiles, presented in Chapter 3, are everywhere continuous and, thus, they suggest that there is no sharp interface between the two zones.

However, since the observed velocity profiles exhibit a lower exponential tail, connected to a linear profile on the upper part, one could infer that the extent of the dense-collisional regime roughly corresponds to that of the upper linear profile. Hence, the interface position could be, ideally, located where the velocity profile becomes almost linear. Yet, this criterion is uncertain and arbitrary because the transition between these two behaviours is rather smooth.

Another geometrical construction to identify the boundary between the exponential and linear profile has been proposed in Midi (2004). In particular, after drawing the tangent line to the upper linear part of the velocity profile, the interface is assumed to be located in correspondence with the intersection of such a tangent line and z axis. However, also this construction is somehow arbitrary because the experimental velocity profiles are not exactly linear in their upper part.

In order to overcome such uncertainties, we propose a more objective criterion for identifying the interface position, obtained on the basis of physical arguments.

5.1.1 Inertial number distributions from experimental data

The inertial number, I , (defined in Eq. (1.5)) is a dimensionless scalar field, defined in the flow domain, governing the dynamics of rigid dry granular flows. In Chapter 1, we have reported that the quasi-static solid-like regime is characterized by a small value of I , while the collisional regime exhibits a larger value of it (e.g. Midi, 2004).

Hence, it is logical to connect the rheological stratification, observed in the case of no-slip bottom boundary condition, with the inertial number distribution inside the flowing pile. By definition (cf. Eq. (1.5)), I increases with $\dot{\gamma}$ and decreases inversely with the square root of the confining normal pressure P . Because of the no-slip boundary condition, $\dot{\gamma}$ is null at the bottom and increases as the distance from the bottom increases. Conversely, the normal pressure, P , increases with the distance from the free surface. It should be noted that, in the case of non-null bottom slip velocity, the behaviour of I along the flow depth is quite different, because everywhere $\dot{\gamma} \neq 0$ and, so, I exhibits non negligible values also at the bottom surface.

It could be very interesting to obtain an estimate of the distribution of the inertial number from the experimental data. In order to so, it is required to numerically calculate $\dot{\gamma}$, on the basis of the experimental velocity profiles, and to estimate the confining pressure P , as well.

Under the simplifying assumption of hydrostatic pressure distribution (acceptable in case of

shallow flows), it is possible to write

$$P(z) = \int_{h-z}^h g \rho(z) dz = \int_{h-z}^h g \phi(z) \rho_g dz = g \rho_g \overline{\phi(z)} (h-z) \quad (5.1)$$

where ρ is the bulk density, ρ_g is the grain density and ϕ represents the volume fraction. Moreover, by the symbol $\overline{\phi(z)}$ we denote the depth-averaged volume fraction along the depth $h-z$. As a matter of fact, ϕ and, hence, ρ depend on the distance from the free surface, $h-z$, and, in particular, they increase with it in surface flows, owing to the rheological stratification (e.g. Midi, 2004). Strictly speaking, in order to calculate the inertial number profiles, the distribution of the volume fraction, ϕ , should be previously measured. Unfortunately, it is quite demanding to get reliable measurements of the volume fraction distributions at the side walls through optical techniques, like *G-PIV*. Moreover, such measurements are unlikely to be representative of the effective volume fraction distribution inside the flowing pile (e.g. Sheng et al., 2011). In the experimental research, reported in Chapter 3, volume fraction distributions have not been measured.

Nonetheless, in dry granular flows, the variation of volume fraction along the flow depth is expected to be rather limited. More precisely, the volume fraction in the quasi-static regime is typically around 0.6 (close to the value at rest), while that of collisional regime is hardly smaller than 0.3 (e.g. Ancey, 2001; Sheng et al., 2011). In dense-collisional regime ϕ is expected to be even bigger than 0.3.

The distributions of the inertial number, I , along the flow depth, have been calculated from the experimental velocity profiles in the following way. The shear rate $\dot{\gamma}(z)$, which is equal to $\partial_z u_x(z)$ in plane shearing, has been numerically approximated by employing the experimental time-averaged flow velocities in a *central difference* formula. At the extrema of the flow domain, i.e. at the free surface and at the bottom, the *backward* and *forward difference* formulae have been used. Since we are interested in obtaining an estimate of the inertial number distribution, that is depth-averaged along the transverse direction (i.e. y direction), the side walls velocity profiles have been previously normalized by means of the ratio u_{mean}/u_{min} , reported in Tables 3.6 and 3.7 of Chapter 3. Namely, we assume that the velocity profile, depth-averaged along the y direction, is equal to the side wall velocity profile, multiplied by the factor, u_{mean}/u_{min} , obtained through the free surface measurements.

As regards the volume fraction distribution, owing to the lack of direct measurements, we assumed several linear distributions along the flow depth, so as to fulfil the following realistic constraints

$$\phi(z) = \phi_{\min} + (\phi_{\max} - \phi_{\min}) \frac{h-z}{h} \quad \text{with} \quad \begin{cases} \phi_{\min} \geq 0.3 \\ \phi_{\max} \leq 0.65 \end{cases} \quad (5.2)$$

Each distribution of ϕ , provided that the $\dot{\gamma}(z)$ distribution is obtained through experimental data, yields an inertial number distribution along the flow depth. Interestingly enough, by comparing the calculations, obtained by using different volume fraction distributions, we found small differences among I distributions, except for the points very near the free surface. The reason of such a behaviour is due to the fact that P depends on the depth-averaged value of ϕ , which acts as a low-pass filter on the effective volume fraction distribution. Moreover, I only depends on the square-root of P : hence, the sensitivity of I on ϕ distribution is found to be very small within the investigated range [0.3, 0.65].

For these reasons, in order to calculate the inertial number distributions, presented here, we have assumed the simple uniform distribution, $\phi(z) = 0.5$. The diagrams of the inertial number, calculated from the velocity profiles of smooth bed runs, are reported in Fig. 5.1. As well, the inertial number distributions, calculated from the velocity profiles of rough bed runs, are reported in Fig. 5.2.

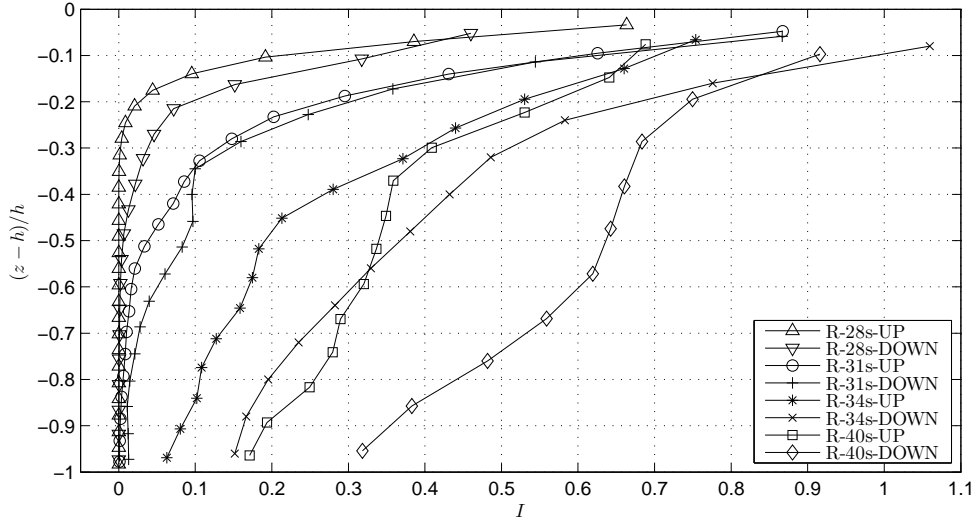


Figure 5.1: Distributions of the inertial number, I , along the flow depth (smooth bed runs).

Firstly, by observing Fig. 5.1, one can immediately notice that I increases with z and its derivative rapidly increases, when approaching the free surface, due to the decrease of the confining pressure, P , near the free surface. Such a behaviour gives a characteristic convex shape to almost all inertial number distributions. Moreover, in experiments with inclination angles 28° and 31° (i.e. runs R-28s and R-31s), the inertial number is almost null near the bottom surface: this is due to the no-slip bottom boundary condition. Instead, in runs R-34s and R-40s, I exhibits a non null value near the bottom surface. In this case, the variations of I along the flow depth are more limited.

A similar behaviour can be observed in the inertial number distributions, related to the rough bed runs (Fig. 5.2). In all these experiments, I is practically null at the bottom surface, because of no-slip bottom boundary condition. It is interesting to note that, differently from the others distributions, in R-40r-DOWN the inertial number distribution exhibits a convex shape near the bottom surface but it is almost constant in the upper part. This is probably due to the slight decrease of $\dot{\gamma}$, observed in the upper part of the velocity profile (cf. Fig. 3.12 in Chap. 3).

5.1.2 Critical inertial number

Now that we have estimated the inertial number distributions for every experimental profiles, an interesting question arises. Is there a *critical* value of the inertial number, common to the whole dataset, corresponding to the position of the interface between quasi-static and dense-collisional

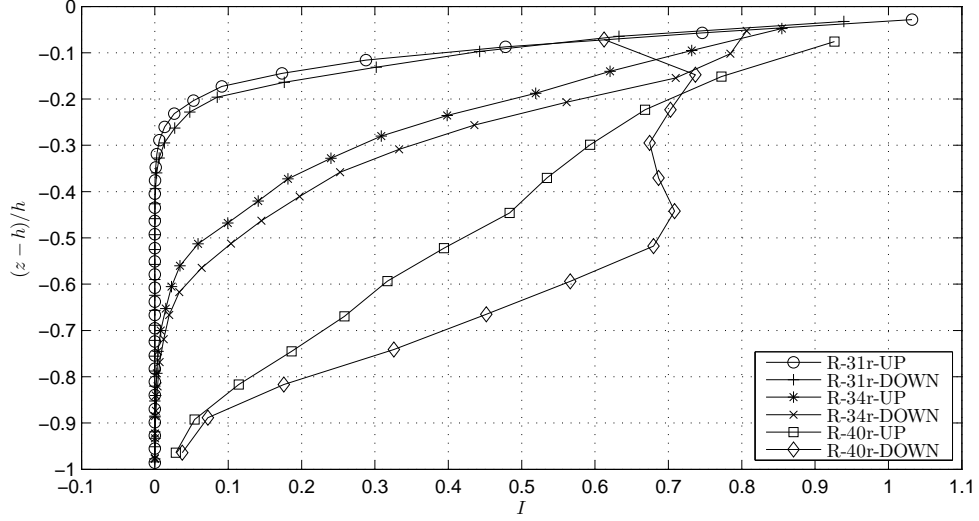


Figure 5.2: Distributions of the inertial number, I , along the flow depth (rough bed runs).

zones?

In order to answer this question, it seems to be useful to address the problem from the slightly different viewpoint of the two-layer mathematical model.

In steady-state condition, the position of the interface between the two layers is unchanging over time in any cross section. It means that the shear stresses at the interface, $t_{1i,xz}$ and $t_{2i,xz}$ (cf. 4.51 and 4.50 in Chap. 4), defined in the mathematical model, have to be equal,

$$t_{1i,xz} = t_{2i,xz} \quad \Rightarrow \quad \left[g_z \rho_1 h_1 k \tan \varphi_{int} + r \rho_1 (|\bar{v}_{1,x} - \bar{v}_{2,x}|)^\beta \right] \text{sgn} (\bar{v}_{1,x} - \bar{v}_{2,x}) = g_z \rho_1 h_1 \tan \varphi_{int} \text{sgn} (\bar{v}_{1,x} - \bar{v}_{2,x}). \quad (5.3)$$

After some simple algebraic manipulation, Eq. (5.3) can be recast

$$\Theta = \frac{r}{(1-k)g \tan \varphi_{int}} = \frac{\cos \alpha h_1}{(\Delta u)^\beta}, \quad (5.4)$$

where $\Delta u = \bar{v}_{1,x} - \bar{v}_{2,x}$. Θ is a quantity, that only depends on the rheological parameters r , k and φ_{int} . Thus, it is expected to be constant in the whole experimental dataset, as the same granular material has been used in all experiments. Please, note that the dimension of Θ is $[L^{1-\beta} T^\beta]$. Equation (5.3) can be regarded as a relation between the parameters r and k and, hence, it reduces to 1 the degrees of freedom for choosing r and k . Moreover, it is noteworthy that Θ can be calculated by using the formula in the left-hand side of Eq. (5.4), which depends on the upper layer flow depth h_1 , on the depth-averaged velocity difference Δu and on the channel inclination α , provided that β has been previously chosen. Such a formula turns out to be very useful, because it allows to calculate Θ directly from steady-state experimental data.

Now, let us explain in detail, how to perform this calculation. Analogously to what done for the calculations of I distributions, also in this case we refer to the velocity profiles, depth-

averaged along y direction. Moreover, in the present investigation, we chose to cut the lower zone of the velocity profiles, which is practically at rest. In order to do so, a threshold velocity, equal to 0.001 m/s (which is carefully chosen one order smaller than the G -PIV accuracy) has been set to separate the “motionless” zone from the flowing zone. Such a treatment is needed for the subsequent comparisons between experimental data and numerical simulations, since in the proposed mathematical model (cf. (4.46)) an uniform velocity distribution in the lower layer has been assumed. However, it should be kept in mind that the separation between the motionless and quasi-static zone is only conceptual. In fact, the lower exponential tail of the velocity profile is found to be larger than that observed through high speed measurements, due to *creep* motion phenomena (Komatsu et al., 2001).

The procedure for the calculation of Θ is composed of the following steps:

1. a value for β is previously chosen, so as to specify the expression for calculating $t_{1i,xz}$ (cf. 4.51 in Chap. 4);
2. an arbitrary position of the interface is set in the experimental velocity profile;
3. the interface divides the velocity profile into two layers, whose flow depths (h_1 and h_2) and depth-averaged velocities ($\overline{v_{1,x}}$, $\overline{v_{2,x}}$) are calculated by means of numerical integration of the experimental velocity profile;
4. once $\overline{v_{1,x}}$, $\overline{v_{2,x}}$ and h_1 are known, the value of Θ , corresponding to the chosen interface position, can be straightforwardly calculated by means of Eq. (5.4).
5. the procedure is repeated by varying the interface position from the bottom to the free surface.

In order to increase the number of the investigated interface positions (Point No. 1) and the precision of the numerical integrations (Point No. 3), the experimental data of velocity profiles have been numerically interpolated by using a piecewise cubic *Hermite* polynomial. These computations have been carried out for all experimental velocity profiles and for different values of β . Typically, in the main rheological approaches, available in Literature, β is assumed to be comprised between 1 and 2 (e.g. Bagnold, 1954; Voellmy, 1955; Nishimura, 1991). In order to determine the optimal value of β in the framework of our numerical model, we performed these computations by varying β in the set $\beta \in [0.5, 1, 2]$.

For each experimental velocity profile, we obtain the function $\Theta(z_{interface})$, which is monotonically decreasing with the distance of the interface from the bottom surface. By way of example, in Fig. 5.3 the diagrams of Θ , obtained by using $\beta = 1$, are reported. It is important to highlight that, although Θ is a quantity introduced in the context of the particular two-layer mathematical model, such calculations have been entirely obtained on the basis of experimental data.

Now, it is interesting to relate the information obtained from the inertial number distributions and that obtained from the Θ profiles. Thanks to the fact that both Θ and I are bijective functions of $z_{interface}$, for each experiment, it is possible to calculate the function $\Theta(I)$. We performed such calculations for all experimental data by varying β . Then, we plotted all the diagrams, $\Theta - I$, related to a given value of β , in the same figure.

The diagrams, $\Theta - I$, obtained by using $\beta = 0.5, 1, 2$, are reported, respectively in Figs. 5.4, 5.5 and 5.6. Black symbols and red symbols correspond to the experiments on smooth and rough

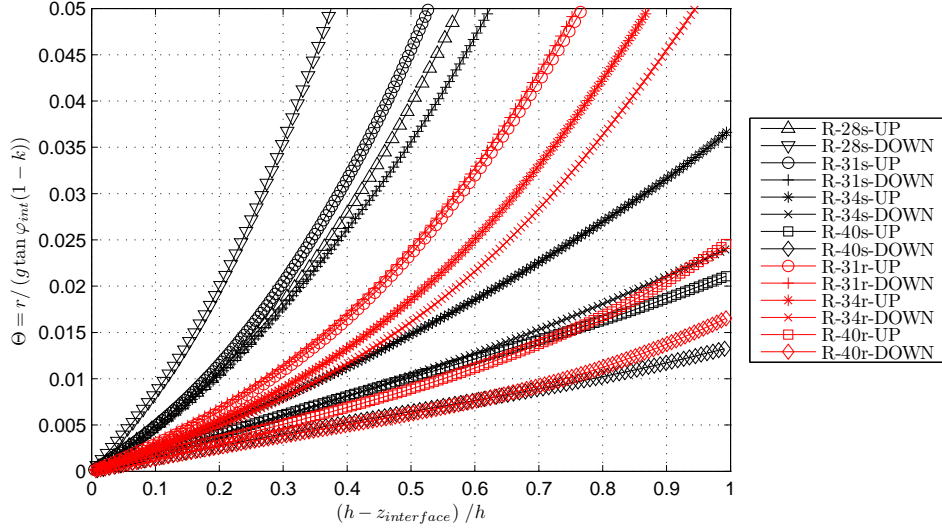


Figure 5.3: Diagrams of $\Theta(z_{interface})$, obtained by using $\beta = 1$. Black symbols and red symbols correspond to the experiments on smooth and rough bed, respectively.

bed, respectively. Firstly, it should be noted that $\Theta(I)$ are monotonically decreasing functions. This is due to the fact that, as Θ increases, the interface position gets near to the basal surface (i.e. $z_{interface}$ decreases), and, thus, also I decreases (cf. Figs. 5.1-5.2). Moreover, please note that, above a certain threshold of Θ , a non-null constant value of I is observed in some $\Theta-I$ diagrams, e.g. R-34s-UP, R-34s-DOWN, R-40s-UP, R-40s-DOWN. This apparently strange behaviour depends on the fact that there is a threshold of Θ , above which the interface position always corresponds to the bottom surface. Because the velocity profiles, R-34s-UP, R-34s-DOWN, R-40s-UP, R-40s-DOWN, exhibit a slip-boundary condition, a non-null value of I is observed at the basal surface. Conversely, large values of I correspond to small values of Θ , because, in that case, the interface gets near to the free surface.

Moreover, as it is evident from the Figures, at any given value of Θ , there is a certain scattering of the values of inertial number, I , calculated from different experimental velocity profiles. The mean function, $\hat{I}(\Theta)$, also shown in Figs. 5.4-5.5- 5.6 (green dashed line), is defined as follows

$$\hat{I}(\Theta) = \sum_{i=1}^N I_i(\Theta). \quad (5.5)$$

where the summation is over all the N values of the inertial numbers, with N being equal to the number of velocity profiles investigated, i.e. 14. If a unique critical inertial number, $I_{critical}$, corresponding to the interface position, exists, the $\Theta - I$ plots should exhibit a small deviation around a particular value of I .

By comparing Figs. 5.4-5.5- 5.6, one can easily notice that the overall dispersions, obtained by using $\beta = 2$, are far bigger than those obtained by assuming $\beta = 0.5$ or $\beta = 1$.

In order to find such a critical value in a more analytical way, the root mean square deviations

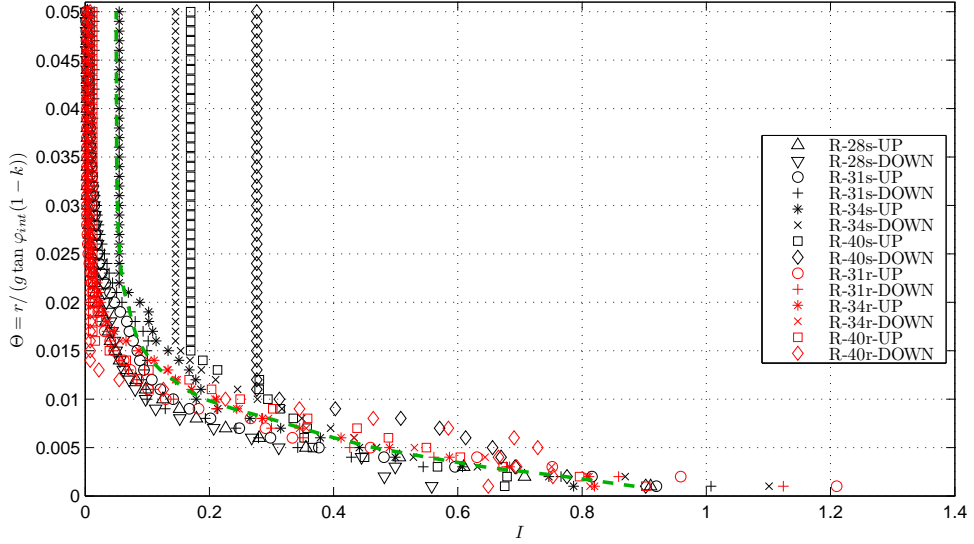


Figure 5.4: Diagrams of $\Theta(I)$, obtained by assuming $\beta = 0.5$ in Eq. (4.51). Black symbols and red symbols correspond to the experiments on smooth and rough bed, respectively. Green dashed line represent the mean curve $\hat{I}(\Theta)$.

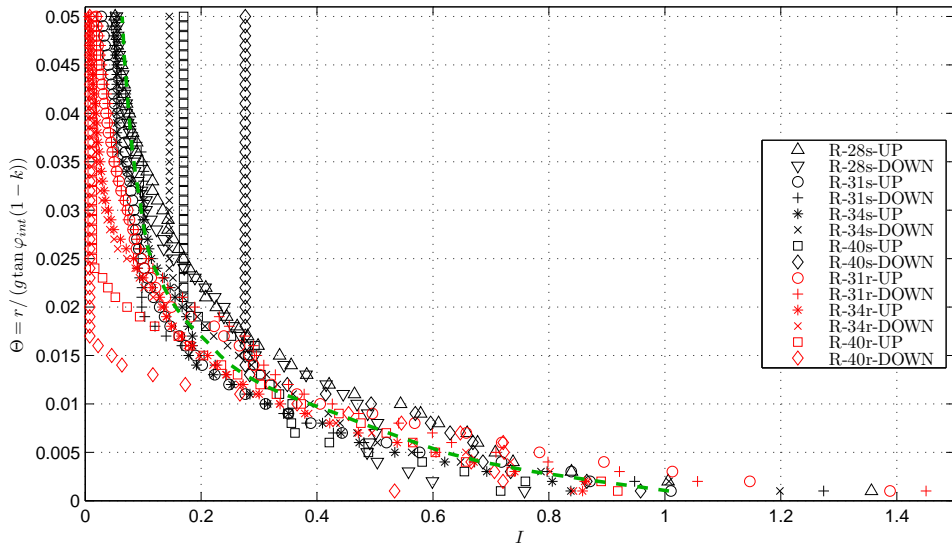
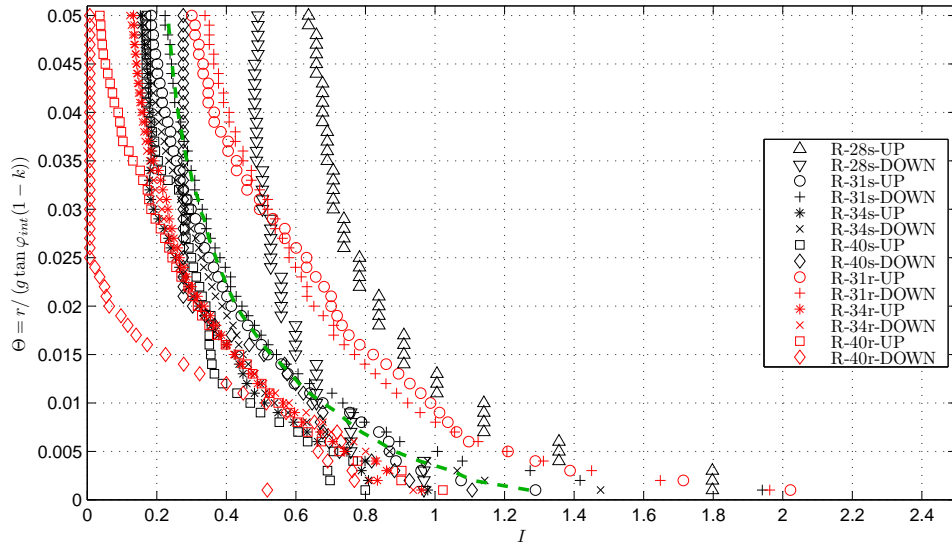


Figure 5.5: Diagrams of $\Theta(I)$, obtained by assuming $\beta = 1.0$.

Figure 5.6: Diagrams of $\Theta(I)$, obtained by assuming $\beta = 2.0$.

(*RMSD*) of I from \hat{I} have been calculated, by means of the following formula

$$RMSD(\Theta) = \sqrt{\frac{1}{N-1} \sum_{i=1}^N (I_i(\Theta) - \hat{I}(\Theta))^2}. \quad (5.6)$$

The diagrams of $RMSD(\Theta)$, in cases of $\beta = 0.5, 1, 2$, are reported respectively in Figs. 5.7, 5.8 and 5.9.

By comparing Figs. 5.7-5.8-5.9, it is found that the minimum dispersions are obtained by assuming $\beta = 1$, for which, the absolute minimum of the *RMSD* function corresponds to $\Theta_{critical} = 0.011$ s. Now, thanks to the fact that $\hat{I}(\Theta)$ is a bijective function, it is possible to calculate also the corresponding critical inertial number, that is approximately equal to $I_{critical} = 0.33$.

This value seems to be very reasonable and congruent with other studies, available in Literature. Savage and Hutter (1989), through an experimental analysis, inferred that a threshold of the *Savage number*, to roughly classify friction-dominated and collision-dominated granular avalanches, could be chosen approximately equal to 0.1. This value is also reported by Iverson (1997) and Iverson and Vallance (2001). Since the inertial number is nothing else than the square root of the *Savage number*, it is easy to notice that the critical value found in the present analysis, $I_{critical} = 0.33$, is perfectly congruent with $N_{Savage} = 0.1$.

In order to check the sensitivity of these results on the volume fraction distribution, used to get inertial number profiles, we repeated the same calculations with several volume fraction distributions, fulfilling Cond. (5.2). It has been found that the smallest overall dispersion of $\Theta - I$ functions is still obtained by using $\beta = 1$. Moreover, the minimum value of the *RMSD* function is exactly the same of that obtained with $\phi(z) = 0.5$, because the volume fraction distribution does not modify the Θ function. The critical inertial numbers, corresponding to $\Theta_{critical}$, are quite near

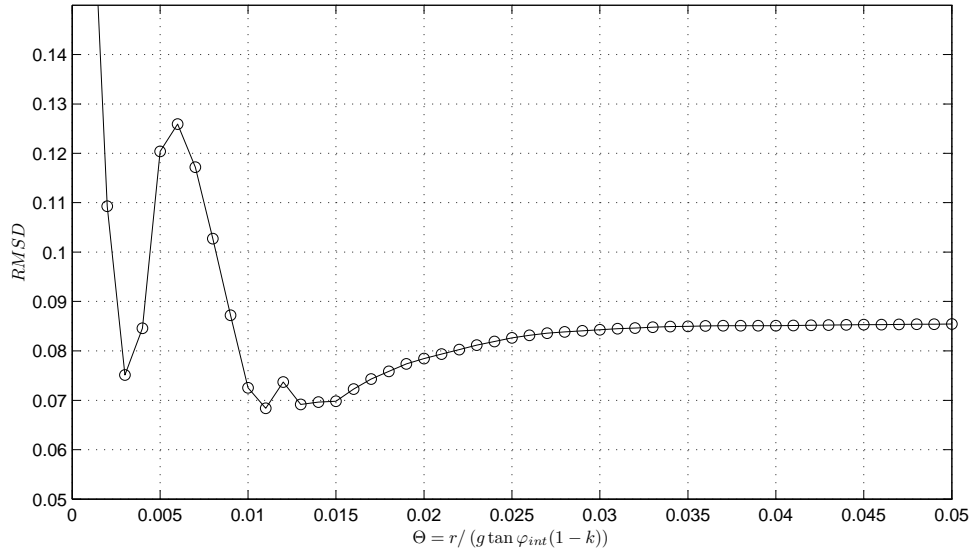


Figure 5.7: Root mean square deviation, $RMSD(\Theta)$, obtained by assuming $\beta = 0.5$.

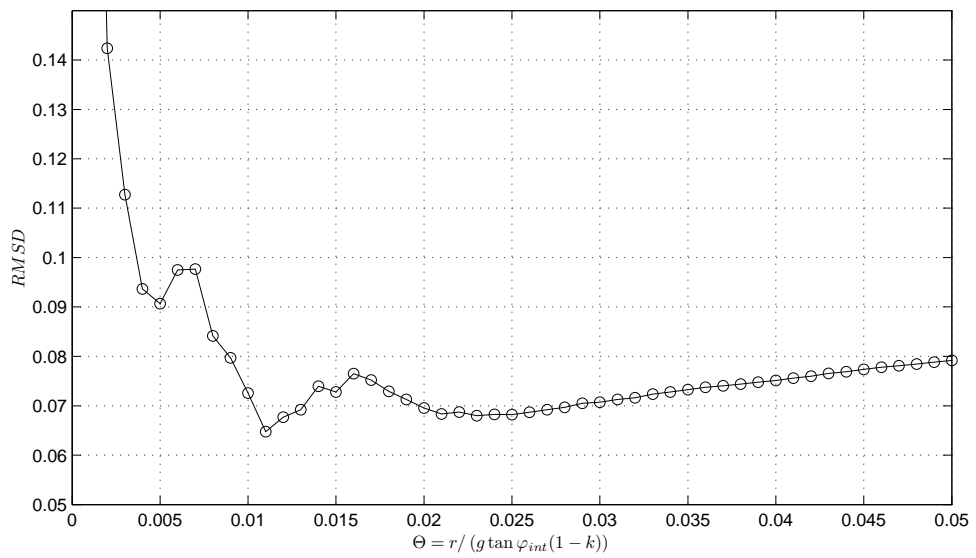


Figure 5.8: Root mean square deviation, $RMSD(\Theta)$, obtained by assuming $\beta = 1.0$.

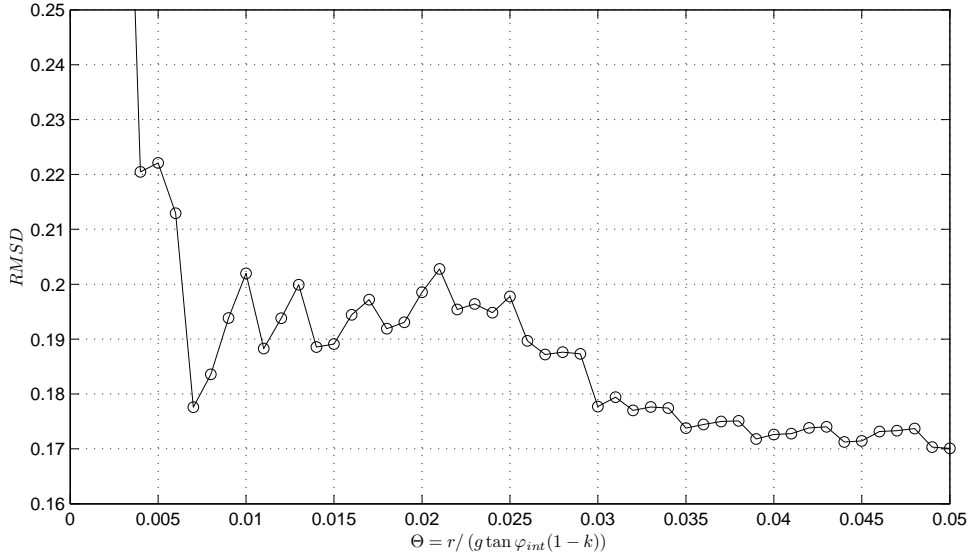


Figure 5.9: Root mean square deviation, $RMSD(\Theta)$, obtained by assuming $\beta = 2.0$.

each other and always within the range $[0.3, 0.4]$. The results of these computations are briefly reported in Table 5.1.

Therefore, the following criterion to identify the interface positions in experimental velocity profiles has been chosen: $z_{interface}$ is where $\Theta_{critical} = 0.011$ s. Namely, for any given velocity profile, we identify $z_{interface}$, that corresponds to $\Theta_{critical}$ (cf. Fig. 5.3). Please, note that it is equally possible to employ the condition on the inertial number, $I_{critical} = 0.33$, as criterion to determine $z_{interface}$. We found that, this alternative calculation yields practically identical results, as long as $\phi(z) = 0.5$ is chosen. However, we prefer to use the criterion on Θ , instead of I , because in this fashion we get rid of the aforementioned arbitrary assumptions on volume fraction distributions.

ϕ_{min}	ϕ_{max}	$\Theta_{critical}[s]$	$I_{critical}$	$min(RMSD)$
0.50	0.50	0.011	0.34	0.065
0.60	0.60	0.011	0.30	0.07
0.40	0.40	0.011	0.37	0.06
0.40	0.60	0.011	0.36	0.07
0.40	0.50	0.011	0.37	0.072
0.30	0.65	0.011	0.40	0.081

Table 5.1: Root mean square deviations, obtained by varying the volume fraction distributions along the flow depths.

It is worth to briefly summarize the interesting results, that emerge from the present investigation.

Firstly, it is interesting that the best correspondence between the proposed two-layer theory and experimental data has been found by assuming $\beta = 1$ in Eq. (4.51), instead of the most obvious quadratic dependence (i.e. $\beta = 2$). Although, from the Bagnold scaling (Bagnold, 1954) and dimensional analysis, rate-dependent stresses in collisional regime are expected to depend on the square of the shear rate, it should be reminded that the shear stresses at the interface are defined as functions of the depth-averaged flow velocities and, so, do not depend directly on the local shear rate (cf. Eq. 4.51). The depth-averaged flow velocities in each layer are obviously influenced also by the side walls resistances. Such resistances have a crucial role in the flow dynamics of channelised granular flows and their complex interplay with basal resistances also influences the steady state conditions. Further experimental investigation would be needed to better understand this topic. In particular, it would be interesting to verify whether similar results can be obtained in different experimental geometries (i.e. by varying the cross-section width) and with different granular materials.

Secondly, it is noteworthy that the critical inertial number, found to be roughly equal to 0.33, is congruent with other experimental works and, in particular, matches quite perfectly with the threshold value of the Savage number, found to be approximatively equal to 0.1 (Savage and Hutter, 1989), to distinguish the friction-dominated regime from the “fluidized” collisional-frictional one. Such a correspondence seems not to be accidental and it is little sensitive to the assumptions about the volume fraction distribution, made in order to calculate the inertial number.

5.1.3 Interface positions in experimental velocity profiles

In this section, the interface positions, obtained by using the aforementioned criterion, are reported.

In Table 5.2, flow depths and depth-averaged velocities, referred to the two layers, together with the total flow depth and the overall depth-averaged velocity are reported. In Figs. 5.10-5.11-5.12-5.13 the velocity profiles (depth-averaged along y direction) related to the smooth bed runs are reported, together with the interface position (dashed line). As well, the interface positions, related to the rough bed runs, are shown in Figs. 5.14-5.15-5.16. The lower zone of all velocity profiles, where velocity is smaller than 0.001 m/s has been cut off.

As one can see from the Figures, the predicted interface positions, in cases of no-slip bed condition (i.e. R-28s, R-31s, R-31-r, R-34r, R-40r), are in very good agreement with the initial conjecture that the dense-collisional zone roughly corresponds to the upper linear profile. Yet, it should be noted that, in cases of slip bed condition (i.e. R-34s and R-40s), the proposed criterion seems to be less reliable, as the predicted interface position appears too far from the bottom surface (e.g. R-40s-UP).

The truncated velocity profiles, related to runs R-31r-UP and R-31r-DOWN, are practically overlapping, as one can see from Figure 5.14. It means that, in the experiment R-31r, a fully developed steady state (i.e. uniform flow) is reached. For this reason, this experiment will be used to calculate the dynamic friction angle, corresponding to the interface.

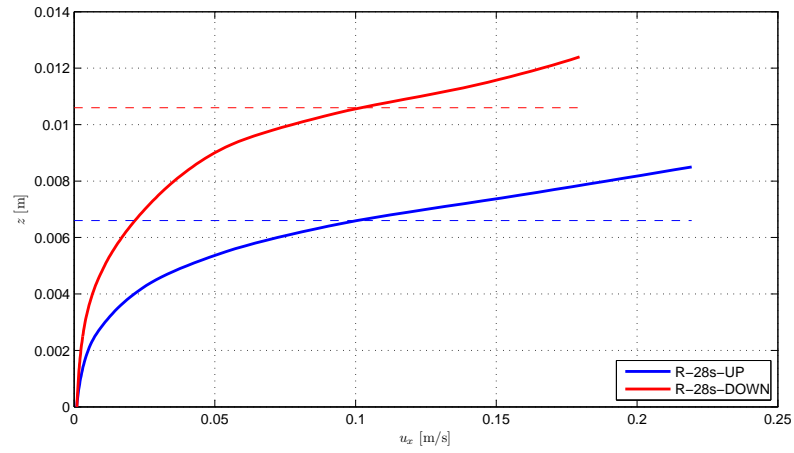


Figure 5.10: Velocity profiles R-28s-UP (blue line) and R-28s-DOWN (red line) and related interfaces (dashed lines).

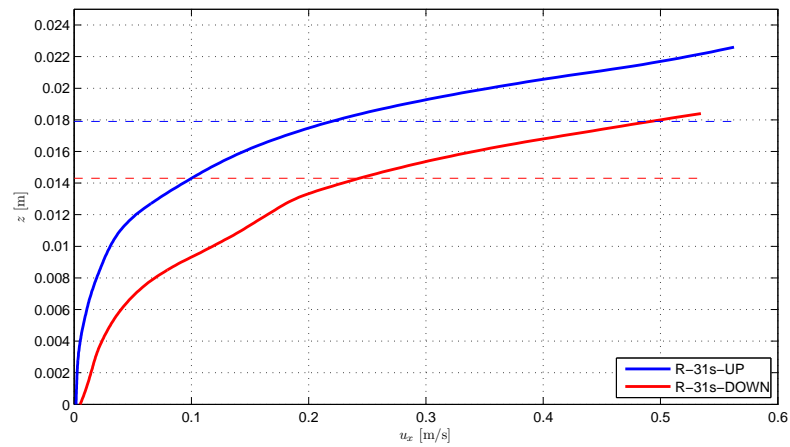


Figure 5.11: Velocity profiles R-31s-UP (blue line) and R-31s-DOWN (red line) together with interfaces between layers (dashed lines).

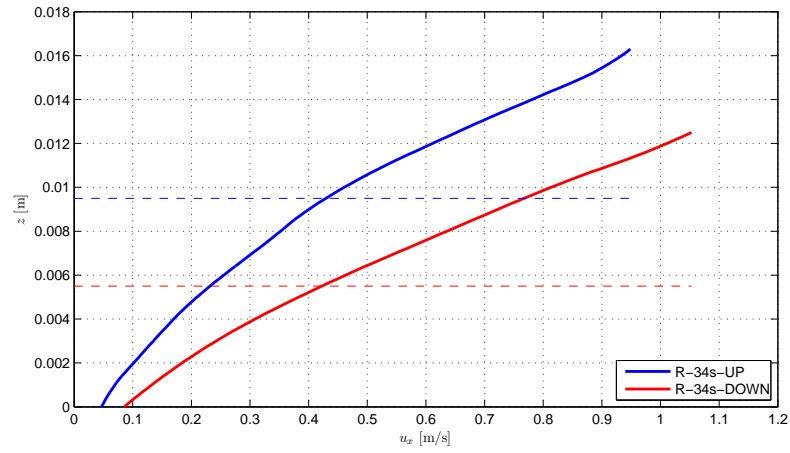


Figure 5.12: Velocity profiles R-34s-UP (blue line) and R-34s-DOWN (red line) and related interfaces (dashed lines).

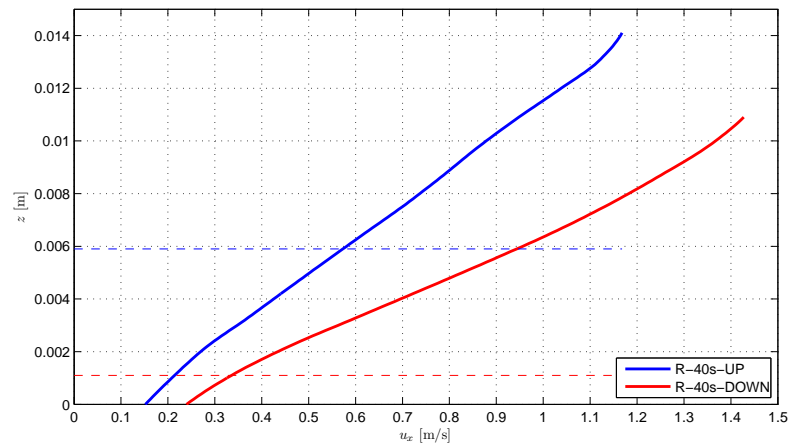


Figure 5.13: Velocity profiles R-40s-UP (blue line) and R-40s-DOWN (red line) and related interfaces (dashed lines).

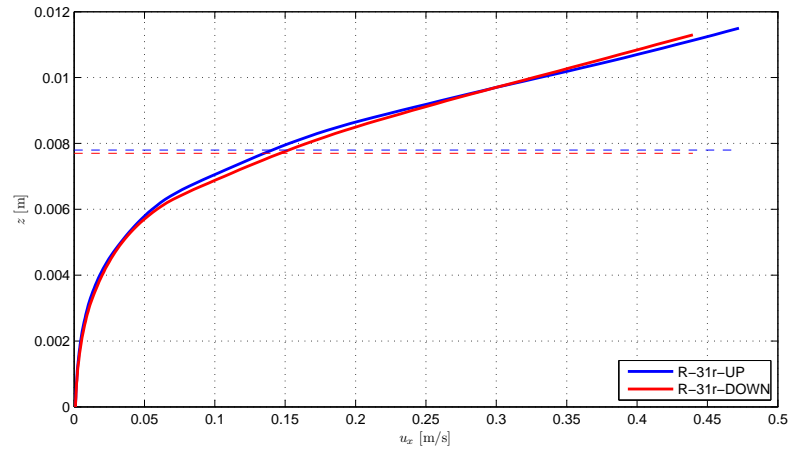


Figure 5.14: Velocity profiles R-31r-UP (blue line) and R-31r-DOWN (red line) and related interfaces (dashed lines).

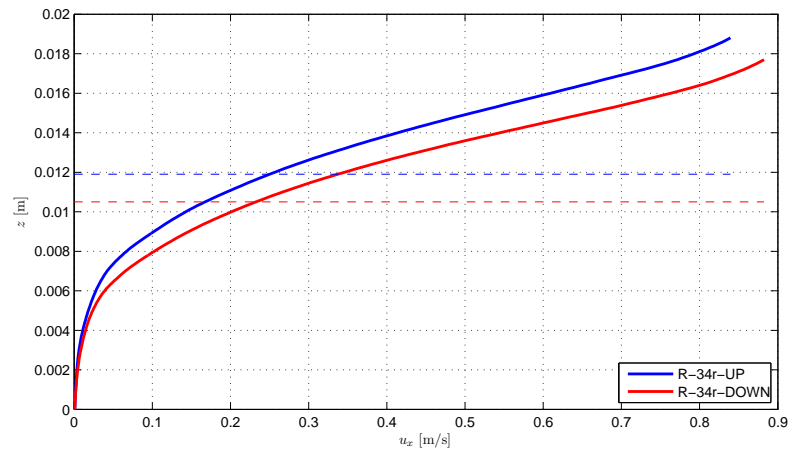


Figure 5.15: Velocity profiles R-34r-UP (blue line) and R-34r-DOWN (red line) and related interfaces (dashed lines).

ID	h_1 [m]	h_2 [m]	$\bar{u}_{1,x}$ [m/s]	$\bar{u}_{2,x}$ [m/s]	h [m]	\bar{u}_x [m/s]
R-28s-UP	0.0017	0.0068	0.167	0.028	0.0085	0.056
R-28s-DOWN	0.0015	0.0109	0.151	0.026	0.0124	0.041
R-31s-UP	0.0043	0.0183	0.396	0.144	0.0226	0.192
R-31s-DOWN	0.0038	0.0146	0.384	0.084	0.0184	0.146
R-34s-UP	0.0063	0.0100	0.709	0.225	0.0163	0.412
R-34s-DOWN	0.0065	0.0060	0.752	0.254	0.0125	0.513
R-40s-UP	0.0076	0.0065	0.906	0.372	0.0141	0.660
R-40s-DOWN	0.0093	0.0016	0.957	0.309	0.0109	0.862
R-31r-UP	0.0034	0.0081	0.312	0.042	0.0115	0.122
R-31r-DOWN	0.0033	0.0080	0.298	0.040	0.0113	0.115
R-34r-UP	0.0065	0.0123	0.564	0.067	0.0188	0.239
R-34r-DOWN	0.0068	0.0109	0.579	0.066	0.0177	0.263
R-40r-UP	0.0083	0.0057	0.670	0.091	0.0140	0.435
R-40r-DOWN	0.0111	0.0030	0.819	0.043	0.0141	0.654

Table 5.2: Experimental flow depths and depth-averaged velocities.

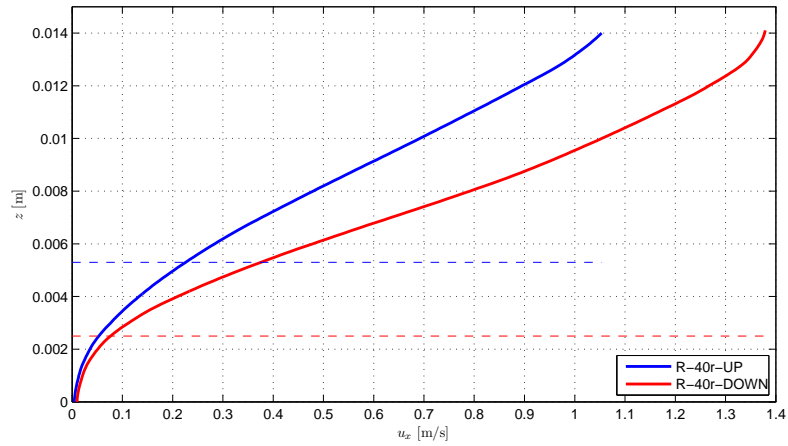


Figure 5.16: Velocity profiles R-40r-UP (blue line) and R-40r-DOWN (red line) and related interfaces (dashed lines).

5.2 Friction angle at the interface

In this section we are going to show how the angles of friction (δ and φ_{int}), employed in the two-layer mathematical model, have been chosen. The procedure we are going to report makes use of the experimental data of R-31r, found to be in uniform condition.

On the basis of dimensional arguments, da Cruz et al. (2005) showed that the dynamics of dry rigid particles is controlled by the inertial number. In plane shearing, such a dependence can be written as

$$\tau = \mu(I)P = \tan \varphi(I)P, \quad (5.7)$$

where P is the confining pressure, τ the shear stress and φ the dynamic angle of friction (Midi, 2004; Jop et al., 2006). It means that the dynamic angle of friction is expected to vary with the local inertial number and, thus, with the distance from the free surface.

It is possible to obtain the function $\varphi(I(z))$ by means of an experimental uniform velocity profile, by following the inverse approach to that employed by Jop et al. (2005) in order to obtain the velocity profile from a known rheology. In uniform conditions, the flow depth and the flow velocity distribution are unchanging over time and over space. With reference to a channelised free surface flow and assuming that x reference axis is parallel to free surface, the x -component of the force balance on a control volume, of length dx and thickness z , delimited by the free surface, a lower surface parallel to it and the side walls, can be written as follows

$$dx W \rho g \sin \vartheta - 2 dx \int_0^z K_y \tan \delta_{side} \rho g z' \cos \vartheta dz' - dx W \tan(\varphi(I(z))) \rho z \cos \vartheta = 0 \quad (5.8)$$

where ϑ is the inclination angle of the free surface, W is the cross section width, δ_{side} is the friction angle at the side walls, ρ is the bulk density and is equal to $\rho_g \phi$, and K_y represents the earth-pressure coefficient to calculate σ_y as function of σ_z . The first term in (5.8) is due to the gravity; the second one represents the resistances at the side walls; the third one represents the resistance exerted along the lower surface, parallel to the free surface. It should be noted that typically ϑ is slightly different from the channel inclination angle. In the case of experiment R-31r, it is found to be equal to 32.6° .

After some manipulations, Eq. (5.8) is recast as

$$\tan \vartheta - K_y \tan \delta_{side} \frac{z}{W} - \tan \varphi(I(z)) = 0. \quad (5.9)$$

The side wall friction δ_{side} between Ottawa sand and Plexiglas has been measured by Tai and Lin (2008) and is found to be approximatively equal to $22 - 23^\circ$. As well, the angle of friction at rest is reported to be $34.1 \pm 1.4^\circ$. Sarno et al. (2011) proposed to use the simple Jaky formula, which is an estimate of the coefficient of earth pressure at rest, to calculate K_y .

From the truncated velocity profile of experiment R-31r (cf. Fig. 5.14), the total flow depth is known, $h = 0.0114$ m. Therefore, it is possible to get a reliable estimate of the dynamic angle of friction at the initiation of motion (i.e. $I = 0+$), by solving Eq. (5.9) with $z = h$. The value obtained is approximately equal to 30.5° . Please note that this value has to be chosen as the basal friction angle, δ , in case of no-slip bottom boundary condition. Such a value is congruently smaller than the angle of repose.

The dynamic friction angle at the interface φ_{int} , can be, as well, calculated by means of Eq. (5.9). More precisely, it is the solution of Eq. (5.9), corresponding to $z = z_{interface}$, which is found

to be equal to 0.033 m in experiment R-31r (cf. Table 5.2). Such a value is found to be equal to $\varphi = 31.9^\circ$. This dynamical friction angle only depends on the local inertial number, which is supposed to be constant at the interface. Thus, it is assumed to be constant among the whole experimental dataset.

5.3 Comparisons

In this section, some comparisons between experimental data and numerical results, obtained from the two-layer model presented in Chapter 4, are reported.

The purpose of these tests is to test the rheological assumptions made in the mathematical model, by comparing the numerical results with experimental steady states. Such comparisons should not be regarded as a validation of the two-layer approach itself. In fact, the two-layer mathematical approach represents a family of models, since the shear stresses formulae (at the bottom and at interface) and the other assumptions (e.g. velocity distributions and earth-pressure coefficients) can be specified in different ways.

Moreover, since we are mainly interested in employing the two-layer approach to better describe the flow dynamics in case of no-slip bottom boundary conditions, experiments R-34s and R-40s have not been considered in these comparisons.

Simulations parameters

The extent of the computational domain, L , is chosen to be equal to the distance of the two experimental cross sections ($x = 20$ cm and $x = 35$ cm), i.e. $L = 0.15$ m. The size of the mesh is set equal to $\Delta x = 0.005$ m. The time step is calculated at each time-advancing, by imposing the condition $CFL = 0.8$. The numerical simulations have been performed over a time domain $T = 15$ s, sufficient to obtain steady state conditions at the final time points for all the investigated cases. In order to verify the occurrence of the steady state, we checked that the maximum relative errors between the solutions at $T = 15$ s and those at $T = 7$ s were less than 1%.

The basal friction angle δ is chosen to be equal to 30.5° , while $\varphi = 31.9^\circ$. It should be remarked that these parameters have been calibrated only on experiment R-31r, as reported in Section 5.2. No calibration has been performed on the other experimental data.

The friction angle at the side walls is $\delta_{side} = 23^\circ$, according to the measurements reported in (Tai and Lin, 2008). The earth-pressure coefficient Ky has been calculated by means of the Jaky formula (Jaky, 1944), as function of the basal friction angle, and it is equal to 0.49.

The volume fractions of the two layers are chosen to be $\phi_1 = 0.4$ and $\phi_2 = 0.6$, similarly to what done in numerical simulations, reported in Chapter 4. Differently from the previous numerical simulations, the shear resistance at the interface as limit from above, i.e. Eq. (4.51), is chosen to have a linear dependence on the shear velocity, namely $\beta = 1$. This choice is motivated by the experimental results, reported in Section 5.1.

The parameters r and k are chosen equal to 0.013 and 0.8 respectively, so as to fulfil the condition $\Theta = \Theta_{critical} = 0.011$ s. It has been found that, although the choice of r and k dramatically influences the flow dynamics in transient state, as widely shown in Chapter 4, their values have a very small influence on the final steady state, provided that the equilibrium condition $\Theta = \Theta_{critical}$

is fulfilled. Moreover, a proper calibration of these parameters would require transient state experimental data and it is beyond the scope of the present dissertation.

The earth-pressure coefficients K_1 and K_2 , to define the momentum fluxes of System (4.46), have been calculated by means of the Savage-Hutter formula (cf. Eq. (2.3) in Chapter 2), with $\delta = \varphi = 30.5^\circ$ and are $K_1 = K_2 = 1.69$.

The friction angles and other relevant parameters, used in the present calculations, are synthetically reported in Table 5.3.

δ	φ_{int}	δ_{side}	r	k
30.5°	31.9°	23°	0.013	0.8

Table 5.3: Parameters used in Test No. 1.

The boundary conditions are imposed in accordance with the experimental data. Firstly, by calculating the number of positive and negative eigenvalues for each boundary through using experimental data reported in Table 5.2, it is known how many boundary conditions have to be imposed in the mathematical problem.

As regards the experiments R-28s, R-31s, R-31r and R-34r, three boundary conditions have to be imposed at the left-hand boundary and one at the right-hand boundary. Therefore, we chose to impose the flow rates of both layers at the left-hand side boundary and the flow depth of the lower layer at the right-hand side boundary,

$$\begin{cases} q(1)|_{\text{left boundary}} = h_1|_{\text{left boundary}} = h_1|_{\text{exp,UP}} \\ q(2)|_{\text{left boundary}} = h_1 u_1|_{\text{left boundary}} = h_1 u_1|_{\text{exp,UP}} \\ q(4)|_{\text{left boundary}} = h_2 u_2|_{\text{left boundary}} = h_2 u_2|_{\text{exp,UP}} \\ q(3)|_{\text{right boundary}} = h_2|_{\text{right boundary}} = h_2|_{\text{exp,DOWN}} \end{cases} \quad (5.10)$$

where the subscripts “exp,UP” and “exp,DOWN” indicate the experimental values measured in the Upper and Lower cross sections, respectively.

As regards experiment R-40r, non-hyperbolic boundary conditions are found in this case: namely, the inner eigenvalues, numerically calculated by using the corresponding experimental boundary conditions, are not real. As stated in Chapter 4, the proposed regularization model to keep the hyperbolicity cannot work in case of ill-posed boundary conditions. Therefore, comparisons with R-40r could not be performed.

The initial conditions of the mathematical problem have been chosen as follows

$$\begin{cases} q(1)|_{t=0} = h_1(x, 0) = h_1|_{\text{exp,UP}} + 0.5 \sin\left(\pi \frac{x}{L}\right) h_1|_{\text{exp,UP}} \\ q(3)|_{t=0} = h_2(x, 0) = h_2|_{\text{exp,DOWN}} + 0.3 \sin\left(\pi \frac{x}{L}\right) h_2|_{\text{exp,DOWN}} \\ q(2)|_{t=0} = (h_1 u_1)(x, 0) = h_1 u_1|_{\text{exp,UP}} \\ q(4)|_{t=0} = (h_2 u_2)(x, 0) = h_2 u_2|_{\text{exp,UP}} \end{cases} \quad (5.11)$$

in which two sinusoidal perturbations have been added, in order to calculate initial flow depth over the whole spatial domain. Differently, the initial values of the flow rates $h_1 u_1$ and $h_2 u_2$ are

chosen to be constant and equal to the left-hand boundary conditions. It has been verified, through several numerical tests, that the steady state solution is practically independent from the chosen initial condition, though, obviously, the time to reach such a the steady state is influenced by it.

Four numerical simulations have been carried out. The ID Codes “SIM-31r”, “SIM-34r”, “SIM-28s” and “SIM-31s” indicate the numerical simulations, related to experiments R-31r, R-34r, R-28s and R-31s, respectively. Each simulation reproduces the flow evolution from the initial condition to the final steady state. In all the numerical simulations, the mass balance in the computational domain has been verified within an error of 0.5% of the initial mass. As regards to the hyperbolicity regularization, in SIM-31r, SIM-28s and SIM-31s, no extra resistance has been added at the interface, as the model was found to be hyperbolic in the whole computational domain. In SIM-34r, the hyperbolicity regularization, Eq. (4.72), sometimes was found to operate during the transient state. The maximum value of the normalized extra resistance, F_{extra}/ρ_1 is found to be equal to $0.002 \text{ m}^2/\text{s}^2$. Such a local correction to the source terms of System (4.46) is small with respect to the other terms in SIM-34r, as being, for instance, about one order smaller than the gravity force term, $h_1 g_x$.

With reference to simulation SIM-31r, the evolutions of flow depths and flow velocities are reported in Figs. 5.17 and 5.18, respectively.

Comparisons

The comparison, presented here, consists of calculating and examining the relative errors between the final steady state solutions, obtained from numerical computations, and experimental data, at the flow boundaries. Naturally, such a comparison makes sense only for the physical quantities, that have not been fixed by the boundary conditions. More precisely, at the left hand-side boundary, relative errors of h_2 and $\overline{u_{2,x}}$ are considered. Similarly, at the right-hand side boundary, relative errors of h_1 , $\overline{u_{1,x}}$ and $\overline{u_{2,x}}$ are taken into account. The average of the relative errors is also calculated in order to have a unique indicator of performance. Relative errors are reported in Table 5.4.

ID	$h_2 _{\text{UP}}$	$u_2 _{\text{UP}}$	$h_1 _{\text{DOWN}}$	$u_1 _{\text{DOWN}}$	$u_2 _{\text{DOWN}}$	Average
SIM-31r	0.021	0.021	0.025	0.064	0.028	0.032
SIM-34r	0.206	0.259	0.077	0.012	0.215	0.154
SIM-28s	0.236	0.191	0.411	0.256	0.604	0.340
SIM-31s	0.311	0.237	0.050	0.235	1.144	0.395

Table 5.4: Relative errors between numerical simulations and experimental data at the domain boundaries.

As one can easily see from Table 5.4, the agreement between the numerical results and experiment R-31r is excellent. The relative errors are always within 6% and their averaged value is about 3%. Although a good agreement was somehow expected, since the most sensitive parameters of the mathematical model (i.e. δ and φ) have been chosen on the basis of R-31r experimental data, this result is noteworthy. In fact, it strongly supports the reliability of the main features of the two-layer approach.

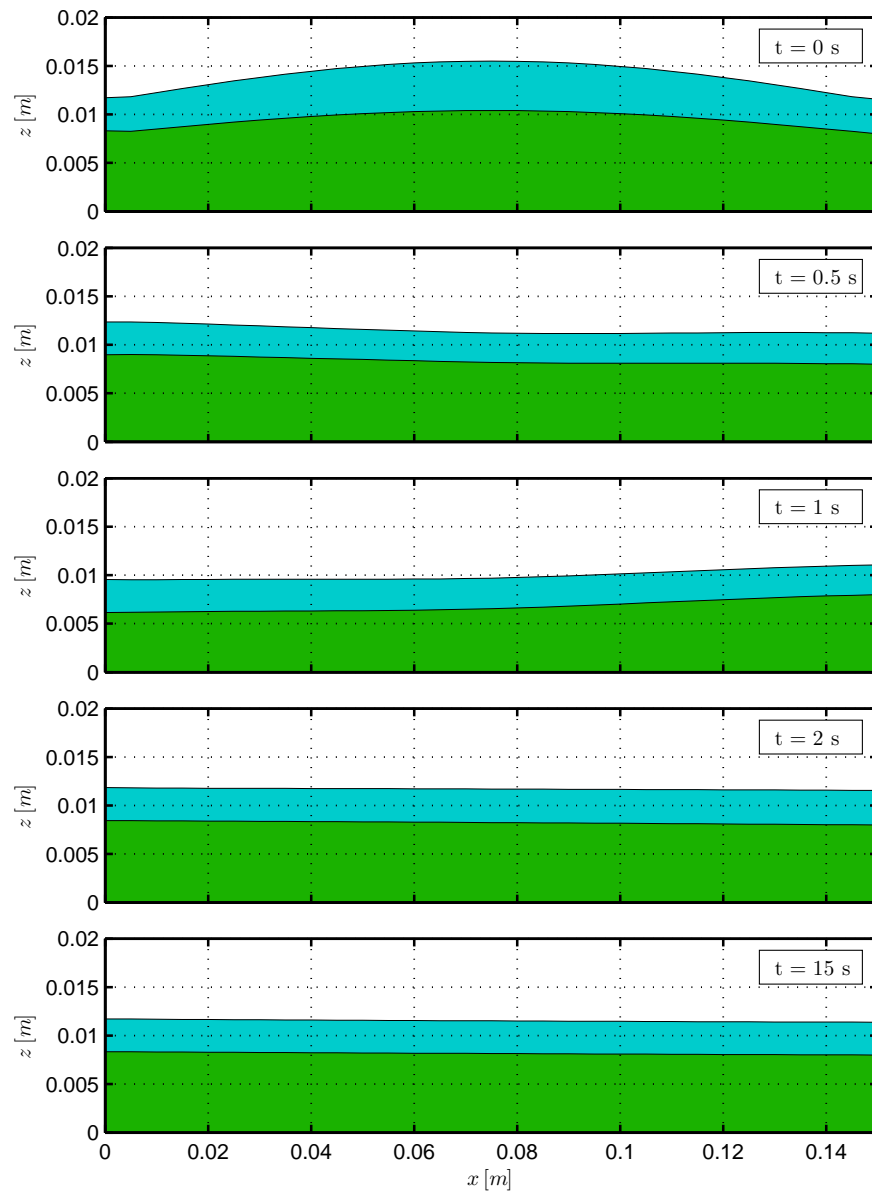


Figure 5.17: Evolution of flow depths (SIM-31r). The flow depths, related to the upper and lower layer, are represented in light-blue and green, respectively.

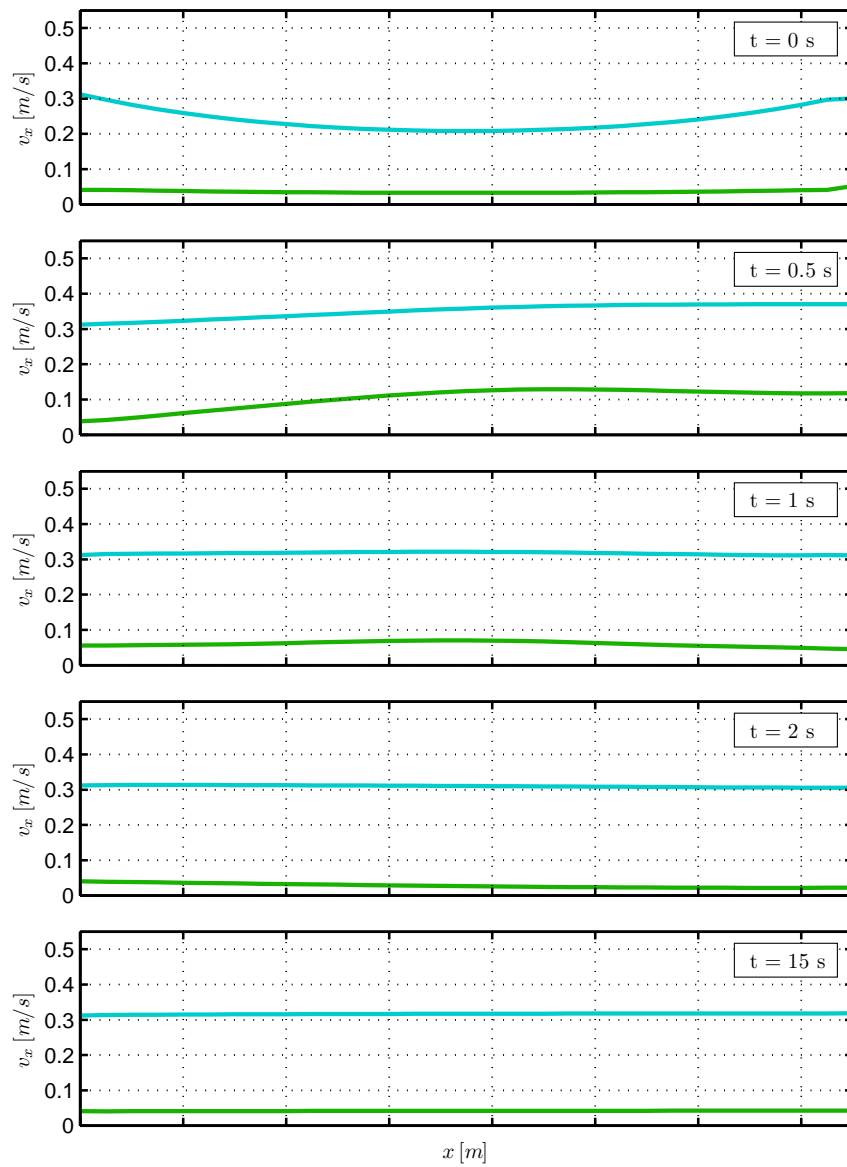


Figure 5.18: Evolution of flow velocities (SIM-31r). The depth-averaged flow velocities, related to the upper and lower layer, are represented by light-blue and green lines, respectively.

By examining the relative errors, related to the other comparisons (i.e. SIM-34r, SIM-28s, SIM-31s), the performance of agreement noticeably decreases. In particular, SIM-34r exhibits a good agreement, as regards the dynamics of the upper layer, with relative errors of 7.7% and 1.2% on $h_1|_{\text{DOWN}}$ and $u_1|_{\text{DOWN}}$, respectively. Nevertheless, at the left-hand boundary, the lower layer flow depth, $h_2|_{\text{UP}}$, is underestimated by about 20%, while the lower layer depth-averaged velocity, $u_2|_{\text{UP}}$, is overestimated by about 25%. As well, at the right-hand boundary, the lower layer depth-averaged velocity, $u_2|_{\text{DOWN}}$ is overestimated by about 20%. The average relative error is about 15%. Even though the overall agreement in SIM-34r is smaller than that observed in SIM-31r, it is still good. Moreover, these results should be regarded as very promising, if one considers that they have been obtained without using back-analysis to adjust the model parameters to experimental data. In SIM-28s and SIM-31s, bigger relative errors have been observed. The average errors in SIM-28s and SIM-31s are equal to 34% and 39.5%. Such relatively big values result from the fact that the mathematical model systematically fails to predict the lower layer velocity at the right-hand boundary, $u_2|_{\text{DOWN}}$, as one can see from Table 5.4. Such a phenomenon could be due to a poor description of the basal resistance in the lower layer momentum equation. In this regard, we suspect that the hypothesis of a pure Coulomb friction at the bottom surface does not work very well, if there is a no-slip bottom boundary condition. Further investigation on this topic is required. A rate-dependent term could be added in the formula for calculating $t_{2b,xz}$ (cf. Eq. 4.49) in a further version of the mathematical model. Moreover, it should be noted that also the assumption of constant velocity profiles in both layers is an important shortcoming of the present model.

Nonetheless, an additional source of error could lie on the boundary conditions, imposed in the numerical simulation. In fact, such conditions are obtained from experimental velocity profiles on the basis of the found interface position, but it is possible that, for some experiments, the interface position, predicted by the aforementioned criterion, is unrealistic. It follows that unrealistic boundary conditions are imposed in the mathematical model, and, consequently, they lead to a steady state, noticeably different from that observed experimentally. In order to avoid these uncertainties, it could be interesting to repeat these comparisons, by varying the interface positions in a more probabilistic approach.

Finally, it should be reminded that the present comparisons are between a one-dimensional model and experimental velocity profiles, measured at the side wall and normalized by means of the ratio $u_{x,\text{mean}}/\min u_x$ by frontal PIV measurements. In this fashion, we assume that such a normalized velocity profile is representative of the effective flow velocity distribution inside the flowing pile. Although this simple assumption is strictly required to perform comparisons between a one-dimensional model and three-dimensional flows, it could lead to important additional errors. For example, the flow depth is expected to vary along y direction and is probably bigger at the centreline of the channel, than at the side walls. This could, obviously, influence also the velocity profile. A further experimental research on this topic would be needed.

References Used in This Chapter

- Ancey, C. (2001). Dry granular flows down an inclined channel: Experimental investigations on the frictional-collisional regime. *Physical Review E* **65**, 1–19.
- Bagnold, R. A. (1954). Experiments on a Gravity-Free Dispersion of Large Solid Spheres in a Newtonian Fluid under Shear. *Proceedings of the Royal Society A: Mathematical, Physical and Engineering Sciences* **225**, 49–63.
- da Cruz, F., Emam, S., Prochnow, M., Roux, J.-N., and Chevoir, F. (2005). Rheophysics of dense granular materials : Discrete simulation of plane shear flows. *Physical Review E* **72**, 24.
- Iverson, R. M. (1997). The physics of debris flows. *Reviews of Geophysics* **35**, 245.
- Iverson, R. M. and Vallance, J. W. (2001). New views of granular mass flows. *Geology* **29**, 115.
- Jaky, J. (1944). The coefficient of earth pressure at rest. *Journal of the Society of Hungarian Architects and Engineers* **78**, 355–358.
- Jop, P., Forterre, Y., and Pouliquen, O. (2005). Crucial role of sidewalls in granular surface flows: consequences for the rheology. *Journal of Fluid Mechanics* **541**, 167–192.
- Jop, P., Forterre, Y., and Pouliquen, O. (2006). A constitutive law for dense granular flows. *Nature* **441**, 727–30.
- Komatsu, T., Inagaki, S., Nakagawa, N., and Nasuno, S. (2001). Creep Motion in a Granular Pile Exhibiting Steady Surface Flow. *Physical Review Letters* **86**, 1757–1760.
- Midi, G. (2004). On dense granular flows. *The European physical journal. E, Soft matter* **14**, 341–65.
- Nishimura, K. (1991). Studies on the Fluidized Snow Dynamics. In *Contributions from the Institute of Low Temperature Science A37*, pages 1–55.
- Sarno, L., Papa, M. N., and Martino, R. (2011). Dam-break flows of dry granular materials on gentle slopes. In Genevois, R., Hamilton, D. L., and Prestininzi, A., editors, *5th Int. Conf. on Debris-Flow Hazards Mitigation: Mechanics, Prediction and Assessment*. Italian Journal of Engineering Geology and Environment. Casa Editrice Università “La Sapienza”.
- Savage, S. B. and Hutter, K. (1989). The motion of a finite mass of granular material down a rough incline. *Journal of Fluid Mechanics* **199**, 177–215.
- Sheng, L.-T., Kuo, C.-Y., Tai, Y. C., and Hsiau, S.-S. (2011). Indirect measurements of stream-wise solid fraction variations of granular flows accelerating down a smooth rectangular chute. *Experiments in Fluids* **51**, 1329–1342.
- Tai, Y. C. and Lin, Y.-C. (2008). A focused view of the behavior of granular flows down a confined inclined chute into the horizontal run-out zone. *Physics of Fluids* **20**, 123302.
- Voellmy, A. (1955). *Über die Zerstörungskraft von Lawinen: L’Espacement des râteliers de retenue de la neige*. W. Jeger & A. Ostertag.

Chapter 6

The two-layer model in curvilinear coordinates

Chapter Summary

In order to better identify the physically negligible terms, a slightly different formulation of the two-layer model is here proposed. The equations of the new model are written in moving curvilinear coordinates, as regards the upper layer, and in Cartesian coordinates, as regards the lower layer. The curvilinear coordinate system is assumed to be attached to the moving interface between the two layers.

The derivation of the model makes use of the Unified Coordinate method (e.g. Hui et al., 1999; Hui, 2004, 2007), combined with the approach proposed by Bouchut and Westdickenberg (2004). The overall procedure for obtaining the final model equations is analogous to that proposed by Tai and Kuo (2008) and also used in works by Tai and Lin (2008) and Tai et al. (2012). The main advantage of this formulation, with respect to a classical curvilinear approach (e.g. Gray et al., 1999), is that it permits to avoid the complicated calculation of Christoffel symbols, with obvious simplifications in the model design and also in its numerical integration.

The procedure for deriving the model equations basically consists of writing the depth-averaged mass and momentum balance equations for each layer and, then, simplifying these equations by means of an ordering argument and some other simplifying assumptions about the velocity profiles inside the layers. The final equations exhibit some interesting advantages with respect to the former Cartesian formulation (cf. Chapter 4), that are carefully discussed.

6.1 The two-layer model in curvilinear coordinates

We are interested in reformulating the one-dimensional two-layer depth-averaged model, proposed in Chapter 4, in a curvilinear coordinate framework. In order to do so, we use the approach proposed by Tai and Kuo (2008), that merges the Unified Coordinate theory (Hui et al., 1999; Hui, 2004, 2007) with the geometrical treatment of the basal surface in Savage-Hutter type models, proposed by Bouchut and Westdickenberg (2004). The main advantage of this recent and promising approach, with respect to the classical curvilinear approach (e.g. Gray et al., 1999), is that it permits to avoid the complicated calculation of Christoffel symbols.

Similarly to the model proposed in Chapter 4, we assume that the granular flow can be ideally divided in two superimposed layers, separated by a sharp non-material interface. The upper layer is aimed to describe the dense-collisional regime, while the lower one corresponds to the quasi-static regime. Similarly to the previous model, it is assumed that the bulk densities, ρ_1 and ρ_2 , are constant within each layer. Moreover, in the present model formulation, for the sake of simplicity, the earth pressure coefficient relating the normal stresses are chosen to be equal to 1 in both of the layers.

The mass and momentum balance equations of the upper layer are written in curvilinear coordinates, that move together with the interface. More precisely, a curvilinear coordinate system, attached to interface, separating the two layers is employed. Differently, the balance equations of the lower layer are written in Cartesian coordinates, analogous to those used in Chapter 4. The Cartesian frame of reference is assumed to be fixed and x axis forms an angle δ with respect to the horizontal equipotential lines, so that the gravity vector components can be written as $\mathbf{g} = (g \sin \delta, -g \cos \delta)^T$. Moreover, an orthogonal curvilinear coordinate system (ξ, ζ) , attached to the interface Γ between the two layers, is considered. The ξ coordinate is everywhere locally parallel to the interface Γ , while ζ is perpendicular to it. We call ϑ the local inclination angle of the reference surface Γ with respect to the reference Cartesian axis x . The convention that $\vartheta > 0$ in case of positive slope is assumed.

In order to avoid notation overload, in this Chapter (unless otherwise specified), we use the symbols \mathbf{v} and \mathbf{w} (instead of \mathbf{v}_1 and \mathbf{v}_2) to represent the upper layer and lower layer flow velocities. Moreover, since the model derivation involves using many equations, the more relevant ones have been put inside boxes in order to highlight them.

The procedure, to obtain the final model equations, is briefly summarized as follows

1. the mass and momentum balance equations are written in curvilinear coordinates for the upper layer and in Cartesian coordinates for the lower one;
2. the kinematic and dynamic boundary conditions are written for each layer;
3. the mass and momentum balance equations are, then, depth integrated along the upper layer and lower layer flow depths;
4. the resulting depth-integrated equations are put in dimensionless form, after making some assumptions about the scaling of the main physical quantities. The main scaling parameter is chosen to be $\varepsilon = H/L$, which is the ratio between a typical flow depth and a typical avalanche span in a similar approach to that used in Savage-Hutter type models (e.g. Savage and Hutter, 1989; Gray et al., 1999; Tai and Kuo, 2008; Tai et al., 2010, 2012);

5. the dimensionless depth-integrated equations are further simplified by neglecting terms of order higher than $O(\varepsilon)$.

A detailed description of the main features of the Unified Coordinate method, relevant for model equation derivation, and of the main features of the coordinate transformation can be found in Appendix B.

6.1.1 Mass and momentum equations in curvilinear coordinates

At the first, in order to write the depth averaged balance equations of the upper layer, it is required to rewrite Eqs. (4.12) and (4.13) with respect to the curvilinear coordinate system, attached to a the moving interface Γ between the two layers.

Thanks to the *UC* relations (B.7) - (B.15), it possible to rewrite the mass balance equation (4.12) in curvilinear coordinates as follows

$$\boxed{\frac{\partial (J \rho)}{\partial \lambda} + \nabla_{\boldsymbol{\xi}} \cdot [J \rho (\mathbf{v}^* - \mathbf{q}^*)] = 0} \quad (6.1)$$

in which $\mathbf{v}^* = (v^\xi, v^\zeta)$ is the flow velocity in $\boldsymbol{\xi}$ coordinates, $\mathbf{q}^* = (q^\xi, q^\zeta)$ is the velocity of the curvilinear frame of reference, J represents the determinant of the Jacobian matrix of coordinate transformation (cf. Appendix B).

Proof. In fact, by virtue of Eq (B.10) and Eq (B.13) we get

$$\begin{aligned} \frac{\partial \rho}{\partial t} &= \frac{1}{J} \left[\frac{\partial (J \rho)}{\partial \lambda} - \nabla_{\boldsymbol{\xi}} \cdot (\rho J \mathbf{q}^*) \right] \\ \nabla_{\mathbf{x}} \cdot (\rho \mathbf{v}) &= \frac{1}{J} \nabla_{\boldsymbol{\xi}} \cdot (\rho \mathbf{v}^*) \end{aligned}$$

from which Eq (6.1) is easily demonstrated. \square

Analogously, with the help of *UC* relations (B.7) - (B.15), also the momentum equation (4.13) can be recast in curvilinear coordinates as follows

$$\boxed{\frac{\partial (J \rho \mathbf{v})}{\partial \lambda} + \nabla_{\boldsymbol{\xi}} \cdot \{ J [\rho \mathbf{v} \otimes (\mathbf{v}^* - \mathbf{q}^*) - T \Omega^{-T}] \} = J \rho \mathbf{g}} \quad (6.2)$$

where $T \Omega^{-T}$ represents the mixed tensor, hereafter simply referred to as Σ .

Proof. Thanks to Eq (B.10) we get

$$\frac{\partial (\rho \mathbf{v})}{\partial t} = \left(\frac{1/J [\partial_\lambda (\rho u_x) - \nabla_{\boldsymbol{\xi}} \cdot (\rho u_x J \mathbf{q}^*)]}{1/J [\partial_\lambda (\rho u_z) - \nabla_{\boldsymbol{\xi}} \cdot (\rho u_z J \mathbf{q}^*)]} \right) = \frac{1}{J} \frac{\partial (J \rho \mathbf{v})}{\partial \lambda} - \nabla_{\boldsymbol{\xi}} \cdot (\rho J \mathbf{v} \otimes \mathbf{q}^*). \quad (6.3)$$

Moreover, by means of Eq (B.13) we obtain

$$\nabla_{\mathbf{x}} \cdot (\rho \mathbf{v} \otimes \mathbf{v}) = \nabla_{\mathbf{x}} \cdot \begin{pmatrix} \rho u_x u_x & \rho u_x u_z \\ \rho u_z u_x & \rho u_z u_z \end{pmatrix} = \nabla_{\mathbf{x}} \cdot \begin{pmatrix} \rho u \mathbf{v} \\ \rho w \mathbf{v} \end{pmatrix} = \left(\frac{1/J \nabla_{\boldsymbol{\xi}} \cdot (\rho u_x \mathbf{v}^*)}{1/J \nabla_{\boldsymbol{\xi}} \cdot (\rho u_z \mathbf{v}^*)} \right) = \frac{1}{J} \nabla_{\boldsymbol{\xi}} \cdot (\rho \mathbf{v} \otimes \mathbf{v}^*) \quad (6.4)$$

and by means of Eq (B.15)

$$\nabla_{\mathbf{x}} \cdot T = \frac{1}{J} \nabla_{\boldsymbol{\xi}} \cdot (J T \Omega^{-T}). \quad (6.5)$$

\square

6.1.2 Upper layer boundary conditions

The local balance equations, (6.1) and (6.2), have to be equipped with kinematic and dynamic conditions at the boundaries, before being depth-integrated along the upper layer flow depth. Also these conditions have to be written in curvilinear coordinates. The upper boundary is represented by the free surface, while the lower boundary is represented by the interface Γ , separating the two layers.

Boundary conditions at the free surface

The free surface can be described by an implicit equation in curvilinear coordinates,

$$\tilde{F}_s(\xi, \zeta) = 0. \quad (6.6)$$

Because the flow is expected to be shallow with respect to the curvilinear reference surface, we assume that it is possible to express ζ into $\tilde{F}_s(\xi, \zeta)$ explicitly, so that Eq. (6.6) can be recast as follows

$$\tilde{F}_s = \zeta - \tilde{s}(\xi, \lambda) = 0. \quad (6.7)$$

From Eq. (6.7) it follows that the unit normal vector of the free surface points towards increasing ζ .

The free surface is a Lagrangian surface, thus the Kinematic Boundary Condition (KBC) there, written in Cartesian coordinates, yields

$$\frac{dF_s}{dt} = \frac{\partial F_s}{\partial t} + \mathbf{v} \cdot \nabla_{\mathbf{x}} F_s = 0 \quad (6.8)$$

where \mathbf{v} is the upper layer flow velocity.

By using the *UC* formulae (B.7) - (B.15), we obtain the corresponding relation in curvilinear coordinate system

$$\boxed{\frac{\partial \tilde{s}}{\partial \lambda} + \frac{\partial \tilde{s}}{\partial \xi} (v^\xi - q^\xi) - (v^\zeta - q^\zeta) = 0.} \quad (6.9)$$

Proof. Thanks to Eq. (B.10), we can write

$$\begin{aligned} \frac{\partial F_s}{\partial t} &= \frac{1}{J} \frac{\partial}{\partial \lambda} (J \tilde{F}_s) - \frac{1}{J} \nabla_{\boldsymbol{\xi}} \cdot (J \tilde{F}_s \Omega^{-1} \mathbf{q}) \\ &= \frac{1}{J} \frac{\partial}{\partial \lambda} [J (\zeta - \tilde{s})] - \frac{1}{J} \frac{\partial}{\partial \xi} [J (\zeta - \tilde{s}) q^\xi] - \frac{1}{J} \frac{\partial}{\partial \zeta} [J (\zeta - \tilde{s}) q^\zeta] \\ &= \frac{\partial (\zeta - \tilde{s})}{\partial \lambda} + \frac{(\zeta - \tilde{s})}{J} \frac{\partial J}{\partial \lambda} - \frac{1}{J} \frac{\partial}{\partial \xi} [J (\zeta - \tilde{s}) q^\xi] - \frac{1}{J} J q^\zeta - \frac{(\zeta - \tilde{s})}{J} \frac{\partial (J q^\zeta)}{\partial \zeta}, \end{aligned}$$

then, by using Eq. (B.7) and after some simplifications, we get

$$\begin{aligned} \frac{\partial F_s}{\partial t} &= -\frac{\partial \tilde{s}}{\partial \lambda} + \frac{(\zeta - \tilde{s})}{J} \left[\frac{\partial}{\partial \xi} (J q^\xi) + \frac{\partial}{\partial \zeta} (J q^\zeta) \right] - \frac{1}{J} J q^\zeta \frac{\partial (\zeta - \tilde{s})}{\partial \xi} \\ &\quad - \frac{(\zeta - \tilde{s})}{J} \frac{\partial}{\partial \xi} (J q^\xi) - q^\zeta - \frac{(\zeta - \tilde{s})}{J} \frac{\partial (J q^\zeta)}{\partial \zeta} = -\frac{\partial \tilde{s}}{\partial \lambda} + q^\xi \frac{\partial \tilde{s}}{\partial \xi} - q^\zeta. \end{aligned} \quad (6.10)$$

Moreover, we can write the convective term as follows

$$\mathbf{v} \cdot \nabla_{\mathbf{x}} F_s = \mathbf{v} \cdot \Omega^{-T} \nabla_{\boldsymbol{\xi}} \tilde{F}_s = \Omega^{-1} \mathbf{v} \cdot \nabla_{\boldsymbol{\xi}} \tilde{F}_s = \mathbf{v}^* \cdot \nabla_{\boldsymbol{\xi}} \tilde{F}_s = v^\xi \frac{\partial \tilde{F}_s}{\partial \xi} + v^\zeta \frac{\partial \tilde{F}_s}{\partial \zeta} = -v^\xi \frac{\partial \tilde{s}}{\partial \xi} + v^\zeta. \quad (6.11)$$

Finally, by summing the terms (6.10) and (6.11), we get finally

$$\frac{\partial \tilde{s}}{\partial \lambda} + \frac{\partial \tilde{s}}{\partial \xi} (v^\xi - q^\xi) - (v^\zeta - q^\zeta) = 0.$$

□

At the free surface, normal and tangential stresses are supposed to be null, hence, the dynamic boundary condition (DBC) there can be written as

$$T \mathbf{n}_s = \Omega (T^* \mathbf{n}_s^*) = (\Omega T^*) \mathbf{n}_s^* = \mathbf{0} \quad (6.12)$$

where \mathbf{n}_s and $\mathbf{n}_s^* = \Omega^T \mathbf{n}_s$ are the normal vectors written in Cartesian coordinates and in curvilinear coordinates, respectively. Please note that, in general, while $\|\mathbf{n}_s\| = 1$, $\|\mathbf{n}_s^*\| \geq 1$ because of the metric (cf. Eq. (B.38)).

Eq. (6.12) can be recast in a more explicit form as follows

$$\Sigma \mathbf{n}_s^* = \begin{pmatrix} \sigma_1 n_s^\xi + \sigma_2 n_s^\zeta \\ \sigma_3 n_s^\xi + \sigma_4 n_s^\zeta \end{pmatrix} = \begin{pmatrix} 0 \\ 0 \end{pmatrix}. \quad (6.13)$$

where $\Sigma = \Omega T^* = T \Omega^{-T}$ represents the mixed tensor.

Boundary conditions at the interface

The lower boundary of the upper layer domain, which corresponds with the interface Γ between the upper layer and the lower layer, can be described by means of the following equation in curvilinear coordinates

$$\tilde{F}_i(\xi, \lambda) = \zeta = 0. \quad (6.14)$$

It should be noted that Eq. (6.14) follows directly from imposing that the curvilinear reference frame moves together with the curve Γ . The unit normal vector points towards increasing ζ . Moreover, it should be noted that, because the unit normal vector \mathbf{n}^* , written in curvilinear coordinates, has zero ξ component, it follows that $\|\mathbf{n}^*\| = \|\mathbf{n}\| = 1$ (cf. (B.38)).

Differently from the free surface, we assume that the interface Γ is not a material surface because mass exchanges between the two layers across the interface may occur. Moreover, the tangent components of flow velocities may exhibit a jump here.

KBC at the interface

Therefore, the kinematic boundary condition (KBC), written in Cartesian coordinates, is the following

$$\frac{dF_i}{dt} = \frac{\partial F_i}{\partial t} + \mathbf{v}_{int} \cdot \nabla_{\mathbf{x}} F_i = 0 \quad (6.15)$$

where \mathbf{v}_{int} is the interface velocity, namely the velocity of a pseudo-particle that moves together with the surface Γ .

By using the *UC* relations (B.7)-(B.15), we simply obtain the following KBC in curvilinear coordinates

$$v_{int}^\zeta - q^\zeta = 0. \quad (6.16)$$

Eq. (6.16) is a constraint to the choice of \mathbf{q} and it is a direct consequence of imposing that the curvilinear frame of reference is coincident with the interface Γ . It is interesting to note that no constraint is imposed to the ξ component of the mesh velocity, q^ξ .

Proof. By using Eqs. (B.10) and (B.7) and after some simplifications, we obtain

$$\begin{aligned}
\frac{\partial F_i}{\partial t} &= \frac{1}{J} \frac{\partial}{\partial \lambda} (J \hat{F}_{z_i}) - \frac{1}{J} \nabla_{\xi} \cdot (\hat{F}_i J \Omega^{-1} \mathbf{q}) \\
&= \frac{1}{J} \frac{\partial}{\partial \lambda} (J \hat{F}_i) - \frac{1}{J} \frac{\partial}{\partial \xi} (\hat{F}_i \Delta q^\xi) - \frac{1}{J} \frac{\partial}{\partial \zeta} (\hat{F}_{z_i} J q^\zeta) \\
&= \frac{J}{J} \frac{\partial \zeta}{\partial \lambda} + \frac{\zeta}{J} \frac{\partial J}{\partial \lambda} - \frac{1}{J} \frac{\partial}{\partial \xi} (\zeta J q^\xi) - \frac{J}{J} q^\zeta - \frac{\zeta}{J} \frac{\partial (J q^\zeta)}{\partial \zeta} \\
&= \frac{\partial \zeta}{\partial \lambda} + \frac{\zeta}{J} \left[\frac{\partial}{\partial \xi} (J q^\xi) + \frac{\partial}{\partial \zeta} (J q^\zeta) \right] - \frac{1}{J} J q^\xi \frac{\partial \zeta}{\partial \xi} - \frac{\zeta}{J} \frac{\partial}{\partial \xi} (J q^\xi) - q^\zeta - \frac{\zeta}{J} \frac{\partial (J q^\zeta)}{\partial \zeta} = -q^\zeta. \tag{6.17}
\end{aligned}$$

Note that $\partial_\lambda \zeta = \partial_\xi \zeta = 0$ because of Eq. (6.14).

Moreover, we can write the convective term as follows

$$\mathbf{v}_{int} \cdot \nabla_{\mathbf{x}} F_i = \mathbf{v}_{int} \cdot \Omega^{-T} \nabla_{\xi} \tilde{F}_i = \Omega^{-1} \mathbf{v}_{int} \cdot \nabla_{\xi} \tilde{F}_i = \mathbf{v}_{int}^* \cdot \nabla_{\xi} \tilde{F}_i = v_{int}^\xi \frac{\partial \zeta}{\partial \xi} + v_{int}^\zeta \frac{\partial \zeta}{\partial \zeta} = v_{int}^\zeta. \tag{6.18}$$

Finally, by summing the terms (6.17) and (6.18), we obtain Eq. (6.16). \square

Similarly to what assumed in the model presented in Chapter 4, a mass flux M_{flux} between the layers may take place. The volume exchanges of each layer have to fulfil the mass conservation equation (4.16). Nonetheless, it is useful now to rewrite their analytical expressions in curvilinear coordinates. The volume variation E_1 of the upper layer can be written as follows

$$\begin{aligned}
E_1 &= \frac{M_{flux}}{\rho_1} = (\mathbf{v} - \mathbf{v}_{int}) \cdot \mathbf{n} = (\mathbf{v} - \mathbf{v}_{int}) \cdot \frac{\nabla_{\mathbf{x}} F_i}{\|\nabla_{\mathbf{x}} F_i\|} \\
&= \Omega (\mathbf{v}^* - \mathbf{v}_{int}^*) \cdot \Omega^{-T} \mathbf{n}^* = (\mathbf{v}^* - \mathbf{v}_{int}^*) \cdot \mathbf{n}^*. \tag{6.19}
\end{aligned}$$

We followed the sign convention according to which $E_1 > 0$ if the upper layer volume increases at the expense of the lower layer. Since $\mathbf{n}^* = (0, 1)^T$, Eq. (6.19) can be further simplified as follows

$$E_1 = \frac{M_{flux}}{\rho_1} = v^\zeta - v_{int}^\zeta. \tag{6.20}$$

Similarly, the volume exchange E_2 of the lower layer is the following

$$E_2 = \frac{M_{flux}}{\rho_2} = (\mathbf{w} - \mathbf{v}_{int}) \cdot \mathbf{n} = (\mathbf{w}^* - \mathbf{v}_{int}^*) \cdot \mathbf{n}^* = w^\zeta - v_{int}^\zeta \tag{6.21}$$

where \mathbf{w} is the flow velocity in the lower layer.

Thanks to Eq. (6.20) and after summing the term $-v^\zeta$ to the l.h.s and r.h.s of Eq. (6.16), the KBC at the interface can be recast as

$$\boxed{q^\zeta - v^\zeta = -\frac{M_{flux}}{\rho_1}}. \tag{6.22}$$

DBC at the interface

As regards the dynamic boundary condition at the interface, similarly to what assumed in Chapter 4, we postulate the existence of a rate-dependent term, beside the Coulomb friction term.

In particular, by using the tension positive convention for stress tensor, the following relation holds

$$T_1 \mathbf{n} - (\mathbf{n} \cdot T_1 \mathbf{n}) \mathbf{n} = \frac{\Delta \mathbf{v}_t}{\|\Delta \mathbf{v}_t\|} \left(k \tan \varphi_{int} (-t^{\zeta \zeta}) + r \rho_1 \|\Delta \mathbf{v}_t\|^{\beta'} \right) \tag{6.23}$$

where T_1 is stress tensor defined in the upper layer, φ_{int} is the dynamical friction angle of the granular material, ρ_1 is the bulk density in the upper layer, k and r are the same empirical parameters, introduced in the model in Chapter 4. Moreover, β' is the exponent of rate-dependent shear stress and, thus, depends on the chosen rheology. $\Delta \mathbf{v}_t = \Delta \mathbf{v}^* - [(\mathbf{v} - \mathbf{w}) \cdot \mathbf{n}] \mathbf{n}$ is the jump of the tangent components of flow velocities at the interface and $-t_{\zeta\zeta}$ is the normal pressure, calculated as limit from above at the interface. Please note that the physical quantity $T_1 \mathbf{n}$ in Eq. (6.23) represents the stress vector exerted by the upper layer on the lower layer.

After left-multiplying the l.h.s. and the r.h.s. by Ω^{-1} and after writing $\|\Delta \mathbf{v}_t\|$ as function of $\|\Delta \mathbf{v}_t^*\|$ (cf. (B.37)), Eq. (6.23) can be written also as follows

$$\mathbf{T}_1^* \mathbf{n}^* - (\mathbf{n}^* \cdot \mathbf{T}_1^* \mathbf{n}^*) \mathbf{n}^* = \frac{\Delta \mathbf{v}_t^*}{\sqrt{G_{11}} \|\Delta \mathbf{v}_t^*\|} \left(k \tan \varphi_{int} (-t^{\zeta\zeta}) + r \rho_1 G_{11} \|\Delta \mathbf{v}_t^*\|^{\beta'} \right) \quad (6.24)$$

where $\Delta \mathbf{v}_t^* = (v^\xi - w^\xi, 0)^T$ and $\mathbf{n}^* = (0, 1)^T$.

After left-multiplying by Ω , Eq. (6.24) is finally recast as

$$\begin{aligned} \Omega (T^* \mathbf{n}^* - (\mathbf{n}^* \cdot T^* \mathbf{n}^*) \mathbf{n}^*) &= \frac{\Omega \Delta \mathbf{v}_t^*}{\sqrt{G_{11}} \|\Delta \mathbf{v}_t^*\|} \left(k \tan \varphi_{int} (-t^{\zeta\zeta}) + r \rho_1 G_{11} \|\Delta \mathbf{v}_t^*\|^{\beta'} \right) \\ &= \Sigma \mathbf{n}^* - t^{\zeta\zeta} \mathbf{n} = \frac{\Delta \mathbf{v}_t^*}{\sqrt{G_{11}} \|\Delta \mathbf{v}_t^*\|} \left(k \tan \varphi_{int} (-t^{\zeta\zeta}) + r \rho_1 G_{11} \|\Delta \mathbf{v}_t^*\|^{\beta'} \right) \end{aligned} \quad (6.25)$$

where

$$\Delta \mathbf{v}_t = \Omega \Delta \mathbf{v}_t^* = (v^\xi - w^\xi, -\tan \vartheta (v^\xi - w^\xi))^T.$$

Please note that, even though normal vectors are covariant and transform according to Eq. (A.11), in this particular case it holds $\mathbf{n} = \Omega^{-T} \mathbf{n}^* = \Omega \mathbf{n}^*$, because $\mathbf{n}^* = (0, 1)^T$.

6.1.3 Depth-integration of the upper layer balance equations

In this section, the local mass and momentum equations (6.1) and (6.2) are depth-integrated along the upper layer flow depth.

Depth-integration of the mass equation

Equation (6.1), depth-integrated from the interface ($\zeta = 0$) up to the free surface ($\zeta = \bar{s}$), with the help of the Leibnitz rule (A.3), can be written as follows

$$\begin{aligned} \frac{\partial}{\partial \lambda} \int_0^{\bar{s}} J \rho_1 d\zeta + 0 - J_{\bar{s}} \rho_1 \frac{\partial \bar{s}}{\partial \lambda} + \frac{\partial}{\partial \xi} \int_0^{\bar{s}} J \rho_1 (v^\xi - q^\xi) d\zeta \\ + 0 - J_{\bar{s}} \rho_1 (v^\xi - q^\xi) \Big|_{\bar{s}} \frac{\partial \bar{s}}{\partial \xi} + J_{\bar{s}} \rho_1 (v^\zeta - q^\zeta) \Big|_{\bar{s}} - J_0 \rho_1 (v^\zeta - q^\zeta) \Big|_0 = 0 \end{aligned} \quad (6.26)$$

where $J_{\bar{s}}$ and J_0 are the determinants of the Jacobian matrix of transformation, calculated at the free surface and at the interface, respectively. Because it is assumed that the bulk density ρ_1 is constant in the upper layer domain, we are allowed to take ρ_1 out of the integrals signs. After

some simplifications and thanks to the KBCs (6.9) (6.22), it is recast

$$\begin{aligned} \frac{\partial}{\partial \lambda} \int_0^{\bar{s}} J d\zeta + \frac{\partial}{\partial \xi} \int_0^{\bar{s}} J (v^\xi - q^\xi) d\zeta \\ - J_{\bar{s}} \underbrace{\left[\frac{\partial \bar{s}}{\partial \lambda} + (v^\xi - q^\xi) \Big|_{\bar{s}} \frac{\partial \bar{s}}{\partial \xi} - (v^\zeta - q^\zeta) \Big|_{\bar{s}} \right]}_{\text{KBC at free surface}} - J_0 \underbrace{(v^\zeta - q^\zeta) \Big|_0}_{\text{KBC at interface}} = 0 \end{aligned} \quad (6.27)$$

and, after substituting the expression at the l.h.s. of Eq. (6.22), we finally obtain

$$\boxed{\frac{\partial}{\partial \lambda} \int_0^{\bar{s}} J d\zeta + \frac{\partial}{\partial \xi} \int_0^{\bar{s}} J (v^\xi - q^\xi) d\zeta = J_0 \frac{M_{flux}}{\rho_1}}. \quad (6.28)$$

Depth-integration of the momentum equation

The same procedure has been done to the momentum equation (6.2). In order to depth-integrate each term separately, it seems useful to we rewrite Eq. (6.2) in a more explicit form

$$\begin{aligned} \frac{\partial (J \rho_1 \mathbf{v})}{\partial \lambda} + \nabla_{\boldsymbol{\xi}} \cdot \left\{ J \left[\begin{pmatrix} \rho_1 v_x (v^\xi - q^\xi) & \rho_1 v_x (v^\zeta - q^\zeta) \\ \rho_1 v_z (v^\xi - q^\xi) & \rho_1 v_z (v^\zeta - q^\zeta) \end{pmatrix} - \begin{pmatrix} \sigma_1 & \sigma_2 \\ \sigma_3 & \sigma_4 \end{pmatrix} \right] \right\} = J \rho_1 \mathbf{g} \Rightarrow \\ \left[\frac{\partial_\lambda (J \rho_1 v_x)}{\partial \lambda} \right] + \left[\frac{\partial^\xi (J \rho_1 v_x (v^\xi - q^\xi)) + \partial^\zeta (J \rho_1 v_x (v^\zeta - q^\zeta))}{\partial \lambda (J \rho_1 v_z)} \right] \\ - \left[\frac{\partial^\xi (J \sigma_1) + \partial^\zeta (J \sigma_2)}{\partial^\xi (J \sigma_3) + \partial^\zeta (J \sigma_4)} \right] = J \rho_1 \begin{pmatrix} g^x \\ g^z \end{pmatrix}. \end{aligned} \quad (6.29)$$

By depth-integrating the first term and with the help of the Leibnitz rule (A.3), we obtain

$$\int_0^{\bar{s}} \frac{\partial (J \mathbf{v})}{\partial \lambda} d\zeta = \frac{\partial}{\partial \lambda} \int_0^{\bar{s}} J \mathbf{v} d\zeta + 0 - [J \mathbf{v}]_{\bar{s}} \frac{\partial \bar{s}}{\partial \lambda}. \quad (6.30)$$

The advective momentum fluxes can be depth-integrated as follows

$$\int_0^{\bar{s}} \frac{\partial (J \mathbf{v} (v^\xi - q^\xi))}{\partial \xi} d\zeta = \frac{\partial}{\partial \xi} \int_0^{\bar{s}} J \mathbf{v} (v^\xi - q^\xi) d\zeta + 0 - [J \mathbf{v} (v^\xi - q^\xi)]_{\bar{s}} \frac{\partial \bar{s}}{\partial \xi} \quad (6.31)$$

$$\int_0^{\bar{s}} \frac{\partial (J \mathbf{v} (v^\zeta - q^\zeta))}{\partial \zeta} d\zeta = [J \mathbf{v} (v^\zeta - q^\zeta)]_{\bar{s}} - [J \mathbf{v} (v^\zeta - q^\zeta)]_0. \quad (6.32)$$

Moreover, depth-integrating momentum fluxes due to stresses yield

$$\int_0^{\bar{s}} \frac{\partial \left(J \begin{pmatrix} \sigma_1 / \rho_1 \\ \sigma_3 / \rho_1 \end{pmatrix} \right)}{\partial \xi} d\zeta = \frac{\partial}{\partial \xi} \int_0^{\bar{s}} J \begin{pmatrix} \sigma_1 / \rho_1 \\ \sigma_3 / \rho_1 \end{pmatrix} d\zeta + 0 - J_{\bar{s}} \begin{pmatrix} \sigma_1 / \rho_1 \\ \sigma_3 / \rho_1 \end{pmatrix} \Big|_{\bar{s}} \frac{\partial \bar{s}}{\partial \xi} \quad (6.33)$$

$$\int_0^{\bar{s}} \frac{\partial \left(J \begin{pmatrix} \sigma_2 / \rho_1 \\ \sigma_4 / \rho_1 \end{pmatrix} \right)}{\partial \zeta} d\zeta = \left(J \begin{pmatrix} \sigma_2 / \rho_1 \\ \sigma_4 / \rho_1 \end{pmatrix} \right) \Big|_{\bar{s}} - \left(J \begin{pmatrix} \sigma_2 / \rho_1 \\ \sigma_4 / \rho_1 \end{pmatrix} \right) \Big|_0. \quad (6.34)$$

By collecting all the aforementioned terms into the balance momentum equation, we obtain

$$\begin{aligned}
& \frac{\partial}{\partial \lambda} \int_0^{\bar{s}} J \mathbf{v} d\zeta + \frac{\partial}{\partial \xi} \int_0^{\bar{s}} J \mathbf{v} (v^\xi - q^\xi) d\zeta - \frac{\partial}{\partial \xi} \int_0^{\bar{s}} J \begin{pmatrix} \sigma_1/\rho_1 \\ \sigma_3/\rho_1 \end{pmatrix} d\zeta \\
& + [J\mathbf{v}]_0 \underbrace{[v^\zeta - q^\zeta]_0}_{\text{KBC at interface}} - [J\mathbf{v}]_{\bar{s}} \underbrace{\left(\frac{\partial \bar{s}}{\partial \lambda} + [v^\xi - q^\xi]_{\bar{s}} \frac{\partial \bar{s}}{\partial \xi} - [v^\zeta - q^\zeta]_{\bar{s}} \right)}_{\text{KBC at free surface}} \\
& + J_{\bar{s}} \underbrace{\left(\begin{pmatrix} \sigma_1/\rho_1 \\ \sigma_3/\rho_1 \end{pmatrix} \Big|_{\bar{s}} \frac{\partial \bar{s}}{\partial \xi} - \begin{pmatrix} \sigma_2/\rho_1 \\ \sigma_4/\rho_1 \end{pmatrix} \Big|_{\bar{s}} \right)}_{\text{DBC at free surface}} + J_0 \begin{pmatrix} \sigma_2/\rho_1 \\ \sigma_4/\rho_1 \end{pmatrix} \Big|_0 = \int_0^{\bar{s}} J \mathbf{g} d\zeta, \quad (6.35)
\end{aligned}$$

and, finally we obtain the following two-vector equation

$$\begin{aligned}
& \frac{\partial}{\partial \lambda} \int_0^{\bar{s}} J \begin{pmatrix} v_x \\ v_z \end{pmatrix} d\zeta + \frac{\partial}{\partial \xi} \int_0^{\bar{s}} J (v^\xi - q^\xi) \begin{pmatrix} v_x \\ v_z \end{pmatrix} d\zeta - \frac{\partial}{\partial \xi} \int_0^{\bar{s}} \begin{pmatrix} J\sigma_1/\rho_1 \\ J\sigma_3/\rho_1 \end{pmatrix} d\zeta \\
& = \int_0^{\bar{s}} J \begin{pmatrix} g_x \\ g_z \end{pmatrix} d\zeta - J_0 \begin{pmatrix} \sigma_2/\rho_1 \\ \sigma_4/\rho_1 \end{pmatrix} \Big|_0 + J_0 \begin{pmatrix} v_x \\ v_z \end{pmatrix} \Big|_0 \frac{M_{flux}}{\rho_1}. \quad (6.36)
\end{aligned}$$

It should be noted that the depth-averaged equations (6.28) and (6.36) have been obtained with the sole simplifying hypothesis of constant density inside the upper layer. All the scaling simplifications are yet to be done. Although for the sake of completeness Eq. (6.36) is written in its vector form, only the first scalar equation will be used in the resulting model.

In the final depth-averaged momentum equation (6.36), the great advantage of this approach is evident. In fact, although Eq.(6.36) has been derived in a curvilinear coordinate system, the flow velocity components inside the vector of unknowns are written in Cartesian coordinates. Such a model design avoids the complicated calculation of Christoffel symbols (Tai and Kuo, 2008).

6.1.4 Depth-integration of the lower layer balance equations

Similarly to what done for the upper layer, now we derive the depth-averaged equations of the lower flowing layer. In this case, the derivation is much simpler because we make use of the mass and momentum equations written in Cartesian coordinates (4.12) and (4.13). Their derivation is analogous to that reported in Chapter 4. At the first, kinematic and dynamic boundary conditions are defined; then, Eqs. (4.12) and (4.13) are depth-integrated along the lower flow depth.

KBC at the bottom

In general, the bottom surface b can be described by the following equation

$$F_b(x, z, t) = z - b(x, t) = 0. \quad (6.37)$$

In the simple case of fixed bed, the bottom surface equation can be recast simply as $F_b(x, z, t) = z - b(x) = 0$. In this particular case, because there is no mass flux across the bed surface, i.e. the bottom surface is a material surface, the KBC there can be written as follows

$$\frac{dF_b}{dt} = \frac{\partial F_b}{\partial t} + \mathbf{w} \cdot \nabla_{\mathbf{x}} F_b = 0 \quad (6.38)$$

where \mathbf{w} stands for the flow velocity field in the lower layer. In order to simplify as much as possible the present model, an even stronger assumption is made, i.e. that the bottom is a plane surface, coincident with the x axis. In other words, we impose that $b(x, t) = 0$. Thus, Eq. (6.38) simplifies into

$$\boxed{w_z = 0.} \quad (6.39)$$

DBC at the bottom

At the bottom, the shear stress is assumed to be of Coulomb type, similarly to what assumed in Savage-Hutter type models (e.g. Hutter et al., 1989; Gray et al., 1999; Tai et al., 2001; Hutter, 2005)

$$T_2 \mathbf{n}_b - (T_2 \mathbf{n}_b \cdot \mathbf{n}_b) \mathbf{n}_b = \frac{\mathbf{w} - (\mathbf{w} \cdot \mathbf{n}_b) \mathbf{n}_b}{\|\mathbf{w} - (\mathbf{w} \cdot \mathbf{n}_b) \mathbf{n}_b\|} \tan \varphi_b N_b \quad (6.40)$$

in which φ_b and N_b are the basal angle of friction and the normal pressure at the bottom, respectively. Since in case of bed surface coincident with x axis, the normal unit vector at the basal surface turns out to be $\mathbf{n}_b = (0, 1)^T$, then $N_b = -t_{2,zz}|_0$. Therefore, after some easy calculations, Eq. (6.40) can be recast as

$$\boxed{t_{2,xz}|_0 = -\operatorname{sgn}(w_x) \tan \varphi_b t_{2,zz}|_0.} \quad (6.41)$$

KBC at the interface

We assume that the interface Γ between the two layers can be described by the following equation

$$F_i = z - z_i(x, t) = 0. \quad (6.42)$$

In general, $z_i = h_2$ is the distance of the interface Γ from the coordinate axis x . The KBC is Eq. (6.15), that can be made explicit as follows

$$-\frac{\partial z_i}{\partial t} - \frac{\partial z_i}{\partial x} v_{int,x} + v_{int,z} = 0. \quad (6.43)$$

With the help of Eq. (6.21) for calculating the volume exchange and by adding $\mathbf{w} \cdot \nabla_{\mathbf{x}} F_i$ to the l.h.s. and the r.h.s. of Eq. (6.43), it is recast as follows

$$\boxed{-\frac{\partial z_i}{\partial t} - \frac{\partial z_i}{\partial x} w_x + w_z = (\mathbf{w} - \mathbf{v}_{int}) \cdot \nabla_{\mathbf{x}} F_i = \frac{M_{flux}}{\rho_2} \|\nabla_{\mathbf{x}} F_i\|.} \quad (6.44)$$

DBC at the interface

Similarly to the assumption made in the model presented in Chapter 4 (cf. Eq. (4.50)), the dynamic boundary condition at the interface is

$$\boxed{T_2 \mathbf{n} - (T_2 \mathbf{n} \cdot \mathbf{n}) \mathbf{n} = \frac{\Delta \mathbf{v}_t}{\|\Delta \mathbf{v}_t\|} \tan \varphi_{int} \left(-t_2^{\zeta\zeta} \right)} \quad (6.45)$$

where \mathbf{n} is the normal unit vector of the interface, $\left(-t_2^{\zeta\zeta} \right)$ is the pressure at the interface, calculated as limit from below and $\Delta \mathbf{v}_t$ is the tangential component of the jump of flow velocities at the

interface, i.e. $\Delta \mathbf{v}_t = (\mathbf{v} - \mathbf{w}) - [(\mathbf{v} - \mathbf{w}) \cdot \mathbf{n}] \mathbf{n}$. After some simple algebraic manipulations of Eq. (6.45), it follows that

$$\boxed{t_2^{\xi\zeta} = \frac{\text{sgn}(v^\xi - w^\xi)}{\sqrt{G_{11}}} \tan \varphi_{int} (-t_2^{\zeta\xi})}. \quad (6.46)$$

Depth integration of the mass equation

We integrate, now, the mass equation (4.12) over the lower layer flow depth, h_2 . With the help of the Leibnitz rule (A.3), it is possible to write

$$\frac{\partial}{\partial t} \int_0^{z_i} \rho_2 dz + \left[\rho_2 \frac{\partial z}{\partial t} \right]_{z_i}^0 + \frac{\partial}{\partial x} \int_0^{z_i} \rho_2 w_x dz + \left[\rho_2 w_x \frac{\partial z}{\partial x} \right]_{z_i}^0 + [\rho_2 w_z]_0^{z_i} = 0. \quad (6.47)$$

where $z_i = h_2$. Then, after some simplification and after collecting the terms in order to use the KBCs (6.43) and (6.39), we get

$$\frac{\partial}{\partial t} h_2 + \frac{\partial}{\partial x} \int_0^{z_i} w_x dz - \underbrace{w_x \Big|_0^{z_i} - \left(\frac{\partial z_i}{\partial t} + w_x \frac{\partial z_i}{\partial x} - w_z \right) \Big|_{z_i}}_{\text{KBC at the interface}} = 0 \quad (6.48)$$

After some further simplifications, it can be recast as

$$\boxed{\frac{\partial h_2}{\partial t} + \frac{\partial (h_2 \overline{w_x})}{\partial x} = -\frac{M_{flux}}{\rho_2} \|\nabla_{\mathbf{x}} F_i\|} \quad (6.49)$$

where we use the over-bar to represent the depth-averaged value along the flow depth (cf. Eq. (4.29)).

6.1.5 Depth integration of the momentum equation

An analogous procedure has been performed in order to obtain the depth-averaged momentum equations. By integrating Eq. (4.13) over h_2 and after some simple simplifications, we obtain

$$\begin{aligned} & \frac{\partial}{\partial t} \int_0^{z_i} \mathbf{w} dz + \frac{\partial}{\partial x} \int_0^{z_i} \begin{pmatrix} w_x w_x \\ w_x w_z \end{pmatrix} dz - \frac{\partial}{\partial x} \int_0^{z_i} \begin{pmatrix} t_{2,xx}/\rho_2 \\ t_{2,zx}/\rho_2 \end{pmatrix} dz + \\ & - \mathbf{w} \Big|_0^{z_i} - \underbrace{\mathbf{w} \Big|_{z_i} \left(\frac{\partial z_i}{\partial t} + w_x \frac{\partial z_i}{\partial x} - w_z \right) \Big|_{z_i}}_{\text{KBC at the interface}} \\ & = \int_0^{z_i} \begin{pmatrix} g_x \\ g_z \end{pmatrix} dz + \left[\begin{pmatrix} t_{2,xx}/\rho_2 \\ t_{2,zx}/\rho_2 \end{pmatrix} \right]_0^{z_i} - \begin{pmatrix} t_{2,xx}/\rho_2 \\ t_{2,zx}/\rho_2 \end{pmatrix} \frac{\partial h_2}{\partial x}. \end{aligned} \quad (6.50)$$

Through using KBCs (6.38) and (6.44), we finally obtain the following two scalar equations. The x -component of the depth-averaged momentum equation reads

$$\boxed{\begin{aligned} & \frac{\partial}{\partial t} (h_2 \overline{w_x}) + \frac{\partial}{\partial x} \left(h_2 \overline{w_x^2} - h_2 \frac{t_{2,xx}}{\rho_2} \right) \\ & = h_2 g_x + \frac{t_{2,xz}}{\rho_2} \Big|_{z_i} - \frac{t_{2,xz}}{\rho_2} \Big|_0 - \frac{t_{2,xx}}{\rho_2} \Big|_{z_i} \frac{\partial h_2}{\partial x} - w_x \Big|_{z_i} \frac{M_{flux}}{\rho_2} \|\nabla_{\mathbf{x}} F_{z_i}\| \end{aligned}} \quad (6.51)$$

The z -component of the depth-averaged momentum equation can be written as follows

$$\boxed{\begin{aligned} & \frac{\partial}{\partial t} (h_2 \overline{w_z}) + \frac{\partial}{\partial x} \left(h_2 \overline{w_x w_z} - h_2 \frac{\overline{t_{2, zx}}}{\rho_2} \right) \\ & = h_2 g_z + \frac{t_{2, zz}}{\rho_2} \Big|_{z_i} - \frac{t_{2, zz}}{\rho_2} \Big|_0 - \frac{t_{2, xz}}{\rho_2} \Big|_{z_i} \frac{\partial h_2}{\partial x} - w_z \Big|_{z_i} \frac{M_{flux}}{\rho_2} \|\nabla_{\mathbf{x}} F_{z_i}\|. \end{aligned}} \quad (6.52)$$

6.2 Jump conditions at the interface

Similarly to what has been assumed in the model presented in Chapter 4, the density, flow velocities and stress tensor are supposed to exhibit a discontinuity across the interface Γ . Previously, we used the symbols \mathbf{v} and \mathbf{w} to denote the velocity fields in the upper and lower layer, respectively. Therefore, the conditions reported in Chapter 4, directly obtained from the Rankine-Hugoniot jump conditions, (4.21) and (4.22), hold also in this case.

In order to use the synthetic notations of Conditions (4.21) and (4.22), only in this section, we recover the former notation for representing flow velocities, i.e. $\mathbf{v}_1 = \mathbf{v}$ and $\mathbf{v}_2 = \mathbf{w}$. Now by left-multiplying both sides of Eq. (4.22) by the inverse of the Jacobian matrix of the transformation, Ω^{-1} and with the help of transformations (A.9), (A.11) and (A.12), we get

$$[\Omega^{-1} \mathbf{v}_i]_2^1 M_{flux} = [\Omega^{-1} T_i]_2^1 \mathbf{n} \Rightarrow [\mathbf{v}_i^*]_2^1 M_{flux} = T^* \mathbf{n}^* \quad (6.53)$$

where $\mathbf{n}^* = (0, 1)^T$ is the unit normal vector written in curvilinear coordinates.

The ξ component of Eq. (6.53) reads

$$\boxed{\left(v_1^\xi - v_2^\xi \right) M_{flux} = t_1^{\xi\xi} - t_2^{\xi\xi}.} \quad (6.54)$$

Eqs. (6.54) permits to calculate the unknown M_{flux} , as function of the other variables. Therefore, it will be used a closure equation of the present model.

As well, the ζ component reads as follows

$$\left(v_1^\zeta - v_2^\zeta \right) M_{flux} = t_1^{\zeta\zeta} - t_2^{\zeta\zeta}. \quad (6.55)$$

Since $v_i^\zeta = \mathbf{v}_i \cdot \mathbf{n}$, with the help of Eq. (4.21), it is recast

$$\boxed{\left(\frac{\rho_2 - \rho_1}{\rho_1 \rho_2} \right) M_{flux}^2 = t_1^{\zeta\zeta} - t_2^{\zeta\zeta}.} \quad (6.56)$$

6.3 Mesh velocity

As already stated before, the quantity \mathbf{q} represents the velocity of a pseudo-particle whose coordinates are (ξ, ζ) in curvilinear coordinates, i.e. it is the velocity of the curvilinear coordinate system. In other words, it can be regarded as the mesh velocity if we take the viewpoint of the numerical scheme. Since we impose that the curvilinear coordinate system moves together with the interface Γ , we have found that the KBC at the interface (6.16) is the following

$$q_0^\zeta = v_{int}^\zeta. \quad (6.57)$$

This is a constraint to \mathbf{q} at any given point on the interface Γ .

However, no constraint is about the tangential component q^ξ , thus, there is a residual degree of freedom in order to chose it. The choice $q^\xi = 0$ has been adopted in Tai and Kuo (2008); Tai et al. (2010, 2012) with some obvious numerical advantages in the case of single layer models. Nevertheless, in the present model there is an underlying moving layer, that continuously exchanges mass with the upper layer. Therefore, it is convenient for the numerical scheme, that the mesh of the upper layer, which is in curvilinear coordinates, always overlaps the mesh of the lower layer. It is why, we choose to impose that

$$\boxed{q_{x,0} = v_{int,x} = 0.} \quad (6.58)$$

The value of $v_{int}^\xi = q^\xi$, which in general is non-zero, can be directly calculated from the contravariant transformation ((A.9)), provided that q_x and q_z are known.

The advantage of imposing $q_x = 0$ is that at the interface Γ the boundaries of the mesh in the upper layer are always coincident with those of the mesh of the lower layer, written in Cartesian coordinates. Nonetheless, it should be noted that because $q^\xi \neq 0$ at the interface, then it varies along the flow depth owing to the local curvature. On the contrary, q^ζ is constant along the flow depth and is equal to $q_0^\zeta = v_{int}^\zeta$. Moreover, together with Eq. (6.58), the KBC at the interface written in Cartesian coordinates, (6.43) implies that

$$\boxed{q_{z,0} = v_{int,z} = \partial_t z_i = \partial_t h_2.} \quad (6.59)$$

6.4 Scaling and approximations

In this section, we write the mass and momentum depth-averaged equations in a dimensionless form, in order to do some scaling approximations. Such a procedure is very important for the quality of the final equation system. In fact, it is in this stage that the most crucial physical and engineering assumptions have to be evaluated and applied in order to obtain a reliable final equation system. Since the asymptotic analysis, here reported, makes wide use of the so-called *big-O* notation, a brief description of such a notation is reported in Appendix C.

6.4.1 The scaling of the upper layer equations

Main scalings

In the present model, we mainly follow the same scaling assumptions proposed in Savage-Hutter type models (Savage and Hutter, 1989; Gray et al., 1999) and employed also in other works that make use of *UC* theory (e.g. Tai and Kuo, 2008; Tai et al., 2012). In order to get an appropriate scale for non-dimensional quantities, we firstly define a characteristic longitudinal length of flow L , namely the typical spread of the avalanche, and its characteristic depth H . Please note that H is referred to the whole flow depth and not only to the upper or lower layer depths. Because the flows under investigation are typically shallow, it is assumed that

$$\varepsilon = \frac{H}{L} \ll 1. \quad (6.60)$$

In the following approximations ε will be regarded as an infinitesimal function, since in real avalanches ε typically exhibits very small values, of order of $10^{-3} - 10^{-4}$, as reported e.g. by Hutter (2005).

The main physical quantities can be non-dimensionalised by means of the following scalings

$$\left\{ \begin{array}{l} (\xi, \zeta) = L (\hat{\xi}, \varepsilon \hat{\zeta}), \\ (v^\xi, v^\zeta) = \sqrt{gL} (\hat{v}^\xi, \varepsilon \hat{v}^\zeta), \\ (v_x, v_z) = \sqrt{gL} (\hat{v}_x, \hat{v}_z), \\ (t^{\xi\xi}, t^{\zeta\zeta}) = \rho_1 g H (\hat{t}^{\xi\xi}, \hat{t}^{\zeta\zeta}), \\ (\sigma_1, \sigma_2, \sigma_3, \sigma_4) = \rho_1 g H (\hat{\sigma}_1, \hat{\sigma}_2, \hat{\sigma}_3, \hat{\sigma}_4), \\ (t^{\xi\zeta}) = \rho_1 g H \tan \varphi_{int} (\hat{t}^{\xi\zeta}) = \rho_1 g H \varepsilon^\beta (\hat{t}^{\xi\zeta}), \\ (\lambda) = \sqrt{L/g} (\hat{\lambda}). \end{array} \right. \quad \begin{array}{l} (6.61) \\ (6.62) \\ (6.63) \\ (6.64) \\ (6.65) \\ (6.66) \\ (6.67) \end{array}$$

where dimensionless variables are written with the symbol $\hat{\cdot}$. Moreover, it is assumed that dimensionless variables are $O(1)$ functions everywhere in the time-space domain, as well as their partial derivatives. Please note that the length scales H and L , together with ρ_1 and g , are independent from time and space, thus, in the following calculations these factors can be put outside of the derivatives and integrals operators.

Now, we are going to provide some explanations about the chosen scalings (cf. Eqs. (6.61)-(6.67)).

By following Savage and Hutter (1989), the ξ -component of flow velocity v_ξ is assumed to be of order \sqrt{gL} . Moreover, it is assumed that $v^\zeta \ll v^\xi$ because of the shallowness assumption, so it is reasonable that v^ζ is of order $\varepsilon\sqrt{gL}$. The flow velocity components in Cartesian coordinates v_x and v_z are of the same order of v^ξ , since they are obtained through a linear combination of v^ξ and v^ζ (cf. Eq. (A.9)). From Eq. (6.62) it follows that the characteristic time (namely the time for the avalanche to cover the distance L) is equal to $\sqrt{L/g}$ (Eq. (6.67)). The normal stresses $t^{\xi\xi}$, $t^{\zeta\zeta}$ are of order $\rho_1 g H$ because their most important term is due to hydrostatic pressure, as it will be shown in the following. On the other hand, $t^{\xi\zeta}$ is of order $\rho_1 g H \tan \varphi_{int}$, analogously to the Savage-Hutter model. Please note that the component of mixed stress tensor σ_i are of order $\rho_1 g H$ because they are calculated as a linear combination of the tensor components in curvilinear coordinates (cf. Appendix C).

Scaling of curvatures

By following Tai and Kuo (2008), another length scale is introduced about the interface curvature. More precisely, it is assumed that the characteristic curvature radius (i.e. the radius of the local osculating circle) is of order R , such that

$$\frac{L}{R} = O(\varepsilon^\alpha), \quad 0 < \alpha \leq 1. \quad (6.68)$$

This assumption is crucial in this model, since it allows many useful simplifications regarding the Jacobian matrix and its inverse matrix.

It also follows that the scaling of the local curvature is

$$k' = - \left(\sqrt{G_{11}} \right)^{-1} \partial_\xi \vartheta = - \cos \vartheta \frac{1}{R} \partial_\xi \hat{\vartheta} = \frac{1}{R} \hat{k}' \quad (6.69)$$

where the dimensionless quantity $\partial_{\xi}\hat{\vartheta}$ is assumed to be of order 1 and we use the symbol \hat{k}' to represent the quantity $-\cos\vartheta\partial_{\xi}\hat{\vartheta}$.

As well, it is useful to define the scaling of the time derivative of the negative local inclination angle $l = -\partial_{\lambda}\vartheta$. This quantity is a kind of *temporal curvature* of the interface. By following the same scaling as before and, provided that $\partial_{\lambda}\hat{\vartheta} = O(1)$, we get

$$l = -\partial_{\lambda}\vartheta = -\frac{L}{R}\sqrt{\frac{g}{L}}\partial_{\lambda}\hat{\vartheta} = -\frac{\sqrt{gL}}{R}\partial_{\lambda}\hat{\vartheta} = \frac{\sqrt{gL}}{R}\hat{l}. \quad (6.70)$$

where \hat{l} stands for $-\partial_{\lambda}\hat{\vartheta}$.

Moreover, according with Gray et al. (1999), the scale of $\tan\varphi_{int}$ is assumed to be

$$\tan\varphi_{int} = O(\varepsilon^{\beta}), \quad 0 < \beta \leq 1. \quad (6.71)$$

This scaling is quite common among the Savage-Hutter type models and it is physically justified by the fact that in real situations, $\tan\varphi_{int}$ is typically around 0.5 or even smaller.

Scaling of the mass flux

By assuming that the shear stress jump, $t_1^{\xi\zeta} - t_2^{\xi\zeta}$, is of order $O(\rho_1 g H)$ and that the velocity jump, $v_1^{\xi\zeta} - v_2^{\xi\zeta}$, is of order $O(gL)$, through using Eq. (6.54), the mass flux can be recast in the following dimensionless form

$$\frac{M_{flux}}{\rho_1} = \frac{H}{L}\sqrt{gL}\frac{\hat{M}_{flux}}{\hat{\rho}_1} = \varepsilon\sqrt{gL}\frac{\hat{M}_{flux}}{\hat{\rho}_1}. \quad (6.72)$$

Mesh velocity

Since $q_{z,0} = \partial_t h_2$ (cf. Eq. (6.59)), it can be easily shown that

$$q_{z,0} = v_{int,z} = \frac{H}{L}\sqrt{gL}\hat{q}_{z,0}. \quad (6.73)$$

As already stated before, q_x and q_z vary with ζ . By using the UC conditions (B.5) and the scaling of l (6.70), it follows that

$$\partial_{\zeta}q_x = \partial_{\lambda}\Omega_{12} = \partial_{\lambda}(\cos\vartheta) = -\sin\vartheta\partial_{\lambda}\vartheta = -\sin\vartheta\sqrt{\frac{g}{L}}\frac{L}{R}\partial_{\lambda}\hat{\vartheta} \quad (6.74)$$

$$\partial_{\zeta}q_z = \partial_{\lambda}\Omega_{22} = \partial_{\lambda}(-\sin\vartheta) = -\cos\vartheta\partial_{\lambda}\vartheta = -\cos\vartheta\sqrt{\frac{g}{L}}\frac{L}{R}\partial_{\lambda}\hat{\vartheta}. \quad (6.75)$$

Then, it is possible to write

$$\begin{aligned} q_x(\zeta) &= q_{x,0} + \int_0^{\zeta} \partial_{\zeta}q_x d\zeta = \frac{H}{L}\sqrt{gL}\hat{q}_{x,0} - \sin\vartheta H\sqrt{\frac{g}{L}}\frac{L}{R} \int_0^{\zeta} \partial_{\zeta}\hat{q}_x d\hat{\zeta} \\ &= \varepsilon\sqrt{gL}\hat{q}_{x,0} - \varepsilon^{1+\alpha} \sin\vartheta\sqrt{gL} \int_0^{\hat{\zeta}} \partial_{\hat{\zeta}}\hat{q}_x d\hat{\zeta} = \boxed{q_{x,0} + O(\varepsilon^{1+\alpha})}. \end{aligned} \quad (6.76)$$

Similarly, it can be shown that

$$\boxed{q_z(\zeta) = q_{z,0} + O(\varepsilon^{1+\alpha})}. \quad (6.77)$$

Please note that these scalings are justified by the hypothesis of small curvature of Γ .

It can be easily shown that the scaling of the mesh velocity, written in curvilinear coordinates, is as follows

$$q^\xi(\zeta) = -\sin\vartheta \cos\vartheta \varepsilon \sqrt{gL} \hat{q}_{z,0} + O(\varepsilon^{1+\alpha}). \quad (6.78)$$

Scaling of the Jacobian matrix

Thanks to the scaling (6.68), it follows

$$\Omega = \Omega_0 + O(\varepsilon^{1+\alpha}) \quad (6.79)$$

$$J = \det \Omega = \det \Omega_0 + O(\varepsilon^{1+\alpha}) \quad (6.80)$$

$$\Omega^{-1} = \Omega_0^{-1} + O(\varepsilon^{1+\alpha}). \quad (6.81)$$

where the elements of the matrices Ω_0 , Ω_0^{-1} and $\det \Omega_0$ are $O(1)$ functions for all $\vartheta \neq \pi/2$.

Proof. Since the matrix Ω can be factorized as follows

$$\Omega = \begin{pmatrix} 1 & \sin\vartheta \\ -\tan\vartheta & \cos\vartheta \end{pmatrix} \begin{pmatrix} 1 - \zeta \partial_x s & 0 \\ 0 & 1 \end{pmatrix} \quad (6.82)$$

where the elements of the first matrix, which actually is Ω_0 , are $O(1)$ for values of $\vartheta \neq \pi/2$.

Since $\partial_x s = k' = 1/Rk'$, i.e. it represents the spatial curvature, it follows that

$$\zeta \partial_x s = O\left(\frac{H}{L} \frac{L}{R}\right) = O(\varepsilon^{1+\alpha}). \quad (6.83)$$

Therefore,

$$\Omega = \Omega_0 + O(\varepsilon^{1+\alpha}). \quad (6.84)$$

Analogously, also Eq. (6.81) can be demonstrated.

Furthermore, thanks to the Binet theorem, we can write

$$\det \Omega = \det \Omega_0 \det \begin{pmatrix} 1 - \zeta \partial_x s & 0 \\ 0 & 1 \end{pmatrix} = \det \Omega_0 (1 - \zeta \partial_x s) = \det \Omega_0 [1 + O(\varepsilon^{1+\alpha})]. \quad (6.85)$$

□

6.4.2 Dimensionless depth-averaged upper layer mass equation

Now that the main scalings of physical quantities have been calculated, we can write the depth-averaged mass equation, (6.28), in dimensionless form. Since $\tilde{s} = h_1$, namely the depth of the upper layer measured normally to the interface Γ , and $h_1 = H \hat{h}_1$ where $\hat{h}_1 = O(1)$, Eq. (6.28) can be recast as follows

$$\frac{H}{\sqrt{L/g}} \frac{\partial}{\partial \hat{\lambda}} \left(\hat{h}_1 \int_0^1 J d\hat{\zeta} \right) + \frac{H}{L} \sqrt{gL} \frac{\partial}{\partial \hat{\xi}} \left(\hat{h}_1 \int_0^1 J (\hat{v}^\xi - \varepsilon \hat{q}^\xi) d\hat{\zeta} \right) = J_0 \frac{H}{L} \sqrt{gL} \frac{\hat{M}_{flux}}{\hat{\rho}_1}. \quad (6.86)$$

After some simplification we get

$$\frac{\partial}{\partial \hat{\lambda}} \left(\hat{h}_1 \int_0^1 (J_0 + O(\varepsilon^{1+\alpha})) d\hat{\zeta} \right) + \frac{\partial}{\partial \hat{\xi}} \left(\hat{h}_1 \int_0^1 (J_0 + O(\varepsilon^{1+\alpha})) (\hat{v}^\xi - \varepsilon \hat{q}^\xi) d\hat{\zeta} \right) = J_0 \frac{\hat{M}_{flux}}{\hat{\rho}_1}. \quad (6.87)$$

Please, note that J_0 does not vary along the flow depth. After collecting all terms that are $O(\varepsilon^{1+\alpha})$ or smaller and by using over-bars to denote depth-averaged quantities, we finally get

$$\frac{\partial}{\partial \hat{\lambda}} \left(\hat{h}_1 \bar{J}_0 \right) + \frac{\partial}{\partial \hat{\xi}} \left(\hat{h}_1 \bar{J}_0 \left(\bar{v}^\xi - \varepsilon \bar{q}^\xi \right) \right) = J_0 \frac{\hat{M}_{flux}}{\hat{\rho}_1} + O(\varepsilon^{1+\alpha}). \quad (6.88)$$

6.4.3 Dimensionless depth-averaged upper layer momentum equations

Similarly to what have been done to the depth-averaged mass equation, we rewrite the dimensionless depth-averaged momentum equations, (6.36), in dimensionless form

$$\begin{aligned}
& \frac{1}{\sqrt{L/g}} \frac{\partial}{\partial \hat{\lambda}} \left[H \hat{h}_1 \int_0^1 J \left(\frac{\sqrt{gL} \hat{v}_x}{\sqrt{gL} \hat{v}_z} \right) d\hat{\zeta} \right] + \frac{1}{L} \frac{\partial}{\partial \hat{\xi}} \left[H \hat{h}_1 \int_0^1 J \left(\frac{\sqrt{gL} \hat{v}_x}{\sqrt{gL} \hat{v}_z} \right) \sqrt{gL} (\hat{v}^\xi - \varepsilon \hat{q}^\xi) d\hat{\zeta} \right] \\
& - \frac{1}{L} \frac{\partial}{\partial \hat{\xi}} \left[H \hat{h}_1 \int_0^1 \begin{pmatrix} JgH\hat{\sigma}_1 \\ JgH\hat{\sigma}_3 \end{pmatrix} d\hat{\zeta} \right] = gH\hat{h}_1 \int_0^1 J \begin{pmatrix} \sin \delta \\ -\cos \delta \end{pmatrix} d\hat{\zeta} - gHJ_0 \begin{pmatrix} \hat{\sigma}_2 \\ \hat{\sigma}_4 \end{pmatrix} \Big|_{\hat{z}_i} \\
& + \varepsilon \sqrt{gL} J_0 \begin{pmatrix} \sqrt{gL} \hat{v}_x \\ \sqrt{gL} \hat{v}_z \end{pmatrix} \Big|_{\hat{z}_i} \frac{\hat{M}_{flux}}{\hat{\rho}_1}.
\end{aligned} \tag{6.89}$$

By collecting all the constant terms outside the integrals and derivative signs and by expressing $J = J_0 + O(\varepsilon^{1+\alpha})$, Eq. (6.89) can be recast as follows

$$\begin{aligned}
& \frac{H\sqrt{gL}}{\sqrt{L/g}} \frac{\partial}{\partial \hat{\lambda}} \left[\hat{h}_1 \int_0^1 (J_0 + O(\varepsilon^{1+\alpha})) \begin{pmatrix} \hat{v}_x \\ \hat{v}_z \end{pmatrix} d\hat{\zeta} \right] \\
& + \frac{H\sqrt{gL}\sqrt{gL}}{L} \frac{\partial}{\partial \hat{\xi}} \left[\hat{h}_1 \int_0^1 (J_0 + O(\varepsilon^{1+\alpha})) \begin{pmatrix} \hat{v}_x \\ \hat{v}_z \end{pmatrix} (\hat{v}^\xi - \varepsilon \hat{q}^\xi) d\hat{\zeta} \right] \\
& - \frac{gH^2}{L} \frac{\partial}{\partial \hat{\xi}} \left[\hat{h}_1 \int_0^1 (J_0 + O(\varepsilon^{1+\alpha})) \begin{pmatrix} \hat{\sigma}_1 \\ \hat{\sigma}_3 \end{pmatrix} d\hat{\zeta} \right] = gH\hat{h}_1 \begin{pmatrix} \sin \delta \\ -\cos \delta \end{pmatrix} \int_0^1 (J_0 + O(\varepsilon^{1+\alpha})) d\hat{\zeta} \\
& - gHJ_0 \begin{pmatrix} \hat{\sigma}_2 \\ \hat{\sigma}_4 \end{pmatrix} \Big|_{\hat{z}_i} + \varepsilon \sqrt{gL}\sqrt{gL}J_0 \begin{pmatrix} \hat{v}_x \\ \hat{v}_z \end{pmatrix} \Big|_{\hat{z}_i} \frac{\hat{M}_{flux}}{\hat{\rho}_1}.
\end{aligned} \tag{6.90}$$

Then, Eq. (6.90) can be further simplified as follows

$$\begin{aligned}
& \frac{\partial}{\partial \hat{\lambda}} \left[J_0 \hat{h}_1 \begin{pmatrix} \overline{\hat{v}_x} \\ \overline{\hat{v}_z} \end{pmatrix} + \underbrace{\int_0^1 O(\varepsilon^{1+\alpha}) \begin{pmatrix} \hat{v}_x \\ \hat{v}_z \end{pmatrix} d\hat{\zeta}}_{O(\varepsilon^{1+\alpha})} \right] \\
& + \frac{\partial}{\partial \hat{\xi}} \left[\hat{h}_1 J_0 \begin{pmatrix} \hat{v}_x (\hat{v}^\xi - \varepsilon \hat{q}^\xi) \\ \hat{v}_z (\hat{v}^\xi - \varepsilon \hat{q}^\xi) \end{pmatrix} + \underbrace{\int_0^1 O(\varepsilon^{1+\alpha}) \begin{pmatrix} \hat{v}_x \\ \hat{v}_z \end{pmatrix} (\hat{v}^\xi - \varepsilon \hat{q}^\xi) d\hat{\zeta}}_{O(\varepsilon^{1+\alpha})} \right] \\
& - \frac{\partial}{\partial \hat{\xi}} \left[\hat{h}_1 J_0 \begin{pmatrix} \varepsilon \overline{\hat{\sigma}_1} \\ \varepsilon \overline{\hat{\sigma}_3} \end{pmatrix} + \underbrace{\int_0^1 O(\varepsilon^{1+\alpha}) \begin{pmatrix} \hat{\sigma}_1 \\ \hat{\sigma}_3 \end{pmatrix} d\hat{\zeta}}_{O(\varepsilon^{1+\alpha})} \right] = \\
& \hat{h}_1 \begin{pmatrix} \sin \delta \\ -\cos \delta \end{pmatrix} [J_0 + O(\varepsilon^{1+\alpha})] - J_0 \begin{pmatrix} \hat{\sigma}_2 \\ \hat{\sigma}_4 \end{pmatrix} \Big|_{\hat{z}_i} + J_0 \begin{pmatrix} \hat{v}_x \\ \hat{v}_z \end{pmatrix} \Big|_{\hat{z}_i} \frac{\hat{M}_{flux}}{\hat{\rho}_1}
\end{aligned} \tag{6.91}$$

After collecting all the terms $O(\varepsilon^{1+\alpha})$, we finally get

$$\boxed{\begin{aligned} & \frac{\partial}{\partial \hat{\lambda}} \left[J_0 \hat{h}_1 \begin{pmatrix} \overline{\hat{v}_x} \\ \overline{\hat{v}_z} \end{pmatrix} \right] + \frac{\partial}{\partial \hat{\xi}} \left[\hat{h}_1 J_0 \begin{pmatrix} \overline{\hat{v}_x (\hat{v}^\xi - \varepsilon \hat{q}^\xi)} \\ \overline{\hat{v}_z (\hat{v}^\xi - \varepsilon \hat{q}^\xi)} \end{pmatrix} \right] - \frac{\partial}{\partial \hat{\xi}} \left[\hat{h}_1 J_0 \begin{pmatrix} \overline{\varepsilon \hat{\sigma}_1} \\ \overline{\varepsilon \hat{\sigma}_3} \end{pmatrix} \right] \\ & = J_0 \hat{h}_1 \begin{pmatrix} \sin \delta \\ -\cos \delta \end{pmatrix} - J_0 \left(\hat{\sigma}_2 \right) \Big|_{\hat{i}} + J_0 \begin{pmatrix} \hat{v}_x \\ \hat{v}_z \end{pmatrix} \Big|_{\hat{i}} \frac{\hat{M}_{flux}}{\hat{\rho}_1} + O(\varepsilon^{1+\alpha}). \end{aligned}} \quad (6.92)$$

In the final equation system we will only utilize the first component of Eq. (6.92). The stress terms involved in this equation, such as $\overline{\hat{\sigma}_1}$ and $\hat{\sigma}_2$, need to be specified. As well, some assumptions about the flow velocity distribution along the flow depth are required, in order to calculate the depth-averaged quantities that involve \hat{v}_x and \hat{v}^ξ and the value of \hat{v}_x at the interface Γ .

6.4.4 Normal stresses in the upper layer

Now, we need to specify the analytical expressions of mixed stresses $\overline{\hat{\sigma}_1}$ and $\hat{\sigma}_2$ at the interface, involved in the first component of the momentum equation (6.92).

Firstly, we need to determine analytical expressions for the normal stresses $\hat{t}^{\zeta\zeta}$ and $\hat{t}^{\xi\xi}$. Since the main purpose of the scaling simplifications is to obtain a final partial differential equation system that will be at least accurate of order $O(\varepsilon)$, we are allowed to use two different approximating formulae for the normal stresses. In fact, in order to calculate the depth averaged term $\overline{\hat{\sigma}_1}$, it is sufficient to have an order ε^α accuracy, because this term is further multiplied by ε in Eq. (6.92) and, thus, the final quantity is of order $\varepsilon^{1+\alpha}$ (e.g. Tai and Kuo, 2008). On the contrary, the quantity $\hat{\sigma}_2$ at the interface needs to be calculated with a better accuracy.

By using the second component of Eq. (6.92) and following a reasoning similar to that employed in Tai and Kuo (2008), it can be shown that the analytical expression of the normal stress $\hat{t}^{\zeta\zeta}$ along the upper layer flow depth, can be written as follows

$$\boxed{\hat{t}^{\zeta\zeta}(\hat{\zeta}) = (\sin \vartheta \sin \delta - \cos \vartheta \cos \delta) (\hat{s} - \hat{\zeta}) + O(\varepsilon^\alpha).} \quad (6.93)$$

Please note that $\hat{s} - \hat{\zeta}$ is the distance of a given point with coordinate $\hat{\zeta}$ from the free surface, thus, Eq. (6.93) corresponds to the hydrostatic assumption, obtained in a less rigorous way by simply applying the long-wave approximation (cf. Chapter 4).

Such an expression is used for calculating the depth averaged normal stress, as follows

$$\begin{aligned} h_1 \overline{\hat{t}^{\zeta\zeta}} &= \int_0^{\hat{s}} \hat{t}^{\zeta\zeta} d\hat{\zeta} = \int_0^{\hat{s}} \left[(\sin \vartheta \sin \delta - \cos \vartheta \cos \delta) (\hat{s} - \hat{\zeta}) + O(\varepsilon^\alpha) \right] d\hat{\zeta} \\ &= (\sin \vartheta \sin \delta - \cos \vartheta \cos \delta) \frac{\hat{h}_1^2}{2} + O(\varepsilon^\alpha). \end{aligned} \quad (6.94)$$

Now, we need to find an analytic expression for the longitudinal normal pressure $\hat{t}^{\xi\xi}$, in order to calculate $\overline{\hat{\sigma}_1}$. For the sake of simplicity, in this model we assume that the pressure coefficient K relating $\hat{t}^{\zeta\zeta}$ and $\hat{t}^{\xi\xi}$ is equal to 1. If the local basis was normalized, i.e. with the same metric of Cartesian frame of reference, it would be simply $\hat{t}^{\xi\xi} = \hat{t}^{\zeta\zeta}$. Nevertheless, we have to deal with the metric of the curvilinear frame of reference. In this regard, it can be easily shown that

$$\hat{t}^{\xi\xi} = \frac{1}{G_{11}} \hat{t}^{\zeta\zeta} = \cos^2 \vartheta \hat{t}^{\zeta\zeta} \quad (6.95)$$

where G_{11} is the first element of the metric tensor (B.16), i.e. $G_{11} = (\mathbf{g}_\xi \cdot \mathbf{g}_\xi)^{-1}$. Thus, the depth averaged normal stress $\overline{t^{\xi\xi}}$ reads

$$\hat{h}_1 \overline{t^{\xi\xi}} = \cos^2 \vartheta (\sin \vartheta \sin \delta - \cos \vartheta \cos \delta) \frac{\hat{h}_1^2}{2} + O(\varepsilon^\alpha). \quad (6.96)$$

Differently, we need to use a more accurate expression for $\hat{t}^{\zeta\zeta}$ in order to calculate $\hat{\sigma}_2|$ at the interface. By still using the second component of Eq. (6.92), it can be easily shown the expression for $\hat{t}^{\zeta\zeta}|_{\hat{z}}$ with accuracy of order ε is the following

$$\hat{t}^{\zeta\zeta}|_{\hat{z}} = (\sin \vartheta \sin \delta - \cos \vartheta \cos \delta) \hat{h}_1 - \varepsilon^\alpha J_0 l \hat{h}_1 \overline{v^\xi} - \varepsilon^\alpha J_0^2 k \hat{h}_1 (\overline{v^\xi})^2 + O(\varepsilon). \quad (6.97)$$

where the first term, of order zero, represents the hydrostatic contribution. Instead, the second and the third terms take into account the curvatures of the reference curve. These terms should be regarded as fictitious forces, that arise because of the curvature (in time and space) of the reference frame.

6.4.5 Expressions of the mixed tensor elements

Now, it is possible to write the analytic expressions of the mixed tensor element Σ , so as to calculate $\overline{\hat{\sigma}_1}$ and $\hat{\sigma}_2$ at the interface, that are in Eq. (6.92). Firstly, thanks to the scaling of Ω (6.79), it is possible to write

$$\begin{pmatrix} \sigma_1 & \sigma_2 \\ \sigma_3 & \sigma_4 \end{pmatrix} = \Omega \begin{pmatrix} t^{\xi\xi} & t^{\xi\zeta} \\ t^{\zeta\xi} & t^{\zeta\zeta} \end{pmatrix} = \Omega_0 \begin{pmatrix} t^{\xi\xi} & t^{\xi\zeta} \\ t^{\zeta\xi} & t^{\zeta\zeta} \end{pmatrix} + O(\varepsilon^{\alpha+1}). \quad (6.98)$$

The depth-averaged term $\overline{\hat{\sigma}_1}$

By using the scaling of stresses (6.64) - (6.66), we obtain

$$\sigma_1 = t^{\xi\xi} + \sin \vartheta t^{\xi\zeta} + O(\varepsilon^{\alpha+1}) \Rightarrow \hat{\sigma}_1 = \hat{t}^{\xi\xi} + \varepsilon^\beta \sin \vartheta \hat{t}^{\xi\zeta} + O(\varepsilon^{\alpha+1}). \quad (6.99)$$

Thanks to Eq. (6.98), it follows that

$$\overline{\hat{\sigma}_1} = \overline{\hat{t}^{\xi\xi}} + \varepsilon^\beta \sin \vartheta \overline{\hat{t}^{\xi\zeta}} + O(\varepsilon^{\alpha+1}). \quad (6.100)$$

Therefore, the term $\partial_{\hat{\xi}} (\varepsilon J_0 \hat{h}_1 \overline{\hat{t}^{\xi\xi}})$ in Eq. (6.92) can be recast as follows

$$\begin{aligned} \frac{\partial}{\partial \hat{\xi}} (\varepsilon J_0 \hat{h}_1 \overline{\hat{\sigma}_1}) &= \varepsilon \frac{\partial}{\partial \hat{\xi}} (J_0 \hat{h}_1 \overline{\hat{t}^{\xi\xi}}) + \varepsilon^{\beta+1} \frac{\partial}{\partial \hat{\xi}} (J_0 \hat{h}_1 \sin \vartheta \overline{\hat{t}^{\xi\zeta}}) \\ &= \varepsilon \frac{\partial}{\partial \hat{\xi}} (J_0 \hat{h}_1 \overline{\hat{t}^{\xi\xi}}) + O(\varepsilon^{\beta+1}). \end{aligned} \quad (6.101)$$

in which $\hat{h}_1 \overline{\hat{t}^{\xi\xi}}$ can be calculated by means of Eq. (6.96).

The term $\hat{\sigma}_2$

Analogously, by using Eq. (6.98), σ_2 can be written as follows

$$\sigma_2 = t^{\zeta\zeta} + \sin \vartheta t^{\zeta\zeta} + O(\varepsilon^{\alpha+1}) \Rightarrow \hat{\sigma}_2 = \varepsilon^\beta \hat{t}^{\zeta\zeta} + \sin \vartheta \hat{t}^{\zeta\zeta} + O(\varepsilon^{\alpha+1}). \quad (6.102)$$

According to the assumptions made about the constitutive law at the interface (cf. Eq. (6.25)), we postulate that the shear stress $t^{\zeta\zeta}$ at the interface is composed of two terms, a Coulomb friction term and a rate-dependent term. In order to find a proper scaling of this term, some assumptions are required. In this regard, it is assumed that $\|\Delta \mathbf{v}_t\|$ is of order $\varepsilon^\iota \sqrt{gL}$, with ι fulfilling the following condition

$$\beta' \iota - 1 \geq \beta \quad (6.103)$$

so as to the contribution, due to the rate-dependent term, is not dominant over the friction term in $t^{\zeta\zeta}$. Such an assumption is physically reasonable because the rate-dependent shear stress is expected to be smaller or at least of the same order of the friction term in dense collisional regime. In this fashion, $t^{\zeta\zeta}$ is still assumed to be of order ε^β , like in the classical Savage-Hutter type models (Savage and Hutter, 1989; Gray et al., 1999).

By making explicit this scaling, Eq. (6.25) can be recast as follows

$$\begin{aligned} \rho_1 g H \hat{\sigma}_2 &= \rho_1 g H \cos \vartheta \operatorname{sgn}(\hat{v}^\xi - \hat{w}^\xi) k \tan \varphi_{int} (-\hat{t}^{\zeta\zeta}) \\ &+ \rho_1 \left(\sqrt{gL}\right)^{\beta'} \cos \vartheta \operatorname{sgn}(\hat{v}^\xi - \hat{w}^\xi) r \frac{(\hat{v}^\xi - \hat{w}^\xi)^{\beta'}}{\cos^2 \vartheta} + \rho_1 g H \sin \vartheta \hat{t}^{\zeta\zeta} \end{aligned} \quad (6.104)$$

where $\hat{t}^{\zeta\zeta}$ can be calculated by means of Eq. (6.97), which has order ε accuracy. After some simplifications the factor, it is recast as

$$\hat{\sigma}_2 = \cos \vartheta \operatorname{sgn}(\hat{v}^\xi - \hat{w}^\xi) k \tan \varphi_{int} (-\hat{t}^{\zeta\zeta}) + \varepsilon^{-1} \cos \vartheta \operatorname{sgn}(\hat{v}^\xi - \hat{w}^\xi) r \frac{(\hat{v}^\xi - \hat{w}^\xi)^{\beta'}}{\cos^2 \vartheta} + \sin \vartheta \hat{t}^{\zeta\zeta}. \quad (6.105)$$

6.5 The scaling of the lower layer equations

Analogously to what done for the upper layer, we now deal with the scalings of the main physical quantities, involved in the lower layer flow dynamics. The following scalings are assumed

$$(x, z) = L (\hat{x}, \varepsilon \hat{z}), \quad (6.106)$$

$$(w_x, w_z) = \sqrt{gL} (\hat{w}_x, \varepsilon \hat{w}_z), \quad (6.107)$$

$$(t_{2,xx}, t_{2,zz}) = \rho_2 g H (\hat{t}_{2,xx}, \hat{t}_{2,zz}), \quad (6.108)$$

$$(t_{2,xz}) = \rho_2 g H \tan \varphi_b (\hat{t}_{2,xz}) = \rho_2 g H \varepsilon^\beta (\hat{t}_{2,xz}), \quad (6.109)$$

$$(t) = \sqrt{L/g} (\hat{t}). \quad (6.110)$$

where H and L are the same lengths, used in the previous scaling, corresponding to the characteristic total flow depth and to the characteristic avalanche spread, respectively. Moreover, also in this case, it is assumed $\varepsilon = H/L \ll 1$ and it is considered an infinitesimal function. The aforementioned scalings are in accordance with many other works on the Savage-Hutter type models (e.g. Gray et al., 1999).

6.5.1 Dimensionless depth-averaged lower layer mass equation

With the help of the Eqs. (6.106) - (6.110), the depth-averaged mass equation of the lower layer (6.48) can be recast as follows

$$\frac{H}{\sqrt{L/g}} \frac{\partial}{\partial \hat{t}} \left(\hat{h}_2 \int_0^1 d\hat{z} \right) + \frac{H\sqrt{gL}}{L} \frac{\partial}{\partial \hat{x}} \left(\hat{h}_2 \int_0^1 \hat{w}_x d\hat{z} \right) = -\frac{H}{L} \sqrt{gL} \frac{\hat{M}_{flu_x}}{\hat{\rho}_2} \|\nabla_{\mathbf{x}} F_i\| \quad (6.111)$$

where $\hat{h}_2 = \hat{z}_i$ is the lower flow depth, measured in z direction. After simplifying all the scaling factors and by using the notation for depth-averaged quantities, Eq. (6.111) is recast

$$\boxed{\frac{\partial}{\partial \hat{t}} (\hat{h}_2) + \frac{\partial}{\partial \hat{x}} (\hat{h}_2 \overline{\hat{w}_x}) = -\frac{\hat{M}_{flu_x}}{\hat{\rho}_2} \|\nabla_{\mathbf{x}} F_i\|} \quad (6.112)$$

It is interesting to note that no negligible terms have been found in Eq. (6.112).

6.5.2 Dimensionless depth-averaged lower layer momentum equation

Similarly, with the help of the scaling (6.106) - (6.110), the x component of the depth-averaged momentum equation of the lower layer (6.50) can be recast as follows

$$\begin{aligned} & \sqrt{\frac{g}{L}} H \sqrt{gL} \frac{\partial}{\partial \hat{t}} \left(\hat{h}_2 \int_0^1 \hat{w}_x d\hat{z} \right) + \frac{1}{L} H \sqrt{gL} \sqrt{gL} \frac{\partial}{\partial \hat{x}} \left(\hat{h}_2 \int_0^1 \hat{w}_x^2 d\hat{z} \right) \\ & - \frac{H}{L} gH \frac{\partial}{\partial \hat{x}} \left(\hat{h}_2 \int_0^1 \hat{t}_{2,xx} d\hat{z} \right) = gH \hat{h}_2 \sin \vartheta + \varepsilon^\beta gH \left(\hat{t}_{2,xz} \Big|_{\hat{z}_i} - \hat{t}_{2,xz} \Big|_{\hat{b}} \right) \\ & - \frac{gH^2}{L} \hat{t}_{2xx} \Big|_{\hat{z}_i} \frac{\partial \hat{z}_i}{\partial \hat{x}} - \sqrt{gL} \frac{H}{L} \sqrt{gL} \hat{w}_x \Big|_{\hat{z}_i} \frac{\hat{M}_{flu_x}}{\hat{\rho}_2} \|\nabla_{\mathbf{x}} F_i\| \end{aligned} \quad (6.113)$$

where $\hat{b} = 0$. After some simplification and with the help of the notation for depth-averaged quantities, it is recast

$$\boxed{\begin{aligned} & \frac{\partial}{\partial \hat{t}} (\hat{h}_2 \overline{\hat{w}_x}) + \frac{\partial}{\partial \hat{x}} (\hat{h}_2 \overline{\hat{w}_x^2}) - \varepsilon \frac{\partial}{\partial \hat{x}} (\hat{h}_2 \overline{\hat{t}_{2,xx}}) = \hat{h}_2 \sin \vartheta \\ & + \varepsilon^\beta \hat{t}_{2,xz} \Big|_{\hat{z}_i} - \varepsilon^\beta \hat{t}_{2,xz} \Big|_{\hat{b}} - \varepsilon \hat{t}_{2xx} \Big|_{\hat{z}_i} \frac{\partial \hat{z}_i}{\partial \hat{x}} - \hat{w}_x \Big|_{\hat{z}_i} \frac{\hat{M}_{flu_x}}{\hat{\rho}_2} \|\nabla_{\mathbf{x}} F_i\| \end{aligned}} \quad (6.114)$$

Obviously, it is necessary to provide analytic expressions for the quantities $\overline{\hat{t}_{2,xx}}$, $\hat{t}_{2,xz} \Big|_{\hat{b}}$ and $\hat{t}_{2,xz} \Big|_{\hat{z}_i}$ in Eq. (6.112). Moreover, some assumptions about the velocity profile in the low layer are required to calculate the depth-averaged quantities, $\overline{\hat{w}_x}$, $\overline{\hat{w}_x^2}$, together with the velocity at the interface $\hat{w}_x \Big|_{\hat{z}_i}$.

Dimensionless shear stress at the basal surface

As regards the basal shear stress in Eq. (6.112), expression (6.41) can be recast in its dimensionless form as follows

$$\boxed{\varepsilon^\beta \hat{t}_{2,xz} \Big|_{\hat{b}} = -\operatorname{sgn}(\hat{w}_x) \tan \varphi_b \hat{t}_{2,zz}.} \quad (6.115)$$

Normal stresses in the lower layer

We need to define the normal stresses distribution in the lower layer, so as to calculate the depth-averaged quantity $\overline{\hat{t}_{xx}}$ in Eq. (6.114). It can be easily shown that the z component of the depth-averaged momentum equation in dimensionless form, can be written as follows

$$\partial_{\hat{z}} \hat{t}_{2,zz} = \cos \delta + O(\varepsilon). \quad (6.116)$$

Then, by integrating Eq. (6.116) between the interface Γ and a given depth z , we obtain

$$\int_{\hat{z}}^{\hat{z}_i} \partial_{\hat{z}} \hat{t}_{2,zz} d\hat{\zeta} = \int_{\hat{z}}^{\hat{z}_i} \cos \delta d\hat{\zeta} \Rightarrow \boxed{\hat{t}_{2,zz}|_{\hat{z}} = \hat{t}_{2,zz}|_{\hat{z}_i} - \cos \delta (\hat{z}_i - \hat{z})}, \quad (6.117)$$

namely, the normal stress, $t_{2,zz}$, exhibits an hydrostatic distribution to order $O(\varepsilon)$. Obviously, it is now required to define the quantity $\hat{t}_{2,zz}|_{\hat{z}_i}$, that corresponds to the normal stress at the interface Γ . By using Eq. (6.56) together with the scaling of M_{flux} (6.72), it can be easily shown that $t_1^{\zeta\zeta} - t_2^{\zeta\zeta} = O(\varepsilon^2)$, therefore we can assume that $t_1^{\zeta\zeta} \approx t_2^{\zeta\zeta}$, without impairing the global accuracy of the mathematical model. The elements of the stress tensor in Cartesian components can be calculated simply by applying the transformation formula, $T = \Omega T^* \Omega^T$ (cf. Eq. (A.12)),

$$\begin{aligned} \begin{pmatrix} t_{2,xx} & t_{2,xz} \\ t_{2,zx} & t_{2,zz} \end{pmatrix} \Big|_{z_i} &= \begin{pmatrix} 1 & \sin \vartheta \\ -\tan \vartheta & \cos \vartheta \end{pmatrix} \begin{pmatrix} t_2^{\xi\xi} & t_2^{\xi\zeta} \\ t_2^{\zeta\xi} & t_2^{\zeta\zeta} \end{pmatrix} \Big|_i \begin{pmatrix} 1 & -\tan \vartheta \\ \sin \vartheta & \cos \vartheta \end{pmatrix} \\ &= \begin{pmatrix} t^{\zeta\zeta} + 2 \sin \vartheta t^{\xi\zeta} & t^{\xi\zeta} (\cos^2 \vartheta - \sin^2 \vartheta) / \cos \vartheta \\ t^{\xi\zeta} (\cos^2 \vartheta - \sin^2 \vartheta) / \cos \vartheta & t^{\zeta\zeta} - 2 \sin \vartheta t^{\xi\zeta} \end{pmatrix} \end{aligned} \quad (6.118)$$

obtained with the help of Eq. (6.95). Then, by using the scaling relations (6.64), (6.66), (6.108) and (6.109), it is possible to write the same relation in dimensionless form

$$\begin{pmatrix} \hat{t}_{2,xx} & \varepsilon^\beta \hat{t}_{2,xz} \\ \varepsilon^\beta \hat{t}_{2,zx} & \hat{t}_{2,zz} \end{pmatrix} \Big|_{\hat{z}_i} = \frac{\rho_1}{\rho_2} \begin{pmatrix} \hat{t}_2^{\zeta\zeta} + \varepsilon^\beta 2 \sin \vartheta \hat{t}_2^{\xi\zeta} & \varepsilon^\beta \hat{t}_2^{\xi\zeta} (\cos^2 \vartheta - \sin^2 \vartheta) / \cos \vartheta \\ \varepsilon^\beta \hat{t}_2^{\xi\zeta} (\cos^2 \vartheta - \sin^2 \vartheta) / \cos \vartheta & \hat{t}_2^{\zeta\zeta} - \varepsilon^\beta 2 \sin \vartheta \hat{t}_2^{\xi\zeta} \end{pmatrix} \Big|_{\hat{z}_i}. \quad (6.119)$$

Now, since in Eq. (6.114) the two terms which require the calculation of \hat{t}_{xx} or \hat{t}_{zz} are both multiplied by ε , it is possible to simplify these quantities as follows

$$\hat{t}_{2,xx}|_{\hat{z}_i} \approx \hat{t}_{2,zz}|_{\hat{z}_i} = \frac{\rho_1}{\rho_2} \hat{t}_2^{\zeta\zeta}|_{\hat{z}_i} + O(\varepsilon^\beta) \quad (6.120)$$

without impairing the global accuracy of the model. In this way Eq. (6.114) has an accuracy of order $\varepsilon^{1+\beta}$.

In the present model, for the sake of simplicity we assume that the pressure coefficient to write $t_{2,xx}$ as function of $t_{2,zz}$ is equal to 1 everywhere along the lower layer flow depth and, thus, $\hat{t}_{2,xx} = \hat{t}_{2,zz}$.

By depth integrating over the lower layer flow depth we finally get

$$\boxed{\hat{h}_2 \overline{\hat{t}_{2,xx}} = \hat{h}_2 \overline{\hat{t}_{2,zz}} = \hat{t}_{2,zz}|_{\hat{z}_i} \hat{h}_2 - \cos \delta \frac{\hat{h}_2^2}{2} = \frac{\rho_1}{\rho_2} \hat{t}_2^{\zeta\zeta}|_{\hat{z}_i} \hat{h}_2 - \cos \delta \frac{\hat{h}_2^2}{2}} \quad (6.121)$$

Dimensionless shear stress at the interface

By using Eq. (6.119) it is possible also to express the term, $\hat{t}_{2,xz}$, at the interface as function of $\hat{t}_2^{\xi\zeta}$. More precisely, it follows

$$\hat{t}_{2,xz}|_{\hat{z}_i} = \frac{\rho_1}{\rho_2} \frac{(\cos^2\vartheta - \sin^2\vartheta)}{\cos\vartheta} \hat{t}_2^{\xi\zeta}|_{\hat{z}_i}. \quad (6.122)$$

where the quantity $\hat{t}_2^{\xi\zeta}$ is the dimensionless form of expression (6.46).

6.6 Hypotheses about the velocity distribution

Upper layer

As regards the upper layer, in order to define the depth-averaged quantities in Eqs. (6.88) and (6.92), such as $\overline{\hat{v}^\xi}$, $\overline{\hat{v}_x}$, $\overline{\hat{v}_x \hat{v}^\xi}$, $\overline{\hat{v}_x \hat{q}^\xi}$ and $\hat{v}^\xi|_{\hat{z}_i}$, it is necessary to make some assumptions about the velocity distribution.

At this stage of investigation, it is simply assumed that the velocity profile is almost uniform along the flow depth. This assumption is quite common in Savage-Hutter type models (e.g. Gray et al., 1999), though it is far from being realistic in some experimental cases, especially in case of no-slip bottom boundary condition (cf. Chapter 3). More precisely, we assume that

$$\hat{v}^\xi(\zeta) = \overline{v^\xi} + O(\varepsilon^{\gamma+1}). \quad (6.123)$$

It follows that

$$\hat{v}^\xi|_{\hat{z}_i} = \overline{v^\xi} + O(\varepsilon^{\gamma+1}). \quad (6.124)$$

where $0 < \gamma \leq 1$. With the aim of calculating the components of the flow velocity in Cartesian coordinates, we employ the Contravariant transformation (A.9) and the scaling of Ω^{-1} (6.81),

$$\begin{pmatrix} v_x \\ v_z \end{pmatrix} = \Omega \begin{pmatrix} v^\xi \\ v^\zeta \end{pmatrix} = \Omega_0 \begin{pmatrix} v^\xi \\ v^\zeta \end{pmatrix} + O(\varepsilon^{\alpha+1}) \approx \sqrt{gL} \Omega_0 \begin{pmatrix} \hat{v}^\xi \\ \varepsilon \hat{v}^\zeta \end{pmatrix} = \sqrt{gL} \Omega_0 \begin{pmatrix} \hat{v}^\xi \\ 0 \end{pmatrix} + O(\varepsilon). \quad (6.125)$$

Therefore, it follows that

$$v_x = v^\xi + \sin\vartheta v^\zeta = v^\xi + O(\varepsilon). \quad (6.126)$$

Then, by using the notation for depth-averaged quantities, we obtain

$$\overline{\hat{v}^\xi} \approx \overline{\hat{v}_x}, \quad (6.127)$$

$$\hat{v}^\xi|_{\hat{z}_i} \approx \overline{\hat{v}_x}, \quad (6.128)$$

$$\overline{\hat{v}^\xi \hat{v}^\xi} = (\overline{\hat{v}_x})^2 + O(\varepsilon^{\gamma+1}), \quad (6.129)$$

$$\overline{\hat{v}_x \hat{v}^\xi} = (\overline{\hat{v}_x})^2 + O(\varepsilon). \quad (6.130)$$

These relations will be used in Eqs. (6.88) and (6.92).

Mesh velocity

Thanks to the Contravariant transformation (A.9) and the scaling of Ω^{-1} (6.81), the ξ -component of the mesh velocity can be written as

$$\begin{pmatrix} q^\xi \\ q^\zeta \end{pmatrix} = \Omega_0^{-1} \begin{pmatrix} q_x \\ q_z \end{pmatrix} + O(\varepsilon^{\alpha+1}) \Rightarrow q^\xi = \cos^2 \vartheta q_x - \sin \vartheta \cos \vartheta q_z, \quad (6.131)$$

then, with the help of the scaling of q_x and q_z , Eqs. (6.76) and (6.77), it is recast as follows

$$q^\xi = \cos^2 \vartheta q_{x,0} - \sin \vartheta \cos \vartheta q_{z,0} + O(\varepsilon^{\alpha+1}) = -\sin \vartheta \cos \vartheta q_{z,0} + O(\varepsilon^{\alpha+1}). \quad (6.132)$$

Finally, we obtain the depth-averaged quantity

$$\overline{q^\xi} = \overline{\hat{q}_0^\xi} + O(\varepsilon^{\alpha+1}) = -\sin \vartheta \cos \vartheta \hat{q}_{z,0} + O(\varepsilon^{\alpha+1}), \quad (6.133)$$

From Eq. (6.133) it follows that

$$\overline{\hat{v}_x \hat{q}^\xi} = \overline{\hat{v}_x} \overline{\hat{q}^\xi} + O(\varepsilon). \quad (6.134)$$

This relation will be used in the depth-averaged momentum equation, (6.92), in order to calculate the term $\overline{\hat{v}_x \hat{q}^\xi}$.

6.6.1 Lower layer

As well, some assumptions on the lower layer velocity profile are required. Similarly, we assume that the velocity profile is almost uniform also in the lower layer. It follows that

$$\hat{w}_x = \overline{\hat{w}_x} + O(\varepsilon^{\gamma+1}), \quad (6.135)$$

$$\hat{w}_x|_{\hat{z}_i} = \overline{\hat{w}_x} + O(\varepsilon^{\gamma+1}), \quad (6.136)$$

$$(\hat{w}_x)^2 = \overline{\hat{w}_x^2} + O(\varepsilon^{\gamma+1}). \quad (6.137)$$

6.7 The final equations

In this section, the final equations of the two-layer model, written in mixed coordinates, are presented. The depth-averaged dimensionless balance equations, referred to both of layers, i.e. Eqs. (6.88), (6.92), (6.112) and (6.114), are considered here, after dropping all terms of order $O(\varepsilon^{1+\alpha})$ or smaller. Moreover, Eqs. (6.127), (6.128), (6.129), (6.130), (6.135), (6.136), (6.137) are used in order to write all the terms as functions of only the two depth-averaged flow velocities, $\overline{\hat{v}_x}$ and $\overline{\hat{w}_x}$.

The resulting PDE system can be written as follows

$$\frac{\partial}{\partial \bar{\lambda}} \left(J_0 \hat{h}_1 \right) + \frac{\partial}{\partial \bar{\xi}} \left(J_0 \hat{h}_1 \left(\bar{v}_x - \varepsilon \bar{q}^\xi \right) \right) = J_0 \frac{\hat{M}_{flux}}{\hat{\rho}_1} \quad (6.138)$$

$$\frac{\partial}{\partial \bar{\lambda}} \left(J_0 \hat{h}_1 \bar{v}_x \right) + \frac{\partial}{\partial \bar{\xi}} \left(J_0 \hat{h}_1 \bar{v}_x \left(\bar{v}_x - \varepsilon \bar{q}^\xi \right) - \varepsilon J_0 \hat{h}_1 \bar{\sigma}_1 \right) = J_0 \hat{h}_1 \sin \vartheta - J_0 \hat{\sigma}_2|_i + J_0 \bar{v}_x \frac{\hat{M}_{flux}}{\hat{\rho}_1} \quad (6.139)$$

$$\frac{\partial}{\partial \hat{t}} \left(\hat{h}_2 \right) + \frac{\partial}{\partial \hat{x}} \left(\hat{h}_2 \bar{w}_x \right) = - \frac{\hat{M}_{flux}}{\hat{\rho}_2} \|\nabla_{\mathbf{x}} F_i\| \quad (6.140)$$

$$\begin{aligned} \frac{\partial}{\partial \hat{t}} \left(\hat{h}_2 \bar{w}_x \right) + \frac{\partial}{\partial \hat{x}} \left(\hat{h}_2 \left(\bar{w}_x \right)^2 - \varepsilon \hat{h}_2 \bar{t}_{2,xx} \right) = \\ \hat{h}_2 \sin \vartheta + \varepsilon^\beta \hat{t}_{2,xz}|_{\hat{z}_i} - \varepsilon^\beta \hat{t}_{2,xz}|_{\hat{b}} - \varepsilon \hat{t}_{2,xx}|_{\hat{z}_i} \frac{\partial \hat{h}_2}{\partial \hat{x}} - \bar{w}_x \frac{\hat{M}_{flux}}{\hat{\rho}_2} \|\nabla_{\mathbf{x}} F_i\|, \end{aligned} \quad (6.141)$$

in which the vector of unknowns is $\mathbf{u} = \left(J_0 \hat{h}_1, J_0 \hat{h}_1 \bar{v}_x, \hat{h}_2, \hat{h}_2 \bar{w}_x \right)^T$.

As regards the upper layer equations (6.138) and (6.139), there are some terms that need to be expressed as function of the unknowns. In particular, thanks to Eqs. (6.96) and (6.101), the term $\hat{h}_1 \bar{\sigma}_1$ can be written as

$$\hat{h}_1 \bar{\sigma}_1 \approx \hat{h}_1 \bar{t}^{\xi\xi} = \frac{1}{2} \cos^2 \vartheta \left(\sin \vartheta \sin \delta - \cos \vartheta \cos \delta \right) \hat{h}_1^2 + O\left(\varepsilon^{1+\gamma}\right). \quad (6.142)$$

with $\gamma = \min(\alpha, \beta)$.

Moreover, $\hat{\sigma}_2$ at the interface is defined by means of Eq. (6.105), here reported again

$$\hat{\sigma}_2 = \cos \vartheta \operatorname{sgn}(\hat{v}^\xi - \hat{w}^\xi) k \tan \varphi_{int}(-\hat{t}^{\zeta\zeta}|_i) + \varepsilon^{-1} \cos \vartheta \operatorname{sgn}(\hat{v}^\xi - \hat{w}^\xi) r \frac{(\hat{v}^\xi - \hat{w}^\xi)^{\beta'}}{\cos^2 \vartheta} + \sin \vartheta \hat{t}^{\zeta\zeta}|_i, \quad (6.143)$$

where $\hat{t}^{\zeta\zeta}|_i$ can be calculated by means of Eq. (6.97), accurate to order (ε) . The ξ component of the lower layer flow velocity w at the interface in Eq. (6.143) can be calculated by means of the contravariant formula. Eq. (A.9)

$$\hat{w}^\xi|_{\hat{z}_i} = \cos^2 \vartheta \hat{w}_x|_{\hat{z}_i} - \varepsilon \sin \vartheta \cos \vartheta \hat{w}_z|_{\hat{z}_i} = \cos^2 \vartheta \hat{w}_x|_{\hat{z}_i} + O(\varepsilon) = \cos^2 \vartheta \bar{w}_x|_{\hat{z}_i} + O(\varepsilon). \quad (6.144)$$

Finally, the term \bar{q}^ξ , which is the depth-averaged value of the ξ -component of the mesh velocity \mathbf{q} , can be calculated with the help of Eq. (6.133) and (6.59) as follows

$$\bar{q}^\xi \approx \bar{q}_0^\xi = -(\sin \vartheta \cos \vartheta) \hat{q}_{z,0} = -(\sin \vartheta \cos \vartheta) \partial_i \hat{h}_2. \quad (6.145)$$

which is accurate to order $O(\varepsilon^{\alpha+1})$.

Similarly, we need to make explicit some terms in the lower layer equations (6.140) and (6.141). In particular, the term $\hat{h}_2 \bar{t}_{2,xx}$ in Eq. (6.141) can be calculated by means of Eq. (6.121),

$$\hat{h}_2 \bar{t}_{2,xx} = \hat{h}_2 \bar{t}_{2,zz} = \hat{t}_{2,zz}|_{\hat{z}_i} \hat{h}_2 - \cos \delta \frac{\hat{h}_2^2}{2} = \frac{\rho_1}{\rho_2} \hat{t}^{\zeta\zeta}|_i \hat{h}_2 - \cos \delta \frac{\hat{h}_2^2}{2}. \quad (6.146)$$

in which the term $\hat{t}^{\zeta\zeta}|_i$ can be calculated by mean of the Eq. (6.93), accurate to order $O(\varepsilon^\alpha)$. The same expression can be used also for calculating the term $\varepsilon \hat{t}_{2,xx}|_{\hat{z}_i} \partial_i \hat{h}_2$, so that the overall accuracy of this term is to order $O(\varepsilon^{1+\alpha})$.

Moreover, the shear stress at the bottom, $\hat{t}_{2,xz}|_{\hat{b}}$, is simply calculated thanks to Eq. (6.115) that is reported as follows

$$\varepsilon^\beta \hat{t}_{2,xz}|_{\hat{b}} = -\operatorname{sgn}(\hat{w}_x) \tan \varphi_b \hat{t}_{2,zz} = \operatorname{sgn}(\hat{w}_x) \tan \varphi_b \left(\cos \delta \hat{h}_2 - \frac{\rho_1}{\rho_2} \hat{t}^{\zeta\zeta}|_{\hat{i}} \right). \quad (6.147)$$

In this case, because the term $\varepsilon^\beta \hat{t}_{2,xz}|_{\hat{b}}$ is of order $O(\varepsilon^\beta)$, the order ε approximation of $\hat{t}^{\zeta\zeta}|_{\hat{i}}$ (cf. Eq. (6.97)) can be used, instead of that one accurate to order ε^α , since it is not known *a priori* whether $\alpha + \beta \geq 1$.

Analogously, the term $\hat{t}_{2,xz}|_{\hat{z}_i}$ can be expressed with the help of Eq. (6.122) as function of $\hat{t}_2^{\zeta\zeta}$ as follows

$$\hat{t}_{2,xz}|_{\hat{z}_i} = \frac{\rho_1}{\rho_2} \frac{(\cos^2 \vartheta - \sin^2 \vartheta)}{\cos \vartheta} \hat{t}_2^{\zeta\zeta}|_{\hat{i}} \quad (6.148)$$

It is useful, now, to rewrite System (6.138)-(6.139)- (6.140)-(6.141) in a slightly different form. With the help of the product rule of partial differentiation, it is possible to write the term $\varepsilon \hat{h}_2 \hat{t}_{2,xz}$ as follows

$$\partial_{\hat{x}} \left(-\varepsilon \hat{h}_2 \overline{\hat{t}_{2,xz}} \right) = \varepsilon \partial_{\hat{x}} \left[\cos \delta \frac{\hat{h}_2^2}{2} - \frac{\rho_1}{\rho_2} \hat{t}^{\zeta\zeta} \hat{h}_2 \right] = \varepsilon \partial_{\hat{x}} \left(\cos \delta \frac{\hat{h}_2^2}{2} \right) - \varepsilon \hat{h}_2 \partial_{\hat{x}} \left(\frac{\rho_1}{\rho_2} \hat{t}^{\zeta\zeta} \right) - \varepsilon \frac{\rho_1}{\rho_2} \hat{t}^{\zeta\zeta} \left(\partial_{\hat{x}} \hat{h}_2 \right). \quad (6.149)$$

Therefore by substituting Eq. (6.149) into Eq. (6.141) and after some further manipulations, the PDE System can be rewritten as follows

$$\frac{\partial}{\partial \hat{\lambda}} \left(J_0 \hat{h}_1 \right) + \frac{\partial}{\partial \hat{\xi}} \left(J_0 \hat{h}_1 \left(\overline{\hat{v}_x} - \varepsilon \overline{\hat{q}^\xi} \right) \right) = J_0 \frac{M_{flux}}{\rho_1} \quad (6.150)$$

$$\begin{aligned} \frac{\partial}{\partial \hat{\lambda}} \left(J_0 \hat{h}_1 \overline{\hat{v}_x} \right) + \frac{\partial}{\partial \hat{\xi}} \left(J_0 \hat{h}_1 \overline{\hat{v}_x} \left(\overline{\hat{v}_x} - \varepsilon \overline{\hat{q}^\xi} \right) + \varepsilon \frac{1}{2} \cos^3 \vartheta (\cos \vartheta \cos \delta - \sin \vartheta \sin \delta) J_0^2 \hat{h}_1^2 \right) = \\ \sin \delta J_0 \hat{h}_1 - J_0 \hat{\sigma}_2|_{\hat{i}} + J_0 \overline{\hat{v}_{1,x}} \frac{M_{flux}}{\rho_1} \end{aligned} \quad (6.151)$$

$$\frac{\partial \hat{h}_2}{\partial \hat{t}} + \frac{\partial \left(\hat{h}_2 \overline{w_x} \right)}{\partial \hat{x}} = -J_0 \frac{M_{flux}}{\rho_2} \quad (6.152)$$

$$\begin{aligned} \frac{\partial}{\partial \hat{t}} \left(\hat{h}_2 \overline{w_x} \right) + \frac{\partial}{\partial \hat{x}} \left(\left(\overline{w_x} \right)^2 \hat{h}_2 + \varepsilon \frac{1}{2} \cos \delta \hat{h}_2^2 \right) = \\ \sin \delta \hat{h}_2 + \varepsilon^\beta \left(\hat{t}_{2,xz}|_{\hat{i}} - \hat{t}_{2,xz}|_{\hat{b}} \right) + \varepsilon \hat{h}_2 \frac{\rho_1}{\rho_2} \frac{\partial}{\partial \hat{x}} \left((\sin \vartheta \sin \delta - \cos \vartheta \cos \delta) \hat{h}_1 \right) - J_0 \overline{w_x} \frac{M_{flux}}{\rho_2}. \end{aligned} \quad (6.153)$$

Given the assumptions made above, the overall accuracy of the present model is at least of order $O(\varepsilon)$. This system has to be equipped with the closure equation for calculating M_{flux} , (6.54), written in dimensionless form, where \hat{w}^ξ can be calculated by means of Eq. (6.144).

6.8 Discussion and conclusions

The proposed model has some valuable advantages with respect to the two-layer model, presented in Chapter 4.

At the first, it should be noted that the employment of scaling approximations is more rigorous than simply applying the *Long-wave approximation* and, it permits a more rational identification of physical negligible terms. Moreover, such a scaling procedure is very versatile, since it allows to

add or remove assumptions quite easily. Namely, after writing the model equations in dimensionless form, it is possible to obtain several final models, depending on the chosen order of accuracy.

As regards the hyperbolicity issues, it is interesting to note that no non-conservative terms, depending on the spatial derivative of the lower layer flow depth, are present in the upper layer depth-averaged momentum equation. This is due to the formulation of the upper layer equations in curvilinear coordinates. The coupling between the two layers is still present, but it appears in a more “diffused” form. Namely, the influence of the lower layer dynamics on the upper layer dynamics is incorporated in the topographic terms, depending on the interface inclination angle, ϑ . These terms are in $\hat{\sigma}_2|_{\hat{z}}$ and also in the flux function. Moreover, it should be noted that all these topographic terms are upper-bounded trigonometric functions of ϑ . This feature suggests that the issues related to the hyperbolicity loss could be avoided or reduced somehow. However, a further investigation about this topic is advisable.

Furthermore, it is important to highlight that the scaling analysis shows that the influence of the upper layer on the lower layer dynamics is weaker than the opposite. In fact, in Eq. (6.153) the only coupling with the upper layer flow dynamics is represented by the term $\varepsilon \hat{h}_2 \rho_1 / \rho_2 \partial_{\hat{x}} (\hat{i}^{\zeta\zeta})$, which is only of order $O(\varepsilon)$ and is also multiplied by $\rho_1 / \rho_2 < 1$. In case of $h_1 \ll h_2$, which is rather realistic in presence of a rheological stratification of the granular flow, this term could be simply neglected. It leads to the derivation of another simplified PDE model, still accurate of order $O(\varepsilon)$, which is hyperbolic.

As regards the numerical integration of the model, it should be noted that the eigenvalue structure of the whole system is not accessible because of different coordinate systems used for deriving Eqs. (6.150)-(6.151) and Eqs. (6.152)-(6.153). In the context of a numerical scheme, the eigenvalues calculation could be performed in a decoupled way. Namely, the eigenvalues of the Jacobian matrix of flux vectors can be calculated independently for each layer. The topographic terms, depending on ϑ , can be treated as spatial varying functions, that adapt in a non-instantaneous way, reminiscent of the relaxation approach proposed by Abgrall and Karni (2009). To this regard, a numerical implementation that makes use of an *f-wave* type finite volume scheme (Bale et al., 2002) is in progress.

Finally, the presented model can be regarded as a particular case of a more complex model that incorporates also basal topographic variations, below the lower layer. In this general case, also the lower layer equations could be written in curvilinear coordinates in order to better identify the physical negligible terms during the subsequent scaling approximation. Moreover, less simplistic assumptions about the velocity profiles inside each layer can be made in a further version of the model.

References Used in This Chapter

- Abgrall, R. and Karni, S. (2009). Two-Layer Shallow Water System: A Relaxation Approach. *SIAM Journal on Scientific Computing* **31**, 1603–1627.
- Bale, D. S., LeVeque, R. J., Mitran, S., and Rossmannith, J. A. (2002). A Wave Propagation Method for Conservation Laws and Balance Laws with Spatially Varying Flux Functions. *SIAM Journal on Scientific Computing* **24**, 955–978.
- Bouchut, F. and Westdickenberg, M. (2004). Gravity driven shallow water models for arbitrary topography. *Communications in Mathematical Sciences* **2**, 359–389.
- Gray, J. M. N. T., Wieland, M., and Hutter, K. (1999). Gravity-driven free surface flow of granular avalanches over complex basal topography. *Proceedings of the Royal Society A: Mathematical, Physical and Engineering Sciences* **455**, 1841–1874.
- Hui, W. H. (2004). A unified coordinates approach to computational fluid dynamics. *Journal of Computational and Applied Mathematics* **163**, 15–28.
- Hui, W. H. (2007). The unified coordinate system in computational fluid dynamics. *Commun. Comput. Phys* **2**, 577–610.
- Hui, W. H., Li, P. Y., and Li, Z. (1999). A Unified Coordinate System for Solving the Two-Dimensional Euler Equations. *Journal of Computational Physics* **153**, 596–637.
- Hutter, K. (2005). Geophysical granular and particle-laden flows: review of the field. *Philosophical transactions. Series A, Mathematical, physical, and engineering sciences* **363**, 1497–505.
- Hutter, K., Savage, S. B., and Nohguchi, Y. (1989). Numerical, analytical, and laboratory experimental studies of granular avalanche flows. *Annals of Glaciology* **13**, 109–116.
- Savage, S. B. and Hutter, K. (1989). The motion of a finite mass of granular material down a rough incline. *Journal of Fluid Mechanics* **199**, 177–215.
- Tai, Y. C., Hutter, K., and Gray, J. M. N. T. (2001). Dense granular avalanches: mathematical description and experimental validation. In Balmforth, N. and Provenzale, A., editors, *Lecture notes in Physics Volume 582*, volume 582, chapter Geomorphol, pages 339–366. Springer, Berlin.
- Tai, Y. C. and Kuo, C. Y. (2008). A new model of granular flows over general topography with erosion and deposition. *Acta Mechanica* **199**, 71–96.
- Tai, Y. C., Kuo, C.-Y., and Hui, W. H. (2012). An alternative depth-integrated formulation for granular avalanches over temporally varying topography with small curvature. *Geophysical & Astrophysical Fluid Dynamics* **106**, 596–629.
- Tai, Y. C., Kuo, C.-Y., Lu, J. W. Z., Leung, A. Y. T., Iu, V. P., and Mok, K. M. (2010). Collapses of Granular Column with Time Varying Topography. In *AIP Conference Proceedings*, pages 845–850.
- Tai, Y. C. and Lin, Y.-C. (2008). A focused view of the behavior of granular flows down a confined inclined chute into the horizontal run-out zone. *Physics of Fluids* **20**, 123302.

Chapter 7

Conclusions

In this brief Chapter, the main findings of this dissertation are summarized and discussed. As well, perspectives and further developments of the present research are highlighted.

Geophysical granular flows, such as avalanches or debris flows, are particularly dangerous events, characterized by the rapid flow of a granular solid phase, embedded in an ambient fluid. The flow dynamics of such phenomena is still far from being completely understood. In an engineering context, one of the main tools, available to describe the propagation of granular flows from initiation to deposit, are the depth-averaged models. In the particular context of dry granular flows, this approach turns out to be sufficiently reliable to describe the flow dynamics and final run-outs, in presence of slip bottom boundary conditions. These models, like the Savage-Hutter model (Savage and Hutter, 1989; Gray et al., 1999), have been extensively validated through many laboratory experiments over smooth basal surfaces. Nevertheless, the reliability of classical depth-averaged models seems to be noticeably reduced, in case of no-slip bottom boundary conditions. Such a condition is rather frequent in real geophysical situations, as occurs in presence of a sufficiently large roughness of the basal surface. In this case, a stratification of different flow regimes (quasi-static and dense collisional regimes) occurs. It makes the utilization of the classical single layer depth-averaged models insufficient, because of important uncertainties about the velocity and shear stress distributions along the flow depths.

The present dissertation aimed at better understanding the dynamics of free surface dry granular flows, in presence of no-slip bottom boundary conditions.

To this regard, the first stage of the present research involved an experimental-numerical study on dam-break flows of granular material, conducted at the LIDAM (University of Salerno), in which acetal grain particles have been used. Tests were carried out on a smooth Plexiglas bed surface, as well as, on a roughened surface. The experimental investigation consisted of capturing the flow depth evolutions over time, through a camera, placed at the side of the channel. After several comparisons between experimental data and numerical results, obtained from some different Savage-Hutter type models, it has been found that a modification to the formula, proposed in the Savage-Hutter model for calculating the earth-pressure coefficient, leads to an increased agreement with experimental data, in presence of no-slip bottom boundary conditions. This approach, which is

similar to that proposed by Hungr (2008), turns out to be very robust in a finite volume framework and yields good agreement with experimental data at the early stages of dam-break flows. The rationale of the proposed modification to the earth-pressure coefficient is the strong curvature of flow lines at the early stages of dam-breaks, owing to high flow depth gradients. Nonetheless, the regularization formula provides no particular improvement in case of slip bottom boundary conditions. It suggests that the shear stresses, as well as the flow velocities, are strongly influenced by the boundary conditions.

In the second stage of the present research, an experimental study on steady state velocity profiles of channelized dry granular flows was carried out at the National Cheng Kung University (Taiwan). The granular material, used in this experimental research, was Ottawa sand, a well-sorted sand compliant to the ASTM C-778 20/30 Standard. The main purpose of these experiments was to better understand the flow dynamics in presence of different boundary conditions, through measuring the flow velocity profiles at the side walls and at the free surface. Such measurements have been obtained, through using *granular-PIV* techniques. The measurements are in good accordance with other experimental studies on different granular materials (Midi, 2004). Moreover, it has been found that a no-slip bottom boundary condition may also occur in presence of smooth bed surfaces, if the side walls resistances are big enough to induce the deposition of a lower wedge of granular material. As well, the dynamical effects of side walls are also evident from the velocity measurements at the free surface, where parabolic-shaped profiles have been observed.

As regards the side wall velocity profile, in case of slip bottom boundary condition, a linear profile from the free surface to the bottom has been observed. Conversely, in case of no-slip boundary condition, the velocity profile is exponential in their lower zone and almost linear in proximity of the free surface. The extent of these two zones is highly variable from one experiment to another. Such experimental findings support the occurrence of a rheological stratification along the flow depth, i.e. the coexistence of different constitutive laws in the same cross section. Such a physical interpretation is also supported by dimensional analysis arguments. In fact, the inertial number, which is the main dimensionless parameter involved in the flow dynamics of stiff dry granular materials, strongly decreases with the distance from the free surface in case of no-slip bottom condition. Therefore, it is natural to infer that also the constitutive law (i.e. the relation between the shear stress and the shear rate tensor) varies noticeably along the flow depth.

In order to better describe such a complex flow dynamics, a two-layer depth-averaged model has been proposed. The main purpose of this approach is to better reproduce the effective velocity distribution along the flow depth and to capture the main dynamical features of such rheological stratification. In the proposed mathematical model, the dynamics of the two layers, ideally corresponding to dense-collisional and quasi-static zones, have been considered independently. Moreover, a rate-dependent term has been considered in the shear stress of the upper layer at the interface, in order to take into account of the effects, due to collisional resistance mechanisms. As well, mass exchanges between the two layers have been implemented and have been calculated through a closure equation, based on the Rankine-Hugoniot jump condition, similar to that proposed in Fraccarollo and Capart (2002).

The well-known mathematical issue of the hyperbolicity loss in two-layer models has been carefully addressed. In order to overcome this problem, a local modification of the source terms of the original mathematical model has been proposed. Such a treatment consists of adding an

extra resistance at the interface, strictly sufficient to avoid the loss of hyperbolicity at any given time-advancing of the numerical scheme. This approach has been found to be very robust, and yields reasonable results, as long as the asymptotic steady state solution and boundary conditions fulfil the hyperbolicity requirements of the original model.

In order to compare the experimental data, obtained through granular PIV techniques, with numerical results from the two-layer model, a physically based criterion, to identify the interface position inside the experimental velocity profiles, has been developed. Such a criterion is based on the assumption that the interface position approximately corresponds to a critical value of the inertial number. This hypothesis is supported by our experimental data, if a linear rate-dependent shear stress at the interface is assumed. Moreover, the critical value of the inertial number has been found to be approximately equal to 0.33. This value is reasonable and in good accordance with a similar criterion, based on the Savage number and proposed to roughly distinguish the friction-dominated from the fluidized collisional regime (Savage and Hutter, 1989; Iverson and Vallance, 2001).

Through comparisons with experimental data, the two-layer approach turns out to be promising to describe the complex flow dynamics in case of no-slip bottom boundary conditions. Yet, it has been found that the velocities of both layers, and, particularly that one of the lower layer, sometimes are not properly predicted. In particular, the experimental comparisons suggest that assuming a pure Coulomb friction law in the lower layer could be insufficient to correctly describe its dynamics.

Nonetheless, it should be noted that these comparisons have been performed without any calibration of the model parameters and could be also affected by some important uncertainties, related to the estimation of the depth-averaged velocity profiles, along the transverse direction, y . These preliminary results, on the one hand, suggest a further experimental investigation on the effective velocity distribution inside the flowing pile. In this regard, it could be very valuable also to obtain measurements of the volume fraction distributions inside the flow. On the other hand, the rheological assumptions of the proposed two-layer model need to be revised. In particular, a more detailed description of the basal shear stress seems to be required and could incorporate a rate-dependent term.

As well, a more detailed description of the effective velocity distribution inside the layers can be implemented in a further version of the mathematical model.

Furthermore, in order to properly calibrate the parameters, r and k , that are in the expression of the upper layer shear stress, a further experimental research on dry granular flows in transient state conditions would be required. As well, a comparison with transient state flows would be very valuable to evaluate the reliability of the model to correctly capture the interface position over time.

In addition to the two-layer model, written in Cartesian coordinates, the same two-layer approach has been employed to obtain a different formulation of the model in curvilinear coordinates. The balance equations of this model are written in moving curvilinear coordinates, as regards the upper layer, and in Cartesian coordinates, as regards the lower layer. The curvilinear coordinate system is assumed to be attached to the moving interface between the two layers. The derivation of the model makes use of the *Unified Coordinate* method (e.g. Hui et al., 1999; Hui, 2004, 2007), combined with the arbitrary coordinate system of Bouchut and Westdickenberg (2004), as proposed by Tai and Kuo (2008). After obtaining the exact depth-averaged balance equations,

a scaling approximation has been performed in order to identify and drop out all the negligible physical terms. This approach has some important advantages with respect to the two-layer model, written in Cartesian coordinates.

Firstly, all the approximations are made through a scaling analysis, where the effective direction of the avalanche is considered. The utilization of scaling approximations permits a more rational identification of physical negligible terms.

Moreover, differently from the two-layer model, written in Cartesian coordinates, there are no non-conservative terms in the upper layer momentum equation. The dynamical coupling between the two layers is still present, but it appears in a more diffused form, due to the different coordinates used for deriving the upper and lower layer balance equations. Namely, the influence of the lower layer on the upper layer dynamics is incorporated in some upper-bounded topographic terms, depending on the interface inclination angle. This feature suggests that the issues related to the hyperbolicity loss could be avoided or reduced somehow. However, a further investigation about this topic is advisable.

The long-term goal of the present research is to provide reliable mathematical-numerical tools to better describe the propagation of dry granular flows, in real situations where a no-slip bottom boundary condition usually occurs. As well, since many mathematical models for describing debris and grain-water flows make use of a two-phase approach (e. g. Iverson, 1997; Iverson and Vallance, 2001), the results of this research could be also applied, after suitable modifications, to debris flow models.

References Used in This Chapter

- Bouchut, F. and Westdickenberg, M. (2004). Gravity driven shallow water models for arbitrary topography. *Communications in Mathematical Sciences* **2**, 359–389.
- Fraccarollo, L. and Capart, H. (2002). Riemann wave description of erosional dam-break flows. *Journal of Fluid Mechanics* **461**, 183–228.
- Gray, J. M. N. T., Wieland, M., and Hutter, K. (1999). Gravity-driven free surface flow of granular avalanches over complex basal topography. *Proceedings of the Royal Society A: Mathematical, Physical and Engineering Sciences* **455**, 1841–1874.
- Hui, W. H. (2004). A unified coordinates approach to computational fluid dynamics. *Journal of Computational and Applied Mathematics* **163**, 15–28.
- Hui, W. H. (2007). The unified coordinate system in computational fluid dynamics. *Commun. Comput. Phys* **2**, 577–610.
- Hui, W. H., Li, P. Y., and Li, Z. (1999). A Unified Coordinate System for Solving the Two-Dimensional Euler Equations. *Journal of Computational Physics* **153**, 596–637.
- Hungr, O. (2008). Simplified models of spreading flow of dry granular material. *Canadian Geotechnical Journal* **45**, 1156–1168.
- Iverson, R. M. (1997). The physics of debris flows. *Reviews of Geophysics* **35**, 245.
- Iverson, R. M. and Vallance, J. W. (2001). New views of granular mass flows. *Geology* **29**, 115.
- Midi, G. (2004). On dense granular flows. *The European physical journal. E, Soft matter* **14**, 341–65.
- Savage, S. B. and Hutter, K. (1989). The motion of a finite mass of granular material down a rough incline. *Journal of Fluid Mechanics* **199**, 177–215.
- Tai, Y. C. and Kuo, C. Y. (2008). A new model of granular flows over general topography with erosion and deposition. *Acta Mechanica* **199**, 71–96.

Appendix A

Mathematical notations and useful formulae

A.1 Main notations

Bold italic symbols (e.g. \mathbf{v}) stand for vectors, unless otherwise specified. Vectors written in curvilinear coordinates, exhibit the superscript $*$. Capital italic symbols stand for matrices and tensors, unless otherwise specified. The symbol \cdot between two vectors indicates the scalar product, while \otimes indicates the dyadic product.

The symbol $\|\mathbf{v}\|$ stands for $\sqrt{\mathbf{v} \cdot \mathbf{v}}$. Because the metric of the curvilinear coordinate system is different from that in Cartesian coordinates, please note that, in general, $\|\mathbf{v}\| \neq \|\mathbf{v}^*\|$. Only the norm, written in Cartesian coordinates, represents a distance in an Euclidean sense.

The absolute value of a given quantity x is written as $|x|$, instead.

Dyadic product

Let \mathbf{v} be a vector field defined in \mathbb{R}^n . The dyadic product is a $n \times n$ matrix, defined as follows

$$\mathbf{v} \otimes \mathbf{v} = \mathbf{v}\mathbf{v}^T.$$

Divergence of a matrix

We need to define a convention to extend the definition of divergence to matrices. This convention will be used in every calculation of the present dissertation.

Let A be an $n \times m$ matrix. Its divergence can be defined as the following column vector

$$\nabla \cdot A = \sum_{j=1}^m \left(\frac{\partial a_{ij}}{\partial x_j} \right) \in \mathbb{R}^n. \quad (\text{A.1})$$

Thus, the divergence of the stress tensor T is

$$\nabla_{\mathbf{x}} \cdot T = \nabla \cdot \begin{pmatrix} t_{xx} & t_{xz} \\ t_{zx} & t_{zz} \end{pmatrix} = \begin{pmatrix} \partial_x t_{xx} + \partial_z t_{xz} \\ \partial_x t_{zx} + \partial_z t_{zz} \end{pmatrix}. \quad (\text{A.2})$$

It is interesting to note that only if the matrix is symmetric, the aforementioned definition is equivalent to that one obtained by summation over the columns instead of rows,

$$\nabla \cdot A = \sum_{i=1}^n \left(\frac{\partial a_{ij}}{\partial x_i} \right) \in \mathbb{R}^m.$$

A.2 Leibniz integral rule

Let $f(x, t)$ be a function such that $\partial_t f$ exists and is continuous, it holds,

$$\frac{\partial}{\partial t} \int_{a(t)}^{b(t)} f(x, t) dt = \int_{a(t)}^{b(t)} \partial_t f(x, t) dt + f(b(t), t) \partial_t b(t) - f(a(t), t) \partial_t a(t). \quad (\text{A.3})$$

This calculus rule, named *Leibniz integral rule* after the mathematician G. Leibniz, is particularly useful to move the partial derivative operator outside the integral sign, or vice versa. This formula has been widely in the present dissertation for the derivation of the depth-averaged model equations.

A.3 Covariance and contravariance

Covariance and *contravariance* are concepts, used for the first time by J. Sylvester in 1853 in multilinear algebra in order to describe how the components of certain physical quantities vary with a change from a coordinate system to another.

A vector undergoes a contravariant transformation if it is transformed in the same way of the coordinate system. On the other hand, a covariant vector transforms oppositely to the coordinates. If the coordinates transformation consists of a simple rotation, there is no difference between contravariant and covariant vectors.

In two-dimensional space, let B be the orthonormal canonical basis of a Cartesian coordinate system

$$B = (\mathbf{e}_1 \ \mathbf{e}_2) = \begin{pmatrix} 1 & 0 \\ 0 & 1 \end{pmatrix}.$$

Let us consider the local tangent basis of a given curve, written in Cartesian coordinates,

$$B^* = (\mathbf{g}_1 \ \mathbf{g}_2)$$

where the local basis vectors are the tangent vectors of the curve, i.e.

$$\mathbf{g}_1 = \frac{\partial \mathbf{x}}{\partial \xi}, \quad \mathbf{g}_2 = \frac{\partial \mathbf{x}}{\partial \zeta}.$$

Such a basis is also called *covariant* local basis.

Let Ω be the Jacobian matrix of the transformation between the Cartesian coordinate system and that defined on the given manifold, defined as follows

$$\Omega = \partial_{\xi} \mathbf{x} = \begin{pmatrix} \partial_{\xi} x & \partial_{\zeta} x \\ \partial_{\xi} z & \partial_{\zeta} z \end{pmatrix} = (\mathbf{g}_1, \ \mathbf{g}_2), \quad (\text{A.4})$$

it can be easily shown that

$$B^* = B\Omega = \Omega \quad (\text{A.5})$$

or equivalently

$$(B^*)^T = \Omega^T B^T = \Omega^T B. \quad (\text{A.6})$$

A.3.1 Contravariant vectors

In Euclidean spaces, the position vector \mathbf{s} , which is a geometrical vector representing the position of a given point P with respect to a reference origin O , can be regarded as the prototype of any contravariant vector. The choice of a particular basis allows \mathbf{s} to be determined by a set of coordinates numbers.

In Euclidean plane, the components vector of any given vector \mathbf{s} can be written as follows

$$\mathbf{c} = (s_x, s_z)^T, \mathbf{c}^* = (s^\xi, s^\zeta)^T \Rightarrow \mathbf{s} = s_x \mathbf{e}_x + s_z \mathbf{e}_z = s^\xi \mathbf{g}_1 + s^\zeta \mathbf{g}_2, \quad (\text{A.7})$$

where \mathbf{c} and \mathbf{c}^* are the coordinate vectors with respect to the basis B and B^* , respectively.

In other words, \mathbf{s} can be written in the following different ways

$$\mathbf{s} = B\mathbf{c} = B^*\mathbf{c}^* = B\Omega\mathbf{c}^* \Rightarrow \mathbf{c} = \Omega\mathbf{c}^*. \quad (\text{A.8})$$

This formula tells how the components of \mathbf{s} transform, owing to the change of basis. Thus, it is possible to write the following transformation formula for contravariant vectors

$$\boxed{\mathbf{v} = \Omega\mathbf{v}^*}. \quad (\text{A.9})$$

A.3.2 Covariant vectors

The gradient of a scalar field can be regarded as the prototype of any covariant vector. Let $f(x, z)$ be a scalar field defined in \mathbb{E}^2 , its gradient is

$$\nabla f = \begin{pmatrix} \partial_x f \\ \partial_z f \end{pmatrix}. \quad (\text{A.10})$$

Because of $x = x(\xi, \zeta)$ and $z = z(\xi, \zeta)$, by using the chain rule we get

$$\begin{aligned} \partial_x f &= \partial_\xi f \partial_x \xi + \partial_\zeta f \partial_x \zeta \\ \partial_z f &= \partial_\xi f \partial_z \xi + \partial_\zeta f \partial_z \zeta. \end{aligned}$$

This implies that

$$\boxed{\nabla_{\mathbf{x}} f = \Omega^{-T} \nabla_{\boldsymbol{\xi}} f}. \quad (\text{A.11})$$

For instance, the normal vector to a given surface is a covariant vector and so transforms according to Eq. (A.11).

A.3.3 Tensor transformation

Tensors are geometrical objects that describe linear relations between scalar, vectors or other tensors. Second order tensors can be represented by a matrix (i.e. a two dimensional array), whose elements vary with the chosen coordinate system in the following way (see e.g. Arfken and Weber, 2005)

$$T = \sum_{i,j} T^{ij} \mathbf{e}_i \otimes \mathbf{e}_j = \sum_{m,n} T^{*mn} \mathbf{g}_m \otimes \mathbf{g}_n$$

in which $T^{i,j}$ and $T^{*m,n}$ are the generic elements of the matrices representing the tensor T with respect to the canonical Cartesian basis, $(\mathbf{e}_1, \mathbf{e}_2)$, and the local covariant basis, $(\mathbf{g}_1, \mathbf{g}_2)$, respectively.

It directly follows that the matrix T , representing a given tensor with respect to the canonical Cartesian basis and the matrix T^* , representing the same tensor with respect to the local basis T^* , are related by the following equation

$$\boxed{T = \Omega T^* \Omega^T.} \quad (\text{A.12})$$

References

Arfken, G. B. and Weber, H. J. (2005). *Mathematical Methods for Physicists*. Elsevier, 6th edition.

Appendix B

Mathematical methods

B.1 The Unified Coordinate system

Here, we briefly describe the key points of the Unified Coordinate theory (also referred to as *UC* theory), proposed by Hui et al. (1999) and applied successfully to several fluid dynamic problems (for more details see Hui and Koudriakov, 2002; Hui, 2004, 2007). The main purpose of this approach is to develop a mathematical tool for modelling fluid mechanics problems in a moving arbitrary curvilinear coordinate system, so as to overcome the typical shortcomings of the classical Eulerian and Lagrangian approaches. The main advantage of the *UC* theory consists of a reformulation of the model equations, so that more reliable numerical schemes can be employed.

Recently, the UC theory, together with the approach proposed by Bouchut and Westdickenberg (2004) for the geometrical description of the basal topography of shallow granular avalanches, has been applied to the context of geophysical granular flows by Tai and Kuo (2008). The extension to three-dimensions of this model is presented by Tai et al. (2012).

The present appendix does not claim to be complete. By following the approach proposed in Tai and Kuo (2008), we simply report the main findings of the *UC* theory that are required for the derivation of the two-layer model, written in curvilinear coordinates and reported in Chapter 6. In the followings, we will only refer to two-dimensional problems. A more detailed description of the transformation relations in UI theory can be found in Hui (2004) or Hui (2007).

Sometimes, it is useful to define a curvilinear coordinate system associated with a manifold, i.e. a plane curve in two-dimensional spaces. Let $\xi \in \mathbb{R}$ be a curvilinear coordinate that follows the curve and ζ be the other curvilinear coordinate locally normal to the curve. We assume that ξ is linked to the Cartesian coordinate x by the bijection

$$x \rightarrow \xi(x) \in \mathbb{R}.$$

It is also assumed that ξ and ζ are time varying because the curve with which the coordinate system is associated is moving.

In UC theory the following relations hold between differential quantities, written in Cartesian

and curvilinear coordinates

$$\begin{cases} dt &= d\lambda \\ dx &= U d\lambda + A d\xi + P d\zeta \\ dz &= W d\lambda + C d\xi + R d\zeta \end{cases} \Rightarrow d\mathbf{x} = \mathbf{q} d\lambda + \Omega d\boldsymbol{\xi}$$

in which

$$\mathbf{x} = \begin{pmatrix} x \\ z \end{pmatrix}, \quad \mathbf{q} = \begin{pmatrix} U \\ W \end{pmatrix}, \quad \Omega = \begin{pmatrix} \mathbf{a} & \mathbf{p} \end{pmatrix} = \begin{pmatrix} A & P \\ C & R \end{pmatrix} = \begin{pmatrix} \partial_\xi x & \partial_\zeta x \\ \partial_\xi z & \partial_\zeta z \end{pmatrix}.$$

The vector \mathbf{q} can be regarded as the velocity of the moving mesh $\boldsymbol{\xi}$ with respect to the Cartesian coordinate system, namely the velocity of a pseudo-particle whose coordinates are (ξ, ζ) . In fact,

$$\frac{d\mathbf{q}}{dt} \boldsymbol{\xi} = \frac{d\mathbf{q}}{dt} \begin{pmatrix} \xi \\ \zeta \end{pmatrix} = \mathbf{0} \quad (\text{B.1})$$

where the operator $\frac{d\mathbf{q}}{dt}$ represents the total derivative $\partial_t + \mathbf{q} \cdot \nabla_{\mathbf{x}}$.

Proof of Eq (B.1). By considering the matrices of the total transformation (including the time variables t and λ)

$$\Omega_T = \begin{pmatrix} \partial_\lambda t & \partial_\xi t & \partial_\zeta t \\ \partial_\lambda x & \partial_\xi x & \partial_\zeta x \\ \partial_\lambda z & \partial_\xi z & \partial_\zeta z \end{pmatrix} = \begin{pmatrix} 1 & 0 & 0 \\ U & \partial_\xi x & \partial_\zeta x \\ W & \partial_\xi z & \partial_\zeta z \end{pmatrix}$$

$$\Omega_T^{-1} = \begin{pmatrix} \partial_t \lambda & \partial_x \lambda & \partial_z \lambda \\ \partial_t \xi & \partial_x \xi & \partial_z \xi \\ \partial_t \zeta & \partial_x \zeta & \partial_z \zeta \end{pmatrix} = \begin{pmatrix} 1 & 0 & 0 \\ \partial_t \xi & \partial_x \xi & \partial_z \xi \\ \partial_t \zeta & \partial_x \zeta & \partial_z \zeta \end{pmatrix}$$

so that

$$d\mathbf{x} = \Omega_T d\boldsymbol{\xi}.$$

Since

$$\Omega_T^{-1} \Omega_T = I,$$

we can write

$$I(2, 1) = 0 \Rightarrow (\partial_t \xi, \partial_x \xi, \partial_z \xi)^T (\partial_\lambda t, \partial_\lambda x, \partial_\lambda z) = \partial_t \xi + U \partial_x \xi + W \partial_z \xi = 0 \Rightarrow \frac{D\mathbf{q}}{Dt} \xi = 0.$$

Analogously,

$$I(3, 1) = 0 \Rightarrow (\partial_t \zeta, \partial_x \zeta, \partial_z \zeta)^T (\partial_\lambda t, \partial_\lambda x, \partial_\lambda z) = \partial_t \zeta + U \partial_x \zeta + W \partial_z \zeta = 0 \Rightarrow \frac{D\mathbf{q}}{Dt} \zeta = 0. \quad \square$$

Since the inverse relation holds

$$\boldsymbol{\xi} = \Omega^{-1} (d\mathbf{x} - \mathbf{q} dt), \quad (\text{B.2})$$

it follows that

$$\frac{\partial \boldsymbol{\xi}}{\partial t} \equiv \frac{\partial \boldsymbol{\xi}}{\partial t} \Big|_{d\mathbf{x}=\mathbf{0}} = -\Omega^{-1} \mathbf{q} = -\mathbf{q}^* \quad (\text{B.3})$$

where \mathbf{q}^* is the velocity of the mesh, written in curvilinear coordinates. Note that the contravariant transformation rule has been used (cf. Eq. (A.9)).

Apparently there are 6 degrees of freedom to choose these parameters (i.e. U, W, A, P, C, R) but, in fact, in order $d\mathbf{x}$ and $d\boldsymbol{\xi}$ to be total differentials, the following compatibility conditions have to be fulfilled

$$\begin{cases} \partial_\xi \mathbf{q} = \partial_\lambda \mathbf{a}, & (\text{B.4}) \\ \partial_\zeta \mathbf{q} = \partial_\lambda \mathbf{p}, & (\text{B.5}) \\ \partial_\zeta \mathbf{a} = \partial_\xi \mathbf{p}. & (\text{B.6}) \end{cases}$$

These conditions have been obtained by simply applying the Schwartz's theorem about mixed partial derivatives.

A more general explanation of the compatibility conditions in three dimensions can be found in Hui (2007).

B.1.1 Useful relations

In the UC theory some useful relations can be obtained. These formulae have been widely used in Tai and Kuo (2008); Tai et al. (2012) and are needed for the derivation of the two-layer model equations, presented in Chapter (6) of the present dissertation. In this section, we introduce and demonstrate these formulae.

Transformation formula no. 1

$$\boxed{\frac{\partial J}{\partial \lambda} = \nabla_{\boldsymbol{\xi}} \cdot (J\Omega^{-1}\mathbf{q}) = \nabla_{\boldsymbol{\xi}} \cdot (J\mathbf{q}^*)} \quad (\text{B.7})$$

where $J = \det(\Omega)$. This formula relates the temporal partial derivative of the determinant of the transformation matrix Ω to the spatial divergence of $J\mathbf{q}^*$.

Proof of Eq. (B.7). By using the adjoint formula, the inverse of the transformation matrix Ω can be calculated as follows

$$\Omega^{-1} = \frac{1}{J} \begin{pmatrix} \Omega_{22} & -\Omega_{12} \\ -\Omega_{21} & \Omega_{11} \end{pmatrix} = \frac{1}{J} \begin{pmatrix} \mathbf{d}_1^T \\ \mathbf{d}_2^T \end{pmatrix}$$

where

$$\mathbf{d}_1^T = (d_{11}, d_{12}) = (\Omega_{22}, -\Omega_{12}), \quad \mathbf{d}_2^T = (d_{21}, d_{22}) = (-\Omega_{21}, \Omega_{11}). \quad (\text{B.8})$$

Please note that \mathbf{d}_1 does not depend on \mathbf{a} and \mathbf{d}_2 does not depend on \mathbf{p} . By virtue of the condition ((B.6)), it can be shown that

$$\frac{\partial d_{11}}{\partial \xi} + \frac{\partial d_{21}}{\partial \zeta} = 0, \quad \frac{\partial d_{12}}{\partial \xi} + \frac{\partial d_{22}}{\partial \zeta} = 0,$$

thus, it follows that

$$\forall \mathbf{a} \equiv (a_1, a_2)^T, \quad a_1 \frac{\partial d_{11}}{\partial \xi} + a_2 \frac{\partial d_{12}}{\partial \xi} + a_1 \frac{\partial d_{21}}{\partial \zeta} + a_2 \frac{\partial d_{22}}{\partial \zeta} = \mathbf{a} \cdot \frac{\partial \mathbf{d}_1}{\partial \xi} + \mathbf{a} \cdot \frac{\partial \mathbf{d}_2}{\partial \zeta} = 0. \quad (\text{B.9})$$

Since the determinant J is function of all the elements of the matrix Ω , by applying the chain rule for partial derivatives (e.g. Arfken and Weber, 2005), we can write

$$\frac{\partial J}{\partial \lambda} = \sum_{ij} \left(\frac{\partial J}{\partial \Omega_{ij}} \frac{\partial \Omega_{ij}}{\partial \lambda} \right) = \text{tr} \left[\left(\frac{\partial J}{\partial \Omega^T} \right)^T \frac{\partial \Omega}{\partial \lambda} \right] = \text{tr} \left[\begin{pmatrix} d_{11} & d_{12} \\ d_{21} & d_{22} \end{pmatrix} \begin{pmatrix} \frac{\partial \mathbf{a}}{\partial \lambda}, \frac{\partial \mathbf{p}}{\partial \lambda} \end{pmatrix} \right],$$

then, with the help of Eqs. (B.4), (B.5) and (B.9), finally we get

$$\begin{aligned} \frac{\partial J}{\partial \lambda} &= \mathbf{d}_1 \cdot \frac{\partial \mathbf{a}}{\partial \lambda} + \mathbf{d}_2 \cdot \frac{\partial \mathbf{p}}{\partial \lambda} = \mathbf{d}_1 \cdot \frac{\partial \mathbf{q}}{\partial \xi} + \mathbf{d}_2 \cdot \frac{\partial \mathbf{q}}{\partial \zeta} \\ &= \frac{\partial}{\partial \xi} (\mathbf{d}_1 \cdot \mathbf{q}) + \frac{\partial}{\partial \zeta} (\mathbf{d}_2 \cdot \mathbf{q}) = \nabla_{\boldsymbol{\xi}} \cdot (J\Omega^{-1}\mathbf{q}) = \nabla_{\boldsymbol{\xi}} \cdot (J\mathbf{q}^*). \end{aligned}$$

□

Transformation formula no. 2

$$\boxed{\frac{\partial f}{\partial t} = \frac{1}{J} \left[\frac{\partial(Jf)}{\partial \lambda} - \nabla_{\boldsymbol{\xi}} \cdot (Jf\Omega^{-1}\mathbf{q}) \right] = \frac{1}{J} \left[\frac{\partial(Jf)}{\partial \lambda} - \nabla_{\boldsymbol{\xi}} \cdot (Jf\mathbf{q}^*) \right]} \quad (\text{B.10})$$

Proof of Eq. (B.10). By applying the chain rule and the eq ((B.3)), we get

$$\frac{\partial f}{\partial t} = \frac{\partial f}{\partial \lambda} \frac{\partial \lambda}{\partial t} + \frac{\partial f}{\partial \xi} \frac{\partial \xi}{\partial t} + \frac{\partial f}{\partial \zeta} \frac{\partial \zeta}{\partial t} = \frac{\partial f}{\partial \lambda} - q^\xi \frac{\partial f}{\partial \xi} - q^\zeta \frac{\partial f}{\partial \zeta} = \frac{\partial f}{\partial \lambda} - \mathbf{q}^* \cdot \nabla_\xi f. \quad (\text{B.11})$$

By virtue of eq (B.7), we can write

$$J \frac{\partial f}{\partial \lambda} = \frac{\partial}{\partial \lambda} (Jf) - f \frac{\partial J}{\partial \lambda} = \frac{\partial}{\partial \lambda} (Jf) - f \nabla_\xi \cdot (J\Omega^{-1} \mathbf{q}) = \frac{\partial}{\partial \lambda} (Jf) - f \nabla_\xi \cdot (J\mathbf{q}^*). \quad (\text{B.12})$$

Therefore, by substituting Expr. (B.12) into Eq. (B.11) we get

$$\begin{aligned} \frac{\partial f}{\partial t} &= \frac{1}{J} \left[\frac{\partial}{\partial \lambda} (Jf) - f \nabla_\xi \cdot (J\mathbf{q}^*) \right] - \mathbf{q}^* \cdot \nabla_\xi f \\ &= \frac{1}{J} \left[\frac{\partial}{\partial \lambda} (Jf) - f \nabla_\xi \cdot (J\mathbf{q}^*) - J\mathbf{q}^* \cdot \nabla_\xi f \right] = \frac{1}{J} \left[\frac{\partial}{\partial \lambda} (Jf) - \nabla_\xi \cdot (Jf\mathbf{q}^*) \right]. \end{aligned}$$

□

Transformation formula no. 3

$$\boxed{\forall f, \quad \nabla_{\mathbf{x}} f = \Omega^{-T} \nabla_\xi f} \quad (\text{B.13})$$

Proof of Eq. (B.13). Eq. (B.13) can be easily demonstrated, since the gradient of a scalar function is a covariant vector (e.g. Arfken and Weber, 2005). □

Transformation formula no. 4

$$\boxed{\nabla_{\mathbf{x}} \cdot \mathbf{v} = \frac{1}{J} \nabla_\xi \cdot (J\Omega^{-1} \mathbf{v}) = \frac{1}{J} \nabla_\xi \cdot (J\mathbf{v}^*)} \quad (\text{B.14})$$

Proof of Eq. (B.14). Let \mathbf{v} be a vector field whose Cartesian components are (u, w) . By applying the chain rule of partial differentiation and thanks to Defs. (B.8), we get

$$\nabla_{\mathbf{x}} \mathbf{v} = \frac{\partial u}{\partial x} + \frac{\partial w}{\partial z} = \frac{\partial u}{\partial \xi} \frac{\partial \xi}{\partial x} + \frac{\partial u}{\partial \zeta} \frac{\partial \zeta}{\partial x} + \frac{\partial w}{\partial \xi} \frac{\partial \xi}{\partial z} + \frac{\partial w}{\partial \zeta} \frac{\partial \zeta}{\partial z} = \frac{1}{J} \left(\mathbf{d}_1 \cdot \frac{\partial \mathbf{v}}{\partial \xi} + \mathbf{d}_2 \cdot \frac{\partial \mathbf{v}}{\partial \zeta} \right).$$

Then, by means of Eq. (B.9), the previous equation can be recast into the following form

$$\nabla_{\mathbf{x}} \mathbf{v} = \frac{1}{J} \left[\frac{\partial}{\partial \xi} (\mathbf{d}_1 \cdot \mathbf{v}) + \frac{\partial}{\partial \zeta} (\mathbf{d}_2 \cdot \mathbf{v}) \right] = \frac{1}{J} \nabla_\xi \cdot (J\Omega^{-1} \mathbf{v}) = \frac{1}{J} \nabla_\xi \cdot (J\mathbf{v}^*).$$

□

Transformation formula no. 5

$$\boxed{\nabla_{\mathbf{x}} \cdot T = \frac{1}{J} \nabla_\xi \cdot (JT\Omega^{-T}) = \frac{1}{J} \nabla_\xi \cdot (J\Sigma)} \quad (\text{B.15})$$

in which Σ represents the mixed tensor $T\Omega^{-T}$.

Proof. As we consider the elements of the tensor matrix T as $t_{ij} = f(x(\xi, \zeta), z(\xi, \zeta))$ by using the chain rule and the divergence formula for matrices (Def. (A.1)), we obtain

$$\nabla_{\mathbf{x}} \cdot T = \begin{pmatrix} \partial_x t_{xx} + \partial_z t_{xz} \\ \partial_x t_{zx} + \partial_z t_{zz} \end{pmatrix} = \begin{pmatrix} \partial_\xi t_{xx} \partial_x \xi + \partial_\zeta t_{xx} \partial_x \zeta + \partial_\xi t_{xz} \partial_z \xi + \partial_\zeta t_{xz} \partial_z \zeta \\ \partial_\xi t_{zx} \partial_x \xi + \partial_\zeta t_{zx} \partial_x \zeta + \partial_\xi t_{zz} \partial_z \xi + \partial_\zeta t_{zz} \partial_z \zeta \end{pmatrix}.$$

Let $\mathbf{t}_1 = (t_{xx}, t_{xz})^T$ and $\mathbf{t}_2 = (t_{zx}, t_{zz})^T$, by using Defs. (B.8) and by means of Eq. (B.9), we finally get

$$\begin{aligned} &= \begin{pmatrix} 1/J (\partial_\xi \mathbf{t}_1 \cdot \mathbf{d}_1 + \partial_\zeta \mathbf{t}_1 \cdot \mathbf{d}_2) \\ 1/J (\partial_\xi \mathbf{t}_2 \cdot \mathbf{d}_1 + \partial_\zeta \mathbf{t}_2 \cdot \mathbf{d}_2) \end{pmatrix} = \\ &= \frac{1}{J} \begin{pmatrix} \partial_\xi (\mathbf{t}_1 \cdot \mathbf{d}_1) + \partial_\zeta (\mathbf{t}_1 \cdot \mathbf{d}_2) \\ \partial_\xi (\mathbf{t}_2 \cdot \mathbf{d}_1) + \partial_\zeta (\mathbf{t}_2 \cdot \mathbf{d}_2) \end{pmatrix} = \frac{1}{J} \begin{pmatrix} \nabla_\xi \cdot \begin{pmatrix} J\mathbf{t}_1 \Omega^{-T} \\ J\mathbf{t}_2 \Omega^{-T} \end{pmatrix} \end{pmatrix} = \frac{1}{J} \nabla_\xi \cdot (JT\Omega^{-T}). \end{aligned}$$

□

B.2 Coordinate transformation

In this section, we report the main features of the coordinate transformation, used in Chapter 6. In particular, we are going to tell how to factorize the Jacobian matrix of the transformation Ω . The following approach is analogous to that used in Tai and Kuo (2008). An extension to the three-dimensional case, can be found in Tai et al. (2012).

We refer to an orthogonal curvilinear two-dimensional coordinate system, such that ξ axis is parallel to the interface Γ , that separates the two layers, and ζ is perpendicular to it everywhere. We call ϑ the local inclination angle of the reference surface Γ with respect to the reference Cartesian axis x . The convention that $\vartheta > 0$ in case of positive slope is assumed.

Let the metric tensor of the curvilinear coordinate system be defined as follows

$$G = \begin{pmatrix} (\partial_\xi x)^2 + (\partial_\xi z)^2 & (\partial_\xi x \partial_\zeta x) + (\partial_\xi z \partial_\zeta z) \\ (\partial_\zeta x \partial_\xi x) + (\partial_\zeta z \partial_\xi z) & (\partial_\zeta x)^2 + (\partial_\zeta z)^2 \end{pmatrix} = \begin{pmatrix} 1/\cos^2\vartheta & 0 \\ 0 & 1 \end{pmatrix} \quad (\text{B.16})$$

so that the scale factor for lengths measured on ξ coordinate is

$$h_\xi = \sqrt{G_{11}} = 1/\cos\vartheta. \quad (\text{B.17})$$

Namely, it is like imposing a unit length on the curvilinear coordinate ξ that is $1/\cos\vartheta$ times bigger than that used in Cartesian coordinates.

Once the curvilinear system is chosen, in any point of the Euclidean plane it is possible to define a set of two vectors, that are tangent to the curvilinear coordinates. This set is usually called local covariant tangent basis (e.g. Arfken and Weber, 2005).

For any point P on the reference surface Γ , the tangent basis vectors can be written as follows

$$\mathbf{g}_{\xi, \mathbf{o}} = \frac{\partial \mathbf{r}_0}{\partial \xi}, \quad \mathbf{g}_{\zeta, \mathbf{o}} = \frac{\partial \mathbf{r}_0}{\partial \zeta} \quad (\text{B.18})$$

in which \mathbf{r}_0 is the position vector of the point P , i.e. the displacement from the reference origin O to P , written in Cartesian coordinates. Please, note that vectors in (B.18) have the components in Cartesian coordinates. In curvilinear coordinates the components of the local basis vectors are simply $(1, 0)^T$ and $(0, 1)^T$, respectively.

Besides, it should be pointed out that, while the vector $\mathbf{g}_{\zeta, \mathbf{o}}$ is a unit vector, $\|\mathbf{g}_{\xi, \mathbf{o}}\| \neq 1$, as it follows directly from the chosen metric (B.16).

Provided that the upper flowing layer is thin (i.e. everywhere the flow depth is locally smaller than the radius of curvature), the Cartesian coordinates of any point P , which is above the interface Γ and placed inside the upper flowing layer, can be uniquely decomposed as follows

$$\mathbf{r} = (x, z)^T = (x_0, z_0)^T + \zeta \mathbf{n} \quad (\text{B.19})$$

where (x_0, z_0) are the coordinates of the point P_0 on the reference surface Γ , that is on the normal line to Γ passing through the point P , and \mathbf{n} is the normal unit vector to Γ in P_0 (i.e. $\mathbf{g}_{\zeta, \mathbf{o}}$).

Therefore, the covariant tangent basis vectors at any point inside the flow can be written as follows

$$\mathbf{g}_\xi = \frac{\partial \mathbf{r}}{\partial \xi} = \mathbf{g}_{\xi, \mathbf{o}} + \zeta \frac{\partial \mathbf{n}}{\partial \xi}, \quad \mathbf{g}_\zeta = \frac{\partial \mathbf{r}}{\partial \zeta} = \left(\mathbf{g}_{\zeta, \mathbf{o}} + \zeta \frac{\partial \mathbf{n}}{\partial \zeta} \right). \quad (\text{B.20})$$

According to the Eq. (B.16), it can be shown that

$$\mathbf{g}_{\xi, \mathbf{0}} = (1, -\tan \vartheta)^T, \quad \mathbf{g}_{\zeta, \mathbf{0}} = (\sin \vartheta, \cos \vartheta)^T. \quad (\text{B.21})$$

The Jacobian matrix of the transformation is the following

$$\Omega = \partial_{\xi} \mathbf{x} = \begin{pmatrix} \partial_{\xi} x & \partial_{\zeta} x \\ \partial_{\xi} z & \partial_{\zeta} z \end{pmatrix}, \quad (\text{B.22})$$

such that $d\mathbf{x} = \Omega d\xi$, as required by the chain rule of partial differentiation, since $x(\xi, \zeta)$ and $z(\xi, \zeta)$. Analogously, the inverse Jacobian matrix can be written as

$$\Omega^{-1} = \partial_{\mathbf{x}} \xi = \begin{pmatrix} \partial_x \xi & \partial_z \xi \\ \partial_x \zeta & \partial_z \zeta \end{pmatrix}. \quad (\text{B.23})$$

Moreover, thanks to Eq. (A.5), it is possible to write Ω and, in particular, Ω_0 , as function of the covariant basis vectors

$$\Omega = \begin{pmatrix} \mathbf{g}_{\xi} & \mathbf{g}_{\zeta} \end{pmatrix}, \quad \Omega_0 = \begin{pmatrix} \mathbf{g}_{\xi, \mathbf{0}} & \mathbf{g}_{\zeta, \mathbf{0}} \end{pmatrix} = \begin{pmatrix} 1 & \sin \vartheta \\ -\tan \vartheta & \cos \vartheta \end{pmatrix}. \quad (\text{B.24})$$

These relations hold for any point in the upper layer and on the reference surface Γ , respectively.

Let $F_i(x, z, t) = z - z_i(x, t) = 0$ be the equation representing the reference curve Γ . The normal unit vector can be written as

$$\mathbf{n} = \frac{\nabla_{\mathbf{x}} F_i}{\|\nabla_{\mathbf{x}} F_i\|} = (-s, c)^T, \quad (\text{B.25})$$

where

$$c = 1/\|\nabla_{\mathbf{x}} F_i\| = \left[1 + (\partial_x z_i)^2\right]^{-1/2}, \quad s = c \partial_x z_i. \quad (\text{B.26})$$

Please note that $c = \cos \vartheta$, $\partial_x z_i = -\tan \vartheta$ and, so, $s = -\sin \vartheta$.

B.2.1 The factorization of the Jacobian matrix

By following the same approach of Tai and Kuo (2008), the Jacobian matrix Ω can be usefully factorised as follows

$$\Omega = \begin{pmatrix} (1 - \zeta \partial_x s) & -s \\ \frac{s}{c} (1 - \zeta \partial_x s) & c \end{pmatrix} = \begin{pmatrix} 1 & -s \\ \frac{s}{c} & c \end{pmatrix} \begin{pmatrix} (1 - \zeta \partial_x s) & 0 \\ 0 & 1 \end{pmatrix} = \begin{pmatrix} 1 & \sin \vartheta \\ -\tan \vartheta & \cos \vartheta \end{pmatrix} \begin{pmatrix} (1 - \zeta \partial_x s) & 0 \\ 0 & 1 \end{pmatrix}. \quad (\text{B.27})$$

This factorization will be particularly useful for the further scaling simplifications.

Proof of Eq. (B.27). From the Eqs. (B.26), it follows that

$$s^2 + c^2 = 1.$$

Because of $\partial_x (s^2 + c^2) = 0$,

$$\partial_x s = -c/s \partial_x c.$$

Moreover, by using the definition of s it turns out that

$$\partial_x s = c^3 \partial_{xx} z_i.$$

Now, thanks to Eqs. (B.19) and (B.25), it is possible to express the elements of Ω as follows

$$\partial_\xi x = \partial_\xi x_0 - \partial_\xi (\zeta s) = (\partial_\xi x_0 - \zeta \partial_x s \partial_\xi x_0) = (1 - \zeta \partial_x s) \partial_\xi x_0 \quad (\text{B.28})$$

$$\partial_\zeta x = \partial_\zeta x_0 - \partial_\zeta (\zeta s) = 0 - s = -s \quad (\text{B.29})$$

$$\partial_\xi z = \partial_\xi z_0 + \partial_\xi (\zeta c) = (\partial_x z_0 + \zeta \partial_x c) \partial_\xi x_0 \quad (\text{B.30})$$

$$\partial_\zeta z = \partial_\zeta z_0 + \partial_\zeta (\zeta c) = 0 + c = c. \quad (\text{B.31})$$

With the help of Eqs. (B.26) and (B.2.1), Eq. (B.30) can be further recast as follows

$$\partial_\xi z = (\partial_x z_0 + \zeta \partial_x c) \partial_\xi x_0 = s/c (1 - \zeta \partial_x s) \partial_\xi x_0 = s/c \partial_\xi x$$

and finally, we are allowed to write

$$\Omega = \begin{pmatrix} \partial_\xi x & -s \\ s/c \partial_\xi x & c \end{pmatrix} = \begin{pmatrix} (1 - \zeta \partial_x s) & -s \\ s/c (1 - \zeta \partial_x s) & c \end{pmatrix}. \quad (\text{B.32})$$

Thus, Eq. (B.27) can be easily obtained. \square

Then, by using the *adjoint formula*, Ω^{-1} yields

$$\Omega^{-1} = \frac{1}{\det \Omega} \text{adj}(\Omega) = \frac{c}{1 - \zeta \partial_x s} \begin{pmatrix} c & s \\ -s/c & 1 - \zeta \partial_x s \end{pmatrix}. \quad (\text{B.33})$$

Eq. (B.33) can be easily factorised as follows

$$\begin{aligned} \Omega^{-1} &= \frac{c}{1 - \zeta \partial_x s} \begin{pmatrix} 1 & 0 \\ 0 & 1 - \zeta \partial_x s \end{pmatrix} \begin{pmatrix} c & s \\ -s/c & 1 \end{pmatrix} \\ &= \begin{pmatrix} 1 - \zeta \partial_x s & 0 \\ 0 & 1 \end{pmatrix} \begin{pmatrix} \cos^2 \vartheta & -\sin \vartheta \cos \vartheta \\ \sin \vartheta & \cos \vartheta \end{pmatrix}. \end{aligned} \quad (\text{B.34})$$

The Ω_0^{-1} at the reference interface Γ , obviously is a particular case of (B.34), and, thus, it can be written as follows

$$\Omega_0^{-1} = c \begin{pmatrix} c & s \\ -s/c & 1 \end{pmatrix} = \begin{pmatrix} \cos^2 \vartheta & -\sin \vartheta \cos \vartheta \\ \sin \vartheta & \cos \vartheta \end{pmatrix}. \quad (\text{B.35})$$

Local curvature

The local curvature k' of Γ is equal to $\partial_x s$ (Tai and Kuo, 2008). Owing to the metric of the curvilinear coordinate system, it follows that

$$k' = \partial_x s = \partial_x (-\sin \vartheta) = -\cos \vartheta \partial_x \vartheta = -\cos \vartheta (\partial_\xi \vartheta \partial_x \xi + \partial_\zeta \vartheta \partial_x \zeta) = -\cos \vartheta \partial_\xi \vartheta. \quad (\text{B.36})$$

Norms

In general $\|\mathbf{v}\| \neq \|\mathbf{v}^*\|$ because of the different metric. It is useful to specify how the Euclidean norm (calculated according to the norm of Cartesian coordinate system) of an arbitrary contravariant vector \mathbf{v} can be calculated from its curvilinear coordinates. More precisely, it can be shown that the following relations holds

$$\|\mathbf{v}\| = \sqrt{v_x^2 + v_z^2} = \sqrt{(\sqrt{G_{11}} v_\xi)^2 + v_\zeta^2}, \quad (\text{B.37})$$

where (v_x, v_z) are the Cartesian components of the vector \mathbf{v} , while (v_ξ, v_ζ) are its components with respect to the covariant local basis. Besides, $G_{11} = 1/\cos^2\vartheta$ is the first element of the metric tensor G . The multiplication of the ξ component by $\sqrt{G_{11}}$ is required to counterbalance the measure along ξ axis that are reduced by a factor $1/\sqrt{G_{11}}$ in curvilinear coordinates.

Conversely, the following relation relates the Euclidean norm of any covariant vector \mathbf{n} with its components in curvilinear coordinates

$$\|\mathbf{n}\| = \sqrt{n_x^2 + n_z^2} = \sqrt{\left(\frac{n_\xi}{\sqrt{G_{11}}}\right)^2 + n_\zeta^2}. \quad (\text{B.38})$$

It is interesting to note that in this case the ξ component requires to be normalized by a factor $1/\sqrt{G_{11}}$ in order to counterbalance the measures along ξ axis that are magnified by a factor $\sqrt{G_{11}}$.

References

- Arfken, G. B. and Weber, H. J. (2005). *Mathematical Methods for Physicists*. Elsevier, 6th edition.
- Bouchut, F. and Westdickenberg, M. (2004). Gravity driven shallow water models for arbitrary topography. *Communications in Mathematical Sciences* **2**, 359–389.
- Hui, W. H. (2004). A unified coordinates approach to computational fluid dynamics. *Journal of Computational and Applied Mathematics* **163**, 15–28.
- Hui, W. H. (2007). The unified coordinate system in computational fluid dynamics. *Commun. Comput. Phys* **2**, 577–610.
- Hui, W. H. and Koudriakov, S. (2002). Computation of the Shallow Water Equations Using the Unified Coordinates. *SIAM Journal on Scientific Computing* **23**, 1615–1654.
- Hui, W. H., Li, P. Y., and Li, Z. (1999). A Unified Coordinate System for Solving the Two-Dimensional Euler Equations. *Journal of Computational Physics* **153**, 596–637.
- Tai, Y. C. and Kuo, C. Y. (2008). A new model of granular flows over general topography with erosion and deposition. *Acta Mechanica* **199**, 71–96.
- Tai, Y. C., Kuo, C.-Y., and Hui, W. H. (2012). An alternative depth-integrated formulation for granular avalanches over temporally varying topography with small curvature. *Geophysical & Astrophysical Fluid Dynamics* **106**, 596–629.

Appendix C

Big O notation

In this appendix a short description of the *Big O* notation is given.

This notation, which describes the behaviour of a given function around a particular value or infinity, belongs to the wide family of symbols called Bachmann-Landau notations, after the mathematicians P. Bachmann and E. Landau who introduced them at the end of the 19th century. It is commonly used in mathematics in order to describe the error magnitude of finite series approximations of a given function (i.e. truncated Taylor series). In a more engineering context, such a notation is useful in numerical analysis to describe the rate of convergence of a numerical scheme. As well, it is employed in asymptotic analysis of mathematical models.

Let f and g be two functions, defined in $X \in \mathbb{R}$. It is said that $f(x) = O(g(x))$ in a neighbourhood of $x_0 \in X$ if and only if

$$\exists \delta > 0, K > 0 : |f(x)| \leq K |g(x)| \text{ for } |x - x_0| < \delta. \quad (\text{C.1})$$

Analogously, if $g(x)$ is non-zero around x_0 , this alternative definition holds

$$f(x) = O(g(x)) \iff \lim_{x \rightarrow x_0} \left| \frac{f(x)}{g(x)} \right| \in \mathbb{R} < \infty. \quad (\text{C.2})$$

This notation provides an upper bound on the growth rate of the function f around x_0 , by using a simpler function g . Strictly speaking, it should be written $f \in O(g)$ instead of $f = O(g)$ because $O(g)$ is, in fact, a class of functions. However, in the present dissertation we always make use of the equal sign instead of \in for the sake of simplicity. In practical cases, the point to which the behaviour of f is evaluated is often $x_0 = \infty$ or $x_0 = 0$: these kinds of analysis are called *infinite asymptotic* and *infinitesimal asymptotic*, respectively. Sometimes, it is useful to simplify a mathematical equation, representing a physical phenomenon, by omitting the terms with smaller growth rates. In these problems it is crucial to express the various terms of the equation as *Big O* of different power functions of the same infinitesimal function g . It should be noted that the big O notation does not mean “of order of” in an engineering sense. In fact, the constant factor K in Def. (C.1) could be bigger than 1.

Properties

There are some properties of the *Big O* notation that are very useful in calculations. In the following they are briefly reported.

Product rule

$$f_1(x) = O(g_1(x)), f_2(x) = O(g_2(x)) \Rightarrow f_1(x)f_2(x) = O(g_1(x)g_2(x)). \quad (\text{C.3})$$

Sum rule

$$f_1(x) = O(g_1(x)), f_2(x) = O(g_2(x)) \Rightarrow f_1(x) + f_2(x) = O(|g_1(x)| + |g_2(x)|). \quad (\text{C.4})$$

Multiplication by a constant

Let c be a non-zero constant.

$$f(x) = O(cg(x)) \Rightarrow f(x) = O(g(x)). \quad (\text{C.5})$$

Analogously,

$$f(x) = O(g(x)) \Rightarrow cf(x) = O(g(x)). \quad (\text{C.6})$$

Note. Any function which is continuous in a given point x_0 is $O(1)$ there, since

$$\lim_{x \rightarrow x_0} f(x) \in \mathbb{R} < \infty.$$

Difference between *Big O* and *Small o* notations

Now, it could be useful also to recall the *small o* notation which has a different meaning.

Let f and g be two functions defined in $X \in \mathbb{R}$. It is said that $f \in o(g)$ in a neighbourhood of $x_0 \in X$ if and only if

$$\forall \varepsilon > 0, \exists \delta > 0 : |f(x)| \leq \varepsilon |g(x)| \text{ for } |x - x_0| < \delta. \quad (\text{C.7})$$

In this case the function g grows by far faster than f around x_0 . Hence, this condition is stronger than $f(x) = O(g(x))$. It is important to stress that, although $f = o(g) \Rightarrow f = O(g)$, the opposite implication is not necessarily true.

Complete Bibliography

- Abgrall, R. and Karni, S. (2009). Two-Layer Shallow Water System: A Relaxation Approach. *SIAM Journal on Scientific Computing* **31**, 1603–1627.
- Adrian, R. and Westerweel, J. (2010). *Particle image velocimetry*, volume 30. Cambridge University Press.
- Ancey, C. (2001a). Dry granular flows down an inclined channel: Experimental investigations on the frictional-collisional regime. *Physical Review E* **65**, 1–19.
- Ancey, C. (2001b). Snow Avalanches. In Balmforth, N. J. and Provenzale, A., editors, *Geomorphological fluid mechanics - Lecture notes in Physics Volume 582*, pages 319–338. Springer.
- Ancey, C. (2007). Plasticity and geophysical flows: A review. *Journal of Non-Newtonian Fluid Mechanics* **142**, 4–35.
- Ancey, C., Coussot, P., and Evesque, P. (1999). A theoretical framework for granular suspensions in a steady simple shear flow. *Journal of Rheology* **43**, 1673–1699.
- Arfken, G. B. and Weber, H. J. (2005). *Mathematical Methods for Physicists*. Elsevier, 6th edition.
- Armanini, A., Capart, H., Fraccarollo, L., and Larcher, M. (2005). Rheological stratification in experimental free-surface flows of granular-liquid mixtures. *Journal of Fluid Mechanics* **532**, 269–319.
- Armanini, A., Larcher, M., and Fraccarollo, L. (2009). Intermittency of rheological regimes in uniform liquid-granular flows. *Physical Review E* **79**, 051306.
- Audusse, E. (2005). A multilayer Saint-Venant model: Derivation and numerical validation. *Discrete and Continuous Dynamical Systems - Series B* **5**, 189–214.
- Audusse, E. and Bristeau, M.-O. (2007). Finite-Volume Solvers for a Multilayer Saint-Venant System. *International Journal of Applied Mathematics and Computer Science* **17**, 311–320.
- Bagnold, R. A. (1954). Experiments on a Gravity-Free Dispersion of Large Solid Spheres in a Newtonian Fluid under Shear. *Proceedings of the Royal Society A: Mathematical, Physical and Engineering Sciences* **225**, 49–63.
- Bale, D. S., LeVeque, R. J., Mitran, S., and Rossmannith, J. A. (2002). A Wave Propagation Method for Conservation Laws and Balance Laws with Spatially Varying Flux Functions. *SIAM Journal on Scientific Computing* **24**, 955–978.

- Bartelt, P., Salm, B., and Gruber, U. (1999). Calculating dense-snow avalanche runout using a Voellmyfluid model with active/passive longitudinal straining. *Journal of Glaciology* **45**, 242–254.
- Bouchut, F. and Westdickenberg, M. (2004). Gravity driven shallow water models for arbitrary topography. *Communications in Mathematical Sciences* **2**, 359–389.
- Brivois, O., Bonelli, S., and Borghi, R. (2007). Soil erosion in the boundary layer flow along a slope: a theoretical study. *European Journal of Mechanics - B/Fluids* **26**, 707–719.
- Brown, G. L. and Roshko, A. (1974). On density effects and large structure in turbulent mixing layers. *Journal of Fluid Mechanics* **64**, 775–816.
- Campbell, C. S. (1990). Rapid granular flows. *Annual Review of Fluid Mechanics* **22**, 57–90.
- Capart, H. and Young, D. (2002). Two-layer shallow water computations of torrential geomorphic flows. In *Proceedings of River Flow*, pages 1003–1012.
- Castro, M., Macías, J., and Parés, C. (2002). A Q -scheme for a class of systems of coupled conservation laws with source term. Application to a two-layer 1-D shallow water system. *ESAIM: Mathematical Modelling and Numerical Analysis* **35**, 107–127.
- Castro, M. J., Frings, J., Noelle, S., Parés, C., and Puppo, G. (2010). On the hyperbolicity of two-and three-layer shallow water equations. In *Series in Contemporary Applied Mathematics: Proceedings of the 13th International Conference on Hyperbolic Problems*.
- Castro, M. J., García-Rodríguez, J. A., González-Vida, J. M., Macías, J., Parés, C., and Vázquez-Cendón, M. (2004). Numerical simulation of two-layer shallow water flows through channels with irregular geometry. *Journal of Computational Physics* **195**, 202–235.
- Castro-Díaz, M. J., Fernández-Nieto, E. D., González-Vida, J. M., and Parés-Madroñal, C. (2011). Numerical Treatment of the Loss of Hyperbolicity of the Two-Layer Shallow-Water System. *Journal of Scientific Computing* **48**, 16–40.
- Chen, S.-C. and Peng, S.-H. (2006). Two-dimensional numerical model of two-layer shallow water equations for confluence simulation. *Advances in Water Resources* **29**, 1608–1617.
- Chen, S.-C., Peng, S.-H., and Capart, H. (2007). Two-layer shallow water computation of mud flow intrusions into quiescent water. *Journal of Hydraulic Research* **45**, 13–25.
- Crosta, G. B., Imposimato, S., and Roddeman, D. (2009). Numerical modeling of 2-D granular step collapse on erodible and nonerodible surface. *Journal of Geophysical Research* **114**,
- da Cruz, F., Emam, S., Prochnow, M., Roux, J.-N., and Chevoir, F. (2005). Rheophysics of dense granular materials : Discrete simulation of plane shear flows. *Physical Review E* **72**, 24.
- Denlinger, R. P. and Iverson, R. M. (2001). Flow of variably fluidized granular masses across three-dimensional terrain: 2. Numerical predictions and experimental tests. *Journal of Geophysical Research* **106**, 553.

- Doyle, E. E., Hogg, A. J., and Mader, H. M. (2010). A two-layer approach to modelling the transformation of dilute pyroclastic currents into dense pyroclastic flows. *Proceedings of the Royal Society A: Mathematical, Physical and Engineering Sciences* **467**, 1348–1371.
- Drake, T. G. (1990). Structural features in granular flows. *Journal of Geophysical Research* **95**, 8681–8696.
- Eckart, W. and Gray, J. M. N. T. (2003). Particle Image Velocimetry (PIV) for granular avalanches on inclined planes. In Hutter, K. and Kirchner, N., editors, *Lecture Notes in Applied & Computational Mechanics (Vol. 11)*, chapter Dynamic Response of Granular and Porous Materials under Large Catastrophic Deformations, pages 195–218. Springer.
- Ertas, D., Grest, G. S., Halsey, T. C., Levine, D., and Silbert, L. E. (2001). Gravity-driven dense granular flows. *Europhysics Letters (EPL)* **56**, 214–220.
- Fernández-Nieto, E., Bouchut, F., Bresch, D., Castro Díaz, M., and Mangeney, A. (2008). A new Savage-Hutter type model for submarine avalanches and generated tsunamis. *Journal of Computational Physics* **227**, 7720–7754.
- Forterre, Y. and Pouliquen, O. (2008). Flows of Dense Granular Media. *Annual Review of Fluid Mechanics* **40**, 1–24.
- Fraccarollo, L. and Capart, H. (2002). Riemann wave description of erosional dam-break flows. *Journal of Fluid Mechanics* **461**, 183–228.
- Fraccarollo, L., Capart, H., and Zech, Y. (2003). A Godunov method for the computation of erosional shallow water transients. *International Journal for Numerical Methods in Fluids* **41**, 951–976.
- Goldhirsch, I. (2003). Rapid Granular Flows. *Annual Review of Fluid Mechanics* **35**, 267–293.
- Gray, J. (1999). Loss of hyperbolicity and ill-posedness of the viscous-plastic sea ice rheology in uniaxial divergent flow. *Journal of physical oceanography* **29**, 2920–2929.
- Gray, J. M. N. T., Irmer, A., Tai, Y. C., and Hutter, K. (1999). Plane and oblique Shocks in shallow granular flows. In *22nd International Symposium on Shock Waves*, pages 1447–1452, London, U.K. Imperial College.
- Gray, J. M. N. T., Tai, Y. C., and Noelle, S. (2003). Shock waves, dead zones and particle-free regions in rapid granular free-surface flows. *Journal of Fluid Mechanics* **491**, 161–181.
- Gray, J. M. N. T., Wieland, M., and Hutter, K. (1999). Gravity-driven free surface flow of granular avalanches over complex basal topography. *Proceedings of the Royal Society A: Mathematical, Physical and Engineering Sciences* **455**, 1841–1874.
- Greco, M., Iervolino, M., and Vacca, A. (2008). Boundary conditions in a two-layer geomorphological model: Application to a hydraulic jump over a mobile bed. *Journal of Hydraulic Research* **46**, 856–860.

- Greve, R. and Hutter, K. (1993). Motion of a Granular Avalanche in a Convex and Concave Curved Chute: Experiments and Theoretical Predictions. *Philosophical Transactions of the Royal Society A: Mathematical, Physical and Engineering Sciences* **342**, 573–600.
- Greve, R., Koch, T., and Hutter, K. (1994). Unconfined Flow of Granular Avalanches along a Partly Curved Surface. I. Theory. *Proceedings of the Royal Society A: Mathematical, Physical and Engineering Sciences* **445**, 399–413.
- Harten, A., Lax, P., and Leer, B. V. (1983). On upstream differencing and Godunov-type schemes for hyperbolic conservation laws. *SIAM review* **25**, 35–61.
- Hui, W. H. (2004). A unified coordinates approach to computational fluid dynamics. *Journal of Computational and Applied Mathematics* **163**, 15–28.
- Hui, W. H. (2007). The unified coordinate system in computational fluid dynamics. *Commun. Comput. Phys* **2**, 577–610.
- Hui, W. H. and Koudriakov, S. (2002). Computation of the Shallow Water Equations Using the Unified Coordinates. *SIAM Journal on Scientific Computing* **23**, 1615–1654.
- Hui, W. H., Li, P. Y., and Li, Z. (1999). A Unified Coordinate System for Solving the Two-Dimensional Euler Equations. *Journal of Computational Physics* **153**, 596–637.
- Hungr, O. (1995). A model for the runout analysis of rapid flow slides, debris flows, and avalanches. *Canadian Geotechnical Journal* **32**, 610–623.
- Hungr, O. (2008). Simplified models of spreading flow of dry granular material. *Canadian Geotechnical Journal* **45**, 1156–1168.
- Hungr, O. and Morgenstern, N. (1984a). Experiments on the flow behaviour of granular materials at high velocity in an open channel. *Geotechnique* **34**,
- Hungr, O. and Morgenstern, N. (1984b). High velocity ring shear tests on sand. *Geotechnique* **34**,
- Hunt, M. L., Zenit, R., Campbell, C. S., and Brennen, C. E. (2002). Revisiting the 1954 suspension experiments of R. A. Bagnold. *Journal of Fluid Mechanics* **452**, 1–24.
- Hutter, K. (2005). Geophysical granular and particle-laden flows: review of the field. *Philosophical transactions. Series A, Mathematical, physical, and engineering sciences* **363**, 1497–505.
- Hutter, K. and Koch, T. (1991). Motion of a Granular Avalanche in an Exponentially Curved Chute: Experiments and Theoretical Predictions. *Philosophical Transactions of the Royal Society A: Mathematical, Physical and Engineering Sciences* **334**, 93–138.
- Hutter, K., Savage, S. B., and Nohguchi, Y. (1989). Numerical, analytical, and laboratory experimental studies of granular avalanche flows. *Annals of Glaciology* **13**, 109–116.
- Hutter, K., Wang, Y., and Pudasaini, S. P. (2005). The Savage-Hutter avalanche model: how far can it be pushed? *Philosophical transactions. Series A, Mathematical, physical, and engineering sciences* **363**, 1507–28.

- Iverson, R. M. (1997). The physics of debris flows. *Reviews of Geophysics* **35**, 245.
- Iverson, R. M. and Vallance, J. W. (2001). New views of granular mass flows. *Geology* **29**, 115.
- Jaky, J. (1944). The coefficient of earth pressure at rest. *Journal of the Society of Hungarian Architects and Engineers* **78**, 355–358.
- Jop, P., Forterre, Y., and Pouliquen, O. (2005). Crucial role of sidewalls in granular surface flows: consequences for the rheology. *Journal of Fluid Mechanics* **541**, 167–192.
- Jop, P., Forterre, Y., and Pouliquen, O. (2006). A constitutive law for dense granular flows. *Nature* **441**, 727–30.
- Josserand, C., Lagrée, P.-Y., and Lhuillier, D. (2004). Stationary shear flows of dense granular materials: a tentative continuum modelling. *The European physical journal. E, Soft matter* **14**, 127–35.
- Katzenbach, R., Bergmann, C., Bachmann, G., Gutberlet, C., and Hutter, K. (2011). *Particle Image Velocimetry Measuring Methods for Soil Movements in Geotechnics*. Number 20. Darmstadt, darmstadt edition.
- Keane, R. D. and Adrian, R. J. (1993). Theory of cross-correlation analysis of piv images. In *Flow visualization and image analysis*, pages 1–25. Springer.
- Kim, J. and LeVeque, R. J. (2008). Two-layer shallow water system and its applications. In *12th International Conference on Hyperbolic Problems*, volume m, pages 1–8, College Park, Maryland.
- Komatsu, T., Inagaki, S., Nakagawa, N., and Nasuno, S. (2001). Creep Motion in a Granular Pile Exhibiting Steady Surface Flow. *Physical Review Letters* **86**, 1757–1760.
- Lambe, T. and Whitman, R. (1991). *Soil Mechanics*. Series in Soil Engineering. Wiley.
- Lawrence, G. A. (1990). On the hydraulics of Boussinesq and non-Boussinesq two-layer flows. *Journal of Fluid Mechanics* **215**, 457.
- Lê, L. and Pitman, E. B. (2010). A Model for Granular Flows over an Erodible Surface. *SIAM Journal on Applied Mathematics* **70**, 1407–1427.
- LeVeque, R. (2002). *Finite volume methods for hyperbolic problems*, volume 31. Cambridge university press.
- LeVeque, R. and George, D. (2008). High-resolution finite volume methods for the shallow water equations with bathymetry and dry states. *Advanced numerical models for simulating tsunami waves and runoff* **10**, 43–73.
- Long, R. R. (1956). Long waves in a two-fluid system. *Journal of Meteorology* **13**, 70–74.
- Luca, I., Hutter, K., Kuo, C. Y., and Tai, Y. C. (2010). Two-layer models for shallow avalanche flows over arbitrary variable topography. *International Journal of Advances in Engineering Sciences and Applied Mathematics* **1**, 99–121.

- Lueptow, R. M., Akonur, A., and Shinbrot, T. (2000). PIV for granular flows. *Experiments in Fluids* **28**, 183–186.
- Mangeney-Castelnau, A., Bouchut, F., Vilotte, J., Lajeunesse, E., Aubertin, A., and Pirulli, M. (2005). On the use of saint venant equations to simulate the spreading of a granular mass. *Journal of Geophysical Research: Solid Earth (1978–2012)* **110**,.
- Midi, G. (2004). On dense granular flows. *The European physical journal. E, Soft matter* **14**, 341–65.
- Nishimura, K. (1991). Studies on the Fluidized Snow Dynamics. In *Contributions from the Institute of Low Temperature Science A37*, pages 1–55.
- Noelle, S. (2010). The dynamics of shallow fluid flows : Modeling and numerical analysis. In *i-MATH School on Numerical Solutions of Partial Differential Equations*, pages 1–9, Malaga.
- Pouliquen, O. (1999). Scaling laws in granular flows down rough inclined planes. *Physics of fluids* **11**, 542–548.
- Pouliquen, O. (2009). Granular Flows. In *Séminaire Poincaré XIII*, pages 69–100.
- Pouliquen, O. and Chevoir, F. (2002). Dense flows of dry granular material. *Comptes Rendus Physique* **3**, 163–175.
- Pouliquen, O. and Forterre, Y. (2002). Friction law for dense granular flows: application to the motion of a mass down a rough inclined plane. *Journal of Fluid Mechanics* **453**, 133–151.
- Pudasaini, S. P. and Hutter, K. (2007). *Avalanche dynamics: dynamics of rapid flows of dense granular avalanches*. Springer.
- Pudasaini, S. P., Hutter, K., Hsiau, S.-S., Tai, S.-C., Wang, Y., and Katzenbach, R. (2007). Rapid flow of dry granular materials down inclined chutes impinging on rigid walls. *Physics of fluids* **19**, 053302.
- Raffel, M., Willert, C., and Kompenhans, J. (1998). *Particle Image Velocimetry: A Practical Guide*. Experimental Fluid Mechanics. Springer.
- Rankine, W. M. (1870). On the thermodynamic theory of waves of finite longitudinal disturbance. *Philosophical Transactions of the Royal Society of London* pages 277–288.
- Reynolds, O. (1885). On the dilatancy of media composed of rigid particles in contact. *Philos. Mag. Ser. 5* **50**,.
- Roberts, A. (1969). An investigation of the gravity flow of noncohesive granular materials through discharge chutes. *J. Eng. Ind.* **91**,.
- Roe, P. (1981). Approximate Riemann solvers, parameter vectors, and difference schemes. *Journal of Computational Physics* **43**, 357–372.
- Salm, B. (2004). A short and personal history of snow avalanche dynamics. *Cold Regions Science and Technology* **39**, 83–92.

- Sarno, L., Carravetta, A., Martino, R., and Tai, Y.-C. (2011). A two-layer approach to describe granular flows over rough surface. In *The 35th National Conference on Theoretical and Applied Mechanics*. Society of Theoretical and Applied Mechanics of the Republic of China.
- Sarno, L., Carravetta, A., Martino, R., and Tai, Y.-C. (2012). The pressure coefficient in dam-breaks flows of dry granular matter. *Submitted to Journal of Hydraulic Engineering*.
- Sarno, L., Papa, M. N., and Martino, R. (2011). Dam-break flows of dry granular materials on gentle slopes. In Genevois, R., Hamilton, D. L., and Prestininzi, A., editors, *5th Int. Conf. on Debris-Flow Hazards Mitigation: Mechanics, Prediction and Assessment*. Italian Journal of Engineering Geology and Environment. Casa Editrice Università “La Sapienza”.
- Savage, S. (1984). The mechanics of rapid granular flows. *Advances in applied mechanics* **24**, 289–366.
- Savage, S. B. (1979). Gravity flow of cohesionless granular materials in chutes and channels. *Journal of Fluid Mechanics* **92**, 53–96.
- Savage, S. B. and Hutter, K. (1989). The motion of a finite mass of granular material down a rough incline. *Journal of Fluid Mechanics* **199**, 177–215.
- Savage, S. B. and Hutter, K. (1991). The dynamics of avalanches of granular materials from initiation to runout. Part I: Analysis. *Acta Mechanica* **86**, 201–223.
- Savary, C. and Zech, Y. (2007). Boundary conditions in a two-layer geomorphological model. Application to a hydraulic jump over a mobile bed. *Journal of Hydraulic Research* **45**, 316–332.
- Seminara, G. and Tubino, M. (1993). Debris flows: Meccanica, controllo e previsione. *Gruppo Nazionale per la Difesa dalle Catastrofi Idrogeologiche. Roma, CNR, Presidenza del Consiglio del Ministri, Dipartimento della Protezione Civile* pages 3–8.
- Sheng, L.-T., Kuo, C.-Y., Tai, Y. C., and Hsiau, S.-S. (2011). Indirect measurements of stream-wise solid fraction variations of granular flows accelerating down a smooth rectangular chute. *Experiments in Fluids* **51**, 1329–1342.
- Tai, Y. C. and Gray, J. M. N. T. (1998). Limiting stress states in granular avalanches. *Annals of Glaciology* **26**, 272–276.
- Tai, Y. C., Hutter, K., and Gray, J. M. N. T. (2001). Dense granular avalanches: mathematical description and experimental validation. In Balmforth, N. and Provenzale, A., editors, *Lecture notes in Physics Volume 582*, volume 582, chapter Geomorphol, pages 339–366. Springer, Berlin.
- Tai, Y. C. and Kuo, C. Y. (2008). A new model of granular flows over general topography with erosion and deposition. *Acta Mechanica* **199**, 71–96.
- Tai, Y. C., Kuo, C.-Y., and Hui, W. H. (2012). An alternative depth-integrated formulation for granular avalanches over temporally varying topography with small curvature. *Geophysical & Astrophysical Fluid Dynamics* **106**, 596–629.

- Tai, Y. C., Kuo, C.-Y., Lu, J. W. Z., Leung, A. Y. T., Iu, V. P., and Mok, K. M. (2010). Collapses of Granular Column with Time Varying Topography. In *AIP Conference Proceedings*, pages 845–850.
- Tai, Y. C. and Lin, Y.-C. (2008). A focused view of the behavior of granular flows down a confined inclined chute into the horizontal run-out zone. *Physics of Fluids* **20**, 123302.
- Tai, Y. C., Noelle, S., Gray, J. M. N. T., and Hutter, K. (2002). Shock-Capturing and Front-Tracking Methods for Granular Avalanches. *Journal of Computational Physics* **175**, 269–301.
- Voellmy, A. (1955). *Über die Zerstörungskraft von Lawinen: L'Espacement des râteliers de retenue de la neige*. W. Jegher & A. Ostertag.
- Vollmöller, P. (2004). A shock-capturing wave-propagation method for dry and saturated granular flows. *Journal of Computational Physics* **199**, 150–174.
- Zhang, W. and Cundy, T. W. (1989). Modeling of two-dimensional overland flow. *Water Resources Research* **25**, 2019–2035.